

# Topological spectral form factor reveals emergent non-Hermitian single-particle $\mathcal{PT}$ transitions from many-body quantum chaos

Daniel Harkin\*

*Department of Physics, Lancaster University, Lancaster LA1 4YB, United Kingdom*

Chun Y. Leung<sup>†</sup>

*Department of Mathematics, Physics and Electrical Engineering,  
Northumbria University, Newcastle upon Tyne NE1 8ST, United Kingdom and  
Department of Physics, Lancaster University, Lancaster LA1 4YB, United Kingdom*

Amos Chan<sup>‡</sup>

*Department of Physics, University of Warwick, Coventry, CV4 7AL, United Kingdom and  
Department of Physics, Lancaster University, Lancaster LA1 4YB, United Kingdom*

(Dated: June 18, 2026)

In equilibrium physics, topological defect insertions in quantum and classical partition functions provide non-perturbative probes of phase transitions beyond local observables. In non-equilibrium physics, the spectral form factor provides a minimal probe of universal quantum dynamics, and admits a representation as a product of two partition functions at imaginary inverse temperature. We define the topological spectral form factor (TopSFF) by inserting topological defects acting non-trivially on the doubled partition functions, producing mismatched spacetime world-sheet topologies. For the minimal  $\mathbb{Z}_2$  spatially extended defect, implemented by the global swap operator, we derive an exact mapping of the TopSFF of a generic 1D many-body chaotic system to an emergent (3+1)D non-Hermitian single-particle problem describing a temporal domain wall (tDW). We show analytically that the effective tDW dynamics undergoes a  $\mathcal{PT}$  symmetry breaking transition at a finite interaction strength  $\epsilon_{\text{EP}}$ : below  $\epsilon_{\text{EP}}$ , the leading modes are polarized into Gaussian or non-Gaussian tDW sectors and the TopSFF varies monotonically and exponentially with system size; above  $\epsilon_{\text{EP}}$ , the tDW sectors hybridize and the TopSFF oscillates with system size; at the exceptional point  $\epsilon_{\text{EP}}$ , Jordan non-diagonality produces a linear-in-system-size enhancement. For temporally extended topological defects, we derive exact universal scaling forms for the TopSFF free energy in systems with time reversal or time translation symmetry, and verify them numerically in independent models.

Topological defects are robust non-perturbative structures that arise when locally ordered degrees of freedom cannot be made globally consistent, providing probes of global properties beyond the reach of local observables [1, 2]. In equilibrium statistical mechanics and quantum field theory, inserting a topological defect  $\hat{\mathcal{D}}$  into the partition function,  $Z_{\mathcal{D}}(\beta) := \text{Tr}(\hat{\mathcal{D}}e^{-\beta\hat{H}})$ , with Hamiltonian  $\hat{H}$  and inverse temperature  $\beta$ , diagnoses symmetry breaking, dualities, anomalies and topological phases [3–7]. Their key feature is topological invariance: subject to local commutation relations, topological defects can be deformed without changing the partition function.

In non-equilibrium quantum dynamics, the partition function viewpoint has a natural analogue: The analytically continued partition function,  $Z(\beta = it) := \text{Tr}e^{-i\hat{H}t} = \text{Tr}\hat{U}(t)$ , is the trace of the propagator and probes the model-dependent one-point spectral density. The minimal universal probe is instead the spectral form factor (SFF),  $K(t) = |Z(it)|^2$ , the Fourier transform of the two-level spectral correlation function [8, 9]. Equivalently, the SFF is a doubled partition function at imaginary inverse temperature, or a double sum over Feynman paths. In generic many-body quantum chaotic systems [10–12], the connected SFF displays the bump-

ramp-plateau behaviour [13]. The ramp and plateau are well-known universal signatures of quantum chaos [9, 13–24], whereas the bump is an intrinsically many-body phenomenon: it arises from spatial domain walls between locally distinct pairings of Feynman paths [13], can be probed as topological defects via twisted boundary conditions [25], and exhibits universality beyond random matrix theory (RMT) [21, 26, 27]. Related deviations from RMT in the SFF bump regime have since been identified across a range of many-body systems [28–35].

Exploiting the doubled structure of the SFF, we define the topological spectral form factor (TopSFF) by inserting a topological defect that acts non-trivially on the doubled partition function [Fig. 2],

$$K_{\text{top}} := \text{Tr} \left[ \hat{\mathcal{D}}(\hat{U}_p \otimes \hat{U}_p^*) \right], \quad \left[ f_{\text{d}}(\hat{\mathcal{D}}), f_{\text{q}}(\hat{U}_p \otimes \hat{U}_p^*) \right] = 0. \quad (1)$$

Here  $\hat{\mathcal{D}}$  is a defect operator and  $\hat{U}_p \otimes \hat{U}_p^*$  is the doubled many-body evolution operator, both acting on the doubled Hilbert space. In general, extended topological defects may be inserted at arbitrary locations, orientations and slices in spacetime. We focus on two representative orientations: spatially extended defects with  $p = \text{t}$ , which probe the interplay between topological defects and unitary time evolution; temporally extended defects

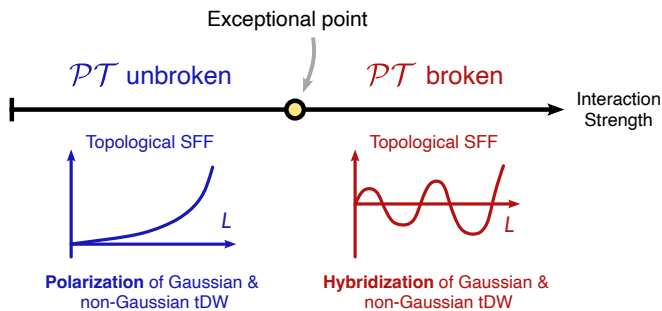


FIG. 1. **Topological SFF and  $\mathcal{PT}$  transitions.** In generic quantum many-body chaotic systems, TopSFF with global swap operator inserted as a spatially extended defect exhibits an emergent  $\mathcal{PT}$  symmetry breaking transition at a finite interaction strength. In the  $\mathcal{PT}$  unbroken phase, the leading modes are polarised into Gaussian or non-Gaussian temporal domain walls (tDW), producing monotonic exponential scaling in system size  $L$  at sufficiently large  $L$ . In the  $\mathcal{PT}$  broken phase, the two tDW species hybridise, producing oscillations in  $L$  with an exponential envelope. At the exceptional point, mode coalescence renders the effective tDW dynamics non-diagonalizable, producing a Jordan-block contribution with an additional polynomial prefactor in  $L$ .

with  $p = s$ , which probe the generally non-unitary spatial propagation. The commutation relation encodes the local pulling-through condition responsible for the topological invariance of the TopSFF. The model-dependent maps  $f_d$  and  $f_q$  select, respectively, the defect component and the corresponding component of the doubled evolution that commute locally. In this manuscript, we focus on the minimal non-trivial  $\mathbb{Z}_2$  defect  $\hat{\mathcal{D}} = \hat{O} \otimes \hat{1}$ , implemented by the global swap operator  $\hat{O} = \hat{S}$ , inserted into the doubled evolution of generic quantum many-body chaotic circuits  $\hat{U}(t, L)$  [Fig. 3(a)]. In one dimension, acting on  $L$  qudits,  $\hat{S} |a_1, a_2, \dots, a_L\rangle = |a_L, \dots, a_2, a_1\rangle$ .  $f_d$  is the identity map, while  $f_q(\hat{U}_p(t, L) \otimes \hat{U}_p^*(t, L))$  selects the time evolution operator (orange) for  $p = t$ , or the dual transfer matrix (purple) for  $p = s$  in Fig. 3(a). The commutation relation is local in both space and time after the folding procedure discussed below in Fig. 3(b). We emphasize that the asymmetric and non-trivial insertion onto the doubled partition function is needed to create mismatched world-sheet topologies – a Klein bottle and a torus [Fig. 2(b)] – thereby inducing a topological defect in the pairing structure of Feynman paths; see also [25]. In contrast, with the matched insertion  $\hat{\mathcal{D}} = \hat{S} \otimes \hat{S}$ , the TopSFF reduces to the ordinary SFF of a system with a twisted boundary condition, and does not generate mismatched pairing topologies and emergent single-particle defect dynamics described below, see [36] and [37]. More complicated topological defects will be discussed in an upcoming work [38]. After the Heisenberg scale, set by the Hilbert space dimension, the TopSFF in generic chaotic systems displays plateau behaviour predicted by RMT, whose explicit solution is given in [36].

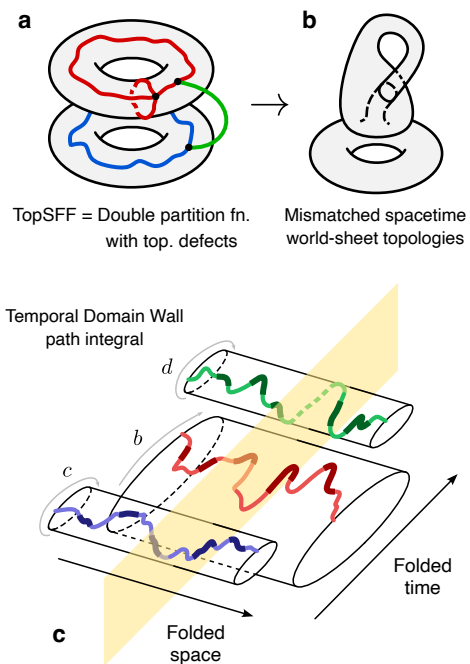
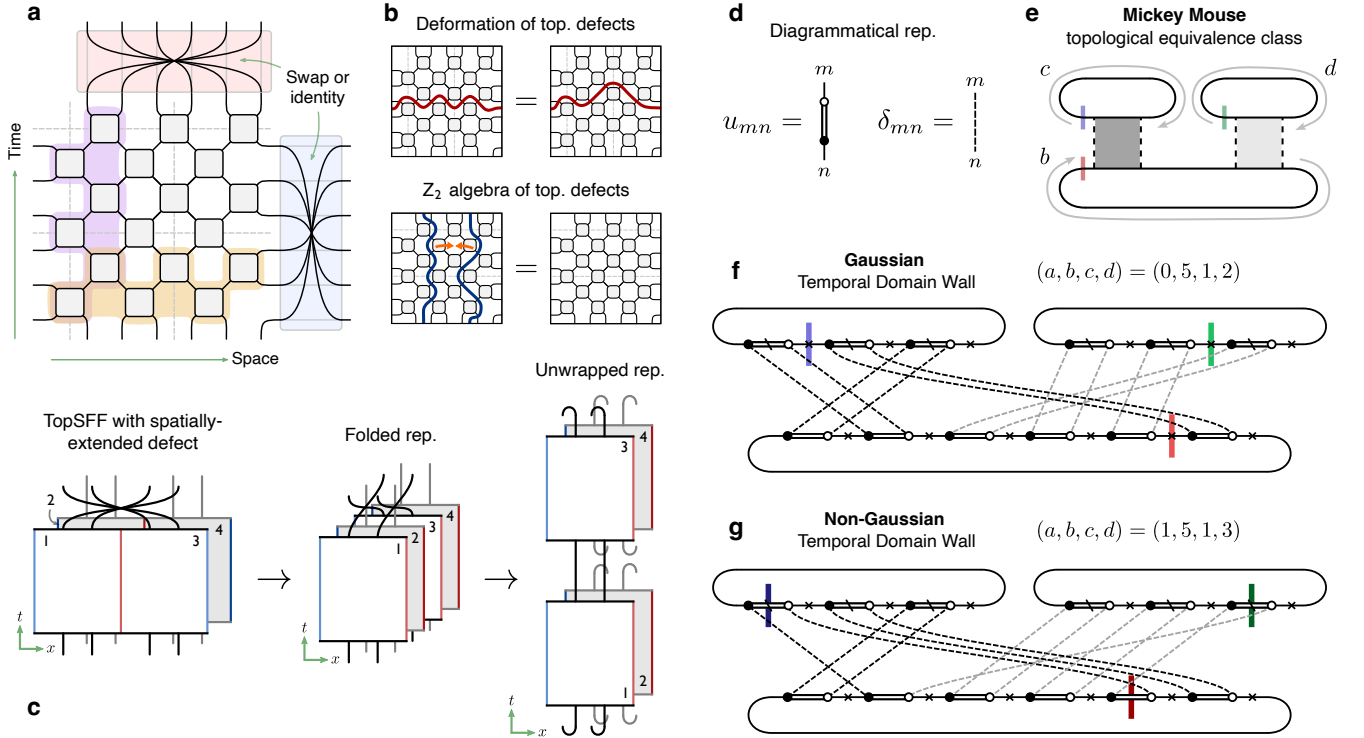


FIG. 2. **Topological SFF as path integral of temporal domain walls.** (a) TopSFF is constructed by inserting non-trivial topological defects onto SFF as double partition functions, leading to (b) mismatched spacetime world-sheet topologies. (c) For a  $(1 + 1)$ D generic quantum many-body chaotic system, the ensemble-averaged TopSFF with a spatially extended global swap defect exactly maps to an effective  $(3 + 1)$ D path integral of emergent tDW (yellow slice). The tDW has two species, Gaussian and non-Gaussian (lighter and darker colours), and is specified by three folded-time loop coordinates while propagating along space as a non-Hermitian single particle.

From now on, we focus instead on universal many-body effects beyond RMT in TopSFF in the pre-Heisenberg regime.

**Path integral of temporal domain walls.** We first consider the TopSFF of a spatially extended global swap defect  $\hat{\mathcal{D}} = \hat{S} \otimes \hat{1}$  acting in generic quantum many-body chaotic systems  $\hat{U}_t(t, L) = \hat{U}^t$  with discrete time translational symmetry, realised by the parity inversion symmetric Random Phase Model (RPM) with local Hilbert space dimension  $q$  (see Methods). The tensor network for  $K_{\text{top}} = \text{Tr}[\hat{S}\hat{U}^t] \text{Tr}[\hat{U}^{*t}]$  contains two mismatched world-sheets [Fig. 3(c)]. Folding along the parity inversion axes stacks parity-related degrees of freedom, while unwrapping each folded site in the time direction exposes three folded-time loops: one long  $b$ -loop associated with  $\text{Tr}[\hat{S}\hat{U}^t]$ , and two shorter loops, denoted the  $c$ - and  $d$ -loops, associated with  $\text{Tr}[\hat{U}^{*t}]$ . We represent each local Haar-random unitary gate element  $u_{mn}$  of the RPM with two dots connected by a double line, representing the incoming and outgoing degrees of freedom  $m$  and  $n$  of  $u_{mn}$  [Fig. 3(d)]. Upon Haar averaging, the indices of local unitary gates and their complex conjugations



**FIG. 3. Temporal domain walls and Mickey Mouse diagrams.** (a) A global swap defect or the identity operator may be inserted along the spatial or temporal direction of the worldsheet describing a quantum many-body system evolved by local unitary gates. (b) Topological invariance allows local deformations of the defect line after folding described in (c), while two swap defects fuse to the identity, realizing the  $\mathbb{Z}_2$  algebra. (c) For the TopSFF with a spatially extended global swap defect, worldsheets 3 and 4 are folded onto worldsheets 1 and 2 along the parity inversion axes (red and blue), so that parity-related degrees of freedom are stacked. Unwrapping each folded site in the time direction yields three loops at each folded site: one large loop formed by worldlines in  $\text{Tr}[\hat{S}\hat{U}]$  passing through sheets 1 and 3, and two smaller loops formed by worldlines in  $\text{Tr}[\hat{U}^*]$  passing through sheets 2 and 4. (d) Diagrammatic notation for a local Haar-random unitary gate element  $u_{mn}$  and for the contraction  $\delta_{mn}$  generated from ensemble averaging. (e) We prove that at large  $q$ , the leading local diagrams form the “Mickey Mouse” topological equivalence class, where dashed ribbons denote a series of parallel contractions in (d) [36]. (f,g) Mickey Mouse diagrams contain temporal domain walls (tDW). The red, blue and green vertical lines mark the tDW positions on the three folded-time loops. Each tDW is labelled by  $(a, b, c, d)$ , where  $(b, c, d)$  specify the folded-time loop coordinates, while  $a = 0, 1$  distinguishes the Gaussian tDW. A Gaussian tDW crosses a physical worldline represented by a single line, whereas a non-Gaussian tDW crosses a unitary double line.

are contracted with weights given by Weingarten functions [19, 39, 40] [Fig. 3(d) right]. In the large- $q$  limit, we prove that the leading local diagrams belong to the “Mickey Mouse” topological equivalence class [Fig. 3(e)]. Each Mickey Mouse diagram contains a temporal domain wall (tDW), separating two locally distinct domains along folded time: one with parallel contractions between the  $b$ - and  $c$ -loops, and the other with contractions between the  $b$ - and  $d$ -loops. The equivalence class is defined modulo independent cyclic rotations along the three folded-time loops, labelled  $b$ ,  $c$  and  $d$ . There are two types of tDW. A Gaussian tDW crosses the physical worldline of the long  $b$ -loop, whereas a non-Gaussian tDW crosses the unitary double line, i.e. the two matrix indices of the associated unitary are contracted separately with  $c$ - and  $d$ -loops [Fig. 3(f,g)]. A local tDW configuration is labelled by  $\rho = (a, b, c, d)$ , with  $a = 0, 1$  distinguishing the Gaussian and non-Gaussian species,

and  $(b, c, d) \in \{1, \dots, 2t\} \times \{1, \dots, t\}^2$  specifying the three folded-time loop coordinates, giving  $4t^3$  configurations in total. Importantly, the corresponding leading Weingarten weights differ by a sign:  $+1$  for a Gaussian tDW and  $-1$  for a non-Gaussian tDW. The interacting gates generate a generalized Boltzmann factor  $\mathcal{B}(\rho_1, \rho_2)$  between neighbouring folded sites. Translational invariance along the three folded-time loops allows  $\mathcal{B}$  to be Fourier transformed into momentum (or frequency) sectors  $k = (k_b, k_c, k_d)$  as  $\tilde{\mathcal{B}}$ . Upon ensemble-averaging, the TopSFF can be evaluated as a discrete path integral of an emergent tDW propagating along folded space as a non-Hermitian single particle [36],

$$\overline{\mathcal{K}_{\text{top}}} = \sum_k \phi(-k)^T \tilde{\mathcal{B}}(k)^{L_e} \phi(k), \quad \tilde{\mathcal{B}} = \begin{pmatrix} \tilde{\mathcal{B}}_{00} & \tilde{\mathcal{B}}_{01} \\ \tilde{\mathcal{B}}_{10} & \tilde{\mathcal{B}}_{11} \end{pmatrix}. \quad (2)$$

Non-trivially,  $\tilde{\mathcal{B}}_{00}, \tilde{\mathcal{B}}_{11} \in \mathbb{R}$ ,  $\tilde{\mathcal{B}}_{01}, \tilde{\mathcal{B}}_{10} \in i\mathbb{R}$ . The complex-

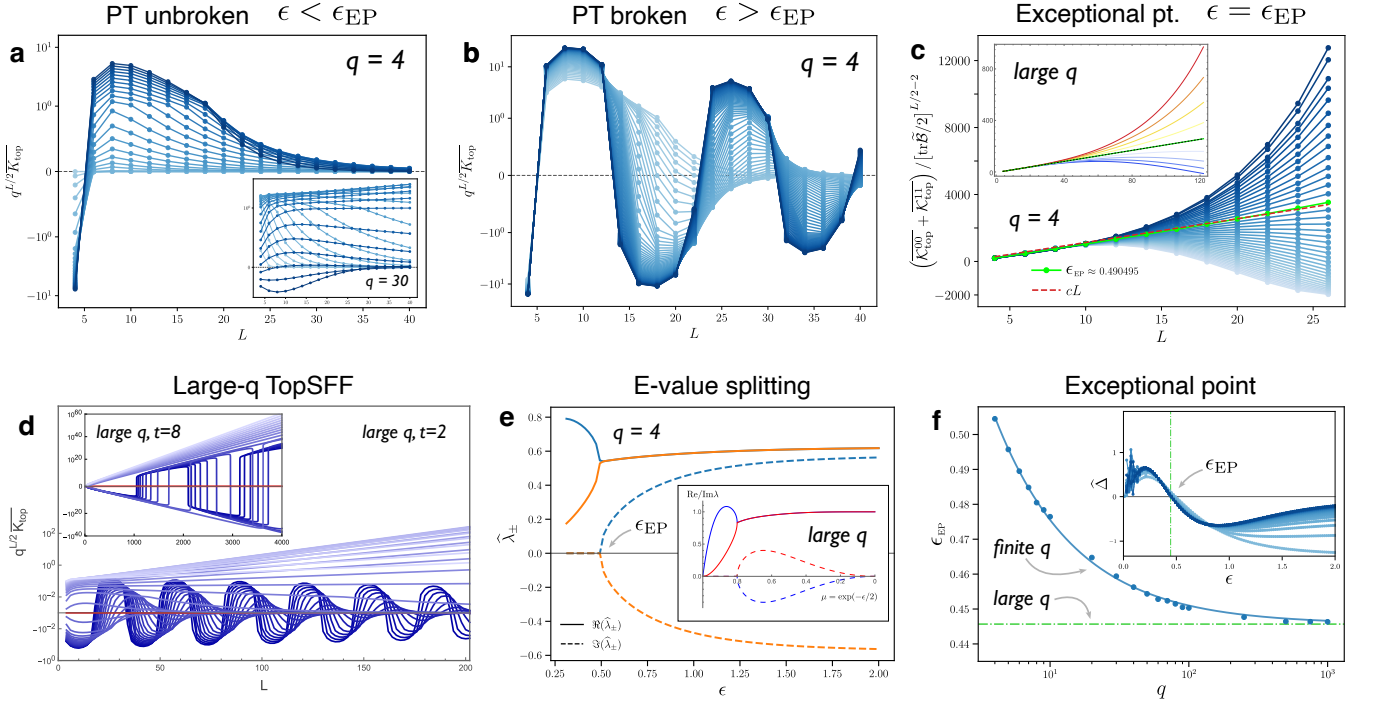


FIG. 4. **Finite- $q$  and large- $q$  signatures of TopSFF  $\mathcal{PT}$  transition.** We exactly compute TopSFF in the  $k = (\pi, \pi, 0)$  sector, with finite- $q$  data at  $t = 2$  and with large- $q$  results for arbitrary  $t$  in the pre-Heisenberg regime. Darker lines denote stronger interaction strength. (a) In the  $\mathcal{PT}$  unbroken phase, the TopSFF at  $q = 4$  displays exponential scaling with system size  $L$  at sufficiently large  $L$ . The inset in (a) shows that TopSFF can exponentially increase for sufficiently large  $q$ , e.g.  $q = 30$ , consistent with the large- $q$  spectrum of TopSFF in (e) and [36]. (b) In the  $\mathcal{PT}$  broken phase, TopSFF at  $q = 4$  exhibits oscillatory behaviour with an exponential envelope. (c) At the exceptional point, eigenvector coalescence produces a Jordan-block contribution, giving the boundary-resolved TopSFF a prefactor linear in system size at  $q = 4$ . The inset shows the corresponding large- $q$  result. (d) Large- $q$  exact TopSFF displays  $\mathcal{PT}$  transition at  $t = 2$  (main panel) and generally larger  $t$ , e.g.  $t = 8$  (inset). (e) Eigenvalue splitting across the transition. The real eigenvalues in the  $\mathcal{PT}$  unbroken phase coalesce at the exceptional point and become a complex-conjugate pair in the  $\mathcal{PT}$  broken phase. Solid and dashed curves denote real and imaginary parts, respectively. Remarkably, the finite  $q$  spectrum is qualitatively consistent with the large- $q$  spectrum in the inset, with eigenvalue moduli reduced at finite  $q$  but increasing with  $q$  [36]. (f) Finite- $q$  exceptional points extracted from the Cayley-Hamilton discriminant converge towards the analytic large- $q$  prediction as  $q$  increases. The inset shows the finite- $q$  discriminant crossing used to locate the transition.

valued generalized Boltzmann factor  $\tilde{\mathcal{B}}$ , equivalently the transfer matrix, is written in the two-species tDW basis, with  $|G\rangle$  and  $|nG\rangle$  denoting respectively the Gaussian and non-Gaussian state for each momentum sector. The matrix element  $\tilde{\mathcal{B}}_{aa'}(k)$  gives the transition amplitude from species  $a$  to species  $a'$ . We use the normalization  $\mathcal{K}_{\text{top}} := q^{L/2} K_{\text{top}}$ , and the effective propagation length is  $L_e = L/2 - 1$ .  $\phi(k)$  is the physical boundary vector generated by the couplings along the parity-inversion axes. For period-one driving along the axes, the boundary vector is  $\phi = (1, i)^T$ , an equal-weight superposition of Gaussian and non-Gaussian tDW sectors. The factor of  $i$  originates from the relative Weingarten sign. The trace and determinant of  $\tilde{\mathcal{B}}$  are always real, and therefore, the two eigenvalues are either real or a complex conjugate pair. Further,  $\tilde{\mathcal{B}}$  exhibits an emergent antiunitary  $(\mathcal{PT})\tilde{\mathcal{B}}(k)(\mathcal{PT})^{-1} = \tilde{\mathcal{B}}(-k)$ , with complex conjugation  $\mathcal{T}$  and  $\mathcal{P} = \sigma_z$  acting on the Gaussian/non-Gaussian tDW index  $a = 0, 1$ . We prove that this antiunitary symme-

try becomes a  $\mathcal{PT}$  symmetry [41] for  $k_b + k_c + k_d = 0 \pmod{\pi}$  [36]. The emergence of antiunitary symmetry intrinsically follows from the relative Weingarten sign of Gaussian and non-Gaussian tDWs: conversion between the two types of tDW carries a factor of  $i$ .

In the large- $q$  limit, for each momentum sector  $k$ , the generalized Boltzmann factor is an exactly solvable two-by-two transfer matrix, with eigenvalues and eigenvectors obtained explicitly in [36]. The eigenvalues are  $\lambda_{\pm}(k) = [\tilde{\mathcal{B}}_{00}(k) + \tilde{\mathcal{B}}_{11}(k)]/2 \pm \sqrt{\Delta(k)}$ , and real or complex conjugate pairs depending on the sign of discriminant

$$\Delta(k, \epsilon) = \underbrace{\left[ \frac{\tilde{\mathcal{B}}_{00} - \tilde{\mathcal{B}}_{11}}{2} \right]^2}_{\text{detuning}} + \underbrace{\tilde{\mathcal{B}}_{01}\tilde{\mathcal{B}}_{10}}_{\text{conversion}}. \quad (3)$$

Thus the spectral bifurcation, corresponding to the  $\mathcal{PT}$  transition in  $\mathcal{PT}$  symmetric sectors, is controlled by the

competition between the Gaussian/non-Gaussian detuning  $|(\tilde{\mathcal{B}}_{00} - \tilde{\mathcal{B}}_{11})/2|^2$  and the inter-species conversion term  $|\tilde{\mathcal{B}}_{01}\tilde{\mathcal{B}}_{10}|$ , with modulus taken because the conversion amplitudes are purely imaginary. Numerous momentum sectors of  $\tilde{\mathcal{B}}$  exhibit  $\mathcal{PT}$  transitions. Hereafter, we focus on the sector  $k = (\pi, \pi, 0)$ , which is distinguished by the coexistence of two features: (i) leading eigenvalues have moduli exceeding unity, giving the exponential growth with system size discussed below, and (ii) an exceptional point (EP) exactly solvable at large- $q$  as

$$\epsilon_{\text{EP}} = \log \left[ \frac{\sqrt{(t-1)^2 + 8t} - (t-1)}{2} \right] \xrightarrow{t \gg 1} \log 2, \quad (4)$$

which remains *finite* even at large  $t$ , within the pre-Heisenberg regime of the large- $q$  analytics. The special role of  $k = (\pi, \pi, 0)$  follows from the momentum structure of the exact large- $q$  transfer matrix. This sector satisfies the  $\mathcal{PT}$  symmetric condition  $k_b + k_c + k_d = 0 \pmod{\pi}$ , while combining a zero momentum on one folded-time loop with alternating  $\pi$  phase factors on the other two loops. The zero momentum gives a non-oscillatory enhancement, whereas the alternating signs reduce the Gaussian–non-Gaussian detuning without eliminating their off-diagonal mixing. This balance allows  $\Delta(k, \epsilon)$  to change sign at finite  $\epsilon$  unlike, for example, the zero-momentum sector  $k = (0, 0, 0)$  where the  $\pi$  phase factors are absent. The  $k = (\pi, \pi, 0)$  sector is accessible in ordinary time evolution through computing TopSFF with period-two driving specifically along the parity inversion axes [36]. More directly, we gain access to the  $k = (\pi, \pi, 0)$  sector via non-unitary spatial propagation under the dual transfer matrix for small  $t$  and large  $L$  [13, 20, 31, 42] (Methods).

**Emergent  $\mathcal{PT}$  transition.** In the  $\mathcal{PT}$  unbroken phase, with  $\epsilon < \epsilon_{\text{EP}}$  and  $\Delta > 0$ , detuning dominates conversion in (3), and the eigenvalues of  $\tilde{\mathcal{B}}$  are real. For sufficiently large  $L$ , the TopSFF is controlled by the eigenvalue of largest modulus and therefore grows or decays monotonically and exponentially according to a single dominant eigenmode,

$$\overline{\mathcal{K}_{\text{top}}} \propto \lambda_+^{L_e}, \quad \epsilon < \epsilon_{\text{EP}}, \quad (5)$$

where  $|\lambda_+| > |\lambda_-|$ . This leading eigenmode is generally a superposition of Gaussian tDW and non-Gaussian tDW, polarized predominantly towards one of them, i.e.,  $|G\rangle$  or  $|nG\rangle$ . We emphasize that this  $\mathcal{PT}$  unbroken phase lies within the strongly interacting chaotic regime.

In the  $\mathcal{PT}$  broken phase, with  $\epsilon > \epsilon_{\text{EP}}$  and  $\Delta < 0$ , Gaussian–non-Gaussian conversion dominates detuning. The eigenvalues form a complex conjugate pair,  $\lambda_{\pm} = |\lambda|e^{\pm i\theta}$ , and the propagating tDW eigenmodes are hybridized Gaussian and non-Gaussian tDW superpositions,  $|\pm\rangle \propto (|G\rangle \pm |nG\rangle)$ . The TopSFF is controlled by a coherent superposition of the two leading tDW eigen-

modes. Under spatial propagation, these two modes acquire opposite phases, and their linear combination produces constructive and destructive interference as  $L$  is varied. Consequently, the TopSFF acquires an oscillatory dependence on system size with an exponential envelope,

$$\overline{\mathcal{K}_{\text{top}}} \propto |\lambda|^{L_e} \sin(L_e \theta + \varphi), \quad \epsilon > \epsilon_{\text{EP}}, \quad (6)$$

with a phase offset  $\varphi$  fixed by the boundary vectors.

At the exceptional point,  $\epsilon = \epsilon_{\text{EP}}$  and  $\Delta = 0$ , the eigenvalues become degenerate,  $\lambda_+ = \lambda_- \equiv \lambda_{\text{EP}}$ , and the corresponding eigenvectors coalesce, rendering  $\tilde{\mathcal{B}}$  non-diagonalizable. Writing  $\tilde{\mathcal{B}}(k)|_{\text{EP}} = \lambda_{\text{EP}}\mathbb{1} + N$ , with  $N^2 = 0$ , gives  $\tilde{\mathcal{B}}(k)^{L_e}|_{\text{EP}} = \lambda_{\text{EP}}^{L_e}\mathbb{1} + L_e\lambda_{\text{EP}}^{L_e-1}N$ . The second term is the characteristic Jordan-block contribution, producing a polynomial enhancement in  $L_e$ . For the boundary vector above,  $\phi = (1, i)^T$ , an equal weight superposition of Gaussian and non-Gaussian tDW sectors, the Jordan contribution has vanishing overlap at the exceptional point, and therefore does not directly reveal the non-diagonalizability. We instead resolve the TopSFF into Gaussian and non-Gaussian boundary components via  $\overline{\mathcal{K}_{\text{top}}^{mn}} := [\phi^{(m)}]^T \tilde{\mathcal{B}}(k)^{L_e} \phi^{(n)}$ , with  $m, n \in \{0, 1\}$ ,  $\phi^{(0)} = (1, 0)^T$  and  $\phi^{(1)} = (0, i)^T$ . The exceptional point and its Jordan non-diagonality are then directly exposed through

$$\frac{\overline{\mathcal{K}_{\text{top}}^{00}} + \overline{\mathcal{K}_{\text{top}}^{11}}}{[\text{tr } \tilde{\mathcal{B}}/2]^{L_e-1}} \propto L, \quad \epsilon = \epsilon_{\text{EP}}. \quad (7)$$

At the EP, dividing by the degenerate eigenvalue removes the exponential envelope and isolates the Jordan prefactor.

**Evidence from simulations.** We now present numerical evidence for these signatures in the large- $q$  theory, and show that they persist at finite  $q$ . In the large- $q$  theory, Fig. 4 displays the exact TopSFF across the  $\mathcal{PT}$  transition [(d)], confirming (5) and (6); at the EP [(c) inset], confirming (4) and (7); and the associated eigenvalue splitting [(e) inset and (f)]. The EP is further accompanied by divergent eigenvector overlap diagnostics, including the Petermann factor [43], reflecting the non-orthogonality of the coalescing eigenvectors [36]. At finite  $q$ , we devise exact simulations of TopSFF at  $t = 2$ , varying large  $L$ , and arbitrary finite  $q$  (Methods). In the strongly interacting regime, the CH extraction reveals the same three finite- $q$  signatures in Fig. 4: exponential dependence in the  $\mathcal{PT}$  unbroken regime [(a)], oscillations in the  $\mathcal{PT}$  broken regime [(b)], and a linear prefactor in  $L$  from Jordan non-diagonality at the EP [(c)]. The extracted  $\epsilon_{\text{EP}}$  converges remarkably well to the large- $q$  prediction as  $q$  increases [Fig. 4(f)], while the eigenvalue splitting shows qualitative agreement with the large- $q$  behaviour [Fig. 4(e)]. As  $q$  increases, the leading eigenvalue moduli eventually exceed unity [36], producing the increasing exponential behaviour shown in the inset of Fig. 4(a). Although the finite- $q$  simulations shown

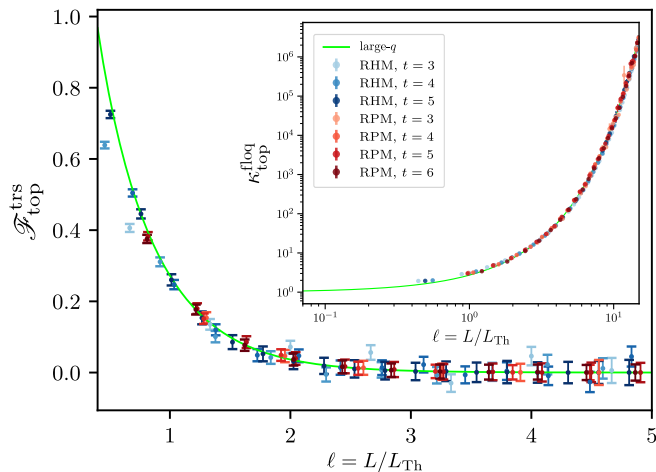


FIG. 5. **Finite- $q$  TopSFF collapse for temporally extended defects.** Topological free energy  $\mathcal{F}_{\text{top}}^{\text{trs}}$  of a temporally extended global swap defect in the TRS RPM at  $q = 3$  (red), and the TRS Random Hamiltonian Model (RHM) [36] at  $q = 2$  (blue), compared with the large- $q$  scaling form (green). Inset: finite- $q$  collapse of the TopSFF  $\mathcal{K}_{\text{top}}^{\text{floq}}$  with temporally extended translation defect for the corresponding Floquet models (without TRS).

here are restricted to  $t = 2$ , their agreement with the large- $q$  theory supports the same underlying  $\mathcal{PT}$  transition mechanism at finite  $q$ . Crucially, the exact large- $q$  analysis shows that these signatures persist to large  $t$  within the pre-Heisenberg regime, e.g.  $t = 8$  in Fig. 4(d) inset and Ref. [36], with a finite interaction strength transition and an exponentially increasing TopSFF.

**Temporally extended defects.** We next study TopSFFs with temporally extended defects  $\hat{D}$  inserted in the spatial evolution  $\hat{U}_s \otimes \hat{U}_s^*$ , where  $\hat{U}_s(t, L) = \prod_{i=1}^L \hat{V}_i(t)$  is generated by the space-time dual transfer matrices of the RPM [Fig. 3(a), purple]. We consider  $\hat{D} = \hat{O} \otimes \hat{1}$ , with  $\hat{O} = \hat{S}$  the global swap defect of the time reversal symmetric (TRS) RPM, or  $\hat{O} = \hat{T}$  the time translation defect of the Floquet RPM with  $\hat{T}|a_1, a_2, \dots, a_t\rangle = |a_t, a_1, \dots, a_{t-1}\rangle$ . For the global swap case, at large  $q$ , the averaged TopSFF is equivalent to an Ising partition function with a spin-flip defect. This defect forces a spatial domain wall (sDW), i.e. a kink in the pairing or Ising variable along the spatial direction, in the sense of Ref. [25]. The partition function evaluates to  $\overline{K}_{\text{top}}^{\text{trs}} = [1 + e^{-\epsilon\alpha(t)}]^L - [1 - e^{-\epsilon\alpha(t)}]^L$ , with  $\alpha(t) := t - 1 - \delta_{0, t \bmod 2}$ . The ordinary SFF is obtained by replacing the minus sign by a plus sign [44]. In generic many-body chaotic systems, the Thouless length  $L_{\text{Th}}$  is the crossover scale separating the 0D RMT regime,  $L \ll L_{\text{Th}}$ , from the many-body regime,  $L \gtrsim L_{\text{Th}}$ . In the Thouless double scaling limit [26] where  $t, L \rightarrow \infty$  at fixed  $\ell := L/L_{\text{Th}} = Le^{-\epsilon t}$  fixed, an exact universal scaling form of TopSFF can be

derived at large  $q$ ,

$$\kappa_{\text{top}}^{\text{trs}} := \lim_{\substack{L, t \rightarrow \infty \\ \ell = L/L_{\text{Th}}}} \overline{K}_{\text{top}}^{\text{trs}} = 2 \sinh \ell. \quad (8)$$

The analogous scaling form of SFF is derived in [44]. The effective free energy cost of the spatial domain wall (sDW) is then  $\Delta F_{\text{top}}^{\text{trs}} := -\frac{1}{t} \log(\overline{K}_{\text{top}}^{\text{trs}}/K^{\text{trs}}) = -\frac{1}{t} \log[\tanh(L \operatorname{atanh} e^{-\epsilon\alpha(t)})]$ . In the Thouless scaling limit, the TopSFF free energy scaling form at large  $q$  is

$$\mathcal{F}_{\text{top}}^{\text{trs}} \equiv \lim_{\substack{L, t \rightarrow \infty \\ \ell = L/L_{\text{Th}}}} t \Delta F_{\text{top}}^{\text{trs}} = -\ln \tanh \ell. \quad (9)$$

A complementary Thouless limit with fixed  $\tau := t/t_{\text{Th}} = \epsilon t / \log L$  gives a scaling function  $\mathcal{F}_{\text{top}}^{\text{trs}} = \epsilon(1 - \tau^{-1})\Theta(\tau - 1)$  with step function  $\Theta$ , implying a sharp crossover at  $\tau = 1$ , but with logarithmically slow finite size convergence [36].

For the time translation case, analogously, the averaged TopSFF is the  $t$ -state Potts partition function [13] with color-flip defect, forcing an sDW in the Potts color or pairing structure. It evaluates as  $\overline{K}_{\text{top}}^{\text{floq}} = [1 + (t-1)e^{-\epsilon t}]^L - (1 - e^{-\epsilon t})^L$ . Taking the Thouless scaling limit gives the TopSFF universal scaling form

$$\kappa_{\text{top}}^{\text{floq}} := \lim_{\substack{L, t \rightarrow \infty \\ \ell = L/L_{\text{Th}}}} \left( \overline{K}_{\text{top}}^{\text{floq}} + 1 \right) = e^\ell. \quad (10)$$

with  $L_{\text{Th}} = e^{\epsilon t}/t$ . The analogous scaling form for the ordinary SFF is derived in [26]. Again, comparing TopSFF and SFF gives the topological free energy difference  $\Delta F_{\text{top}}^{\text{floq}} := -\frac{1}{t} \log(\overline{K}_{\text{top}}^{\text{floq}}/K^{\text{floq}}) = -\frac{1}{t} \ln \frac{1 - \omega^L}{1 + (t-1)\omega^L}$  with  $\omega = (1 - e^{-\epsilon t})/[1 + (t-1)e^{-\epsilon t}]$ . In the large- $q$  limit, the universal scaling form of TopSFF with time translation defect is

$$\mathcal{F}_{\text{top}}^{\text{floq}} \equiv \lim_{\substack{L, t \rightarrow \infty \\ \ell = L/L_{\text{Th}}}} \left( t \Delta F_{\text{top}}^{\text{floq}} - \ln t \right) = -\ln(e^\ell - 1), \quad (11)$$

capturing the free energy cost of sDW [13, 25]. The convergence to Eq. (11) requires  $\ell \ll \ln t$ . Since  $\ln t$  grows only logarithmically, this window is narrow in the numerically accessible regime, and we test the TopSFF scaling form (10), rather than the free energy scaling form (11). In Fig. 5, finite- $q$  simulations of two independent models show excellent agreement with the universal free energy scaling form for the TRS case (9) and with the universal TopSFF scaling form for the time-translation case (10).

The TopSFF free energy scaling forms capture the universal sDW physics of generic many-body chaotic systems beyond the 0D RMT regime [13, 25, 44]. (9) identifies Thouless length  $L_{\text{Th}}$  as the sole remaining length scale, acting as the effective correlation length of the sDW theory. For  $L \ll L_{\text{Th}}$ ,  $\mathcal{F}_{\text{top}}^{\text{trs}} \simeq \ln(L_{\text{Th}}/L)$ , i.e., a forced sDW is rare and costly, and the system behaves as a

0D chaotic system described by a single random matrix. For  $L \gg L_{\text{Th}}$ , proliferating sDW screen the defect insertion, causing the free energy to vanish exponentially and producing universal many-body deviations from the 0D RMT behaviour. The time translation defect has the same interface free energy interpretation, but the sDW also carries a  $t$ -fold entropy, giving the  $\ln t$  subtraction in Eq. (11).

**Discussion.** Generic strongly interacting quantum many-body systems are notoriously difficult to analyse. The naturalness of the TopSFF formulation as a defect-decorated doubled partition function enables exact analytic access to universal non-perturbative signatures of generic strongly interacting quantum systems that are not resolved by conventional observables like SFF. These include an emergent  $\mathcal{PT}$  transition within the many-body chaotic regime and universal scaling forms of topological defect free energy. These results expose an interplay between unitary evolution in time and non-unitary propagation in space, manifested in the distinct physics of temporal and spatial domain walls. In particular, the tDW defect dynamics provides an unexpected bridge between unitary or Hermitian many-body quantum chaos and non-Hermitian single-particle physics. Together, these results establish the TopSFF as a distinct non-local observable that captures intrinsically many-body phenomena and universal structures beyond RMT.

Can the  $\mathcal{PT}$  transition in the TopSFF be classically simulated? To test this, we exactly compute the TopSFF with a spatially extended swap defect in an RPM without time translation symmetry, where each random local unitary appears only twice in the time evolution. Although the TopSFF of this model can be reproduced by classically simulable Clifford/stabilizer circuits [45], it exhibits only an asymptotic  $\mathcal{PT}$  transition [36], lacking the finite-interaction-strength competition between Gaussian–non-Gaussian detuning and conversion found in the time translation symmetric case.

This work opens many directions for future studies [38]. Beyond conventional symmetries such as  $U(1)$ , generalized symmetry defects and defect junctions define a rich class of defect-resolved observables [6, 7]. The emergent non-Hermitian generalized Boltzmann factors also call for field-theoretic descriptions, tDW trajectory analysis, and a topological classification of exceptional points and topological invariants. Another interesting direction is to study TopSFF in the Sachdev-Ye-Kitaev model [46, 47] with topological defects, potentially connecting defect-resolved observables to their dual gravitational descriptions. Finally, TopSFF may be experimentally accessible by adapting existing measurement protocols [48–51] to incorporate a non-trivial defect insertion in the doubled evolution. We leave the development of concrete measurement protocols and the analysis of their sampling complexity to future work.

## METHODS

**Models.** The Random Phase Model [13] is a one-dimensional random quantum circuit [52] acting on  $L$  qudits of local Hilbert-space dimension  $q$ . A single RPM bilayer is  $\hat{U}_{\text{RPM}} = \hat{U}_2 \hat{U}_1$ , where  $\hat{U}_1 = \bigotimes_{r=1}^L u_r$  is a layer of independent Haar-random one-site gates  $u_r \in \text{CUE}(q)$ , and  $\hat{U}_2 = \prod_r \Theta_{r,r+1}$  is a layer of commuting two-site diagonal phase gates, containing Gaussianly distributed random phases. In the computational basis, we have  $[\Theta_{r,r+1}]_{ab}^{cd} = \delta_{ac} \delta_{bd} e^{i\phi_{ab}^{(r)}}$  and  $\phi_{ab}^{(r)} \in \mathcal{N}(0, \epsilon)$ . The variance  $\epsilon$  controls the interaction strength. To verify the generality of our results, we also use the Random Hamiltonian Model (RHM) [53, 54] with the corresponding symmetry constraints, defined explicitly in [36].

To impose parity inversion symmetry, gates related by  $r \leftrightarrow L - r + 1$  are identified. The one-site gates are mirrored across the inversion axis, and the two-site phase gates are chosen in mirror-related pairs. Gates straddling the inversion axis are locally parity symmetric, which for the diagonal RPM gate means  $\phi_{ab} = \phi_{ba}$ . The TRS RPM [44] is obtained by imposing the corresponding reflection constraint in the time direction. We work in the  $\mathcal{T}^2 = 1$  class and choose a basis such that  $\mathcal{T}$  is the complex conjugation. A random half-circuit  $w(t, L)$  is sampled from the above RPM ensemble and the TRS circuit is generated via transposition as  $\hat{U}(t, L) = w(t, L)^T w(t, L)$ , so that  $\hat{U}^T = \hat{U}$  and  $\mathcal{T}\hat{U}(t)\mathcal{T}^{-1} = \hat{U}^\dagger(t)$ . See explicit definition in [36].

**Large- $q$  exact TopSFF.** Using the Cayley-Hamilton relation, for the boundary vector  $\varphi = (\varphi_1, \varphi_2)^T$  supported in momentum sector  $k$ , the TopSFF is exactly evaluated at large  $q$  as

$$\overline{\mathcal{K}_{\text{top}}} = \varphi^T \tilde{\mathcal{B}}(k)^{L_e} \varphi = g u_{L_e} - h \det \tilde{\mathcal{B}} u_{L_e - 1}, \quad (12)$$

where  $h = \varphi_1^2 + \varphi_2^2$ , and  $g(k) = \tilde{\mathcal{B}}_{00} \varphi_1^2 + [\tilde{\mathcal{B}}_{01} + \tilde{\mathcal{B}}_{10}] \varphi_1 \varphi_2 + \tilde{\mathcal{B}}_{11} \varphi_2^2$ . The system size dependence is encoded in

$$u_{L_e}(k) = \begin{cases} \frac{\lambda_+^{L_e}(k) - \lambda_-^{L_e}(k)}{\lambda_+(k) - \lambda_-(k)}, & \Delta(k) \neq 0, \\ L_e \left[ \frac{\text{tr} \tilde{\mathcal{B}}(k)}{2} \right]^{L_e - 1}, & \Delta(k) = 0. \end{cases} \quad (13)$$

where  $\lambda_\pm$  and  $\Delta(k)$  are defined around (3). For  $\Delta(k) \neq 0$ , the eigenvalues  $\lambda_\pm(k)$  are distinct. At the EP,  $\Delta(k) = 0$ , they coalesce, and the second line gives the corresponding Jordan-block contribution. Explicit exact large- $q$  expressions for the generalized Boltzmann factor  $\tilde{\mathcal{B}}(k)$  in all momentum sectors are given in [36].

**$(\pi, \pi, 0)$  momentum sector.** For the momentum sector  $\pi_e \equiv (\pi, \pi, 0)$ , the large- $q$  generalized Boltzmann factor  $\tilde{\mathcal{B}}$  is a  $\mathcal{PT}$  symmetric dimer, which displays a  $\mathcal{PT}$  phase transition at finite interaction strength. Defining  $S_2(n) := (1 - \mu^{-2n})/(1 - \mu^{-2})$ ,  $S_4(n) := (1 - \mu^{-4n})/(1 -$

$\mu^{-4}$ ),  $A_n := \sum_{r=1}^n (\mu^{-2r} - 1)^2 = \mu^{-4} S_4(n) - 2\mu^{-2} S_2(n) + n$ , and  $C_n := A_n - (\mu^{-2} - 1)^2$ , we write the exact solution of  $\tilde{\mathcal{B}}$  as

$$\begin{aligned}\tilde{\mathcal{B}}_{00}^{\pi_e} &= 1 + \mu^{4t-4} + (t-2)(\mu^{2t} + \mu^{4t-2}) \\ &\quad - 2(t-1)\mu^{4t+2} + 2t\mu^{4t-4}(t-1)S_2(t-1) \\ &\quad - 2t(t-1)\mu^{4t} + 2\mu^{4t}C_t + 2\mu^{4t}(1-\mu^2), \\ \tilde{\mathcal{B}}_{01}^{\pi_e} = \tilde{\mathcal{B}}_{10}^{\pi_e} &= i\mu^{4t} \left[ (\mu^{-2t} - 1)^2 + (\mu^{-2} - 1)^2 \right. \\ &\quad + t\{(\mu^{-2t} - 1) + (\mu^{-2} - 1)\} \\ &\quad + (\mu^{-2} + \mu^{-4})(t-1)S_2(t-1) - 2(t-1)\} \\ &\quad \left. + A_{t-1} + C_t \right], \\ \tilde{\mathcal{B}}_{11}^{\pi_e} &= -\mu^{4t} \left[ (\mu^{-2t} - 1)^2 + 2A_{t-1} \right. \\ &\quad + t\{(\mu^{-2t} - 1) \\ &\quad \left. + 2\mu^{-2}(t-1)S_2(t-1) - 2(t-1)\} \right],\end{aligned}$$

with interaction strength parametrised as  $\mu \equiv e^{-\epsilon/2}$ .

**Finite- $q$  simulations and analysis.** At finite  $q$ , we compute the TopSFF by two complementary methods. First, we estimate the TopSFF by sampling over random circuit realizations. Second, by constructing a transfer matrix after the ensemble average of the RPM tensor network, we exactly compute TopSFF for small  $t$  and arbitrary  $L$ , free from sample-to-sample fluctuations [36]. To diagnose the  $\mathcal{PT}$  transition, we use the large- $q$  Cayley-Hamilton (CH) relation as an ansatz for finite  $q$ ,  $\overline{\mathcal{K}}_{\text{top}}(L_e + 2) = \hat{\mathbf{t}} \overline{\mathcal{K}}_{\text{top}}(L_e + 1) - \hat{\mathbf{d}} \overline{\mathcal{K}}_{\text{top}}(L_e)$ , and extract the effective trace  $\hat{t}$ , determinant  $\hat{d}$ , discriminant  $\hat{\Delta} := \hat{t}^2 - 4\hat{d}$ , and eigenvalues  $\hat{\lambda}_{\pm} := (\hat{t} \pm \sqrt{\hat{\Delta}})/2$  from finite- $q$  TopSFF data. In finite  $q$ , the CH relation is overdetermined over a range of  $L_e$ . In practice, the extracted quantities  $\hat{\mathbf{t}} = \hat{\mathbf{t}}_{L_e}$  and  $\hat{\mathbf{d}} = \hat{\mathbf{d}}_{L_e}$  depend on  $L_e$ , and are interpreted as effective trace and determinant only when they are stable upon varying  $L_e$ . In SI [36], we show that, for  $q \geq 4$ , the CH relation is robust over an extended region of the  $\epsilon$ - $L$  plane including across the finite-interaction-strength EP  $\epsilon_{\text{EP}}$ . Its breakdown at small  $\epsilon$  may reflect many-body localization physics [55–57], which we leave for future investigation.

## ACKNOWLEDGMENTS

We are grateful to Subhajyoti Bid, Weitao Chen, Ilyoun Na, Hisanori Oshima, and, particularly, David Huse for helpful discussions. AC thanks John Chalker, Andrea De Luca, and Saumya Shivam for previous collaboration on related works. The numerical simulation was carried out using both Lancaster University’s High End Computing facility and the Higgs HPC system at Northumbria University.

\* daniel.harkin@lancaster.ac.uk

† c.y.leung2@lancaster.ac.uk

‡ amos.chan@warwick.ac.uk

- [1] T. W. B. Kibble, Topology of Cosmic Domains and Strings, *J. Phys. A* **9**, 1387 (1976).
- [2] N. D. Mermin, The topological theory of defects in ordered media, *Rev. Mod. Phys.* **51**, 591 (1979).
- [3] L. P. Kadanoff and H. Ceva, Determination of an operator algebra for the two-dimensional ising model, *Phys. Rev. B* **3**, 3918 (1971).
- [4] V. Petkova and J.-B. Zuber, Generalised twisted partition functions, *Physics Letters B* **504**, 157–164 (2001).
- [5] J. Fröhlich, J. Fuchs, I. Runkel, and C. Schweigert, Kramers-wannier duality from conformal defects, *Phys. Rev. Lett.* **93**, 070601 (2004).
- [6] D. Gaiotto, A. Kapustin, N. Seiberg, and B. Willett, Generalized global symmetries, *Journal of High Energy Physics* **2015**, 10.1007/jhep02(2015)172 (2015).
- [7] D. Aasen, P. Fendley, and R. S. Mong, Topological defects on the lattice: dualities and degeneracies, arXiv preprint arXiv:2008.08598 (2020).
- [8] M. L. Mehta, *Random Matrices* (Academic Press, 2004).
- [9] M. V. Berry, Semiclassical theory of spectral rigidity, *Proceedings of the Royal Society of London A* **400**, 229 (1985).
- [10] J. M. Deutsch, Quantum statistical mechanics in a closed system, *Phys. Rev. A* **43**, 2046 (1991).
- [11] M. Srednicki, Chaos and quantum thermalization, *Phys. Rev. E* **50**, 888 (1994).
- [12] M. Rigol, V. Dunjko, and M. Olshanii, Thermalization and its mechanism for generic isolated quantum systems, *Nature* **452**, 854–858 (2008).
- [13] A. Chan, A. De Luca, and J. T. Chalker, Spectral statistics in spatially extended chaotic quantum many-body systems, *Phys. Rev. Lett.* **121**, 060601 (2018).
- [14] O. Bohigas, M.-J. Giannoni, and C. Schmit, Characterization of chaotic quantum spectra and universality of level fluctuation laws, *Physical Review Letters* **52**, 1 (1984).
- [15] M. Sieber and K. Richter, Correlations between periodic orbits and their rôle in spectral statistics, *Physica Scripta* **2001**, 128 (2001).
- [16] S. Müller, S. Heusler, P. Braun, F. Haake, and A. Altland, Semiclassical foundation of universality in quantum chaos, *Phys. Rev. Lett.* **93**, 014103 (2004).
- [17] J. S. Cotler, G. Gur-Ari, M. Hanada, J. Polchinski, P. Saad, S. H. Shenker, D. Stanford, A. Streicher, and M. Tezuka, Black holes and random matrices, *Journal of High Energy Physics* **2017**, 10.1007/jhep05(2017)118 (2017).
- [18] P. Kos, M. Ljubotina, and T. Prosen, Many-body quantum chaos: Analytic connection to random matrix theory, *Physical Review X* **8**, 10.1103/physrevx.8.021062 (2018).
- [19] A. Chan, A. De Luca, and J. T. Chalker, Solution of a minimal model for many-body quantum chaos, *Phys. Rev. X* **8**, 041019 (2018).
- [20] B. Bertini, P. Kos, and T. Prosen, Exact spectral form factor in a minimal model of many-body quantum chaos, *Physical review letters* **121**, 264101 (2018).

- [21] A. J. Friedman, A. Chan, A. De Luca, and J. T. Chalker, Spectral statistics and many-body quantum chaos with conserved charge, *Phys. Rev. Lett.* **123**, 210603 (2019).
- [22] P. Saad, S. H. Shenker, and D. Stanford, A semiclassical ramp in syk and in gravity (2019), arXiv:1806.06840 [hep-th].
- [23] J. Li, T. Prosen, and A. Chan, Spectral statistics of non-hermitian matrices and dissipative quantum chaos, *Physical review letters* **127**, 170602 (2021).
- [24] B. Bertini, P. Kos, and T. Prosen, Random matrix spectral form factor of dual-unitary quantum circuits, *Communications in Mathematical Physics* **387**, 597 (2021).
- [25] S. J. Garratt and J. T. Chalker, Local pairing of feynman histories in many-body floquet models, *Phys. Rev. X* **11**, 021051 (2021).
- [26] A. Chan, S. Shivam, D. A. Huse, and A. D. Luca, Many-body quantum chaos and space-time translational invariance (2021), arXiv:2109.04475 [cond-mat.stat-mech].
- [27] S. Shivam, A. De Luca, D. A. Huse, and A. Chan, Many-body quantum chaos and emergence of ginibre ensemble, *Physical Review Letters* **130**, 10.1103/physrevlett.130.140403 (2023).
- [28] H. Gharibyan, M. Hanada, S. H. Shenker, and M. Tezuka, Onset of random matrix behavior in scrambling systems, *Journal of High Energy Physics* **2018**, 10.1007/jhep07(2018)124 (2018).
- [29] M. Winer and B. Swingle, Hydrodynamic theory of the connected spectral form factor, *Phys. Rev. X* **12**, 021009 (2022).
- [30] J. Šuntajs, J. Bonča, T. c. v. Prosen, and L. Vidmar, Quantum chaos challenges many-body localization, *Phys. Rev. E* **102**, 062144 (2020).
- [31] A. Chan, A. De Luca, and J. T. Chalker, Spectral lyapunov exponents in chaotic and localized many-body quantum systems, *Phys. Rev. Res.* **3**, 023118 (2021).
- [32] D. Roy and T. c. v. Prosen, Random matrix spectral form factor in kicked interacting fermionic chains, *Phys. Rev. E* **102**, 060202 (2020).
- [33] T. Yoshimura, S. J. Garratt, and J. Chalker, Operator dynamics in floquet many-body systems, *Physical Review B* **111**, 094316 (2025).
- [34] A. Altland, K. W. Kim, and T. Micklitz, Path integral approach to quantum thermalization, *Physical Review Research* **8**, 023076 (2026).
- [35] M. F. Kieler, F. Fritzsche, and A. Bäcker, Semiclassical foundation of universality in chaotic quantum circuits, arXiv preprint arXiv:2605.27052 (2026).
- [36] D. Harkin, C. Y. Leung, and A. Chan, Supplementary information for “topological spectral form factor reveals emergent non-hermitian single-particle  $\mathcal{PT}$  transitions from many-body quantum chaos”.
- [37] R. Nakai, T. Guo, and S. Ryu, Discrete time crystals detected by time-translation twist, *Phys. Rev. B* **112**, 165138 (2025).
- [38] C. Y. Leung, D. Harkin, and A. Chan, in preparation.
- [39] D. Weingarten, Asymptotic behavior of group integrals in the limit of infinite rank, *Journal of Mathematical Physics* **19**, 999 (1978).
- [40] P. W. Brouwer and C. W. J. Beenakker, Diagrammatic method of integration over the unitary group, with applications to quantum transport in mesoscopic systems, *Journal of Mathematical Physics* **37**, 4904 (1996).
- [41] C. M. Bender and S. Boettcher, Real spectra in non-hermitian hamiltonians having  $\mathcal{PT}$  symmetry, *Phys. Rev. Lett.* **80**, 5243 (1998).
- [42] M. Akila, D. Waltner, B. Gutkin, and T. Guhr, Particle-time duality in the kicked ising spin chain, *Journal of Physics A: Mathematical and Theoretical* **49**, 375101 (2016).
- [43] K. Petermann, Calculated spontaneous emission factor for double-heterostructure injection lasers with gain-induced waveguiding, *IEEE Journal of Quantum Electronics* **15**, 566 (1979).
- [44] W. Wu, S. Shivam, and A. Chan, Many-body quantum chaos and time reversal symmetry (2025), arXiv:2503.23475 [cond-mat.stat-mech].
- [45] S. Aaronson and D. Gottesman, Improved simulation of stabilizer circuits, *Physical Review A* **70**, 052328 (2004).
- [46] S. Sachdev and J. Ye, Gapless spin-fluid ground state in a random quantum heisenberg magnet, *Physical Review Letters* **70**, 3339–3342 (1993).
- [47] A. Kitaev, A simple model of quantum holography, in *KITP strings seminar and Entanglement* (2015) <http://online.kitp.ucsb.edu/online/entangled15/kitaev/>; <http://online.kitp.ucsb.edu/online/entangled15/kitaev2/>.
- [48] D. Poulin, R. Laflamme, G. J. Milburn, and J. P. Paz, Testing integrability with a single bit of quantum information, *Physical Review A* **68**, 10.1103/physreva.68.022302 (2003).
- [49] L. K. Joshi, A. Elben, A. Vikram, B. Vermersch, V. Galitski, and P. Zoller, Probing many-body quantum chaos with quantum simulators (2021), arXiv:2106.15530 [quant-ph].
- [50] H. Dong, P. Zhang, C. B. Dağ, Y. Gao, N. Wang, J. Deng, X. Zhang, J. Chen, S. Xu, K. Wang, Y. Wu, C. Zhang, F. Jin, X. Zhu, A. Zhang, Y. Zou, Z. Tan, Z. Cui, Z. Zhu, F. Shen, T. Li, J. Zhong, Z. Bao, H. Li, Z. Wang, Q. Guo, C. Song, F. Liu, A. Chan, L. Ying, and H. Wang, Measuring the spectral form factor in many-body chaotic and localized phases of quantum processors, *Phys. Rev. Lett.* **134**, 010402 (2025).
- [51] A. K. Das, C. Cianci, D. G. Cabral, D. A. Zarate-Herrada, P. Pinney, S. Pilatowsky-Cameo, A. S. Matsoukas-Roubeas, V. S. Batista, A. del Campo, E. J. Torres-Herrera, *et al.*, Proposal for many-body quantum chaos detection, *Physical Review Research* **7**, 013181 (2025).
- [52] A. Nahum, J. Ruhman, S. Vijay, and J. Haah, Quantum entanglement growth under random unitary dynamics, *Phys. Rev. X* **7**, 031016 (2017).
- [53] J. Bensa and M. Žnidarič, Two-step phantom relaxation of out-of-time-ordered correlations in random circuits, *Phys. Rev. Research* **4**, 013228 (2022).
- [54] K. Huang, X. Li, D. A. Huse, and A. Chan, Out-of-time-order correlator, many-body quantum chaos, light-like generators, and singular values (2023), arXiv:2308.16179 [quant-ph].
- [55] D. Basko, I. Aleiner, and B. Altshuler, Metal-insulator transition in a weakly interacting many-electron system with localized single-particle states, *Annals of Physics* **321**, 1126 (2006).
- [56] V. Oganesyan and D. A. Huse, Localization of interacting fermions at high temperature, *Phys. Rev. B* **75**, 155111 (2007).
- [57] D. A. Abanin, E. Altman, I. Bloch, and M. Serbyn, Colloquium: Many-body localization, thermalization, and entanglement, *Reviews of Modern Physics* **91**, 021001 (2019).

- [58] R. Orús, A practical introduction to tensor networks: Matrix product states and projected entangled pair states, *Annals of Physics* **349**, 117–158 (2014).

## Supplementary Information

# Topological spectral form factor reveals emergent non-Hermitian single-particle $\mathcal{PT}$ transitions from many-body quantum chaos

Daniel Harkin<sup>1</sup>, Chun Y. Leung<sup>2,1</sup>, and Amos Chan<sup>3,1</sup>

<sup>1</sup>Department of Physics, Lancaster University, Lancaster LA1 4YB, United Kingdom

<sup>2</sup>Department of Mathematics, Physics and Electrical Engineering, Northumbria University, Newcastle upon Tyne NE1 8ST, United Kingdom

<sup>3</sup>Department of Physics, University of Warwick, Coventry CV4 7AL, United Kingdom

### OVERVIEW

This Supplementary Information is organized as follows. Appendix A defines the random circuit models and their parity inversion, time reversal, and time translation symmetric variants. Appendices B to D collect exact results for TopSFF in RMT, SFF without topological defects, and SFFs with twisted boundary conditions. Appendix E derives the exact solution of generalized Boltzmann factor for the TopSFF with a spatially extended swap defect at large  $q$ , including momentum-space formulation, Lemma E.2 that leading local diagrams of temporal domain wall belong to the Mickey Mouse topological equivalence class, Proposition E.3 on  $\mathcal{PT}$  symmetry, and boundary states. Appendix E derives the exact large- $q$  generalized Boltzmann factor for the TopSFF with a spatially extended swap defect. It includes Lemma E.2 showing that the leading local temporal domain wall diagrams belong to the Mickey Mouse topological equivalence class, and Proposition E.3 classifying the  $\mathcal{PT}$  symmetric momentum sectors. Appendix F gives the exact large- $q$  evaluation of the spatially extended TopSFF. Appendix G interprets the TopSFF in terms of emergent  $\mathcal{PT}$  symmetric dimers. Appendix H analyses the exceptional points and their signatures across the  $\mathcal{PT}$  transition appearing in TopSFF at large  $q$ . Appendix I presents the exact finite- $q$  evaluation of the TopSFF with a spatially extended swap defect, including an analytic calculation at  $t = 1$ . Appendix J studies TopSFF with spatially extended defects in systems without discrete time-translation symmetry. Appendix K derives the corresponding results for temporally extended defects. Appendix L presents finite- $q$  numerical simulations that support the  $\mathcal{PT}$  transition in the TopSFF with spatially extended defects, as well as the universal scaling forms for temporally extended defects.

### CONTENTS

A. Models	13
1. Dynamics in time	13
2. Parity inversion symmetric models	14
a. Parity inversion symmetric Random Phase Model	14
b. Parity inversion symmetric Random Hamiltonian Model	14
3. Time reversal symmetric models	15
a. TRS Random Phase Model	15
b. TRS Random Hamiltonian Model	16
4. Time translational symmetric only models	18
a. Random Phase Model	18
b. Random Hamiltonian Model	18
B. TopSFF for RMT	19
1. Gaussian and circular ensembles	19
2. Ginibre ensembles	20
C. Review of exact solutions of SFF without topological defects	21
1. Parity inversion symmetry	21
2. TRS	21

3. Time translational symmetry	22
D. SFF with twisted boundary conditions	22
1. Spatially extended twisted boundary condition	22
2. Temporally extended twisted boundary condition	22
E. Generalized Boltzmann factor of TopSFF with spatially extended defects	23
1. Mickey Mouse diagrams	23
2. Boltzmann factor $\mathcal{B}$ in position space	27
3. Properties of $\mathcal{B}$	29
4. Boltzmann factor $\tilde{\mathcal{B}}$ in momentum space	30
5. Properties of $\tilde{\mathcal{B}}$	32
6. $\mathcal{PT}$ symmetry of $\tilde{\mathcal{B}}$	33
7. Boundary states	35
a. Discrete time translational symmetry and parity inversion symmetry	36
b. No coupling	36
c. General periodic driving	36
F. Exact TopSFF with spatially extended defects at large $q$	37
1. TopSFF and Cayley-Hamilton	38
a. Boundary-resolved TopSFF	39
2. TopSFF for fixed momentum sectors	40
a. TopSFF for $(k_b, k_c, k_d) = (0, 0, 0)$	41
b. TopSFF for $(k_b, k_c, k_d) = (0, k, -k)$	41
c. TopSFF for $(k_b, k_c, k_d) = (\pi, \pi, 0)$	41
d. TopSFF for $(k_b, k_c, k_d) = (\pi, k, \pi - k)$	42
3. TopSFF with time translational symmetry	42
4. TopSFF with engineered parity inversion axes	44
a. No coupling	44
b. Period-2 driving	44
c. Isolating $(k_b, k_c, k_d) = (\pi, \pi, 0)$ sector by engineering parity inversion axes	45
G. Emergent $\mathcal{PT}$ symmetric dimers	45
1. Review of $\mathcal{PT}$ symmetric dimers	45
2. TopSFF and $\mathcal{PT}$ dimers	46
H. TopSFF and exceptional points (EP)	48
1. EP in selected momentum sectors	48
a. EP for $(k_b, k_c, k_d) = (0, k, -k)$	49
b. EP for $(k_b, k_c, k_d) = (0, 0, 0)$	49
c. EP for $(k_b, k_c, k_d) = (\pi, \pi, 0)$	50
d. EP for $(k_b, k_c, k_d) = (\pi, k, \pi - k)$	50
2. EP data	51
3. Eigenvalue and eigenvector coalescence at EP	51
I. Exact TopSFF with spatially extended defects at finite $q$	56
1. Exact finite- $q$ symbolic evaluation of TopSFF	56
2. Exact finite- $q$ analytical evaluation of TopSFF at $t = 1$	58
J. TopSFF with spatially extended topological defects without time translational symmetry	59
1. Boltzmann factor $\mathcal{B}$ in position space	59
2. Boltzmann factor $\tilde{\mathcal{B}}$ in momentum space	61
3. Properties of $\tilde{\mathcal{B}}(k)$ and $\mathcal{PT}$ symmetry	62
4. Boundary states	63
5. Exact expression of TopSFF without time translational symmetry	64
6. Consistency check with finite- $q$ result at $t = 1$	65

K. Temporally extended topological defects	65
1. Temporally extended global swap defects	65
a. TRS and time translation symmetry	66
2. Temporally extended time translation defects.	67
L. Finite- $q$ numerical simulations	68
1. Spatially extended topological defects	68
a. Cayley-Hamilton extraction and stability	72
b. Cayley-Hamilton extraction and $\mathcal{PT}$ transitions	74
2. Temporally extended topological defects	75

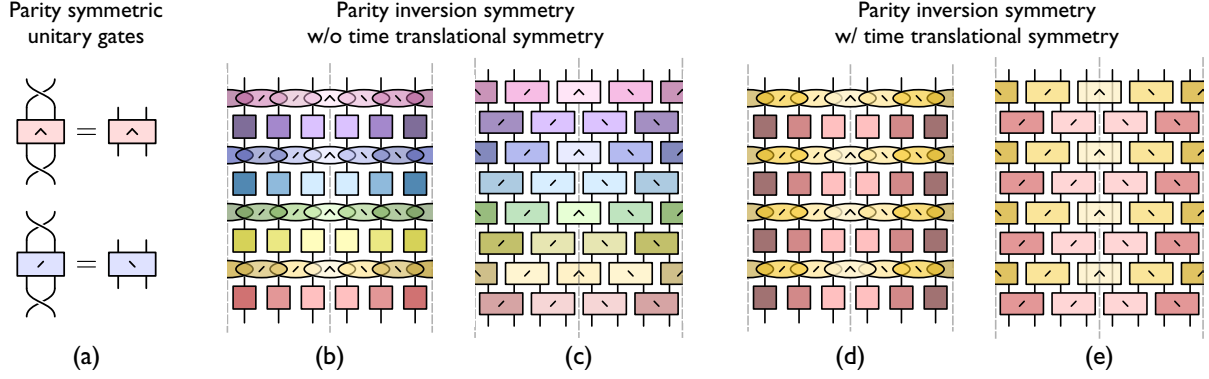


FIG. S1. **Parity inversion symmetric models.** (a) Transformation property of gates that straddle (top) or do not straddle (bottom) across the inversion axis. (b,c) Many-body quantum circuits with parity inversion symmetry and without time translational symmetry for the random phase model (b) and the random Hamiltonian model (c). (d,e) Many-body quantum circuits with parity inversion symmetry and discrete time translational symmetry for the random phase model (d) and the random Hamiltonian model (e). The grey dashed lines denote the inversion axis. Gates of the same color are identical. Periodic boundary conditions are imposed.

## Appendix A: Models

In this appendix, we define the one-dimensional random circuit ensembles used throughout this work. We first specify the temporal structure of the dynamics – temporally random, globally time-reversal symmetric, and Floquet – and then introduce the parity inversion, time reversal, and time translation symmetric Random Phase Model (RPM) and Random Hamiltonian Model (RHM) models.

### 1. Dynamics in time

We are interested in three classes of dynamics in time: (i) temporal random models, (ii) global time reversal symmetric models, and (iii) discrete time translational symmetric (Floquet) models. Specifically, they are defined by the following unitary time evolution operators at time  $t$ ,

$$\text{temporal random:} \quad \mathcal{U}_r(t; u) = \prod_{t'=1}^t u(t'), \quad (\text{SA.1})$$

$$\text{Global TRS:} \quad \mathcal{U}_{\text{trs}}(t; w) = w^T(t) w(t), \quad (\text{SA.2})$$

$$\text{Discrete time translational invariant (Floquet):} \quad \mathcal{U}_f(t; u) = u^t, \quad (\text{SA.3})$$

where  $u$  and  $w$  denote certain choices or distributions of unitary operators.

## 2. Parity inversion symmetric models

We consider one-dimensional quantum circuits  $U$  that act on the Hilbert space of  $L$  qudits with Hilbert space dimension  $q^L$ . These models are parity inversion symmetric in the sense that the quantum circuit commutes with the global swap operator  $S$ , i.e.,  $[U, S] = 0$ , where  $S$  is defined by the action  $S|a_1, a_2, \dots, a_{L-1}, a_L\rangle = |a_L, a_{L-1}, \dots, a_2, a_1\rangle$ . The universal signatures of parity inversion symmetry in quantum many-body chaotic systems are discussed in detail in a forthcoming manuscript [38].

### a. Parity inversion symmetric Random Phase Model

The random phase model (RPM) [13] is a one-dimensional quantum circuit that acts on the Hilbert space of  $L$  qudits with Hilbert space dimension  $q^L$ . The RPM without symmetries is known to be chaotic for  $q \geq 3$ , and not chaotic for  $q = 2$  [13]. In the parity inversion symmetric RPM, the parity inversion axis lies on the bond  $(L/2, L/2+1)$  for the open boundary condition (obc), and on the bonds  $(L/2, L/2+1)$  and  $(L, 1)$  for the periodic boundary condition (pbc). Specifically, the parity inversion symmetric RPM (p-RPM)  $U_{\text{p-RPM}}$  [Fig. S1] is defined by

$$\text{Temporal random:} \quad U_{\text{r-p-RPM}} = \mathcal{U}_{\text{r}}(t; \mathcal{U}_{\text{p-RPM}}), \quad (\text{SA.4})$$

$$\text{Discrete time translational invariant (Floquet):} \quad U_{\text{f-p-RPM}} = \mathcal{U}_{\text{f}}(t; \mathcal{U}_{\text{p-RPM}}), \quad (\text{SA.5})$$

where a single bi-layer is given by

$$\mathcal{U}_{\text{p-RPM}}(t, L) = \mathcal{U}_2(t, L) \mathcal{U}_1(t, L), \quad \mathcal{U}_1(t, L) = \bigotimes_{r=1}^L u(t, r), \quad \mathcal{U}_2(t, L) = \bigotimes_{r=1}^L w(t, r). \quad (\text{SA.6})$$

The gates within  $\mathcal{U}_1(t, L)$  consist of

$$\begin{aligned} u(t, r) &\in \text{CUE} && \text{if } r \in [1, 2, \dots, L/2], \\ u(t, r) &= S u(t, L - r + 1) S && \text{if } r \in [L/2 + 1, L/2 + 2, \dots, L]. \end{aligned} \quad (\text{SA.7})$$

where  $u(t, r)$  acts on site  $r$ , and is randomly and independently drawn from the Circular Unitary Ensemble (CUE). The gates within  $\mathcal{U}_2(t, L)$  consist of

$$\begin{aligned} [w(t, r)]_{ab}^{cd} &= \delta_{ac} \delta_{bd} \exp[i\phi_{ab}(t, r)], & \phi_{ab}(t, r) &\in \mathcal{N}(0, \epsilon) && \text{if } r \in [1, 2, \dots, L/2 - 1], \\ [w(t, r)]_{ab}^{cd} &= \delta_{ac} \delta_{bd} \exp[i\phi_{ab}(t, r)], & \phi_{ab}(t, r) &\in \mathcal{N}(0, \epsilon) \text{ and } \phi_{ab} = \phi_{ba}, && \text{if } r = L/2, L, \\ w(t, r) &= S w(t, L - r) S && && \text{if } r \in [L/2 + 1, \dots, L - 1], \end{aligned} \quad (\text{SA.8})$$

where  $\phi_{\mu\nu}(t, r)$  are independent real Gaussian variables with mean zero and variance  $\epsilon$ . The diagonal random phase gates  $w(t, r)$  with  $r = L/2$  and  $L$  are chosen such that  $S w(t, r) S^{-1} = w(t, r)$ . Again,  $S$  is the global swap operator defined by the action  $S|a_1, a_2, \dots, a_{L-1}, a_L\rangle = |a_L, a_{L-1}, \dots, a_2, a_1\rangle$ , and  $|a_1, a_2, \dots, a_{L-1}, a_L\rangle$  is the computational basis state with  $a_i = 0, 1, \dots, q - 1$ . Note that for obc (pbc), the 2-site gate straddling across sites  $L$  and  $1$ , namely  $w(t, r = L)$ , is removed (kept).

### b. Parity inversion symmetric Random Hamiltonian Model

The random Hamiltonian model (RHM) is a one-dimensional quantum circuit that acts on the Hilbert space of  $L$  qudits with Hilbert space dimension  $q^L$ . The RHM is utilized to numerically simulate generic quantum many-body chaotic dynamics at  $q = 2$ . The RHM is defined similarly to the RPM, except that the random phase gate is replaced with a coupling gate with more independent parameters, leading to quantum chaotic dynamics. Specifically, the parity inversion symmetric RHM (p-RHM) is defined by

$$\text{Temporal random:} \quad U_{\text{r-p-RHM}} = \mathcal{U}_{\text{r}}(t; \mathcal{U}_{\text{p-RHM}}), \quad (\text{SA.9})$$

$$\text{Discrete time translational invariant (Floquet):} \quad U_{\text{f-p-RHM}} = \mathcal{U}_{\text{f}}(t; \mathcal{U}_{\text{p-RHM}}), \quad (\text{SA.10})$$

where  $\mathcal{U}_{\text{p-RHM}}$  is a bilayer unitary operator with the brickwall geometry given by

$$\mathcal{U}_{\text{p-RHM}}(t, L) = \mathcal{U}_2(t, L)\mathcal{U}_1(t, L), \quad \mathcal{U}_m(t, L) = \bigotimes_{r \in 2\mathbb{Z} + m \bmod 2} w(t, r). \quad (\text{SA.11})$$

$w(t, r)$  is a two-site unitary quantum gate acting on sites  $r$  and  $r + 1$ . For periodic boundary condition (pbc), the product is over  $2\mathbb{Z} + 1 \equiv \{1, 3, 5, \dots, L-1\}$  or  $2\mathbb{Z} \equiv \{2, 4, 6, \dots, L\}$ . For open boundary condition (obc), the 2-site gate straddling across sites  $L$  and  $1$ , namely  $u(t, r = L)$ , is removed, and we have a product over  $2\mathbb{Z} \equiv \{2, 4, 6, \dots, L-2\}$ . For simplicity, we only consider quantum circuits of even system sizes, i.e.  $L \in 2\mathbb{Z}$ .  $w(t, r)$  is defined by

$$\begin{aligned} w(t, r) &= \exp \left[ i \sum_{\mu, \nu=0,1,2,3} a_{\mu\nu} \sigma_\mu \otimes \sigma_\nu \right] [u(t, r) \otimes u(t, r+1)], & \text{if } r \in [1, 2, \dots, L/2 - 1], \\ &\text{with } a_{\mu\nu} \in \mathcal{N}(0, \eta), \quad u(t, r) \in \text{CUE}, \\ w(t, r) &= \exp \left[ i \sum_{\mu, \nu=0,1,2,3} b_{\mu\nu} \sigma_\mu \otimes \sigma_\nu \right] [u(t, r) \otimes u(t, r)], & \text{if } r = L/2, L, \\ &\text{with } b_{\mu\nu} \in \mathcal{N}(0, \eta) \text{ and } b_{\mu\nu} = b_{\nu\mu}, \quad u(t, r) \in \text{CUE}, \\ w(t, r) &= S w(t, L-r) S & \text{if } r \in [L/2 + 1, \dots, L-1], \end{aligned} \quad (\text{SA.12})$$

where  $a_{\mu\nu}$  and  $b_{\mu\nu}$  are independent real Gaussian variables with mean zero and variance  $\eta$ . For computational efficiency, we adopt RHM models in which, for each realization of  $\mathcal{U}_{\text{r-p-RHM}}$  and  $\mathcal{U}_{\text{f-p-RHM}}$ , only a single set of  $a_{\mu\nu}$  and a single set of  $b_{\mu\nu}$  are sampled and used across both space and time. Again, note that for obc (pbc), the 2-site gate straddling across sites  $L$  and  $1$ , namely  $w(t, r = L)$ , is removed (kept). Note that for sites without local parity inversion symmetry, i.e. for  $r \notin L/2$  and  $L$ , the generator of  $w(t, r)$  can equivalently be written as the Gaussian Unitary Ensemble (GUE).

### 3. Time reversal symmetric models

We consider one-dimensional time reversal symmetric quantum circuits  $U$  that act on the Hilbert space of  $L$  qubits with Hilbert space dimension  $q^L$  with  $q = 2$ . We adopt the framework and models of Ref. [44] to analyze quantum many-body chaos in time reversal symmetric systems. A quantum system described by a Hamiltonian  $H(t)$  at time  $t$  is time reversal symmetric (TRS) if  $H(t) = \mathcal{T}H(-t)\mathcal{T}^{-1}$ , where  $\mathcal{T}$  is an antiunitary operator. A quantum system described by a unitary operator  $U(t)$  is TRS if  $\mathcal{T}U(t)\mathcal{T}^{-1} = U^\dagger(t)$ . It can be shown that the antiunitary operator satisfies  $\mathcal{T}^2 = \pm 1$ , where the plus and minus signs correspond to the cases of systems with TRS with integer and half-integer spins respectively. Here we focus on dynamical and spectral properties of TRS quantum many-body systems with  $\mathcal{T}^2 = 1$ . For any unitary  $u$  satisfying equation  $\mathcal{T}u\mathcal{T}^{-1} = u^\dagger$ , in the basis where  $\mathcal{T}$  is complex conjugation operator,  $u = u^T$  is symmetric. Therefore,  $u$  always has a spectral decomposition  $u = \mathcal{S}\Lambda\mathcal{S}^T$  where the superscript  $T$  denotes transposition,  $\Lambda$  is the diagonal matrix of eigenvalues, and the similarity matrix  $\mathcal{S}$  satisfies  $\mathcal{S}^T\mathcal{S} = \mathbb{1}$ . In other words, we can always decompose  $u = vv^T$  and we call  $v = \mathcal{S}\sqrt{\Lambda}$  a half gate of  $u$ . As an example, if  $u$  is drawn from the Circular Orthogonal Ensemble (COE), then it has a natural decomposition  $u = vv^T$  with  $v$  drawn from the CUE, and so  $v$  from CUE is a half gate of  $u$  from COE. In the following, we will use half gates at the first and last time steps of quantum circuits. Lastly, as discussed in [44], if the many-body quantum circuit  $U$  is TRS, then  $V$ , the spacetime dual of  $U$ , commutes with the global swap operator  $S$  in the spatial direction, i.e.  $[V, S] = 0$ , where  $S$  acts on the dual Hilbert space.

#### a. TRS Random Phase Model

The random phase model (RPM) [13] is a one-dimensional quantum circuit that acts on the Hilbert space of  $L$  qudits with Hilbert space dimension  $q^L$ . The model is composed of  $q$ -by- $q$  one-site gates

$$u^{(r)}(s) \in \text{CUE or COE}, \quad (\text{SA.13})$$

acting on site  $r$ , where CUE and COE stand for Circular Unitary Ensemble and the Circular Orthogonal Ensemble respectively; and  $q^2$ -by- $q^2$  two-site gates,

$$[\Theta^{(r, r+1)}(s, \epsilon)]_{a_r a_{r+1}, b_r b_{r+1}} = \delta_{a_r, b_r} \delta_{a_{r+1}, b_{r+1}} \exp[i\varphi_{a_r, a_{r+1}}^{(r)}(s, \epsilon)], \quad (\text{SA.14})$$

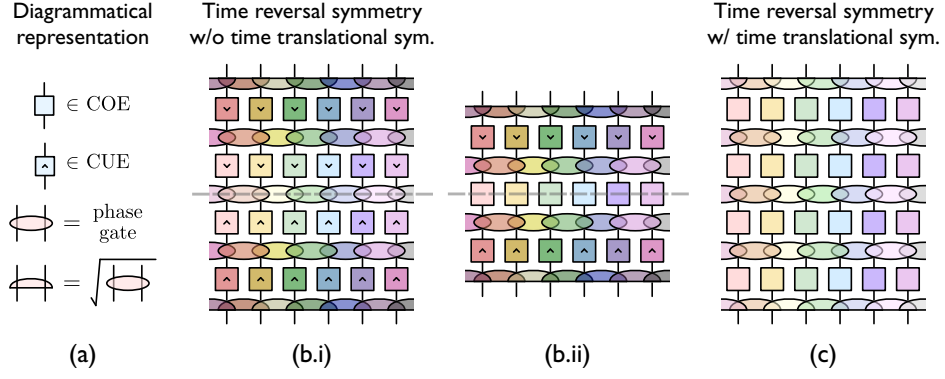


FIG. S2. **TRS Random Phase Models.** Gates with the same color are identical. (a) Dictionary of the diagrammatic representation. (b) Illustrations of the t-RPM without time translational symmetry at (b.i)  $t = 4$  and (b.ii)  $t = 3$ . Note that gates reflected across the time reversal axes (dashed lines) are identified under transposition. (c) Illustrations of t-RPM with discrete time translational symmetry at  $t = 4$ .

coupling neighbouring sites via a diagonal random phase ( $a_r = 1, 2, \dots, q$ ). Each coefficient  $\varphi_{a_r, a_{r+1}}^{(r)}(s)$  is an independent Gaussian random real variable with mean zero and variance  $\epsilon$ , which controls the coupling strength between neighbouring spins.

Then, we can define monolayers of one-site gates, of two-site gates and of two-site half gates as

$$\text{1-site gate monolayer:} \quad w_h(s; u) = \bigotimes_{r=1}^L u^{(r)}(s), \quad (\text{SA.15})$$

$$\text{2-site gate monolayer:} \quad w_{\text{ph}}(s; \epsilon) = \prod_{r=1}^L \Theta^{(r, r+1)}(s, \epsilon), \quad (\text{SA.16})$$

$$\text{RPM bilayer:} \quad w_{\text{bl}}(s, \epsilon; u) = w_{\text{ph}}(s; \epsilon) w_h(s; u) \quad (\text{SA.17})$$

$$\text{Shifted RPM bilayer:} \quad w_{\text{sbl}}(s, \epsilon; u) = w_{\text{ph}}(s; \epsilon/4) w_h(s; u) w_{\text{ph}}(s; \epsilon/4) \quad (\text{SA.18})$$

where the variable  $s$  allows the freedom for different bilayer labelled by  $s$  to be independent of each other.

Note that in the shifted TRS, the first and the third layers are drawn from the same ensemble. The variances in these layers are chosen such that  $w_{\text{ph}}(s; \epsilon/4)^2 = w_{\text{ph}}(s; \epsilon)$ .

Now we define RPM with various types of TRS. For the RPM with global TRS without discrete time translational symmetry, we define

$$w_{\text{g-trs}}(t, L) = \begin{cases} w_h((t-1)/2 + 1; u_{\text{CUE}}) \left[ \prod_{s=1}^{(t-1)/2} w_{\text{bl}}(s, \epsilon; u_{\text{CUE}}) \right] w_{\text{ph}}((t-1)/2 + 1; \epsilon/4), & t \text{ odd,} \\ w_{\text{ph}}(t/2; \epsilon/4) w_h(t/2; u_{\text{CUE}}) \left[ \prod_{s=1}^{t/2-1} w_{\text{bl}}(s, \epsilon; u_{\text{CUE}}) \right] w_{\text{ph}}(0; \epsilon/4), & t \text{ even,} \end{cases} \quad (\text{SA.19})$$

which governs the first half of the global TRS circuits. The entire global TRS circuits are then generated by extending the above circuits with their transpositions, as defined below. The Floquet TRS RPM can be defined by repeated action of a shifted RPM bilayer. Together, we define

$$\text{Global TRS:} \quad U_{\text{g-trs-RPM}}(t, L) = \mathcal{U}_{\text{trs}}[w_{\text{g-trs}}(t, L)], \quad (\text{SA.20})$$

$$\text{Floquet TRS:} \quad U_{\text{f-trs-RPM}}(t, L) = \mathcal{U}_{\text{f}}[t; w_{\text{sbl}}(1, \epsilon; u_{\text{COE}})]. \quad (\text{SA.21})$$

See Fig. S2 for illustrations of the TRS RPMs.

### b. TRS Random Hamiltonian Model

The random Hamiltonian model (RHM) is a one-dimensional quantum circuit that acts on the Hilbert space of  $L$  qudits with Hilbert space dimension  $q^L$ . The RHM is utilized to numerically simulate generic quantum many-body chaotic dynamics at  $q = 2$ . The TRS RHM is defined similarly to the t-RPM, except that the random phase gate is replaced with a coupling gate with more independent parameters, leading quantum chaotic dynamics at  $q = 2$ . Due

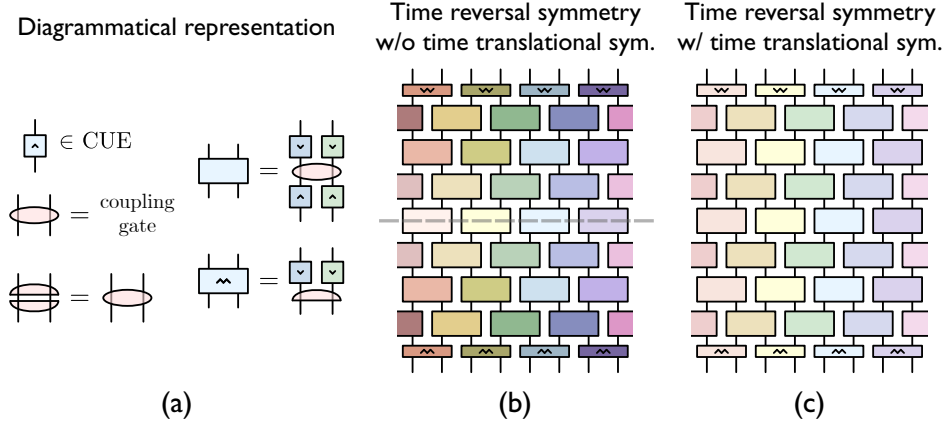


FIG. S3. **TRS Random Hamiltonian Models.** Gates with the same color are identical. (a) Dictionary of the diagrammatic representation. (b) Illustrations of the t-RHM (b) without and (c) with discrete time translational symmetry at  $t = 4$ . Note that gates reflected across the time reversal axes (dashed lines) are identified under transposition.

to the non-commuting interaction among the coupling gates, we construct RHM with a brick-wall geometry composed of two-site gates acting on the  $r$ -th and  $(r + 1)$ -th qudits,

$$u_{\text{RHM}}(t, r) = \left( \left[ u_1^{(r)}(t) \right]^T \otimes \left[ u_2^{(r)}(t) \right]^T \right) \exp \left( i \sum_{\mu, \nu=0,1,2,3} a_{\mu\nu} \sigma_\mu \otimes \sigma_\nu \right) \left( u_1^{(r)}(t) \otimes u_2^{(r)}(t) \right) \quad (\text{SA.22})$$

$$u_1^{(r)}(t), u_2^{(r)}(t) \in \text{CUE}, \quad a_{\mu\nu} \in \mathcal{N}(0, \eta), \quad a_{\rho 2} = a_{2\rho} = 0 \text{ for } \rho = 0, 1, 3.$$

where  $a_{\mu\nu}$  are independent real Gaussian variables with mean zero and variance  $\eta$ .  $u_1$  and  $u_2$  are  $q$ -by- $q$  unitaries drawn from the CUE. The constraints on  $a_{\rho 2}$  and  $a_{2\rho}$  arise as follows: Since we are focusing on  $\mathcal{T}^2 = 1$ , we can choose a basis such that the anti-unitary symmetry operator can be written as  $\mathcal{T} = \mathcal{K}$ , the complex conjugation operator. In this basis, the generators of the exponential in Eq. (SA.22) are real. Since  $\sigma_2$  is purely imaginary,  $\mathcal{T}$  invariance requires the coefficient for the basis elements with an odd number of  $\sigma_2$  to vanish, leading to  $a_{\rho 2} = a_{2\rho} = 0$  for  $\rho = 0, 1, 3$ . As before, for computational efficiency, we adopt RHM models in which, for each realization in the ensemble, only a single set of  $a_{\mu\nu}$  is sampled and used across both space and time.

As discussed in the beginning of the section, for any unitary  $u$  satisfying equation  $\mathcal{T}u\mathcal{T}^{-1} = u^\dagger$ , there always exists a basis such that  $u$  is symmetric, and we can decompose  $u = vv^T$  with a half gate  $v$ . In the definitions below, for each  $u_{\text{RHM}}(t, r)$ , we will use its half gate  $v_{\text{RHM}}(t, r)$  satisfying  $u_{\text{RHM}}(t, r) = v_{\text{RHM}}v_{\text{RHM}}^T$ . Specifically, we respectively define a monolayer and a bilayer of two-site gates in the brick-wall geometry with even system sizes as

$$\text{Brick-wall monolayer:} \quad w_m(s; u) = \bigotimes_{j \in 2\mathbb{Z} + m \bmod 2} u^{(r, r+1)}(s), \quad (\text{SA.23})$$

$$\text{Brick-wall bilayer:} \quad w_{\text{bl}}(s; u_{\text{RHM}}) = w_2(s; u_{\text{RHM}}) w_1(s; u_{\text{RHM}}), \quad (\text{SA.24})$$

$$\text{Shifted TRS brick-wall bilayer:} \quad w_{\text{sbl}}(s) = w_1(s, v_{\text{RHM}})^T w_2(s; u_{\text{RHM}}) w_1(s; v_{\text{RHM}}), \quad (\text{SA.25})$$

where the variable  $s$  allows the freedom for different bilayer labelled by  $s$  to be independent of each other. Note that in the shifted TRS, by construction, the first and the third layers are drawn from the same ensemble.

Now we define the TRS RHM with and without discrete time translational symmetry. To define the latter, we define

$$w_{\text{trs}}(t, L) = w_t(t; v_{\text{RHM}}) \left[ \prod_{s=2}^{t-1} w_s(s; u_{\text{RHM}}) \right] w_1(1; v_{\text{RHM}}), \quad (\text{SA.26})$$

which governs the first half of the global TRS circuits. The entire global TRS circuits are then generated by extending the above circuits with their transpositions, as defined below. Note that the first and last layers of  $w_{\text{g-TRS}}$  are drawn from half gates, such that, upon the extension with transposition, we can construct a full gate across the time reversal axis (dashed lines in Fig. S3), using the construction,  $u_{\text{RHM}} = v_{\text{RHM}}v_{\text{RHM}}^T$ . To define the Floquet TRS RHM, we can

simply repeatedly act a shifted brick-wall bilayer. Together, we define for both odd and even  $t$ ,

$$\text{Global TRS RHM: } U_{\text{g-trs-RHM}}(t, L) = \mathcal{U}_{\text{trs}}[w_{\text{TRS}}(t, L)], \quad (\text{SA.27})$$

$$\text{Floquet TRS RHM: } U_{\text{f-trs-RHM}}^{\text{F}}(t, L) = \mathcal{U}_{\text{f}}[t; w_{\text{sbl}}(1)]. \quad (\text{SA.28})$$

Again, note that for obc (pbc), the 2-site gate straddling across sites  $L$  and 1, namely  $w(t, r = L)$ , is removed (kept). See Fig. S3 for illustrations of the TRS RHM.

#### 4. Time translational symmetric only models

We now define quantum circuits with discrete time translational symmetry, without imposing parity inversion symmetry or time reversal symmetry. In these models, a unitary circuit layer, which may itself consist of multiple sublayers, is sampled once and then repeated periodically in time.

##### a. Random Phase Model

The random phase model (RPM) [13] is a one-dimensional quantum circuit that acts on the Hilbert space of  $L$  qudits with Hilbert space dimension  $q^L$ . The RPM without additional symmetries is known to be quantum chaotic for  $q \geq 3$ , and not quantum chaotic for  $q = 2$  [13]. The Floquet RPM is defined by repeated action of a single bilayer unitary operator,

$$\text{Discrete time translational invariant (Floquet): } U_{\text{f-RPM}}(t, L) = \mathcal{U}_{\text{f}}(t; \mathcal{U}_{\text{RPM}}), \quad (\text{SA.29})$$

where a single bilayer is given by

$$\mathcal{U}_{\text{RPM}}(L) = \mathcal{U}_2(L) \mathcal{U}_1(L), \quad \mathcal{U}_1(L) = \bigotimes_{r=1}^L u(r), \quad \mathcal{U}_2(L) = \prod_{r=1}^L w(r). \quad (\text{SA.30})$$

Here  $u(r)$  is a one-site unitary gate acting on site  $r$ , drawn independently from the Circular Unitary Ensemble (CUE),

$$u(r) \in \text{CUE}, \quad r = 1, 2, \dots, L, \quad (\text{SA.31})$$

and  $w(r)$  is a two-site diagonal random phase gate acting on sites  $(r, r + 1)$ , defined by

$$[w(r)]_{ab}^{cd} = \delta_{ac} \delta_{bd} \exp[i\phi_{ab}(r)], \quad \phi_{ab}(r) \in \mathcal{N}(0, \epsilon). \quad (\text{SA.32})$$

The real Gaussian variables  $\phi_{ab}(r)$  are independent with mean zero and variance  $\epsilon$ , which controls the coupling strength between neighbouring sites. For pbc, the product in  $\mathcal{U}_2(L)$  includes the gate straddling sites  $(L, 1)$ . For obc, this gate is removed.

##### b. Random Hamiltonian Model

The random Hamiltonian model (RHM) is a one-dimensional quantum circuit that acts on the Hilbert space of  $L$  qubits with Hilbert space dimension  $q^L$  and  $q = 2$ . The RHM is used to numerically simulate generic quantum many-body chaotic dynamics at  $q = 2$ . In the absence of additional symmetries, the Floquet RHM is defined by repeated action of a brick-wall bilayer,

$$\text{Discrete time translational invariant (Floquet): } U_{\text{f-RHM}}(t, L) = \mathcal{U}_{\text{f}}(t; \mathcal{U}_{\text{RHM}}), \quad (\text{SA.33})$$

where

$$\mathcal{U}_{\text{RHM}}(L) = \mathcal{U}_2(L) \mathcal{U}_1(L), \quad \mathcal{U}_m(L) = \bigotimes_{r \in 2\mathbb{Z} + m \bmod 2} w(r). \quad (\text{SA.34})$$

Here  $w(r)$  is a two-site unitary gate acting on sites  $(r, r + 1)$ , of the form

$$w(r) = \exp \left[ i \sum_{\mu, \nu=0}^3 a_{\mu\nu}(r) \sigma_\mu \otimes \sigma_\nu \right] [u(r) \otimes u(r + 1)], \quad (\text{SA.35})$$

with

$$a_{\mu\nu}(r) \in \mathcal{N}(0, \eta), \quad u(r) \in \text{CUE}. \quad (\text{SA.36})$$

The coefficients  $a_{\mu\nu}(r)$  are independent real Gaussian variables with mean zero and variance  $\eta$ , while the one-site gates  $u(r)$  are independently drawn from the CUE. The parameter  $\eta$  controls the interaction strength between neighbouring qubits. For pbc, the products in  $\mathcal{U}_1(L)$  and  $\mathcal{U}_2(L)$  are over  $2\mathbb{Z} + 1 \equiv \{1, 3, 5, \dots, L - 1\}$  and  $2\mathbb{Z} \equiv \{2, 4, 6, \dots, L\}$  respectively. For obc, the two-site gate straddling sites  $(L, 1)$  is removed, and the product over even bonds becomes  $2\mathbb{Z} \equiv \{2, 4, 6, \dots, L - 2\}$ . For simplicity, we consider even system sizes, i.e.  $L \in 2\mathbb{Z}$ . As in the Floquet RPM, the same sampled bilayer  $\mathcal{U}_{\text{RHM}}(L)$  is repeated at each Floquet period.

## Appendix B: TopSFF for RMT

The Gaussian unitary ensemble (GUE) and the circular unitary ensemble (CUE) are valuable because they provide effective universal descriptions of quantum many-body chaotic systems at late times [14]. Likewise, the non-Hermitian Ginibre unitary ensemble (GinUE) provides an effective universal description of quantum many-body chaotic systems in the large-system-size limit [27]. In this section, we evaluate the topological spectral form factor (TopSFF) in random matrix theory (RMT), focusing on the GUE, CUE, and Ginibre unitary ensemble. We note, however, that the TopSFF considered here is not genuinely ‘‘topological’’ since the random matrices are not required to commute with the defect operator. Nevertheless, these calculations remain valuable, as they provide useful benchmarks for quantum many-body systems in the late time regime or in the large system size limit.

### 1. Gaussian and circular ensembles

We evaluate the ensemble average of

$$K_{\text{h-RMT}}^{\text{top}}(D_1, D_2; \alpha, \beta) = \text{Tr}[D_1^\alpha U(t)] \text{Tr}[D_2^\beta U^\dagger(t)] \quad (\text{SB.1})$$

where  $D_1$  and  $D_2$  are arbitrary defect operators, and the binary exponents  $\alpha, \beta = 0, 1$  are used to toggle the defect operators on or off.  $U(t)$  is defined by

$$\begin{aligned} U_{\text{r-h-RMT}}(t) &:= \prod_{\tau=1}^t u(\tau), & \text{Random,} \\ U_{\text{f-h-RMT}}(t) &:= u^t, & \text{Floquet,} \end{aligned} \quad (\text{SB.2})$$

with  $u(\tau)$  and  $u$  drawn from the circular unitary ensemble (CUE) of  $N$ -by- $N$  unitary matrices, or with  $u(\tau) = \exp[iH(\tau)]$  and  $u = \exp(iH)$  with  $H$  drawn from the Gaussian unitary ensemble (GUE) of  $N$ -by- $N$  Hermitian matrices. We use ‘‘h-RMT’’ to denote ensembles of unitary or Hermitian matrices, as opposed to the non-Hermitian matrices considered in the next subsection. In either case,  $u$  can be diagonalized via  $u = W\Lambda W^\dagger$ , where  $\Lambda$  is a diagonal matrix of the eigenvalues of  $u$ , and  $W$ , the eigenvector matrix of  $u$ , is yet another unitary matrix drawn from the CUE. The first moment of a pair of unitary  $u$  and its complex conjugate  $u^*$  drawn from the CUE can be evaluated as  $\overline{u_{ab}u_{a'b'}^*} = (N)^{-1}\delta_{aa'}\delta_{bb'}$ , and their second moment is  $\overline{u_{a_1b_1}u_{a'_1b'_1}^*u_{a_2b_2}u_{a'_2b'_2}^*} = (N^2 - 1)^{-1}(\delta_{a_1a'_1}\delta_{b_1b'_1}\delta_{a_2a'_2}\delta_{b_2b'_2} + \delta_{a_1a'_2}\delta_{b_1b'_2}\delta_{a_2a'_1}\delta_{b_2b'_1}) - [N(N^2 - 1)]^{-1}(\delta_{a_1a'_1}\delta_{b_1b'_2}\delta_{a_2a'_2}\delta_{b_2b'_1} + \delta_{a_1a'_2}\delta_{b_1b'_1}\delta_{a_2a'_1}\delta_{b_2b'_2})$ , where the prefactors follow from the Weingarten functions for the CUE [39]. Now we can directly evaluate TopSFF for the random RMT model as

$$\begin{aligned} \overline{K_{\text{h-RMT}}^{\text{top}}(D_1, D_2; \alpha, \beta)} &= \frac{1}{N} \text{tr} [D_1^\alpha D_2^\beta] \\ &= \begin{cases} 1, & \alpha = \beta = 0, \\ \frac{1}{N} \text{tr} D_1, & \alpha = 1, \beta = 0, \\ \frac{1}{N} \text{tr} D_2, & \alpha = 0, \beta = 1, \\ \frac{1}{N} \text{tr} [D_1 D_2], & \alpha = \beta = 1. \end{cases} \quad (\text{SB.3}) \end{aligned}$$

TopSFF for the Floquet RMT model can be evaluated as

$$\begin{aligned}
& \overline{K_{\text{h-RMT}}^{\text{top}}(D_1, D_2; \alpha, \beta)} \\
&= \frac{\overline{\text{tr } D_1^\alpha \text{tr } D_2^\beta - N^{-1} \text{tr}(D_1^\alpha D_2^\beta)}}{N^2 - 1} \overline{K_{\text{h-RMT}}(t)} + \frac{N \text{tr}(D_1^\alpha D_2^\beta) - \text{tr } D_1^\alpha \text{tr } D_2^\beta}{N^2 - 1} \\
&= \begin{cases} \overline{K_{\text{h-RMT}}(t)}, & \alpha = \beta = 0, \\ \frac{\text{tr } D_1}{N} \overline{K_{\text{h-RMT}}(t)}, & \alpha = 1, \beta = 0, \\ \frac{\text{tr } D_2}{N} \overline{K_{\text{h-RMT}}(t)}, & \alpha = 0, \beta = 1, \\ \frac{N \text{tr } D_1 \text{tr } D_2 - \text{tr}(D_1 D_2)}{N(N^2 - 1)} \overline{K_{\text{h-RMT}}(t)} + \frac{N \text{tr}(D_1 D_2) - \text{tr } D_1 \text{tr } D_2}{N^2 - 1}, & \alpha = \beta = 1. \end{cases} \quad (\text{SB.4})
\end{aligned}$$

where

$$\overline{K_{\text{h-RMT}}(t)} := \overline{\text{Tr}[U(t)] \text{Tr}[U^\dagger(t)]} = \begin{cases} \overline{K_{\text{CUE}}(t)}, & \text{if } U(t) = u^t, \quad u \in \text{CUE}, \\ \overline{K_{\text{GUE}}(t)}, & \text{if } U(t) = \exp(iHt), \quad H \in \text{GUE}. \end{cases} \quad (\text{SB.5})$$

is the ensemble averaged SFF without operator insertions for unitary matrices drawn from the CUE or Hermitian matrices drawn from the GUE.

Figure S27 in Appendix L confirms the late-time RMT limit of the TopSFF in the parity-symmetric RPM: after  $t_{\text{Hei}} \propto q^L$ ,  $\overline{K_{\text{top}}}$  saturates to the  $q^{L/2}$  plateau predicted by Eq. (SB.4). However, unlike the conventional SFF, the TopSFF does not show a clear ramp plateau behaviour in the pre-Heisenberg regime. The TopSFF behaviour in the pre-Heisenberg regime is investigated in the main text and below.

## 2. Ginibre ensembles

Let  $G$  denote an  $N \times N$  complex Ginibre matrix with probability distribution  $P(G) \propto \exp[-\frac{N}{v} \text{Tr}(GG^\dagger)]$ , so that its matrix elements satisfy  $\overline{G_{ab} G_{cd}^*} = \frac{v}{N} \delta_{ac} \delta_{bd}$  and  $\overline{G_{ab}} = 0$ . For the standard normalization of the Ginibre ensemble one sets  $v = 1$ , and we adopt this convention below. We now evaluate the TopSFF for the Ginibre unitary ensemble,

$$K_{\text{nh-RMT}}^{\text{top}}(D_1, D_2; \alpha, \beta; L) := \text{Tr}[D_1^\alpha G(L)] \text{Tr}[D_2^\beta G^\dagger(L)], \quad (\text{SB.6})$$

with  $\alpha, \beta \in \{0, 1\}$ . The matrices  $G(\ell)$  are independently drawn from the Ginibre ensemble, while  $G$  in the Floquet case is drawn once and then repeated,

$$\begin{aligned}
G_{\text{r-nh-RMT}}(L) &:= \prod_{\ell=1}^L G(\ell), & \text{Random,} \\
G_{\text{f-nh-RMT}}(L) &:= G^L, & \text{Floquet.} \end{aligned} \quad (\text{SB.7})$$

We use ‘‘nh-RMT’’ to denote ensembles of non-Hermitian matrices, as opposed to the unitary or Hermitian matrices considered in the previous subsection. For the random case, we can evaluate the TopSFF using the second moments of  $G(\ell)$  as

$$\overline{K_{\text{nh-RMT}}^{\text{top}}(D_1, D_2; \alpha, \beta; L)} = \frac{1}{N} \text{tr}[D_1^\alpha D_2^\beta] = \begin{cases} 1, & \alpha = \beta = 0, \\ \frac{1}{N} \text{tr } D_1, & \alpha = 1, \beta = 0, \\ \frac{1}{N} \text{tr } D_2, & \alpha = 0, \beta = 1, \\ \frac{1}{N} \text{tr}(D_1 D_2), & \alpha = \beta = 1. \end{cases} \quad (\text{SB.8})$$

For the Floquet case, we use the Schur decomposition  $G = UTU^\dagger$ , where  $U$  is Haar distributed and independent of the upper-triangular matrix  $T$ . Writing the eigenvalues of  $G$  as  $\{z_i\}_{i=1}^N$ , the diagonal entries of  $T^L$  are simply  $z_i^L$ , the

trace becomes  $\text{Tr}(D_1^\alpha G^L) = \sum_{i=1}^N z_i^L (U^\dagger D_1^\alpha U)_{ii}$ . Applying the second moment of Haar random unitaries from the previous subsection, we obtain

$$\begin{aligned}
& \overline{K_{\text{nh-RMT}}^{\text{top}}(D_1, D_2; \alpha, \beta; L)} \\
&= \frac{\text{tr } D_1^\alpha \text{tr } D_2^\beta - \frac{1}{N} \text{tr}(D_1^\alpha D_2^\beta)}{N^2 - 1} \overline{K_{\text{nh-RMT}}(N, L)} + \frac{N \text{tr}(D_1^\alpha D_2^\beta) - \text{tr } D_1^\alpha \text{tr } D_2^\beta}{N(N^2 - 1)} \overline{C_{\text{nh-RMT}}(N, L)} \\
&= \begin{cases} \overline{K_{\text{nh-RMT}}(N, L)}, & \alpha = \beta = 0, \\ \frac{\text{tr } D_1}{N} \overline{K_{\text{nh-RMT}}(N, L)}, & \alpha = 1, \beta = 0, \\ \frac{\text{tr } D_2}{N} \overline{K_{\text{nh-RMT}}(N, L)}, & \alpha = 0, \beta = 1, \\ \frac{N \text{tr } D_1 \text{tr } D_2 - \text{tr}(D_1 D_2)}{N(N^2 - 1)} \overline{K_{\text{nh-RMT}}(N, L)} + \frac{N \text{tr}(D_1 D_2) - \text{tr } D_1 \text{tr } D_2}{N(N^2 - 1)} \overline{C_{\text{nh-RMT}}(N, L)}, & \alpha = \beta = 1. \end{cases} \quad (\text{SB.9})
\end{aligned}$$

where

$$\begin{aligned}
\overline{K_{\text{nh-RMT}}(N, L)} &:= \overline{|\text{Tr}(G^L)|^2} = N^2 \delta_{L,0} + \frac{1}{N^L (L+1)(N-1)!} \left[ (L+N)! - \frac{N!(N-1)!}{(N-L-1)!} \right], \\
\overline{C_{\text{nh-RMT}}(N, L)} &:= \sum_{i=1}^N |z_i|^{2L} = \frac{(N+L)!}{N^L (L+1)(N-1)!}, \quad (\text{SB.10})
\end{aligned}$$

are respectively the regular SFF and the contact term of the Ginibre ensemble obtained in [27]. A useful check is that if  $D_1 = D_2 = \mathbb{1}$ , then (SB.9) reduces to the ordinary Ginibre SFF,  $\overline{K_{\text{nh-RMT}}^{\text{top}}(\mathbb{1}, \mathbb{1}; 1, 1; L)} = \overline{K_{\text{nh-RMT}}(N, L)}$ .

### Appendix C: Review of exact solutions of SFF without topological defects

In this appendix, we collect exact large- $q$  results for the ordinary SFF, without topological defect insertions, in the three symmetry settings relevant to this work: parity inversion symmetry, time reversal symmetry, and discrete time translation symmetry.

#### 1. Parity inversion symmetry

Here we review the analytical solutions of SFF in the parity inversion symmetric many-body quantum chaotic models derived in [38]. The approach can be used to evaluate  $d$ -dimensional parity inversion symmetric RPM models defined in A 2 a. In particular, for one-dimensional parity inversion symmetric RPM with periodic boundary condition, the SFF can be evaluated exactly in large- $q$  limit as

$$\overline{K_{\text{r-p-RPM}}(t, L)} = 2(1 + e^{-2\epsilon t})^{L_e}. \quad (\text{SC.1})$$

where  $L_e$  counts the number of bonds in the folded picture as described in the main text, with  $L_e = L/2 - 1$  for even  $L$ , and  $L_e = (L-1)/2 - 1$  for odd  $L$ .  $\epsilon$  is the variance of the random phases in the RPM, which controls the coupling strength of the many-body system. For Floquet parity inversion symmetric RPM with periodic boundary condition we have

$$\begin{aligned}
\overline{K_{\text{f-p-RPM}}(t, L)} &= (2t-2)(e^{-\epsilon t} - 1)^2 (e^{-\epsilon t} - 1)^{2L_e} \\
&\quad + 2[(t-1)e^{-\epsilon} + 1]^2 [(2t^2 - 2t + 1)e^{-2\epsilon t} + 2(t-1)e^{-\epsilon t} + 1]^{L_e}. \quad (\text{SC.2})
\end{aligned}$$

where  $L_e$  and  $\epsilon$  are defined as above.

#### 2. TRS

Here we review the analytical solutions of SFF in the TRS many-body quantum chaotic models derived in [44]. The approach can be used to evaluate  $d$ -dimensional TRS RPM models defined in A 3 a. In particular, for one-dimensional global TRS RPM with periodic boundary condition, the SFF can be evaluated exactly in large- $q$  limit as

$$\overline{K_{\text{trs-RPM}}(t, L)} = \left[ 1 + e^{-\epsilon(t-1-\delta_{0,t \pmod{2}})} \right]^L + \left[ 1 - e^{-\epsilon(t-1-\delta_{0,t \pmod{2}})} \right]^L. \quad (\text{SC.3})$$

where  $\epsilon$  is the variance of the random phases in the RPM.

### 3. Time translational symmetry

Here we review the analytical solutions of SFF in many-body quantum chaotic models with discrete time translational symmetry (but without other symmetries) in [13]. The approach can be used to evaluate  $d$ -dimensional RPM models with time translational symmetry defined in A 4. In particular, for one-dimensional RPM with periodic boundary condition, the SFF can be evaluated exactly in large- $q$  limit as

$$\overline{K_{\text{RPM}}(t, L)} = (t-1)(1-e^{-\epsilon t})^L + [1+(t-1)e^{-\epsilon t}]^L \quad (\text{SC.4})$$

where, again,  $\epsilon$  is the variance of the random phases in the RPM.

## Appendix D: SFF with twisted boundary conditions

For completeness, we contrast the TopSFF with the SFF under twisted boundary conditions in space or in time. A twisted boundary condition inserts the same defect in both  $U$  and  $U^*$ , leaving the two world-sheets topologically matched. As a result, these observables do not isolate the domain-wall sectors responsible for the universal scaling forms and emergent  $\mathcal{PT}$  transition discussed in the main text.

### 1. Spatially extended twisted boundary condition

We consider the SFF of a generic quantum many-body chaotic system with a spatially extended twisted boundary condition,  $K_{\text{parity}}^{\text{twisted}} = \left| \text{Tr}[\hat{S}\hat{U}_t(t, L)] \right|^2$ . Here  $\hat{S}$  is the global swap operator acting in the time direction. The generic chaotic system is realised by the RPM with parity inversion and discrete time translation symmetries, defined in Eq. (SA.21), which satisfies  $[\hat{S}, \hat{U}_t(t, L)] = 0$ . The tensor network for  $K_{\text{parity-RPM}}^{\text{twisted}}$  consists of two space-time world-sheets with identical topology. Under the folding and unwrapping procedure of App. E, the local diagrammatics contains two long loops, from  $\text{Tr}[\hat{S}\hat{U}^t]$  and  $\text{Tr}[\hat{S}\hat{U}^{*t}]$ , but without Mickey Mouse structure or associated temporal domain walls of the type described in the main text and App. E 1. Applying the methods of App. E, one computes exactly in the large- $q$  limit

$$\overline{K_{\text{parity-RPM}}^{\text{twisted}}} = \mathcal{Z}_{2t\text{-Potts}} = 2t(2t-1+e^{-2\epsilon t})^{L/2-1}, \quad (\text{SD.1})$$

where  $\mathcal{Z}_{2t\text{-Potts}} = \phi^T \mathcal{B}^{L/2-1} \phi$  is the partition function of a  $2t$ -state Potts model with open boundary conditions. Here  $[\mathcal{B}]_{mn} = 1 + \delta_{mn}(e^{-2\epsilon t} - 1)$  with  $m, n = 1, \dots, 2t$ , and  $\phi = (1, 1, \dots, 1)^T$ . This observable closely resembles the SFF of the parity-invariant RPM with open boundary conditions, cf. Eq. (SC.2), and does not isolate temporal domain walls responsible for the universal scaling captured in TopSFF.

### 2. Temporally extended twisted boundary condition

We consider the SFF of a generic quantum many-body chaotic system with a temporally extended twisted boundary condition,  $K_{\text{trs}}^{\text{twisted}} = |\text{Tr}[\hat{S}\hat{U}_s(t, L)]|^2$ . Here  $\hat{S}$  is the global swap operator acting in the spatial direction, and  $\hat{U}_s(t, L) := \prod_{i=1}^L \hat{V}_i(t)$  is generated by the dual transfer matrices  $\hat{V}_i(t)$  [Fig. 3(a), purple] of the RPM defined in Eq. (SA.20). The RPM satisfies  $[\hat{V}_i(t), \hat{S}] = 0$ , and therefore has global time reversal symmetry. The tensor network for  $K_{\text{trs}}^{\text{twisted}}$  consists of two space-time world-sheets with identical topology. Using the methods described in App. E and [44], one finds in the large- $q$  limit that

$$\overline{K_{\text{trs-RPM}}^{\text{twisted}}} = \overline{K_{\text{trs-RPM}}}, \quad (\text{SD.2})$$

where the analytical expression of  $\overline{K_{\text{trs-RPM}}}$  is given in (SC.3) and [44]. The exactness of the equality in (SD.2) is model-dependent, and generally relies on the defect operator commuting with all symmetries of the quantum many-body system. Nevertheless, we expect Eq. (SD.2) to hold approximately in generic chaotic systems, and the SFF of twisted boundary condition does not isolate spatial domain walls responsible for the universal scaling captured in TopSFF.

## Appendix E: Generalized Boltzmann factor of TopSFF with spatially extended defects

Here we analytically evaluate the ensemble average of TopSFF

$$K_{\text{top}}(t, L) = \text{Tr}[\hat{\mathcal{D}}(\hat{U} \otimes \hat{U}^*)] = \text{Tr}[\hat{S}\hat{U}] \text{Tr}[\hat{U}^*], \quad [\hat{\mathcal{D}}, (\hat{U} \otimes \hat{U}^*)] = 0, \quad (\text{SE.1})$$

where the spatially extended topological defect is  $\hat{\mathcal{D}} = \hat{S} \otimes 1$ . Here  $\hat{S}$  is the global swap operator, which reverses the ordering of the  $L$  qudits according to  $\hat{S}|a_1, a_2, \dots, a_{L-1}, a_L\rangle = |a_L, a_{L-1}, \dots, a_2, a_1\rangle$ , with  $a_i = 1, \dots, q$ . We analyse  $K_{\text{top}}$  in a generic many-body quantum chaotic system satisfying  $[\hat{\mathcal{D}}, \hat{U} \otimes \hat{U}^*] = 0$ , i.e. the system possesses parity inversion symmetry. Such a system is minimally realised by the Random Phase Model (RPM) with parity inversion symmetry and discrete time translation symmetry, defined in App. A 2 a, i.e.,  $\hat{U} = \hat{U}_{\text{f-p-RPM}}$ . The local Hilbert-space dimension is denoted by  $q$ . Our calculation uses the diagrammatic representation of random quantum circuits introduced in Ref. [19]. We provide exact analytic results in the large- $q$  limit, exact analytical results for finite  $q$  and small  $t$ , and numerical simulations at finite  $q$  and small  $t$ . For simplicity, the derivation below is presented for even system size  $L$ , although the method applies equally to both even and odd  $L$ .

In Appendix E 1, we identify the leading local TopSFF diagrams in the large- $q$  expansion. These diagrams form the topological equivalence class of the Mickey Mouse diagram and are parametrized by  $\rho = (a, b, c, d)$ , where  $a = 0, 1$  distinguishes Gaussian and non-Gaussian temporal domain walls. In E 2, we derive the generalized Boltzmann factor  $\mathcal{B}$  underlying TopSFF in position space, and in E 3 we describe its main properties, including translation symmetries, exchange symmetries, and reality constraints. In E 4, we Fourier transform the generalized Boltzmann factor, and in E 5 we discuss its momentum space properties, including its trace, determinant, eigenvalue structure, and special momentum sector features. In E 6, we prove that, for generic interaction strength,  $\tilde{\mathcal{B}}(k_b, k_c, k_d)$  is  $\mathcal{PT}$  symmetric precisely when  $k_b + k_c + k_d \equiv 0 \pmod{\pi}$ . In E 7, we evaluate the boundary states in the folded representation in both position and momentum space.

### 1. Mickey Mouse diagrams

**Tensor network, folding and unwrapping.** We represent the TopSFF diagrammatically using the tensor network representation, see e.g. [58]. The quantum circuit  $U_{\text{f-p-RPM}}$  in Eq. (SA.4) is represented as in Fig. S1(b), where time runs vertically from bottom to top and space horizontally from left to right. Each line denotes the worldline of a single qudit, each square denotes a local unitary gate drawn from the circular unitary ensemble (CUE), and each oval denotes a two-site coupling gate. The trace operation in the TopSFF is represented by forming a close loop from the qudit worldline at each site. The TopSFF is represented schematically in Fig. S4(a) using two world-sheets:  $\text{Tr}[\hat{S}\hat{U}(t)]$ , shown in white, and  $\text{Tr}[\hat{U}^\dagger(t)]$ , shown in grey. The open legs at the top are identified with the corresponding legs at the bottom, thereby forming the trace. The parity-inversion axes are shown in red and blue, with axes of the same colour identified.

We fold the world-sheet in half along the parity inversion axis as illustrated in Fig. S4(b), so that gates related by the parity inversion symmetry are stacked on top of each other after folding. Specifically, each world-sheet,  $\text{Tr}_t[\hat{S}\hat{U}(t, L)]$  or  $\text{Tr}_t[\hat{U}(t, L)]$ , is divided into two halves along the inversion axes, labeled 1 to 4. Folding according to Fig. S4 (a,b) produces a representation in which every space-time coordinate contains two identical unitary gates together with their two complex conjugates. In this folded picture, we construct an effective spatial chain by grouping all gates at sites  $i$  and  $L - i$  from both  $\text{Tr}_t[\hat{S}\hat{U}(t, L)]$  and  $\text{Tr}_t[\hat{U}(t, L)]$ . For even  $L$ , the folded chain has length  $L/2$ . The global swap operator now realizes a local operation exchanging the replica labelled by 1 and 3 in Fig. S4. In the folded representation, the swap operator locally commutes with the parity symmetric many-body quantum systems.

**Ensemble average of Haar-random unitaries.** The RPM ensemble average is performed in two steps: first, by integrating over the Haar-random unitary gates, or equivalently over the circular unitary ensemble (CUE), and second, by averaging over the random phases in the coupling gates. For  $q \times q$  unitary matrices  $u$  drawn from the Haar measure on the unitary group, the ensemble average is given by

$$\overline{u_{a_1 b_1} \cdots u_{a_n b_n} u_{c_1 d_1}^* \cdots u_{c_n d_n}^*} = \sum_{\sigma, \tau \in S_n} \text{Wg}(\sigma^{-1}\tau, q) \prod_{j=1}^n \delta_{a_j, c_{\sigma(j)}} \delta_{b_j, d_{\sigma'(j)}}. \quad (\text{SE.2})$$

Here  $S_n$  is the symmetric group on  $n$  elements. The Weingarten function  $\text{Wg}$  depends only on the cycle structure  $\{c_1, \dots, c_k\}$  of the permutation  $\sigma^{-1}\tau$ , where  $c_\ell$  denotes the length of the  $\ell$ -th cycle. For example, for  $n = 1$ , one finds  $\text{Wg}(\{1\}, q) = 1/q$ , while for  $n = 2$ , the two possible cycle structures give  $\text{Wg}(\{1, 1\}, q) = 1/(q^2 - 1)$  and  $\text{Wg}(\{2\}, q) =$

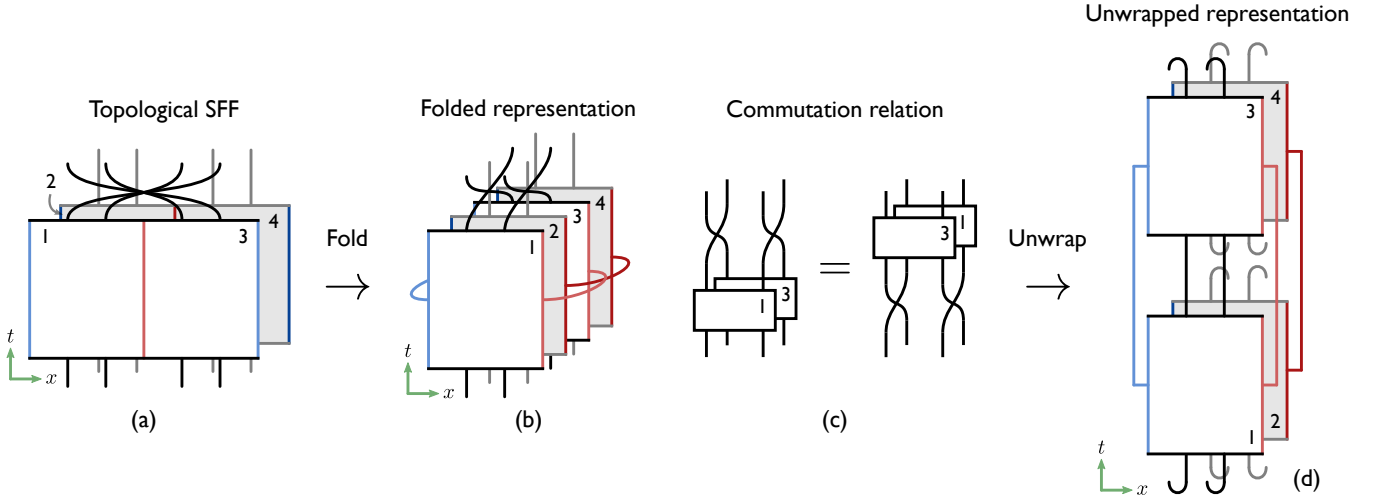


FIG. S4. **Folding and unwrapping of TopSFF with spatially extended topological defects.** (a) TopSFF  $K_{\text{top}}(t, L) = \text{Tr}[\hat{\mathcal{D}}(\hat{U} \otimes \hat{U}^*)] = \text{Tr}[\hat{S}\hat{U}] \text{Tr}[\hat{U}]$  is represented using two world-sheets:  $\text{Tr}[\hat{S}\hat{U}(t)]$  in white, and  $\text{Tr}[\hat{U}(t)^\dagger]$  in grey. The open legs at the top are identified with the corresponding legs at the bottom, forming a trace. The parity inversion axes are shown in reds and blues, with the axes of the same colors identified. (b) For parity symmetric one-dimensional many-body quantum circuits, the folded representation stacks identical gates related by parity inversion symmetry in the world-sheets. (c) In the folded representation, gates locally commute with the swap operator, which acts as the topological defect. (d) We further unwrap the folded world-sheets in (b), yielding an equivalent representation in which each folded site contains three loops.

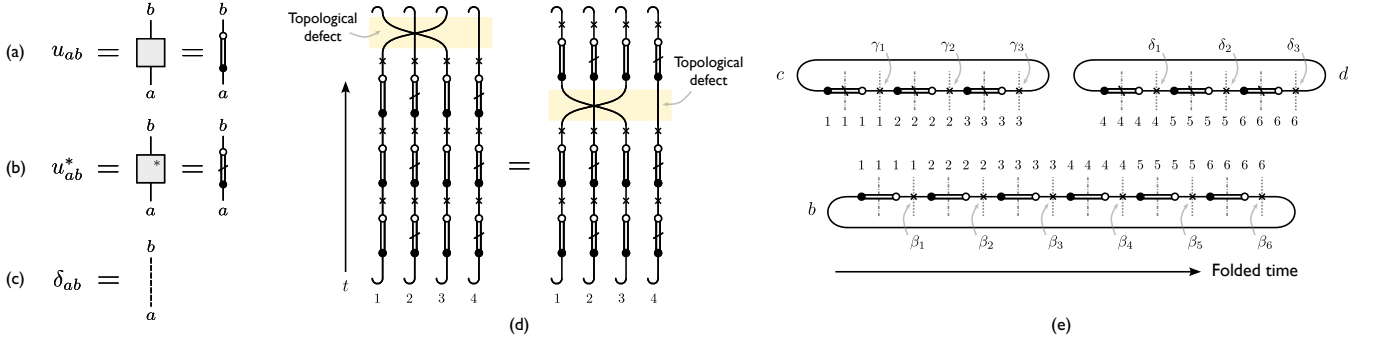


FIG. S5. **Diagrammatic representation of the TopSFF before averaging** in the presence of a spatially extended topological defect. For parity-symmetric quantum many-body systems, we use the graphical notation for (a) unitary gates, (b) complex conjugated unitary gates, and (c) Kronecker-delta contractions. Panel (d) shows the local tensor network diagrams contributing to the TopSFF at  $t = 3$  in Fig. S4(b), with the spatially extended topological defect highlighted in yellow. Panel (e) shows the corresponding local diagrams obtained from unwrapping the folded representation in Fig. S4(d).

$-1/[q(q^2 - 1)]$ . Explicit expressions for  $\text{Wg}$  can be obtained recursively [40]. Importantly, the asymptotic behaviour of the Weingarten function depends only on the total number of cycles of  $\sigma^{-1}\tau$ ,  $\text{Wg}[\{c_1, c_2, \dots, c_k\}; q] = O(q^{k-2} \sum_{i=1}^k c_i)$ . We call a permutation pair  $(\sigma, \tau)$  *Gaussian* if all loop lengths of  $\sigma^{-1}\tau$  are one, i.e.  $c_m = 1$  for all  $m$ , and *non-Gaussian* otherwise.

The ensemble average over Haar-random unitary matrices admits a natural diagrammatic representation [40] as illustrated in Fig. S5, which is used to analyse many-body quantum chaotic systems in [19]. Specifically, from the tensor network diagrammatic representation of observables like TopSFF, each unitary gate drawn from the CUE is replaced by a pair of filled and empty dots, connected by double lines, as shown in Fig. S5(a). Its complex conjugate is similarly represented except that a slash is added to distinguish the conjugation as in Fig. S5(b). Delta functions in (SE.2) are represented by dashed lines in Fig. S5(c), which we will refer to as contractions. The random phase gates, denoted as crosses, couple a local diagram at a given site with another local diagram at another site. Together, in the folded representation, the local diagrams in a single effective site are given by Fig. S5(d) after folding, and by Fig. S5(e) after unwrapping.

The permutation pair  $(\sigma, \tau) \in S_{2t} \times S_{2t}$  associated with each summand in Eq. (SE.2) has a direct diagrammatic

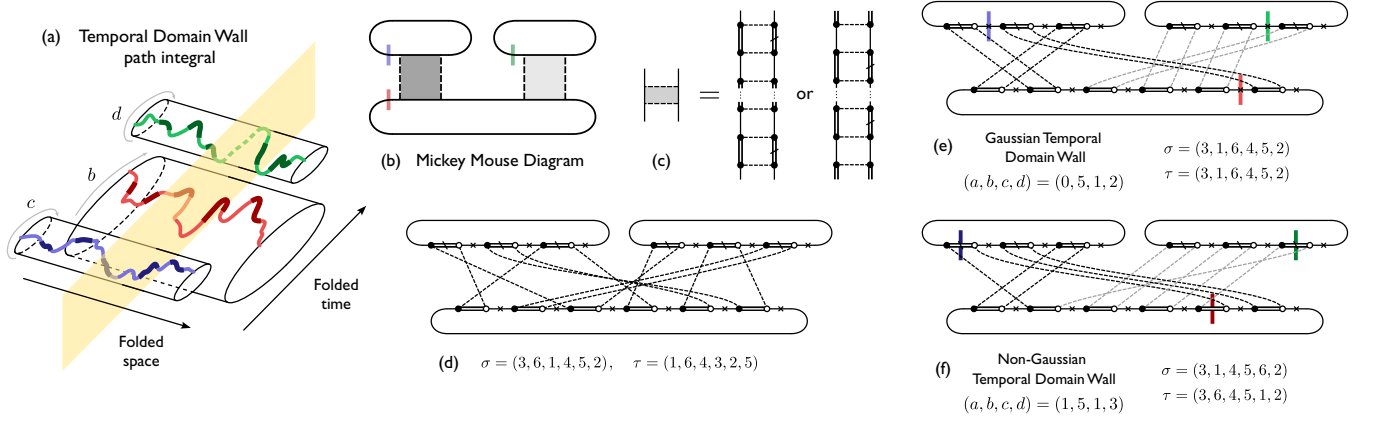


FIG. S6. **Diagrammatic representation of the TopSFF after averaging** in the presence of a spatially extended topological defect for parity-symmetric quantum many-body systems. (a) Ensemble averaging of TopSFF lead to an effective statistical mechanical problem of temporal domain walls, which lives on the loops labelled by  $b$ ,  $c$ , and  $d$ . (b) The leading local diagrams are the “Mickey Mouse” diagram, where the dashed ribbons represent a series of contraction as illustrated in (c). (d) A representative of an ensemble averaged local diagram, labelled by the permutation data  $\sigma$  and  $\tau$ . In the limit of large local Hilbert space dimension  $q$ , the leading diagrams are (e) Gaussian temporal domain wall diagram ( $a = 0$ ) and (f) non-Gaussian temporal domain wall diagram ( $a = 1$ ).

interpretation:  $\sigma$  specifies the contractions between the black dots of the unitary gates and those of the complex-conjugated unitary gates, while  $\tau$  specifies the corresponding contractions between the white dots. We label the black and white dots of the unitary gates along the  $b$ -loop by  $1, 2, \dots, 2t$ , as shown in Fig. S5(e). The black and white dots of the complex-conjugated unitary gates are labelled by  $1, \dots, t$  along the  $c$ -loop and by  $t + 1, \dots, 2t$  along the  $d$ -loop. With this convention, the permutation  $\sigma$  maps the  $m$ -th black dot of the unitary gates to the  $\sigma(m)$ -th black dot of the complex-conjugated unitary gates, while  $\tau$  analogously maps the  $m$ -th white dot to the  $\tau(m)$ -th white dot. Hereafter, we write permutations in one-line notation, e.g.  $\sigma = (\sigma(1), \dots, \sigma(2t)) \in S_{2t}$ , and similarly for  $\tau$ .

A local TopSFF diagram is algebraically represented by a permutation pair  $(\sigma, \tau) \in S_{2t} \times S_{2t}$ , where  $\sigma$  specifies the contractions of black dots and  $\tau$  specifies the contractions of white dots. There is a natural topological equivalence relation [44] among subsets of diagrams with identical scaling order in the local Hilbert-space dimension  $q$ . Intuitively, this relation is obtained by first suppressing the distinction between black and white dots, and then identifying diagrams related by cyclic rotations along the  $b$ -,  $c$ -, and  $d$ -loops.

**Definition E.1. Topological equivalence classes of TopSFF diagrams.** Given a local TopSFF diagram represented by  $(\sigma, \tau) \in S_{2t} \times S_{2t}$ , we construct a single uncoloured contraction permutation  $\Pi_{\sigma, \tau} \in S_{4t}$  as follows. In Fig. S5(e), we order the  $4t$  endpoints on the  $b$ -loop by interlacing black and white dots, so that the  $(2m - 1)$ -st and  $2m$ -th endpoints correspond to the black and white dots at position  $m$ , respectively. We use the same convention for the  $c$ - and  $d$ -loops, with the first  $2t$  endpoints belonging to the  $c$ -loop and the last  $2t$  endpoints belonging to the  $d$ -loop. The uncoloured contraction permutation associated with  $(\sigma, \tau)$  is then defined by

$$\Pi_{\sigma, \tau}(2m - 1) = 2\sigma(m) - 1, \quad \Pi_{\sigma, \tau}(2m) = 2\tau(m), \quad m = 1, \dots, 2t, \quad (\text{SE.3})$$

i.e.,  $\Pi_{\sigma, \tau}$  records the contraction pattern after the black/white distinction has been removed. Let  $[x]_n := 1 + \text{Mod}(x - 1, n)$ . We define cyclic rotations of the uncoloured endpoints by

$$R_b^{(r)}(i) := [i + r]_{4t}, \quad (\text{SE.4})$$

for the  $b$ -loop, and

$$R_c^{(s)}(i) := \begin{cases} [i + s]_{2t}, & 1 \leq i \leq 2t, \\ i, & 2t + 1 \leq i \leq 4t, \end{cases} \quad R_d^{(u)}(i) := \begin{cases} i, & 1 \leq i \leq 2t, \\ 2t + [i - 2t + u]_{2t}, & 2t + 1 \leq i \leq 4t, \end{cases} \quad (\text{SE.5})$$

for the  $c$ - and  $d$ -loops, respectively. Two local TopSFF diagrams  $(\sigma, \tau)$  and  $(\sigma', \tau')$  are said to belong to the same *topological equivalence class* if their uncoloured contraction permutations are related by cyclic rotations of the three loops, i.e. if there exist integers  $r, s, u$  such that

$$\Pi_{\sigma', \tau'} = R_c^{(s)} \circ R_d^{(u)} \circ \Pi_{\sigma, \tau} \circ R_b^{(r)}. \quad (\text{SE.6})$$

Here composition is understood from right to left. Equivalently, the topological class of  $(\sigma, \tau)$  is the orbit of  $\Pi_{\sigma, \tau}$  under independent cyclic rotations of the  $b$ -,  $c$ -, and  $d$ -loops.

This definition preserves the cyclic ordering of endpoints on each loop, but suppresses the black/white distinction. In particular, Gaussian and non-Gaussian contraction patterns may belong to the same topological equivalence class. Note that, depending on the symmetries of the ensemble, additional operations may also be included, such as generalizations of relative twists between  $\text{Tr}[\hat{U}(t)]$  and  $\text{Tr}[\hat{U}^\dagger(t)]$  in Ref. [44], in which topological equivalence classes in systems with time reversal symmetry are defined.

*Example.* For panels (e) and (f) in Fig. S6, we have  $t = 3$ . The Gaussian diagram in panel (e) has  $\sigma_{(e)} = \tau_{(e)} = (3, 1, 6, 4, 5, 2)$ , while the non-Gaussian diagram in panel (f) has  $\sigma_{(f)} = (3, 1, 4, 5, 6, 2)$  and  $\tau_{(f)} = (3, 6, 4, 5, 1, 2)$ . The corresponding uncoloured contraction permutations, written in one-line notation, are  $\Pi_{(e)} = (5, 6, 1, 2, 11, 12, 7, 8, 9, 10, 3, 4)$  and  $\Pi_{(f)} = (5, 6, 1, 12, 7, 8, 9, 10, 11, 2, 3, 4)$ . They are related by the explicit cyclic rotations  $\Pi_{(f)} = R_c^{(5)} \circ R_d^{(1)} \circ \Pi_{(e)} \circ R_b^{(1)}$ . Thus panels (e) and (f) lie in the same topological equivalence class once the black/white distinction is forgotten. The fact that panel (e) has  $\sigma = \tau$ , whereas panel (f) has  $\sigma \neq \tau$ , reflects the distinction between Gaussian and non-Gaussian temporal domain walls, but they both belong to the Mickey Mouse topological equivalence class.

**Leading local diagrams – Mickey Mouse diagrams.** Let  $a \in \{0, 1\}$ ,  $b \in \{1, \dots, 2t\}$ , and  $c, d \in \{1, \dots, t\}$ . We use the one-based modulo convention  $[x]_n := 1 + \text{Mod}(x - 1, n)$ , so that  $[x]_n \in \{1, \dots, n\}$ . Let  $\rho_n$  denote the right cyclic shift on an  $n$ -tuple,  $\rho_n(x_1, x_2, \dots, x_n) := (x_n, x_1, \dots, x_{n-1})$ , and let  $\rho_n^r$  denote its  $r$ -fold composition, with powers to be modulo  $n$ . For two tuples  $X = (x_1, \dots, x_m)$  and  $Y = (y_1, \dots, y_n)$ , we define their concatenation by  $X||Y := (x_1, \dots, x_m, y_1, \dots, y_n)$ . Denote the  $c$ -fold right cyclic shift on the tuple  $(1, 2, \dots, t)$ , and  $d$ -fold right cyclic shift on the tuple  $(t + 1, t + 2, \dots, 2t)$  respectively as

$$f_c := \rho_t^{c-1}(1, 2, \dots, t), \quad f_d := \rho_t^{d-1}(t + 1, t + 2, \dots, 2t),$$

and the  $b$ -fold-shifted and concatenated object as

$$P(b, c, d) := \rho_{2t}^{b-1}(f_c||f_d) \in S_{2t}.$$

**Lemma E.2. Leading local topological spectral form factor (TopSFF) diagrams for generic quantum many-body quantum chaotic systems with spatially extended topological defects.** Consider the ensemble average of the TopSFF  $K_{\text{top}}(t, L) = \text{Tr}[\hat{\mathcal{D}}(\hat{U} \otimes \hat{U}^*)] = \text{Tr}[\hat{S}\hat{U}] \text{Tr}[\hat{U}]$ , where the spatially extended topological defect is  $\hat{\mathcal{D}} = \hat{S} \otimes \mathbb{1}$  with global swap operator  $\hat{S}$ . For the parity-inversion-symmetric Random Phase Model with discrete time translation symmetry, defined in App. A 2 a, the leading local TopSFF diagrams in the large- $q$  expansion are the permutation pairs  $(\sigma_{abcd}, \tau_{abcd}) \in S_{2t} \times S_{2t}$  given by

$$\begin{aligned} \sigma_{abcd} &= P(b, c, d), \\ \tau_{abcd} &= \begin{cases} P(b, c, d), & a = 0, \\ P([b-1]_{2t}, [c+1]_t, [d+1]_t), & a = 1. \end{cases} \end{aligned} \quad (\text{SE.7})$$

with  $a \in \{0, 1\}$ ,  $b \in \{1, \dots, 2t\}$ , and  $c, d \in \{1, \dots, t\}$ . There are in total  $4t^3$  leading TopSFF diagrams. This set of leading local TopSFF diagrams are topologically equivalent to the Mickey Mouse diagram shown in Fig. S6(b), represented by the equivalence class of the reference diagram

$$(\sigma_{0111}, \tau_{0111}). \quad (\text{SE.8})$$

*Examples.* A Gaussian leading local TopSFF diagram of Floquet TRS RPM at  $t = 3$  is given by Fig. S6 (e) with  $(a, b, c, d) = (0, 5, 1, 2)$  and  $\sigma = \tau = (3, 1, 6, 4, 5, 2)$ . A non-Gaussian leading local TopSFF diagram of Floquet TRS RPM at  $t = 3$  is given by Fig. S6 (f) with  $(a, b, c, d) = (1, 5, 1, 3)$ ,  $\sigma = (3, 1, 4, 5, 6, 2)$ , and  $\tau = (3, 6, 4, 5, 1, 2)$ . An example of non-leading local TopSFF diagrams is given by Fig. S6 (d).

*Proof.* The proof utilizes techniques developed in [19]. The representative diagrams shown in Fig. S6(e,f) are of order  $O(q^{-1})$ , so the leading local diagrams are at least of order  $O(q^{-1})$ . From the diagram before averaging in Fig. S5, observe that any admissible local TopSFF diagram must contain at least two inter-loop contractions: one connecting the  $b$ -loop to the  $c$ -loop, and one connecting the  $b$ -loop to the  $d$ -loop. By the contraction-addition argument of Ref. [19],

this implies that every local TopSFF diagram is of order at most  $O(q^{-1})$ . It remains to identify the diagrams that saturate this bound. Starting from the minimal inter-loop contractions, every subsequent contraction addition must preserve the  $q$ -order. The only order-preserving additions are of ladder type, as illustrated in Fig. S6(b): consecutive endpoints on the  $c$ -loop must be contracted to consecutive endpoints on the  $b$ -loop, and similarly consecutive endpoints on the  $d$ -loop must be contracted to consecutive endpoints on the  $b$ -loop. Hence every leading local TopSFF diagram lies in the topological equivalence class of the Mickey Mouse diagram in Fig. S6(b), equivalently in the same topological class as the representative diagrams in Fig. S6(e,f). To enumerate all leading TopSFF diagrams in the topological equivalence class of the Mickey Mouse diagram, we consider the contraction  $\Pi_{\sigma,\tau}$  defined in E.1. Given a Mickey Mouse diagram,  $\Pi_{\sigma,\tau}$ , we observe that there is a unique adjacent pair of endpoints  $(i, i-1)$  such that the dots  $i$  and  $i-1$  from the  $b$ -loop are contracted to a dot from the  $c$ -loop, and a dot from the  $d$ -loop respectively. Equivalently, we identify  $i$ -th dot such that  $1 \leq \Pi_{\sigma,\tau}(i) \leq 2t$  and  $2t+1 \leq \Pi_{\sigma,\tau}(i-1) \leq 4t$ .  $i$  can either be even (a black dot) or odd (a white dot), which we label as  $a = 0$  and  $a = 1$ . See Fig. S6(e,f) for examples with  $a = 0$  and  $a = 1$  respectively. For each value of  $a$ , independent cyclic rotations of the three loops produce further valid leading diagrams: there are  $2t$  rotations of the  $b$ -loop,  $t$  rotations of the  $c$ -loop, and  $t$  rotations of the  $d$ -loop. Therefore the total number of leading local TopSFF diagrams is  $2 \times (2t) \times t \times t = 4t^3$ . Using the notation  $a \in \{0, 1\}$ ,  $b \in \{1, \dots, 2t\}$ , and  $c, d \in \{1, \dots, t\}$ , these rotations give precisely the permutation pairs  $(\sigma_{abcd}, \tau_{abcd})$  stated in Eq. (SE.7). This completes the proof.  $\square$

**Temporal domain walls (tDW).** Given a Mickey Mouse diagram represented by the permutation  $\Pi_{\sigma,\tau}$ , there is a unique adjacent pair of endpoints  $(i, [i-1]_{4t})$  along the  $b$ -loop such that the endpoint  $i$  is contracted to the  $c$ -loop, while the endpoint  $[i-1]_{4t}$  is contracted to the  $d$ -loop. Equivalently,  $i$  is identified by  $1 \leq \Pi_{\sigma,\tau}(i) \leq 2t$  and  $2t+1 \leq \Pi_{\sigma,\tau}([i-1]_{4t}) \leq 4t$ . With the convention in Fig. S5(e),  $i$  can either be even (a black dot) or odd (a white dot), which we label as  $a = 0$  and  $a = 1$ . We can associate a domain wall at the bond  $(i, [i-1]_{4t})$ , and we call this domain wall a *temporal domain wall* (tDW), since it separates two domains along folded time. Recall that we call a permutation pair  $(\sigma, \sigma')$  Gaussian if all loop lengths of  $\sigma^{-1}\sigma'$  are one, i.e.  $c_m = 1$  for all  $m$ , and non-Gaussian otherwise. The index  $a$  determines the Gaussian or non-Gaussian character of the tDW diagram:

- *Gaussian tDW* ( $a = 0$ ): the diagrams  $\{(\sigma_{0bcd}, \tau_{0bcd})\}$ , where the associated Weingarten factor is  $\text{Wg}(\{1^{2t}\}; q)$  and positive at the leading order in the local Hilbert space dimension  $q$ .
- *Non-Gaussian tDW* ( $a = 1$ ): the diagrams  $\{(\sigma_{1bcd}, \tau_{1bcd})\}$ , where the associated Weingarten factor is  $\text{Wg}(\{1^{2t-2}, 2\}; q)$  and negative at the leading order in the local Hilbert space dimension  $q$ .

Representative examples of a Gaussian tDW diagram with  $a = 0$  and a non-Gaussian tDW diagram with  $a = 1$  are shown in Fig. S6(e,f), respectively, where the tDW on the  $b$ -loop are indicated by red lines.

## 2. Boltzmann factor $\mathcal{B}$ in position space

We now consider the average over two-site random coupling gates, acting on two neighbouring large- $q$  TopSFF configurations  $\rho_1 = (a_1, b_1, c_1, d_1)$  and  $\rho_2 = (a_2, b_2, c_2, d_2)$ . Here  $a_i \in \{0, 1\}$ ,  $b_i = 1, \dots, 2t$ , and  $c_i, d_i = 1, \dots, t$ . The label  $a_i = 0$  denotes a Gaussian tDW, while  $a_i = 1$  denotes a non-Gaussian tDW. We use the modulo convention  $[m]_n := 1 + \text{Mod}(m-1, n)$ . Each configuration  $\rho = (a, b, c, d)$  is associated with an ordered contraction list  $\mathcal{C}_{bcd} = \{(m, n)\}$ . This is an ordered list of pairs  $(m, n)$ , where  $m \in \{1, \dots, 2t\}$  labels an endpoint on the  $b$ -loop, indicated by the dotted lines in Fig. S5(e), while  $n$  labels the corresponding endpoint on the combined  $c$ - and  $d$ -loops. These identifications arise from the delta functions in (SE.2). Explicitly, the contraction pattern associated with  $\rho = (a, b, c, d)$  is given by

$$\begin{aligned} \mathcal{C}_{bcd} := & \{([b-1+i]_{2t}, [c-1+i]_t) : i = 1, \dots, t\} \\ & \cup \{([b-1+i+t]_{2t}, t + [d-1+i]_t) : i = 1, \dots, t\}. \end{aligned} \quad (\text{SE.9})$$

Given  $\mathcal{C}_{bcd}$ , we define the associated permutation  $\pi_\rho \in S_{2t}$  by  $\pi_\rho(m) = n$  defined from  $(m, n) \in \mathcal{C}_{bcd}$ . The distinction between Gaussian and non-Gaussian tDW enters in that for  $a = 0$ , colour variables where the two ladder contractions in the Mickey Mouse diagram separate, i.e.,  $[b-1+2t]_{2t}$  and  $[b-1+t]_{2t}$ , need to be identified. This identification is algebraically written according to the rule

$$R_{a=0,b}^Z : \quad Z_{[b-1+2t]_{2t}} \longmapsto Z_{[b-1+t]_{2t}}, \quad (\text{SE.10})$$

where  $Z$  denotes the formal colour variables associated with the folded site under consideration. For  $a = 1$ , no such replacement is made, i.e.,  $R_{a=1,b}^Z = \emptyset$ . Now consider two neighbouring configurations  $\rho_1 = (a_1, b_1, c_1, d_1)$  and

$\rho_2 = (a_2, b_2, c_2, d_2)$ . We introduce the explicit colour labels  $X_m$  for the  $b$ -loop endpoints of the first site and  $Y_m$  for those of the second site, with  $m = 1, \dots, 2t$ . The phase entering the two-site average is

$$\Phi_{\rho_1, \rho_2} = \left( \sum_{m=1}^{2t} \theta_{X_m, Y_m} - \sum_{m=1}^{2t} \theta_{X_{\pi_{\rho_1}^{-1}(m)}, Y_{\pi_{\rho_2}^{-1}(m)}} \right) \Big|_{R_{a_1, b_1}^X, R_{a_2, b_2}^Y}, \quad (\text{SE.11})$$

where after the contractions are imposed, the endpoint  $m$  on the combined  $c \cup d$  loops is pulled back to the  $b$ -loop by the inverse permutations  $\pi_{\rho_1}^{-1}$  and  $\pi_{\rho_2}^{-1}$ , and we apply the rules  $R^X$  and  $R^Y$  after the pullback. Now expand  $\Phi_{\rho_1, \rho_2} = \sum_{r,s} n_{rs}(\rho_1, \rho_2) \theta_{X_r, Y_s}$ , with  $n_{rs}(\rho_1, \rho_2) \in \mathbb{Z}$ . Since the  $\theta_{X_r, Y_s}$  are independent real Gaussian variables with variance  $\epsilon$ , we have

$$\overline{e^{i\Phi_{\rho_1, \rho_2}}} = \exp \left[ -\frac{\epsilon}{2} \sum_{r,s} n_{rs}(\rho_1, \rho_2)^2 \right]. \quad (\text{SE.12})$$

Combining the two-site phase average with the one-site Haar averages gives the generalized Boltzmann factor

$$\mathcal{B}(\rho_1, \rho_2) = q^{2t} \sqrt{\text{Wg}(\sigma_1^{-1} \tau_1; q)} \exp \left[ -\frac{\epsilon}{2} \sum_{r,s} n_{rs}(\rho_1, \rho_2)^2 \right] \sqrt{\text{Wg}(\sigma_2^{-1} \tau_2; q)}, \quad (\text{SE.13})$$

where we follow the convention in (SE.14), in which a trivial factor of  $q^{-1}$  is extracted outside  $\mathcal{B}$ . For example, when  $t = 2$ ,  $\rho_1 = (0, 4, 2, 2)$  and  $\rho_2 = (1, 3, 2, 1)$ , the above construction gives  $\Phi_{\rho_1, \rho_2} = \theta_{X_1, Y_3} - \theta_{X_1, Y_4} - \theta_{X_4, Y_3} + \theta_{X_4, Y_4}$ . Hence, the generalized Boltzmann factor gives  $\mathcal{B}_{\rho_1, \rho_2} = ie^{-2\epsilon}$ .

With this construction, the TopSFF (SE.1) for  $U_{\text{F-P-RPM}}$  in Eq. (SA.4) can be evaluated exactly in the large- $q$  limit as

$$\begin{aligned} \overline{K}_{\text{top}} &=: q^{-L_e - 1} \overline{\mathcal{K}}_{\text{top}} + O(q^{-L_e - 2}), \\ \overline{\mathcal{K}}_{\text{top}} &= \phi^T \mathcal{B}^{L_e} \phi := \sum_{\rho_1, \rho_2} \phi(\rho_1) [\mathcal{B}^{L_e}]_{\rho_1 \rho_2} \phi(\rho_2), \end{aligned} \quad (\text{SE.14})$$

where  $\mathcal{B}$  and  $\phi$  are respectively the generalized Boltzmann factor encoding for many-body interactions and the boundary state under the folded representation. The effective length is  $L_e = L/2 - 1$  for even  $L$ . For odd  $L$ , TopSFF can be evaluated analogously. The generalized Boltzmann factor  $\mathcal{B}(\rho_1, \rho_2)$  depends only on the relative coordinates between  $\rho_1$  and  $\rho_2$  along the  $b$ -,  $c$ - and  $d$ -loops. Define the relative coordinates  $\Delta b := (b_2 - b_1) \pmod{2t}$ ,  $\Delta c := (c_2 - c_1) \pmod{t}$ , and  $\Delta d := (d_2 - d_1) \pmod{t}$ . Translational invariance implies that the Boltzmann factor can be written as

$$\begin{aligned} \mathcal{B}(\rho_1, \rho_2) &= \mathcal{B}_{\text{G-G}}(\rho_1, \rho_2) + \mathcal{B}_{\text{G-nG}}(\rho_1, \rho_2) + \mathcal{B}_{\text{nG-nG}}(\rho_1, \rho_2) \\ &= [\mathcal{B}_{a_1 a_2}(\Delta b, \Delta c, \Delta d)]_{a_1, a_2=0,1} = \begin{bmatrix} \mathcal{B}_{00} & \mathcal{B}_{01} \\ \mathcal{B}_{10} & \mathcal{B}_{11} \end{bmatrix}. \end{aligned} \quad (\text{SE.15})$$

where the block in the Boltzmann factor has the following interpretation:

- $\mathcal{B}_{\text{G-G}}(\rho_1, \rho_2)$ : Amplitudes for the Gaussian tDW to remain as Gaussian tDW,
- $\mathcal{B}_{\text{nG-nG}}(\rho_1, \rho_2)$ : Amplitudes for the non-Gaussian tDW to remain as non-Gaussian tDW,
- $\mathcal{B}_{\text{G-nG}}(\rho_1, \rho_2)$ : Amplitudes for the DW type conversion.

In the nG-nG sector with  $a_1 = a_2 = 1$ , the Boltzmann factor accounts for the many-body interactions between two non-Gaussian tDWs, and is given by

$$\begin{aligned} \mathcal{B}_{\text{nG-nG}}(\rho_1, \rho_2) &= -\delta_{a_1, 1} \delta_{a_2, 1} \mu^{4t-2} \xi \eta, \\ \eta(\rho_1, \rho_2) &= \eta(\Delta b) := |t - \Delta b|, \\ \xi(\rho_1, \rho_2) &= \xi(\Delta b, \Delta c, \Delta d) = \delta_{\Delta b, \Delta c}^{(t)} + \delta_{\Delta b, \Delta d}^{(t)}. \end{aligned} \quad (\text{SE.16})$$

where  $\eta$  is the cyclic distance on the length- $2t$  cycle up to a shift, and  $\delta_{x,y}^{(t)} = 1$  if  $x \equiv y \pmod{t}$  and 0 otherwise.  $\mu := e^{-\epsilon/2}$  parameterizes the interaction strength, where  $\epsilon$  is the variance of the random phases in the RPM.

In the G-nG sector with  $a_1 + a_2 = 1$ , the Boltzmann factor for the mixed Gaussian-non-Gaussian sector is given by

$$\mathcal{B}_{\text{G-nG}}(\rho_1, \rho_2) = \delta_{a_1+a_2,1} i \mu^{4t-2\xi(\eta+\Theta((a_2-a_1)\Delta b]) \pmod{2t-t}}, \quad (\text{SE.17})$$

Here  $\Theta$  is the Heaviside step function with the convention  $\Theta(0) = 1$ .

In the G-G sector with  $a_1 = a_2 = 0$ , the Boltzmann factor for the Gaussian-Gaussian sector is given by

$$\begin{aligned} \mathcal{B}_{\text{G-G}}(\rho_1, \rho_2) &= \delta_{a_1,0} \delta_{a_2,0} \left[ \delta_{\Delta b,0} \mu^{E_0} + \delta_{\Delta b,t} \mu^{E_t} + (1 - \delta_{\Delta b,0} - \delta_{\Delta b,t}) \mu^{E_\times} \right], \\ E_0 &= 2t[(1 - \delta_c) + (1 - \delta_d)] + 2\alpha(1 - \delta_c)(1 - \delta_d), \\ E_t &= 4t - 2(\delta_c + \delta_d) + 2\alpha(1 - \delta_c)(1 - \delta_d), \\ E_\times &= 4t + 2\alpha \delta_c \delta_d - (\eta + 1)2\xi \end{aligned} \quad (\text{SE.18})$$

where we defined  $\delta_b := \delta_{b_1,b_2} = \delta_{\Delta b,0}$ , and similarly for  $\delta_c$  and  $\delta_d$ .

### 3. Properties of $\mathcal{B}$

The generalized Boltzmann factor  $\mathcal{B}$  has the following properties:

- **$\mathcal{PT}$  symmetry.** The Boltzmann factor  $\mathcal{B}$  obeys an antiunitary  $\mathcal{PT}$  symmetry,

$$(\mathcal{PT}) \mathcal{B} (\mathcal{PT})^{-1} = \mathcal{B} \quad \iff \quad \mathcal{P} \mathcal{B}^* \mathcal{P}^{-1} = \mathcal{B}, \quad (\text{SE.19})$$

where  $\mathcal{T}$  denotes the complex conjugation in the  $\{|a, b, c, d\rangle\}$  basis, and  $\mathcal{P}$  is a unitary involution which acts as the Pauli- $z$  matrix on the  $a$ -space,

$$\mathcal{P} |a, b, c, d\rangle := (-1)^a |a, b, c, d\rangle, \quad \iff \quad \mathcal{P} = \sigma_z \otimes \mathbb{1}_{2t} \otimes \mathbb{1}_t \otimes \mathbb{1}_t. \quad (\text{SE.20})$$

This symmetry condition  $\mathcal{P} \mathcal{B}^* \mathcal{P}^{-1} = \mathcal{B}$  is equivalent to  $\mathcal{B}_{00}$  and  $\mathcal{B}_{11}$  being real while  $\mathcal{B}_{01}$  and  $\mathcal{B}_{10}$  being purely imaginary, which is satisfied by G-G, G-nG, and nG-nG Boltzmann factors. In summary, the Boltzmann factor  $\mathcal{B}$  has an antiunitary  $\mathcal{PT}$ -type symmetry with complex conjugation  $\mathcal{T}$  and  $\mathcal{P} = \sigma_z \otimes \mathbb{1}$ .

- **Reality of  $\text{tr} \mathcal{B}$  and  $\det \mathcal{B}$ , and spectral pairing.** From the  $\mathcal{PT}$  constraint  $\mathcal{P} \mathcal{B}^* \mathcal{P}^{-1} = \mathcal{B}$  and the facts that trace and determinant are invariant under similarity transformations, we obtain the reality condition of the trace and determinant of the Boltzmann factor,

$$\text{tr} \mathcal{B} = \text{tr}(\mathcal{B}^*) = (\text{tr} \mathcal{B})^*, \quad \det \mathcal{B} = \det(\mathcal{B}^*) = (\det \mathcal{B})^*. \quad (\text{SE.21})$$

As a consequence of the reality of  $\text{tr} \mathcal{B}$  and  $\det \mathcal{B}$ , the characteristic polynomial has real coefficients, so the spectrum is closed under complex conjugation, i.e. eigenvalues are real or come in conjugate pairs. Alternatively, since  $\mathcal{B}$  obeys the  $\mathcal{PT}$  constraint, if  $\mathcal{B}v = \lambda v$ , then taking complex conjugation gives  $\mathcal{B}^*v^* = \lambda^*v^*$ , and multiplying by  $\mathcal{P}$  yields

$$\mathcal{B}(\mathcal{P}v^*) = \mathcal{P} \mathcal{B}^*v^* = \lambda^*(\mathcal{P}v^*). \quad (\text{SE.22})$$

Hence  $\lambda^*$  is also an eigenvalue of  $\mathcal{B}$ . Therefore the spectrum is closed under complex conjugation, i.e., eigenvalues are either real or occur in complex-conjugate pairs.

- **Exchange symmetry under  $c \leftrightarrow d$ .** In the position space representation, the domain wall physics is symmetric under the exchange of  $c$  and  $d$ . Consequently, we have

$$\mathcal{B}_{a_1 a_2}(\Delta b, \Delta c, \Delta d) = \mathcal{B}_{a_1 a_2}(\Delta b, \Delta d, \Delta c). \quad (\text{SE.23})$$

- **Reality of  $\bar{\mathcal{K}}_{\text{top}}$ .** Recall that  $\bar{\mathcal{K}}_{\text{top}} = \phi^T \mathcal{B}^{L_e} \phi$ . If the boundary states are  $\mathcal{PT}$  invariant in the sense

$$\mathcal{PT} \phi = \mathcal{P} \phi^* = \phi, \quad \phi^T (\mathcal{PT})^{-1} = \phi^\dagger \mathcal{P} = \phi^T. \quad (\text{SE.24})$$

Then, using  $\mathcal{P} \mathcal{B}^* \mathcal{P}^{-1} = \mathcal{B}$ ,

$$\bar{\mathcal{K}}_{\text{top}}^* = \phi^\dagger (\mathcal{B}^{L_e})^* \phi^* = \phi^\dagger \mathcal{P} \mathcal{B}^{L_e} \mathcal{P} \phi^* = \phi^T \mathcal{B}^{L_e} \phi = \bar{\mathcal{K}}_{\text{top}}. \quad (\text{SE.25})$$

Therefore,  $\bar{\mathcal{K}}_{\text{top}} \in \mathbb{R}$  whenever the boundary states are  $\mathcal{PT}$  invariant.

#### 4. Boltzmann factor $\tilde{\mathcal{B}}$ in momentum space

Utilizing the translational invariance of  $\mathcal{B}$ , we can express the TopSFF in terms of the generalized Boltzmann factor in the momentum space as

$$\bar{\mathcal{K}}_{\text{top}} = \phi^T \mathcal{B}^{L_e} \phi = \sum_{k_b, k_c, k_d} \tilde{\phi}(-k)^T \tilde{\mathcal{B}}(k)^{L_e} \tilde{\phi}(k). \quad (\text{SE.26})$$

The discrete Fourier transform of  $|\phi_i\rangle$  and  $\mathcal{B}$  are defined as

$$\begin{aligned} \tilde{\phi}(a; k_b, k_c, k_d) &:= \frac{1}{\sqrt{2t^3}} \sum_{b=0}^{2t-1} \sum_{c=0}^{t-1} \sum_{d=0}^{t-1} e^{i(k_b b + k_c c + k_d d)} \phi(a, b, c, d), \\ \tilde{\mathcal{B}}_{a_1 a_2}(\mathbf{k}) &:= \sum_{\Delta b=0}^{2t-1} \sum_{\Delta c=0}^{t-1} \sum_{\Delta d=0}^{t-1} \mathcal{B}_{a_1 a_2}(\Delta b, \Delta c, \Delta d) e^{-i(k_b \Delta b + k_c \Delta c + k_d \Delta d)}. \end{aligned} \quad (\text{SE.27})$$

where  $k_b = 2\pi n_b/2t$  with  $n_b = 0, 1, \dots, 2t-1$ ,  $k_c = 2\pi n_c/t$  with  $n_c = 0, 1, \dots, t-1$ , and  $k_d = 2\pi n_d/t$  with  $n_d = 0, 1, \dots, t-1$ .

Now we perform the Fourier transform of  $\mathcal{B}$  in Eq. (SE.15) to obtain  $\tilde{\mathcal{B}}(k_b, k_c, k_d)$  for general momenta. Recall that many sectors depend on  $(\Delta c, \Delta d)$  through  $\xi(\Delta b, \Delta c, \Delta d) = \delta_{\Delta b, \Delta c}^{(t)} + \delta_{\Delta b, \Delta d}^{(t)}$  with  $\delta_{x,y}^{(t)} = 1$  if  $x \equiv y \pmod{t}$ , and on  $\Delta b$  through some integer-valued function  $f(\Delta b)$ . Fix  $\Delta b$  and define  $r := \Delta b \pmod{t} \in \{0, \dots, t-1\}$ , so that  $\delta_{\Delta b, \Delta c}^{(t)} = \delta_{\Delta c, r}$  and  $\delta_{\Delta b, \Delta d}^{(t)} = \delta_{\Delta d, r}$ . Setting  $s := \mu^{-2f(\Delta b)}$ , we can compute the Fourier transform over  $\Delta b$  and  $\Delta c$  as

$$\mathcal{F}(k_c, k_d; r, s) := \sum_{\Delta c, \Delta d=0}^{t-1} e^{-i(k_c \Delta c + k_d \Delta d)} \mu^{-2\xi f(\Delta b)} = \left[ S_t(k_c) + (s-1)e^{-ik_c r} \right] \left[ S_t(k_d) + (s-1)e^{-ik_d r} \right], \quad (\text{SE.28})$$

where  $S_t(k) := \sum_{x=0}^{t-1} e^{-ikx} = t\delta_{k,0 \pmod{2\pi}}$ .

As a first step, we perform the Fourier transform over  $c$  and  $d$ . For the nG-nG sector with  $a_1 = a_2 = 1$ , we perform the Fourier transform on Eq. (SE.16), giving

$$\tilde{\mathcal{B}}_{11}(k_b, k_c, k_d) = -\mu^{4t} \sum_{\Delta b=0}^{2t-1} e^{-ik_b \Delta b} \mathcal{F}(k_c, k_d; r(\Delta b), \mu^{-2\eta(\Delta b)}). \quad (\text{SE.29})$$

For the G-nG sector with  $a_1 + a_2 = 1$ , introduce the convention  $p := a_2 - a_1 \in \{+1, -1\}$ , so that  $p = 1$  corresponds to  $(a_1, a_2) = (0, 1)$ , and  $p = -1$  corresponds to  $(a_1, a_2) = (1, 0)$ . Recall that  $\Gamma_p(\Delta b) := \Theta[(p\Delta b) \pmod{2t} - t]$  with  $\Theta(0) = 1$ , and  $f_p(\Delta b) := \eta(\Delta b) + \Gamma_p(\Delta b)$ . Then we can perform the Fourier transform on Eq. (SE.17), giving

$$\tilde{\mathcal{B}}_{a_1 a_2}(k_b, k_c, k_d) = i\mu^{4t} \sum_{\Delta b=0}^{2t-1} e^{-ik_b \Delta b} \mathcal{F}(k_c, k_d; r(\Delta b), \mu^{-2f_p(\Delta b)}), \quad (\text{SE.30})$$

To perform the Fourier transform on Eq. (SE.18), we consider the Fourier contributions for  $\Delta b = 0$ ,  $\Delta b = t$ , and  $\Delta b \neq t$  separately. For  $\Delta b = 0$  and  $\Delta b = t$ , the Fourier contributions are

$$\begin{aligned} \mathcal{G}_0(k_c, k_d) &:= \sum_{\Delta c, \Delta d=0}^{t-1} e^{-i(k_c \Delta c + k_d \Delta d)} \mu^{E_0} \\ &= 1 + \mu^{2t} [(S_t(k_c) - 1) + (S_t(k_d) - 1)] + \mu^{4t+2\alpha} (S_t(k_c) - 1)(S_t(k_d) - 1), \\ \mathcal{G}_t(k_c, k_d) &:= \sum_{\Delta c, \Delta d=0}^{t-1} e^{-i(k_c \Delta c + k_d \Delta d)} \mu^{E_t} \\ &= \mu^{4t-4} + \mu^{4t-2} [(S_t(k_c) - 1) + (S_t(k_d) - 1)] + \mu^{4t+2\alpha} (S_t(k_c) - 1)(S_t(k_d) - 1). \end{aligned} \quad (\text{SE.31})$$

For  $\Delta b \neq 0, t$ , the Boltzmann factor becomes  $\mu^{E_\times} = \mu^{4t} \mu^{2\alpha \delta_c \delta_d} \mu^{-2(\eta+1)\xi}$ . We can then utilize (SE.28) with  $f_\times(\Delta b) := \eta(\Delta b) + 1$ , and the Fourier transform can be evaluated as

$$\mathcal{G}_\times(\Delta b; k_c, k_d) := \sum_{\Delta c, \Delta d} e^{-i(k_c \Delta c + k_d \Delta d)} \mu^{E_\times} = \mu^{4t} \left[ \mathcal{F}(k_c, k_d; r(\Delta b), \mu^{-2f_\times(\Delta b)}) + (\mu^{2\alpha} - 1) \right]. \quad (\text{SE.32})$$

Together, we have

$$\widetilde{\mathcal{B}}_{00}(k_b, k_c, k_d) = \mathcal{G}_0(k_c, k_d) + e^{-ik_b t} \mathcal{G}_t(k_c, k_d) + \sum_{\substack{\Delta b=0 \\ \Delta b \neq 0, t}}^{2t-1} e^{-ik_b \Delta b} \mathcal{G}_\times(\Delta b; k_c, k_d). \quad (\text{SE.33})$$

Next, we evaluate the remaining sum over  $\Delta b$ . We introduce  $x := \mu^{-2}$ . It is convenient to define the following geometric sums

$$\begin{aligned} \mathbf{E}(k) &:= \sum_{r=1}^{t-1} e^{-ikr} = \begin{cases} \frac{e^{-ik} [1 - e^{-ik(t-1)}]}{1 - e^{-ik}}, & k \not\equiv 0 \pmod{2\pi}, \\ t-1, & k \equiv 0 \pmod{2\pi}, \end{cases} \\ \mathbf{G}(k; y) &:= \sum_{r=1}^{t-1} y^r e^{-ikr} = \frac{ye^{-ik}(1 - (ye^{-ik})^{t-1})}{1 - ye^{-ik}}, \\ \mathbf{J}(k; \alpha, \beta; m) &:= \sum_{r=1}^{t-1} (x^{\alpha r + \beta} - 1)^m e^{-ikr}, \end{aligned} \quad (\text{SE.34})$$

where  $\alpha \in \{+1, -1\}$ ,  $\beta \in \mathbb{Z}$  and  $m \in \{1, 2\}$ . We further define

$$J_1(k) := \mathbf{J}(k; +1, 0; 1) = \sum_{r=1}^{t-1} (x^r - 1) e^{-ikr} = \mathbf{G}(k; x) - \mathbf{E}(k), \quad (\text{SE.35})$$

$$J_2(k) := \mathbf{J}(k; +1, 0; 2) = \sum_{r=1}^{t-1} (x^r - 1)^2 e^{-ikr} = \mathbf{G}(k; x^2) - 2\mathbf{G}(k; x) + \mathbf{E}(k), \quad (\text{SE.36})$$

$$\check{J}_1(k) := \mathbf{J}(k; -1, t; 1) = \sum_{r=1}^{t-1} (x^{t-r} - 1) e^{-ikr} = e^{-ikt} (\mathbf{G}(-k; x) - \mathbf{E}(-k)), \quad (\text{SE.37})$$

$$\check{J}_2(k) := \mathbf{J}(k; -1, t; 2) = \sum_{r=1}^{t-1} (x^{t-r} - 1)^2 e^{-ikr} = e^{-ikt} (\mathbf{G}(-k; x^2) - 2\mathbf{G}(-k; x) + \mathbf{E}(-k)), \quad (\text{SE.38})$$

$$J_1^+(k) := \mathbf{J}(k; +1, 1; 1) = \sum_{r=1}^{t-1} (x^{r+1} - 1) e^{-ikr} = x \mathbf{G}(k; x) - \mathbf{E}(k), \quad (\text{SE.39})$$

$$J_2^+(k) := \mathbf{J}(k; +1, 1; 2) = \sum_{r=1}^{t-1} (x^{r+1} - 1)^2 e^{-ikr} = x^2 \mathbf{G}(k; x^2) - 2x \mathbf{G}(k; x) + \mathbf{E}(k), \quad (\text{SE.40})$$

$$\check{J}_1^+(k) := \mathbf{J}(k; -1, t+1; 1) = \sum_{r=1}^{t-1} (x^{t-r+1} - 1) e^{-ikr} = x e^{-ikt} \mathbf{G}(-k; x) - \mathbf{E}(k), \quad (\text{SE.41})$$

$$\check{J}_2^+(k) := \mathbf{J}(k; -1, t+1; 2) = \sum_{r=1}^{t-1} (x^{t-r+1} - 1)^2 e^{-ikr} = x^2 e^{-ikt} \mathbf{G}(-k; x^2) - 2x e^{-ikt} \mathbf{G}(-k; x) + \mathbf{E}(k). \quad (\text{SE.42})$$

with all sums running from  $r = 1, \dots, t-1$ . For the G-nG sector, it is convenient to introduce the  $p$ -dependent combinations

$$J_m^{(p)}(k) := \frac{1+p}{2} J_m(k) + \frac{1-p}{2} J_m^+(k), \quad (\text{SE.43})$$

$$\check{J}_m^{(p)}(k) := \frac{1+p}{2} \check{J}_m^+(k) + \frac{1-p}{2} \check{J}_m(k). \quad (\text{SE.44})$$

Direct evaluations of the Fourier transforms in  $b$  space give the following closed expressions. Define the combined phases  $k_{bc} := k_b + k_c$ ,  $k_{bd} := k_b + k_d$ ,  $k_{bcd} := k_b + k_c + k_d$ . Denote the summation of phases as  $S_c := S_t(k_c)$ ,  $S_d := S_t(k_d)$  where  $S_t(k) := \sum_{x=0}^{t-1} e^{-ikx} = t \delta_{k,0 \pmod{2\pi}}$ . For  $a_1 = a_2 = 0$ ,

$$\begin{aligned} \widetilde{\mathcal{B}}_{00}(k_b, k_c, k_d) &= \mathcal{G}_0(k_c, k_d) + (-1)^{n_b} \mathcal{G}_t(k_c, k_d) \\ &+ \mu^{4t} \left[ S_c S_d (1 + (-1)^{n_b}) \mathbf{E}(k_b) + S_c (\check{J}_1^+(k_{bd}) + (-1)^{n_b} J_1^+(k_{bd})) + S_d (\check{J}_1^+(k_{bc}) + (-1)^{n_b} J_1^+(k_{bc})) \right. \\ &\left. + (\check{J}_2^+(k_{bcd}) + (-1)^{n_b} J_2^+(k_{bcd})) \right] + \mu^{4t} (\mu^{2\alpha} - 1) (2t \delta_{n_b, 0} - (1 + (-1)^{n_b})). \end{aligned} \quad (\text{SE.45})$$

For  $a_1 = a_2 = 1$ ,

$$\begin{aligned} \tilde{\mathcal{B}}_{11}(k_b, k_c, k_d) = & -\mu^{4t} \left[ S_c S_d (2t \delta_{n_b, 0}) \right. \\ & + S_c \left( (\mu^{-2t} - 1) + \check{J}_1(k_{bd}) + (-1)^{n_b} J_1(k_{bd}) \right) \\ & + S_d \left( (\mu^{-2t} - 1) + \check{J}_1(k_{bc}) + (-1)^{n_b} J_1(k_{bc}) \right) \\ & \left. + \left( (\mu^{-2t} - 1)^2 + \check{J}_2(k_{bcd}) + (-1)^{n_b} J_2(k_{bcd}) \right) \right]. \end{aligned} \quad (\text{SE.46})$$

Lastly, for  $a_1 + a_2 = 1$ ,

$$\begin{aligned} \tilde{\mathcal{B}}_{a_1 a_2}(k_b, k_c, k_d) = & i\mu^{4t} \left[ S_c S_d (2t \delta_{n_b, 0}) \right. \\ & + S_c \left( (\mu^{-2t} - 1) + (-1)^{n_b} (\mu^{-2} - 1) + \check{J}_1^{(p)}(k_{bd}) + (-1)^{n_b} J_1^{(p)}(k_{bd}) \right) \\ & + S_d \left( (\mu^{-2t} - 1) + (-1)^{n_b} (\mu^{-2} - 1) + \check{J}_1^{(p)}(k_{bc}) + (-1)^{n_b} J_1^{(p)}(k_{bc}) \right) \\ & \left. + \left( (\mu^{-2t} - 1)^2 + (-1)^{n_b} (\mu^{-2} - 1)^2 + \check{J}_2^{(p)}(k_{bcd}) + (-1)^{n_b} J_2^{(p)}(k_{bcd}) \right) \right], \end{aligned} \quad (\text{SE.47})$$

## 5. Properties of $\tilde{\mathcal{B}}$

$\tilde{\mathcal{B}}(k_b, k_c, k_d)$  has the following properties, some of which are representation independent and overlap with Appendix E3, but we include them here for completeness.  $\tilde{\mathcal{B}}(k_b, k_c, k_d)$  possesses  $\mathcal{PT}$  symmetry at certain momentum points, which we describe in the next section.

- **Class AI time reversal symmetry (TRS).** For any real  $y$  and any  $k$ , the geometric sums satisfy  $E(k)^* = E(-k)$ , and  $G(k; y)^* = G(-k; y)$ . Consequently, for  $m = 1, 2$ , we have  $J_m(k)^* = J_m(-k)$ , and similarly for  $\check{J}_m, J_m^+, \check{J}_m^+, J_m^{(p)}$ , and  $\check{J}_m^{(p)}$ . The diagonal sectors of  $\tilde{\mathcal{B}}_{a_1 a_2}(k_b, k_c, k_d)$  are real linear combinations of the above geometric sums, whereas its off-diagonal sectors have an overall factor  $i$ . Therefore,  $\tilde{\mathcal{B}}_{a_1 a_2}(k_b, k_c, k_d)$  satisfy the following antiunitary symmetry,

$$(\mathcal{PT})\tilde{\mathcal{B}}(k_b, k_c, k_d)(\mathcal{PT})^{-1} := \sigma_z \tilde{\mathcal{B}}(k_b, k_c, k_d)^* \sigma_z = \tilde{\mathcal{B}}(-k_b, -k_c, -k_d), \quad (\text{SE.48})$$

where  $\sigma_z$  is the Pauli- $z$  matrix acting on the  $a$ -space, and  $(\cdot)^*$  denotes complex conjugation. This symmetry transformation is a class AI TRS symmetry transformation since

$$(\mathcal{PT})^2 = 1. \quad (\text{SE.49})$$

Relatedly, at a given momentum sector  $(k_b, k_c, k_d)$ ,  $\mathcal{PT}$  symmetry of  $\tilde{\mathcal{B}}(k_b, k_c, k_d)$  is  $\tilde{\mathcal{B}}(k_b, k_c, k_d) = \sigma_z \tilde{\mathcal{B}}^*(k_b, k_c, k_d) \sigma_z$ , with  $\mathcal{P}$  set to be  $\sigma_z$  acting on  $a$ -space, and  $\mathcal{T}$  set to be complex conjugation. It is clear that the sector satisfying  $(k_b, k_c, k_d) = (-k_b, -k_c, -k_d)$ , we will discuss the precise criteria in the next section.

- **Spectral pairing under momentum inversion.** The spectral consequence of Eq. (SE.48) is that eigenvalues are paired between momentum-inverted sectors. Suppose that  $\tilde{\mathcal{B}}(k_b, k_c, k_d)v = \lambda(k_b, k_c, k_d)v$ . Taking the complex conjugate and then multiplying by  $\sigma_z$ , one finds

$$\tilde{\mathcal{B}}(-k_b, -k_c, -k_d)(\sigma_z v^*) = \sigma_z \tilde{\mathcal{B}}(k_b, k_c, k_d)^* v^* = \lambda(k_b, k_c, k_d)^*(\sigma_z v^*).$$

Therefore

$$\lambda(k_b, k_c, k_d) \in \text{Spec } \tilde{\mathcal{B}}(k_b, k_c, k_d) \implies \lambda(k_b, k_c, k_d)^* \in \text{Spec } \tilde{\mathcal{B}}(-k_b, -k_c, -k_d). \quad (\text{SE.50})$$

- **Exchange symmetry under  $c \leftrightarrow d$ .** In the position space representation, the domain wall physics is symmetric under the exchange of  $c$  and  $d$ . Consequently,  $\tilde{\mathcal{B}}$  is symmetric under exchanging  $k_c$  and  $k_d$ , i.e.,

$$\tilde{\mathcal{B}}_{a_1 a_2}(k_b, k_c, k_d) = \tilde{\mathcal{B}}_{a_1 a_2}(k_b, k_d, k_c). \quad (\text{SE.51})$$

- **Reality of  $\det \tilde{\mathcal{B}}(k)$  and  $\text{tr} \tilde{\mathcal{B}}(k)$ , and spectral pairing within each momentum sector.** We observe that in the  $a$ -space,  $\tilde{\mathcal{B}}(k)$  can be brought to a generalized  $\mathcal{PT}$  dimer form,

$$\tilde{\mathcal{B}}(k) = \begin{pmatrix} A(k) & iB(k) \\ iC(k) & D(k) \end{pmatrix}, \quad A(k), B(k), C(k), D(k) \in \mathbb{R}, \quad \implies \quad \det \tilde{\mathcal{B}}(k), \text{tr} \tilde{\mathcal{B}}(k) \in \mathbb{R}, \quad (\text{SE.52})$$

i.e.  $\det \tilde{\mathcal{B}}(k)$  is always real. The characteristic polynomial of  $\tilde{\mathcal{B}}$  is  $\chi(\lambda) = \lambda^2 - (\text{tr} \tilde{\mathcal{B}}) \lambda + \det \tilde{\mathcal{B}}$ , so if  $\text{tr} \tilde{\mathcal{B}}, \det \tilde{\mathcal{B}} \in \mathbb{R}$ , then  $\chi(\lambda)$  has real coefficients. Hence the eigenvalues are either both real or form a complex-conjugate pair. Define the discriminant  $\Delta := (\text{tr} \tilde{\mathcal{B}})^2 - 4 \det \tilde{\mathcal{B}}$ . Then the eigenvalues are

$$\lambda_{\pm} = \frac{\text{tr} \tilde{\mathcal{B}} \pm \sqrt{\Delta}}{2}. \quad (\text{SE.53})$$

Therefore, we have

- If  $\Delta > 0$ , then  $\lambda_{\pm} \in \mathbb{R}$  are distinct.
- If  $\Delta = 0$ , then  $\lambda_+ = \lambda_- = \frac{1}{2} \text{tr} \tilde{\mathcal{B}}$  is degenerate. This is the candidate locus for an exceptional point (EP), which occurs when the matrix is not diagonalizable at the degeneracy.
- If  $\Delta < 0$ , then  $\lambda_{\pm}$  form a complex-conjugate pair.

- **Bragg peaks and parity in  $k_b$ .** The momentum dependence enters  $\tilde{\mathcal{B}}$  only through the elementary phases  $k_b, k_c, k_d$  and the combined momenta  $k_{bc} := k_b + k_c$ ,  $k_{bd} := k_b + k_d$ , and  $k_{bcd} := k_b + k_c + k_d$ , together with the Bragg factors

$$S_c := S_t(k_c), \quad S_d := S_t(k_d), \quad S_t(k) := \sum_{x=0}^{t-1} e^{-ikx} = t \delta_{k,0} \pmod{2\pi}. \quad (\text{SE.54})$$

Since  $S_t(k)$  vanishes for generic  $k$  but jumps to  $t$  at reciprocal-lattice momenta  $k \equiv 0 \pmod{2\pi}$ ,  $\tilde{\mathcal{B}}(k_b, k_c, k_d)$  exhibits Bragg-peak-like features in  $(k_c, k_d)$ .

Furthermore, recall that we defined  $k_b = 2\pi n_b / 2t$ , so that  $(-1)^{n_b} = e^{-ik_b t}$ . The dependence on the parity of  $n_b$  is equivalently a dependence on the half translation phase  $e^{-ik_b t}$  along the length- $2t$  loop in  $b$ . Many contributions in TopSFF appear with  $1 \pm (-1)^{n_b}$ , thereby splitting the  $k_b$ -dependence into two parity sectors.

## 6. $\mathcal{PT}$ symmetry of $\tilde{\mathcal{B}}$

Set  $\mathcal{P}$  to be  $\sigma_z$  acting on  $a$ -space, and  $\mathcal{T}$  to be complex conjugation.  $\tilde{\mathcal{B}}(k_b, k_c, k_d)$  is  $\mathcal{PT}$  symmetry if

$$\tilde{\mathcal{B}}(k_b, k_c, k_d) = \sigma_z \tilde{\mathcal{B}}^*(k_b, k_c, k_d) \sigma_z. \quad (\text{SE.55})$$

Firstly, note that the momentum points  $(k_b, k_c, k_d) = (-k_b, -k_c, -k_d)$  and  $(k_b, k_c, k_d) = (-k_b, -k_d, -k_c)$  lead to  $\mathcal{PT}$  symmetry due to the antiunitary symmetry (SE.48) and exchange symmetry (SE.51). We will show that this is a subset of the full  $\mathcal{PT}$  symmetric momentum sectors.

**Proposition E.3.** *Let  $\mathcal{P} = \sigma_z$  act on the  $a$ -space, and let  $\mathcal{T}$  denote complex conjugation. For the Boltzmann factor  $\tilde{\mathcal{B}}(k_b, k_c, k_d)$  in Eqs. (SE.45)–(SE.47), one has for generic  $\mu$ ,*

$$\tilde{\mathcal{B}}(k_b, k_c, k_d) \text{ is } \mathcal{PT} \text{ symmetric} \iff k_b + k_c + k_d \equiv 0 \pmod{\pi}. \quad (\text{SE.56})$$

*Proof.* The  $\mathcal{PT}$  symmetry condition (SE.55) is equivalent to

$$\tilde{\mathcal{B}}_{00}, \tilde{\mathcal{B}}_{11} \in \mathbb{R}, \quad \tilde{\mathcal{B}}_{01}, \tilde{\mathcal{B}}_{10} \in i\mathbb{R}. \quad (\text{SE.57})$$

First, we consider the nG-nG sector, i.e.,  $\tilde{\mathcal{B}}_{11}$  in Eq. (SE.46). It is clear that the only possibly non-real factors are

$$\check{J}_m(q) + (-1)^{n_b} J_m(q). \quad (\text{SE.58})$$

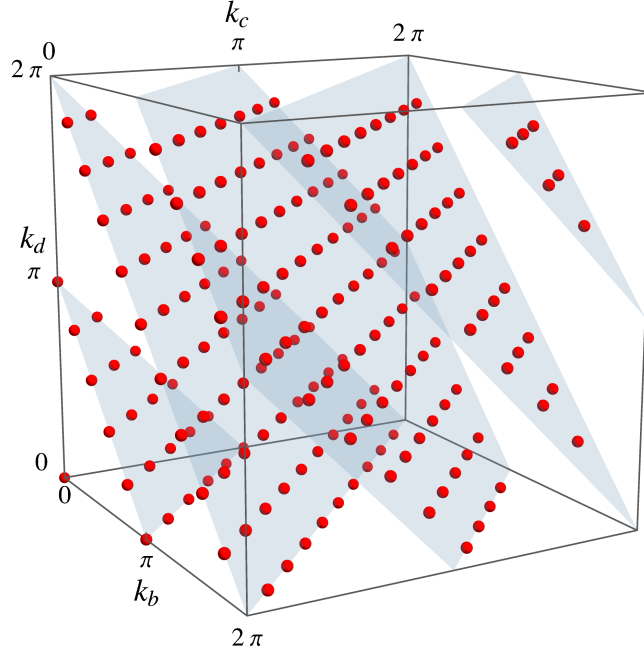


FIG. S7. **EP planes.** Momentum sectors (red dots) at which the generalized Boltzmann factor  $\tilde{\mathcal{B}}$  have  $\mathcal{PT}$  symmetry according to Eq. (SE.56).

Recall the convention  $k_b = \pi n_b/t, k_c = 2\pi n_c/t, k_d = 2\pi n_d/t$ , and that every momentum argument appearing in the geometric sums is of the form  $q \in \{k_b, k_b + k_c, k_b + k_d, k_b + k_c + k_d\} = k_b + \frac{2\pi m}{t}$  for some integer  $m$ . Therefore, the phase factor  $e^{-iqt} = e^{-ik_b t} e^{-i2\pi m} = e^{-i\pi n_b} = (-1)^{n_b}$  becomes a sign. Using

$$\mathbf{E}(q)^* = \mathbf{E}(-q), \quad \mathbf{G}(q; y)^* = \mathbf{G}(-q; y). \quad (\text{SE.59})$$

We write

$$\check{J}_m(q) = e^{-iqt} J_m(-q) = (-1)^{n_b} J_m(q)^*, \quad m = 1, 2. \quad (\text{SE.60})$$

It follows that

$$\check{J}_m(q) + (-1)^{n_b} J_m(q) = 2(-1)^{n_b} [\check{J}_m(q) + \check{J}_m(q)^*] = 2(-1)^{n_b} \Re J_m(q) \in \mathbb{R}, \quad (\text{SE.61})$$

is real. As a consequence, the nG-nG sector is always real, because Eq. (SE.46) only contains real constants, the real factors  $S_c, S_d$ , and the combinations (SE.61). Hence

$$\tilde{\mathcal{B}}_{11}(k) \in \mathbb{R} \quad \text{for all momentum sectors.} \quad (\text{SE.62})$$

Next we consider the G-G and G-nG sectors, and the  $\Leftarrow$  direction of the statement (SE.56). The potentially imaginary factors come from the sums  $J_m^+$  in combinations like

$$\check{J}_m^+(q) + (-1)^{n_b} J_m^+(q), \quad (\text{SE.63})$$

which are not generically real for arbitrary  $q$ . Observe that if

$$q \equiv 0 \pmod{\pi} \quad (\text{SE.64})$$

then every phase  $e^{-iqr}$  is equal to  $\pm 1$ , and therefore

$$\mathbf{E}(q), \mathbf{G}(q; y), J_m(q), J_m^+(q), \check{J}_m(q), \check{J}_m^+(q) \in \mathbb{R}. \quad (\text{SE.65})$$

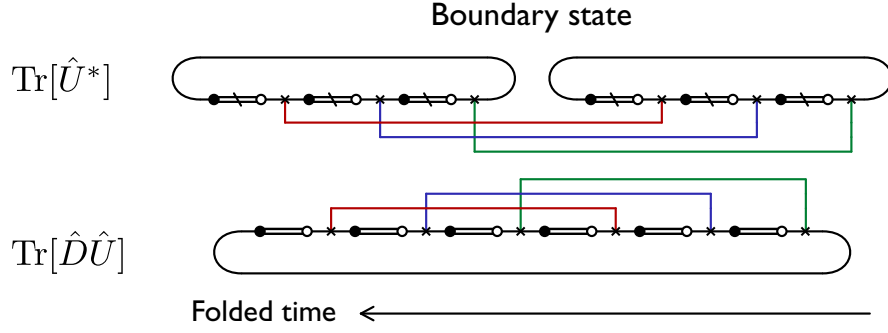


FIG. S8. **Boundary states of TopSFF** are vectors defined on the edge of the emergent system in the folded representation, and encode the presence or absence of coupling across the parity-inversion axes. In this illustration, the random-phase gates are shown in colour, coupling degrees of freedom at  $t = 1$  (red),  $t = 2$  (blue), and  $t = 3$  (green).

In that case,  $\tilde{\mathcal{B}}_{00}$  is real, and  $\tilde{\mathcal{B}}_{01}, \tilde{\mathcal{B}}_{10}$  are purely imaginary, so (SE.55) holds. Next, it is enough to impose (SE.64) on

$$k_{bcd} := k_b + k_c + k_d \equiv 0 \pmod{\pi}, \quad (\text{SE.66})$$

because every potentially non-real term of the form (SE.63) is either already evaluated at  $k_{bcd}$ , or is multiplied by  $S_c$  or  $S_d$ , which force  $k_c = 0$  or  $k_d = 0$ , and hence reduce its argument to  $k_{bd} := k_b + k_d$  or  $k_{bc} := k_b + k_c$ . This proves the  $\Leftarrow$  direction of the statement.

Next, we prove the  $\Rightarrow$  direction for generic non-fine-tuned  $\mu$ . It is enough to inspect the mixed sector with  $p = +1$ , namely  $\tilde{\mathcal{B}}_{01}$  in Eq. (SE.47). The momentum  $k_{bcd} := k_b + k_c + k_d$  appears in Eq. (SE.47) without any prefactor  $S_c$  or  $S_d$ , and is therefore always present through the term

$$\mathcal{C}(k_{bcd}) := (\mu^{-2t} - 1)^2 + (-1)^{n_b} (\mu^{-2} - 1)^2 + \check{J}_2^+(k_{bcd}) + (-1)^{n_b} J_2(k_{bcd}). \quad (\text{SE.67})$$

Using the sum definitions of  $J_2(k_{bcd})$  and  $\check{J}_2^+(k_{bcd})$ , we obtain

$$\mathcal{C}(k_{bcd}) = (\mu^{-2t} - 1)^2 + (-1)^{n_b} (\mu^{-2} - 1)^2 + \sum_{r=1}^{t-1} \left[ (\mu^{-2(t-r+1)} - 1)^2 + (-1)^{n_b} (\mu^{-2r} - 1)^2 \right] e^{-ik_{bcd}r}. \quad (\text{SE.68})$$

As a polynomial in  $\mu^{-2}$ , the coefficient of the highest power  $(\mu^{-2})^{2t}$  is

$$1 + e^{-ik_{bcd}}, \quad (\text{SE.69})$$

because in (SE.68), the first term  $(\mu^{-2t} - 1)^2$  contributes  $(\mu^{-2})^{2t}$ , and the  $r = 1$  term of the third term (corresponding to  $\check{J}_2^+(k_{bcd})$ ) contributes an additional  $e^{-ik_{bcd}} (\mu^{-2})^{2t}$ . Hence, if  $k_{bcd} \not\equiv 0, \pi \pmod{2\pi}$ , then  $1 + e^{-ik_{bcd}} \notin \mathbb{R}$ , and therefore  $\mathcal{C}(k_{bcd})$  is not identically real as a function of  $\mu^{-2}$ . Equivalently, for fixed such  $k_{bcd}$ , the condition  $\mathcal{C}(k_{bcd}) \in \mathbb{R}$  can hold only on a non-generic subset of parameter values  $\mu$ .

Now fixed-block  $\mathcal{PT}$  symmetry requires, by (SE.57), that  $\tilde{\mathcal{B}}_{01} \in i\mathbb{R}$ . Since  $\tilde{\mathcal{B}}_{01} = i\mu^{4t} [\dots + \mathcal{C}(k_{bcd})]$ , this forces the bracket to be real. Therefore, for generic  $\mu$ ,  $k_{bcd} = k_b + k_c + k_d \equiv 0 \pmod{\pi}$ . Combined with the sufficiency condition above, this shows that the generic fixed-block  $\mathcal{PT}$ -symmetric sectors are those satisfying  $k_{bcd} = k_b + k_c + k_d \equiv 0 \pmod{\pi}$ .  $\square$

## 7. Boundary states

The TopSFF with a spatially extended topological defect is given in Eq. (SE.14). In this section, we describe the boundary states in the folded representation, both in position space and in momentum space. Away from the parity-inversion axes, the bulk gates are chosen to obey discrete time translation symmetry and to be compatible with the global swap defect / parity inversion symmetry. Along the parity inversion axes, the parity inversion symmetric couplings determine the form of the boundary states entering Eq. (SE.14). By engineering the couplings along these axes (gates along dashed lines in Fig. S1), we gain access to different momentum sectors of the generalized Boltzmann factor  $\tilde{\mathcal{B}}$ , which in turn allows us to identify the universal signatures of tDW in TopSFF.

a. *Discrete time translational symmetry and parity inversion symmetry*

In the most natural setting, the coupling gates along the parity inversion axes are drawn analogously to the coupling gates away from the parity inversion axes. More precisely, the coupling gates of the RPM are drawn as described by (SA.8) in A 2 subject to the requirements of (i) discrete time translational symmetry, i.e.,  $w(\tau, r) = w(\tau', r)$  for all  $\tau$  and  $\tau'$ , and (ii) parity inversion symmetry SWAP  $w(\tau, r)$  SWAP =  $w(\tau, r)$ , where SWAP denotes the swap operator acting on the same Hilbert space as  $w(\tau, r)$ . This model is illustrated in Fig. S9(b). By performing the ensemble averages over the random phase gates as illustrated in Fig. S8, the boundary state  $\phi$  is found to be

$$\phi(a, b, c, d) = i^{\delta_{a,1}} [\mu^{2t} + (1 - \mu^{2t})\delta_{c,d}] . \quad (\text{SE.70})$$

The Fourier transform of  $\phi$  defined in Eq. (SE.27) can be computed as

$$\tilde{\phi}(a; k_b, k_c, k_d) = i^{\delta_{a,1}} \left[ \sqrt{2t^3} \mu^{2t} \delta_{n_b,0} \delta_{n_c,0} \delta_{n_d,0} + \sqrt{2t} (1 - \mu^{2t}) \delta_{n_b,0} \delta_{n_c+n_d,0} \pmod{t} \right]. \quad (\text{SE.71})$$

where  $k_b = 2\pi n_b/2t$  with  $n_b = 0, 1, \dots, 2t - 1$ ,  $k_c = 2\pi n_c/t$  with  $n_c = 0, 1, \dots, t - 1$ , and  $k_d = 2\pi n_d/t$  with  $n_d = 0, 1, \dots, t - 1$ . Note that imaginary factors arising from Weingarten calculus have been absorbed into the boundary state, and that  $\tilde{\phi}$  has non-zero support only if  $k_b = 0$  and  $k_d \equiv -k_c \pmod{2\pi}$ . The tensor network representation of TopSFF with the boundary condition (SE.70) is illustrated in Fig. S10.

b. *No coupling*

Suppose the coupling gates along the parity-inversion axes of the RPM are turned off, as illustrated in Fig. S9(a). The parity inversion symmetric coupling along the parity inversion axes do not bias any of the TopSFF modes. Consequently, the boundary states in Eq. (SE.14) and their Fourier transforms are

$$\phi(a, b, c, d) = i^{\delta_{a,1}}, \quad \tilde{\phi}(a; k_b, k_c, k_d) = i^{\delta_{a,1}} \sqrt{2t^3} \delta_{n_b,0} \delta_{n_c,0} \delta_{n_d,0}, \quad (\text{SE.72})$$

i.e., the boundary states lie entirely in the momentum sector  $(k_b, k_c, k_d) = (0, 0, 0)$ . This choice provides a useful reference contribution from the zero-momentum sector, which can be subtracted when one wishes to isolate non-zero momentum sectors.

c. *General periodic driving*

A simple way to gain access to different momentum sectors of the generalized Boltzmann factor is to introduce a generalized periodic driving *only* along the parity inversion axes, i.e., along the dashed lines in Fig. S1. The quantum circuits away from the parity inversion axes are unchanged, and hence the generalized Boltzmann factor is unchanged, but the boundary state is. To be more precise, along the parity inversion axes, the coupling gates of RPM are drawn as described by (SA.8) in A 2, except that the coupling gates are drawn independently unless they are related by

$$w(\tau + p, r = L/2, L) = w(\tau, r = L/2, L), \quad (\text{SE.73})$$

where both time  $\tau$  and period  $p$  are discrete. The RPM for  $p = 1$  and  $p = 2$  are illustrated in Fig. S9(b) and (c) respectively. The boundary state in position space is given by

$$\phi(a, b, c, d) = i^{\delta_{a,1}} \left[ \mu^{2t} + (1 - \mu^{2t}) \delta_{[c-b \pmod{t}] \pmod{p}, 0} \delta_{c,d} \right].$$

Thus for  $t = mp$  with some integer  $m$ , the boundary state in momentum space is

$$\tilde{\phi}(a; k_b, k_c, k_d) = i^{\delta_{a,1}} \left[ \mu^{2t} \sqrt{2t^3} \delta_{n_b,0} \delta_{n_c,0} \delta_{n_d,0} + (1 - \mu^{2t}) \frac{\sqrt{2t}}{p} \delta_{n_b \pmod{2t/p}, 0} \delta_{n_c+n_d+n_b/2 \pmod{t}, 0} \right]. \quad (\text{SE.74})$$

A few notable cases:

- **$p = 1$ . Floquet driving with period 1.** For  $p = 1$ , we recover the period-1 Floquet case as described above in E 7 a, where the period along and away from the parity inversion symmetry axes match.

- $p = 2$ . **Floquet driving with period 2.** For  $p = 2$ , i.e. the period-2 Floquet case, we have

$$\tilde{\phi} = i^{\delta_{a,1}} \left[ \mu^{2t} \sqrt{2t^3} \delta_{n_b,0} \delta_{n_c,0} \delta_{n_d,0} + (1 - \mu^{2t}) \sqrt{\frac{t}{2}} \delta_{n_b \pmod{t},0} \delta_{n_c+n_d+n_b/2 \pmod{t},0} \right]. \quad (\text{SE.75})$$

- $p = t$ . **Temporal random driving.** For  $p = t$ , i.e. the temporal random case, we have

$$\tilde{\phi} = i^{\delta_{a,1}} \left[ \mu^{2t} \sqrt{2t^3} \delta_{n_b,0} \delta_{n_c,0} \delta_{n_d,0} + (1 - \mu^{2t}) \sqrt{\frac{2}{t}} \delta_{n_b \pmod{2},0} \delta_{n_c+n_d+n_b/2 \pmod{t},0} \right]. \quad (\text{SE.76})$$

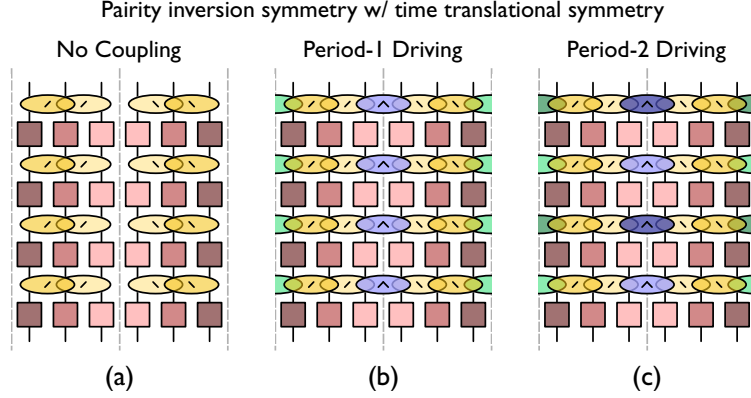


FIG. S9. **Models with periodic driving along parity inversion axes.** We consider quantum chaotic many-body systems described by the parity-inversion-symmetric Random Phase Model with discrete time translational symmetry. Along the parity inversion axes, we study coupling gates corresponding to (a) no coupling, (b) period-one driving, and (c) period-two driving.

### Appendix F: Exact TopSFF with spatially extended defects at large $q$

In this appendix, we present the exact large- $q$  evaluation of the TopSFF with a spatially extended global swap defect, using the generalized Boltzmann factor derived in E. In Sec. F1, we express the TopSFF using the Cayley-Hamilton relation and introduce boundary-resolved TopSFF. In Sec. F2, we evaluate the TopSFF in selected fixed

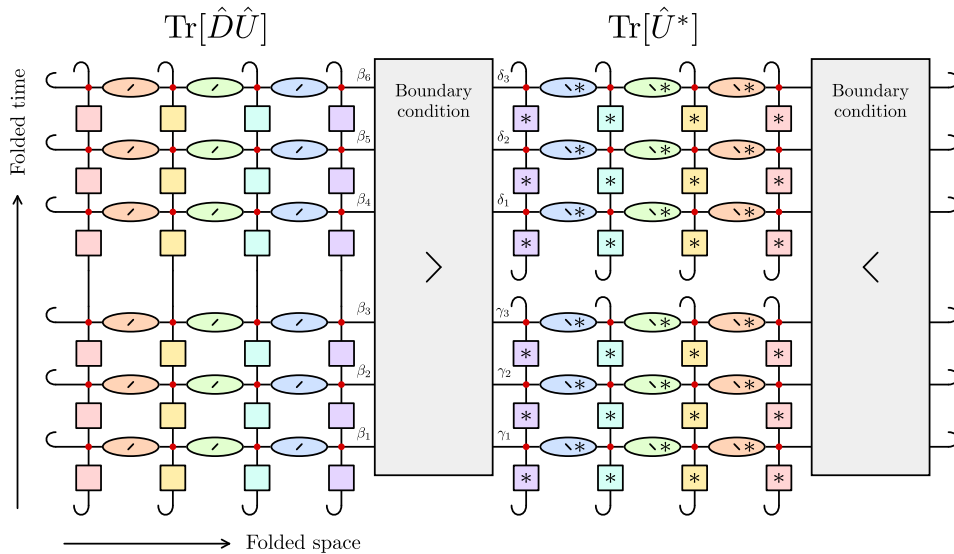


FIG. S10. **Tensor network of TopSFF.** We show the tensor network representation of TopSFF for  $t = 3$  and  $L = 8$ . Gates with identical colours are identified. Red dots label where the degrees of freedom live.

momentum sectors. In Sec. F 3, we combine these sectors to obtain the TopSFF in the time translation symmetric case. Finally, in Sec. F 4, we show how engineered parity-inversion axes, including no-coupling and period-two driving, can be used to access and isolate selected momentum sectors such as  $(\pi, \pi, 0)$ .

### 1. TopSFF and Cayley-Hamilton

The TopSFF with the global swap operator inserted as a spatially extended topological defect in the parity inversion symmetric and discrete time translational invariant RPM can be obtained by evaluating

$$[\tilde{\mathcal{B}}(k_b, k_c, k_d)^L]_{a_1 a_2}. \quad (\text{SF.1})$$

for some positive integer  $L$ . The eigenvalues  $\lambda_{\pm}$  of  $\tilde{\mathcal{B}}$  are

$$\lambda_{\pm} = \frac{\mathbf{t} \pm \sqrt{\Delta}}{2}, \quad \mathbf{t} := \text{tr } \tilde{\mathcal{B}}, \quad \mathbf{d} := \det \tilde{\mathcal{B}}, \quad \Delta := \mathbf{t}^2 - 4\mathbf{d}. \quad (\text{SF.2})$$

We evaluate  $\tilde{\mathcal{B}}(k_b, k_c, k_d)^L$  by applying the Cayley-Hamilton theorem to the  $2 \times 2$  matrix  $\tilde{\mathcal{B}}$ , so that all powers of  $\tilde{\mathcal{B}}$  are controlled by its trace and determinant as

$$\tilde{\mathcal{B}}^L = u_L \tilde{\mathcal{B}} - \mathbf{d} u_{L-1} \mathbb{1}, \quad (\text{SF.3})$$

where  $u_0 = 0$ ,  $u_1 = 1$ , and

$$u_{L+1} = \mathbf{t} u_L - \mathbf{d} u_{L-1}. \quad (\text{SF.4})$$

Thus, the  $L$ -dependence is governed by the two scalar invariants  $\mathbf{t}$  and  $\mathbf{d}$  through the recurrence relation for  $u_L$ . If  $\lambda_+ \neq \lambda_-$ , then

$$\tilde{\mathcal{B}}^L = \frac{\lambda_+^L - \lambda_-^L}{\lambda_+ - \lambda_-} \tilde{\mathcal{B}} + \frac{\lambda_+ \lambda_-^L - \lambda_- \lambda_+^L}{\lambda_+ - \lambda_-} \mathbb{1}. \quad (\text{SF.5})$$

If  $\lambda_+ = \lambda_- = \lambda$  (including exceptional points where  $\tilde{\mathcal{B}}$  is not diagonalizable), then the expression above has the smooth limit

$$\tilde{\mathcal{B}}^L \longrightarrow L\lambda^{L-1}\tilde{\mathcal{B}} + (1-L)\lambda^L\mathbb{1}, \quad \text{as } \Delta \rightarrow 0. \quad (\text{SF.6})$$

TopSFF can be written as a quadratic form of  $\tilde{\mathcal{B}}(k)^L$  with respect to a boundary vector in momentum sector  $k$ . Specifically, if  $\tilde{\phi}(k) = \mathcal{N}(k)\varphi$  with  $\varphi = (\varphi_1, \varphi_2)^T$ , then, using the Cayley-Hamilton identity, we obtain

$$\begin{aligned} \mathbf{K}_k &:= \varphi^T \tilde{\mathcal{B}}(k)^L \varphi = g(k) u_L(k) - h \det \tilde{\mathcal{B}}(k) u_{L-1}(k), \quad \varphi = \begin{pmatrix} \varphi_1 \\ \varphi_2 \end{pmatrix}, \\ h &:= \varphi^T \varphi = \varphi_1^2 + \varphi_2^2, \\ g(k) &:= \varphi^T \tilde{\mathcal{B}}(k) \varphi = \tilde{\mathcal{B}}_{00}(k) \varphi_1^2 + [\tilde{\mathcal{B}}_{01}(k) + \tilde{\mathcal{B}}_{10}(k)] \varphi_1 \varphi_2 + \tilde{\mathcal{B}}_{11}(k) \varphi_2^2. \\ u_L(k) &= \begin{cases} \frac{\lambda_+^L - \lambda_-^L}{\lambda_+ - \lambda_-}, & \Delta(k) \neq 0, \\ L \left(\frac{\mathbf{t}}{2}\right)^{L-1}, & \Delta(k) = 0. \end{cases} \end{aligned} \quad (\text{SF.7})$$

where eigenvalues  $\lambda_{\pm}(k)$  are distinct for  $\Delta \neq 0$ , and the eigenvalues coalesce  $\lambda_+(k) = \lambda_-(k) = \lambda(k)$  for  $\Delta = 0$  at the EP. For certain momentum sectors, the Boltzmann factor has  $\mathcal{PT}$  symmetry, and the boundary vector has the form

$\varphi = (1, i)^T$ , then the TopSFF is given by

$$\begin{aligned} \mathbf{K}_k &:= \varphi^T \tilde{\mathbf{B}}(k)^L \varphi = g(k) u_L(k), & \tilde{\mathbf{B}}(k) &= \begin{pmatrix} \mathbf{A}(k) & i\mathbf{B}(k) \\ i\mathbf{B}(k) & \mathbf{C}(k) \end{pmatrix}, & \varphi &= \begin{pmatrix} 1 \\ i \end{pmatrix}, \\ g(k) &:= \varphi^T \tilde{\mathbf{B}}(k) \varphi = \mathbf{A}(k) - \mathbf{C}(k) - 2\mathbf{B}(k), \\ u_L(k) &= \begin{cases} \frac{\lambda_+(k)^L - \lambda_-(k)^L}{\lambda_+(k) - \lambda_-(k)}, & \Delta(k) > 0 & (\mathcal{PT} \text{ unbroken}), \\ L \left( \frac{\mathfrak{t}(k)}{2} \right)^{L-1}, & \Delta(k) = 0 & (\text{Exceptional point}), \\ \left[ \mathfrak{d}(k) \right]^{\frac{L-1}{2}} \frac{\sin(L\theta(k))}{\sin \theta(k)}, & \theta(k) := \arccos \left( \frac{\mathfrak{t}(k)}{2\sqrt{\mathfrak{d}(k)}} \right), & \Delta(k) < 0 & (\mathcal{PT} \text{ broken}). \end{cases} \end{aligned} \quad (\text{SF.8})$$

where  $h = 0$ , and  $\mathbf{A}(k), \mathbf{B}(k), \mathbf{C}(k) \in \mathbb{R}$ . In the  $\mathcal{PT}$  broken phase, the eigenvalues form a complex-conjugate pair,  $\lambda_{\pm}(k) = \rho(k)e^{\pm i\theta(k)} = x(k) \pm iy(k)$ . The spectral phase  $\theta(k)$ , with  $\tan \theta(k) = y(k)/x(k)$ , controls the oscillation period in  $L$ , while the modulus  $\rho(k) = |\lambda_{\pm}(k)| = \sqrt{\mathfrak{d}(k)}$  controls the exponential envelope. For  $x(k) > 0$ , a smaller ratio  $|y(k)/x(k)|$  gives a smaller  $\theta(k)$  and hence a longer oscillation period  $L_{\text{osc}} \sim 2\pi/\theta(k)$ . In the same phase, TopSFF grows exponentially if  $\rho(k) > 1$ , decays exponentially if  $\rho(k) < 1$ , and is purely oscillatory if  $\rho(k) = 1$ .

#### a. Boundary-resolved TopSFF

At the exceptional point, we would like to observe the linear-in- $L$  behaviour in Eq. (SF.8), which arises from Jordan non-diagonality. However, this contribution can be suppressed if  $g(k) = 0$  at the EP, as will occur in the case considered below. To avoid this cancellation, we instead consider boundary-resolved TopSFFs defined with the boundary vectors

$$v_0 = \begin{pmatrix} 1 \\ 0 \end{pmatrix}, \quad v_1 = \begin{pmatrix} 0 \\ i \end{pmatrix}. \quad (\text{SF.9})$$

which have supports only in the Gaussian tDW basis state and non-Gaussian tDW basis state respectively. We define the three boundary-resolved amplitudes

$$\mathbf{K}_{00} := v_0^T \tilde{\mathbf{B}}(k)^L v_0, \quad (\text{SF.10})$$

$$\mathbf{K}_{11} := v_1^T \tilde{\mathbf{B}}(k)^L v_1, \quad (\text{SF.11})$$

$$\mathbf{K}_{01} := v_0^T \tilde{\mathbf{B}}(k)^L v_1. \quad (\text{SF.12})$$

such that, for  $\varphi = v_0 + v_1 = (1, i)^T$ , we have

$$\mathbf{K}_k := \varphi^T \tilde{\mathbf{B}}(k)^L \varphi = \mathbf{K}_{00} + 2\mathbf{K}_{01} + \mathbf{K}_{11}. \quad (\text{SF.13})$$

Using the Cayley-Hamilton form as before, the boundary-resolved TopSFF are

$$\mathbf{K}_{00} = \mathbf{A}(k)u_L(k) - \mathfrak{d}(k)u_{L-1}(k), \quad (\text{SF.14})$$

$$\mathbf{K}_{11} = -\mathbf{C}(k)u_L(k) + \mathfrak{d}(k)u_{L-1}(k), \quad (\text{SF.15})$$

$$\mathbf{K}_{01} = -\mathbf{B}(k)u_L(k). \quad (\text{SF.16})$$

Equivalently, for  $\Delta(k) \neq 0$ ,

$$\mathbf{K}_{00} = \frac{(\mathbf{A}(k) - \lambda_-(k))\lambda_+(k)^L - (\mathbf{A}(k) - \lambda_+(k))\lambda_-(k)^L}{\lambda_+(k) - \lambda_-(k)}, \quad (\text{SF.17})$$

$$\mathbf{K}_{11} = -\frac{(\mathbf{C}(k) - \lambda_-(k))\lambda_+(k)^L - (\mathbf{C}(k) - \lambda_+(k))\lambda_-(k)^L}{\lambda_+(k) - \lambda_-(k)}, \quad (\text{SF.18})$$

$$\mathbf{K}_{01} = -\mathbf{B}(k) \frac{\lambda_+(k)^L - \lambda_-(k)^L}{\lambda_+(k) - \lambda_-(k)}. \quad (\text{SF.19})$$

At an exceptional point,  $\Delta(k) = 0$ , the two eigenvalues coalesce,

$$\lambda_{\text{EP}}(k) := \lambda_+(k) = \lambda_-(k) = \frac{\text{tr } \tilde{\mathcal{B}}(k)}{2}. \quad (\text{SF.20})$$

The transfer matrix can be written in terms of the identity matrix and a nilpotent matrix,

$$\tilde{\mathcal{B}}(k) = \lambda_{\text{EP}}(k)\mathbb{1} + N(k), \quad N(k)^2 = 0. \quad (\text{SF.21})$$

In the original Gaussian/non-Gaussian basis, the nilpotent matrix is

$$N(k) = \begin{pmatrix} \delta(k) & i\mathbf{B}(k) \\ i\mathbf{B}(k) & -\delta(k) \end{pmatrix}, \quad \delta(k) := \frac{A(k) - C(k)}{2}. \quad (\text{SF.22})$$

At the exceptional point, we have  $\delta(k)^2 = \mathbf{B}(k)^2$ , with  $\delta(k) = s\mathbf{B}(k)$  and  $s = \pm 1$ . Therefore

$$\tilde{\mathcal{B}}(k)^L = \lambda_{\text{EP}}(k)^L \mathbb{1} + L\lambda_{\text{EP}}(k)^{L-1} N(k), \quad (\text{SF.23})$$

and hence

$$\mathbf{K}_{00}|_{\text{EP}} = \lambda_{\text{EP}}(k)^L + L\delta(k)\lambda_{\text{EP}}(k)^{L-1}, \quad (\text{SF.24})$$

$$\mathbf{K}_{11}|_{\text{EP}} = -\lambda_{\text{EP}}(k)^L + L\delta(k)\lambda_{\text{EP}}(k)^{L-1}, \quad (\text{SF.25})$$

$$\mathbf{K}_{01}|_{\text{EP}} = -\mathbf{B}(k)L\lambda_{\text{EP}}(k)^{L-1}. \quad (\text{SF.26})$$

To observe TopSFF's polynomial scaling in  $L$  due to the exceptional point and Jordan non-diagonality, we compute the quantity

$$\left. \frac{\mathbf{K}_{00} + \mathbf{K}_{11}}{[\text{tr } \tilde{\mathcal{B}}(k)/2]^{L-1}} \right|_{\text{EP}} = 2\delta(k)L \propto L, \quad (\text{SF.27})$$

which is linear in  $L$  at the exceptional point. We compute  $(\mathbf{K}_{00} + \mathbf{K}_{11})/[\text{tr } \tilde{\mathcal{B}}(k)/2]^{L-1}$  across the exceptional point at finite  $q$  in Fig. S35 and at large  $q$  in Fig. S20. In both cases, the results show excellent agreement with the linear scaling in  $L$  in Eq. (SF.27).

## 2. TopSFF for fixed momentum sectors

Next, we evaluate the TopSFF for four  $\mathcal{PT}$  symmetric momentum sectors that arises from evaluating TopSFF with period-1 and period-2 driving along the parity inversion axes. It is convenient to define

$$S_2(n) := \frac{1 - \mu^{-2n}}{1 - \mu^{-2}}, \quad S_4(n) := \frac{1 - \mu^{-4n}}{1 - \mu^{-4}}, \quad \widehat{S}_2 := S_2(t-1) = \frac{1 - \mu^{-2(t-1)}}{1 - \mu^{-2}}. \quad (\text{SF.28})$$

and

$$\begin{aligned} A_n &:= \sum_{r=1}^n (\mu^{-2r} - 1)^2 = \mu^{-4} S_4(n) - 2\mu^{-2} S_2(n) + n, \\ B_n &:= \sum_{r=1}^n (t-1 + \mu^{-2r})^2 = n(t-1)^2 + 2(t-1)\mu^{-2} S_2(n) + \mu^{-4} S_4(n), \\ C_t &:= A_t - (\mu^{-2} - 1)^2, \\ D_t &:= B_t - (t-1 + \mu^{-2})^2. \end{aligned} \quad (\text{SF.29})$$

a. *TopSFF for  $(k_b, k_c, k_d) = (0, 0, 0)$*

We consider the TopSFF for  $(k_b, k_c, k_d) = (0, 0, 0)$ , which is  $\mathcal{PT}$  symmetric as derived in E 6. We use the shorthand  $0_e \equiv (k_b, k_c, k_d) = (0, 0, 0)$  for both the momentum sector and the corresponding subscripts. The matrix elements of the generalized Boltzmann factor are

$$\begin{aligned} A_{0_e} &= \left(1 + 2(t-1)\mu^{2t} + (t-1)^2\mu^{4t+2}\right) + \left(\mu^{4t-4} + 2(t-1)\mu^{4t-2} + (t-1)^2\mu^{4t+2}\right) \\ &\quad + 2\mu^{4t}\left(D_t + (t-1)(\mu^2 - 1)\right), \\ B_{0_e} &= 2\mu^{4t}B_t, \\ C_{0_e} &= -\mu^{4t}\left[t^2 + (t-1 + \mu^{-2t})^2 + 2B_{t-1}\right]. \end{aligned}$$

Using Eq. (SF.8), we obtain TopSFF at  $(k_b, k_c, k_d) = (0, 0, 0)$  as

$$K_{0_e} := \varphi^T \tilde{\mathcal{B}}(0, 0, 0)^L \varphi = (A_{0_e} - C_{0_e} - 2B_{0_e}) u_L(0, 0, 0). \quad (\text{SF.30})$$

A representative example of the TopSFF behaviour in the  $(k_b, k_c, k_d) = (0, 0, 0)$  sector is shown in Fig. S11.

b. *TopSFF for  $(k_b, k_c, k_d) = (0, k, -k)$*

We consider the TopSFF for  $(k_b, k_c, k_d) = (0, k, -k)$  with  $k \neq 0$ , which is  $\mathcal{PT}$  symmetric as derived in E 6. We use the shorthand  $0_b \equiv (k_b, k_c, k_d) = (0, k, -k)$  for both the momentum sector and the corresponding subscripts. The matrix elements of the generalized Boltzmann factor are

$$\begin{aligned} A_{0_b} &= \left(1 - 2\mu^{2t} + \mu^{4t+2}\right) + \left(\mu^{4t-4} - 2\mu^{4t-2} + \mu^{4t+2}\right) + 2\mu^{4t}\left(C_t + (t-1)(\mu^2 - 1)\right), \\ B_{0_b} &= 2\mu^{4t}A_t, \\ C_{0_b} &= -\mu^{4t}\left[(\mu^{-2t} - 1)^2 + 2A_{t-1}\right]. \end{aligned} \quad (\text{SF.31})$$

Using Eq. (SF.8), we obtain TopSFF at  $(k_b, k_c, k_d) = (0, k, -k)$  with  $k \neq 0$  as

$$K_{0_b} := \varphi^T \tilde{\mathcal{B}}(0, k, -k)^L \varphi = (A_{0_b} - C_{0_b} - 2B_{0_b}) u_L(0, k, -k), \quad (\text{SF.32})$$

for  $k \neq 0$ . A representative example of the TopSFF behaviour in the  $(k_b, k_c, k_d) = (0, k, -k)$  sector is shown in Fig. S11.

c. *TopSFF for  $(k_b, k_c, k_d) = (\pi, \pi, 0)$*

We consider the TopSFF for  $(k_b, k_c, k_d) = (\pi, \pi, 0)$ , which is  $\mathcal{PT}$  symmetric as derived in E 6. We use the shorthand  $\pi_e \equiv (k_b, k_c, k_d) = (\pi, \pi, 0)$  for both the momentum sector and the corresponding subscripts. The matrix elements of the generalized Boltzmann factor are

$$\begin{aligned} A_{\pi_e} &= 1 + \mu^{4t-4} + (t-2)(\mu^{2t} + \mu^{4t-2}) - 2(t-1)\mu^{4t+2} + 2t\mu^{4t-4}\hat{S}_2 - 2t(t-1)\mu^{4t} + 2\mu^{4t}C_t + 2\mu^{4t}(1 - \mu^2), \\ B_{\pi_e} &= \mu^{4t}\left[t\left((\mu^{-2t} - 1) + (\mu^{-2} - 1) + (\mu^{-2} + \mu^{-4})\hat{S}_2 - 2(t-1)\right) + (\mu^{-2t} - 1)^2 + (\mu^{-2} - 1)^2 + A_{t-1} + C_t\right], \\ C_{\pi_e} &= -\mu^{4t}\left[t\left((\mu^{-2t} - 1) + 2(\mu^{-2}\hat{S}_2 - (t-1))\right) + (\mu^{-2t} - 1)^2 + 2A_{t-1}\right]. \end{aligned} \quad (\text{SF.33})$$

Using Eq. (SF.8), we can simplify  $g_{\pi_e}$  and obtain TopSFF at  $(k_b, k_c, k_d) = (\pi, \pi, 0)$  as

$$K_{\pi_e} := \varphi^T \tilde{\mathcal{B}}(\pi, \pi, 0)^L \varphi = \mu^{4t-4}(1 - \mu^2)\left(2t\mu^4 - t\mu^2 + \mu^2 - 1\right) u_L(\pi, \pi, 0). \quad (\text{SF.34})$$

A representative example of the TopSFF behaviour in the  $(k_b, k_c, k_d) = (\pi, \pi, 0)$  sector with  $\mathcal{PT}$  symmetry breaking transition is shown in Fig. S12. The signatures of  $\mathcal{PT}$  symmetry breaking transition and the exceptional point are discussed in Appendix G 2 and in Appendix H 3.

d. *TopSFF for  $(k_b, k_c, k_d) = (\pi, k, \pi - k)$*

We consider the TopSFF for  $(k_b, k_c, k_d) = (\pi, k, \pi - k)$  with  $k \neq 0, \pi$ , which is  $\mathcal{PT}$  symmetric as derived in E 6. We use the shorthand  $\pi_b \equiv (k_b, k_c, k_d) = (\pi, k, \pi - k)$  for both the momentum sector and the corresponding subscripts. The matrix elements of the generalized Boltzmann factor are

$$\begin{aligned} A_{\pi_b} &= 1 + \mu^{4t-4} - 2\mu^{2t} - 2\mu^{4t-2} + 2\mu^{4t} + 2\mu^{4t}C_t, \\ B_{\pi_b} &= \mu^{4t} \left[ (\mu^{-2t} - 1)^2 + (\mu^{-2} - 1)^2 + A_{t-1} + C_t \right], \\ C_{\pi_b} &= -\mu^{4t} \left[ (\mu^{-2t} - 1)^2 + 2A_{t-1} \right]. \end{aligned} \quad (\text{SF.35})$$

Using Eq. (SF.8), we can simplify  $g_{\pi_b}$  and obtain TopSFF at  $\pi_b \equiv (k_b, k_c, k_d) = (\pi, k, \pi - k)$  with  $k \neq 0, \pi$  as

$$\mathcal{K}_{\pi_b} := \varphi^T \tilde{\mathcal{B}}(\pi, k, \pi - k)^L \varphi = -\mu^{4t-4} (1 - \mu^2)^2 u_L(\pi, k, \pi - k), \quad (\text{SF.36})$$

for  $k \neq 0, \pi$ . A representative example of the TopSFF behaviour in the  $(k_b, k_c, k_d) = (\pi, k, \pi - k)$  sector is shown in Fig. S11.

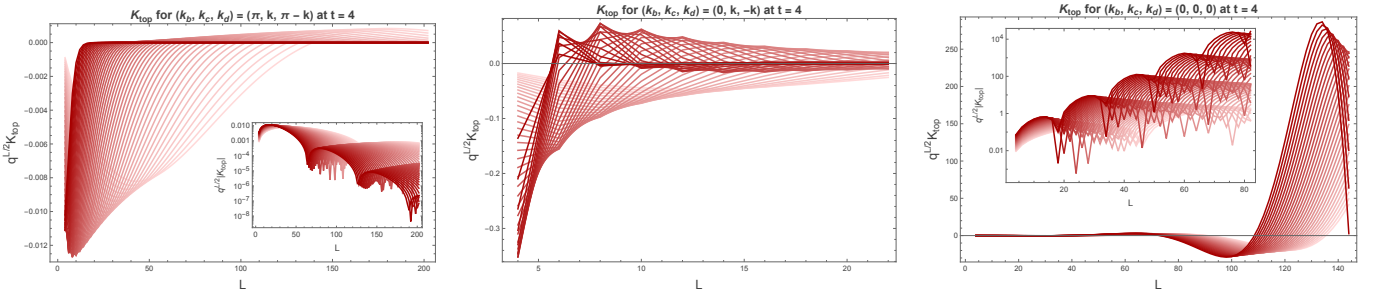


FIG. S11. **Exact large- $q$  TopSFF in different momentum sectors at  $t = 4$ .** We show the exact large- $q$  TopSFF as a function of  $L$  in the momentum sectors  $(k_b, k_c, k_d) = (\pi, k, \pi - k)$ ,  $(0, k, -k)$ , and  $(0, 0, 0)$ , from left to right, respectively. The corresponding  $\mu$  ranges are  $\mu \in [0.6, 0.9]$ ,  $\mu \in [0.7, 0.99]$ , and  $\mu \in [0.6, 0.62]$ , sampled in 50, 40, and 30 slices, respectively, and shown from light to dark red with increasing  $\mu$ . In the left and right panels, the TopSFF exhibits exponentially decaying and exponentially growing oscillatory behaviour, respectively. These oscillations arise from complex-conjugate eigenvalues of the Boltzmann factor, with modulus smaller than 1 in the left panel and larger than 1 in the right panel, see Fig. S14. In the middle panel, the TopSFF mostly displays an exponentially decaying envelope, although an exceptional point exists in this sector, as described by (SH.8), the associated oscillatory behaviour is largely obscured by this decay. Insets in the left and right panels show the corresponding semi-log plots for  $\mu \in [0.6, 0.7]$ , where peaks and troughs correspond to the oscillations in the main panels.

### 3. TopSFF with time translational symmetry

Here we provide exact leading- $q$  solution of TopSFF with the global swap operator inserted as spatially extended topological defects, in the presence of parity inversion symmetry and discrete time translational symmetry. For completeness, we restate the TopSFF in (SE.26) here as

$$\begin{aligned} \bar{\mathcal{K}}_{\text{top}} &=: q^{-L_e-1} \bar{\mathcal{K}}_{\text{top}} + O(q^{-L_e-2}), \\ \bar{\mathcal{K}}_{\text{top}} &= \phi^T \mathcal{B}^{L_e} \phi = \sum_{k_b, k_c, k_d} \tilde{\phi}(-k)^T \tilde{\mathcal{B}}(k)^{L_e} \tilde{\phi}(k). \end{aligned} \quad (\text{SF.37})$$

where  $\mathcal{B}$  and  $\tilde{\mathcal{B}}$  are the generalized Boltzmann factor in position and momentum space respectively. The components of the boundary state in momentum space are given by

$$\tilde{\phi}(a; k_b, k_c, k_d) = i^{\delta_{a,1}} \left[ \sqrt{2t^3} \mu^{2t} \delta_{n_b,0} \delta_{n_c,0} \delta_{n_d,0} + \sqrt{2t} (1 - \mu^{2t}) \delta_{n_b,0} \delta_{n_c+n_d,0 \pmod{t}} \right], \quad (\text{SF.38})$$

which is nonzero only if  $k_b = 0$  and  $k_d \equiv -k_c \pmod{2\pi}$ . Restricted to these momenta, the generalized Boltzmann factor depends only on whether  $(k_b, k_c, k_d) = (0, 0, 0)$  or  $(k_b, k_c, k_d) = (0, k, -k)$ . Note that the generalized Boltzmann

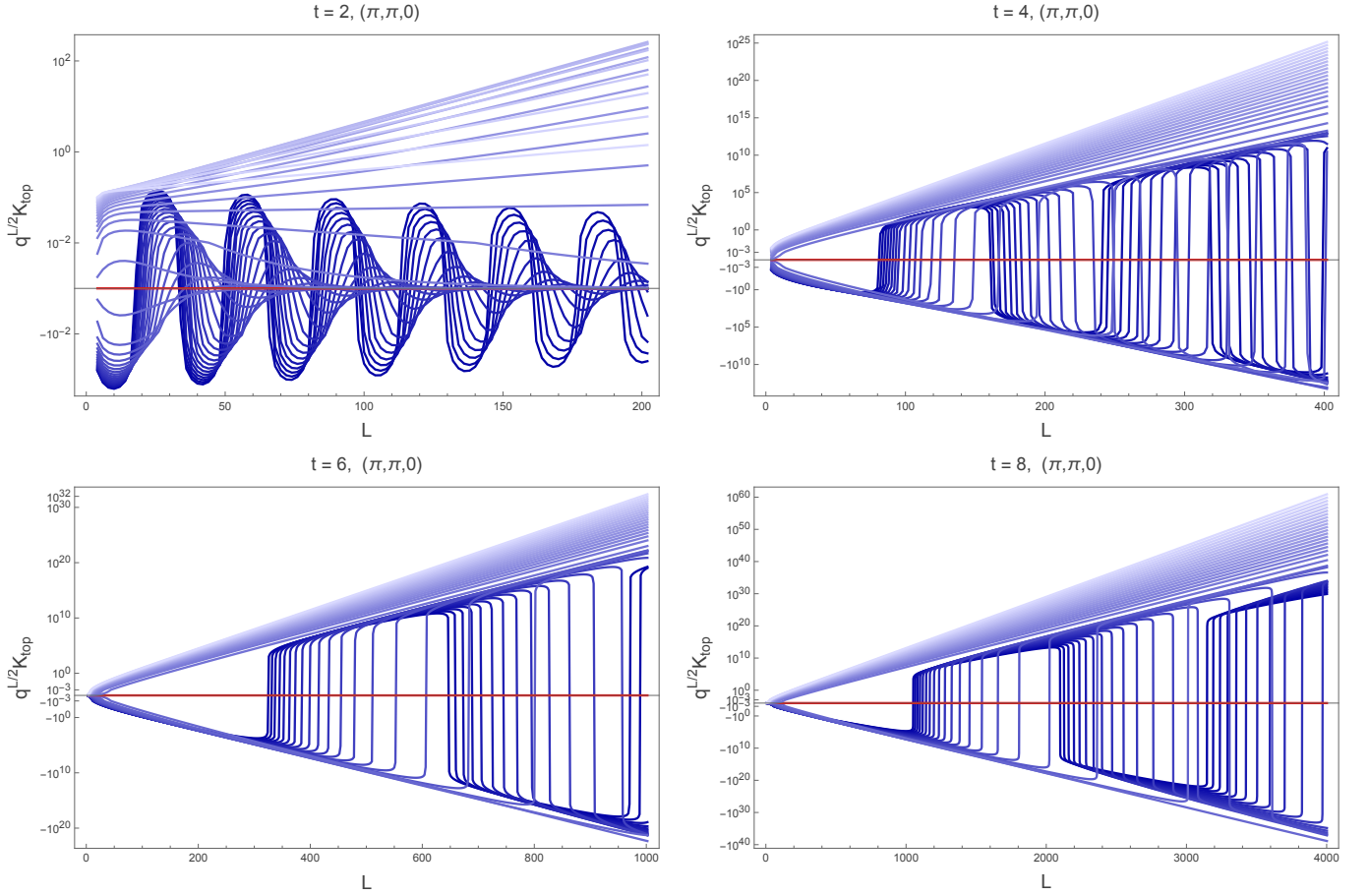


FIG. S12.  $\mathcal{PT}$  symmetry breaking transitions in the exact large- $q$  TopSFF in the  $(\pi, \pi, 0)$  sector. We plot the exact large- $q$  TopSFF as a function of  $L$  for  $t = 2, 4, 6, 8$ , focusing on the neighbourhood  $\mu \in [\mu_{\text{EP}}(t) - \delta\mu, \mu_{\text{EP}}(t) + \delta\mu]$  of the exceptional point  $\mu_{\text{EP}}(t)$  given in Eq. (SH.14). For each value of  $t$ , this interval is sampled using 40 slices in  $\mu$ , with  $\delta\mu = 0.1, 0.02, 0.01, 0.125$  for  $t = 2, 4, 6, 8$ , respectively. Curves at smaller  $\mu$ , corresponding to stronger interaction strength  $\epsilon$ , are shown in darker blue. The TopSFF evaluated exactly at the exceptional point  $\mu = \mu_{\text{EP}}$  is shown in red. Note that for this particular boundary condition, the prefactor multiplying the exceptional point contribution vanishes, and hence the TopSFF is identically zero. The Jordan non-diagonality can be extracted by probing boundary-resolved TopSFF, as shown in Fig. S20 and in Appendix H3.

factors at these momentum sectors have  $\mathcal{PT}$  symmetry. We use the subscript  $0_e$  to denote the momentum sector  $(k_b, k_c, k_d) = (0, 0, 0)$ , and the subscript  $0_b$  to denote the momentum sector  $(k_b, k_c, k_d) = (0, k, -k)$  with  $k \neq 0$ . Thus, TopSFF can be written as

$$\bar{\mathcal{K}}_{\text{top}} = 2t \left[ \mathcal{N}_{0_e}^2 \varphi^T \tilde{\mathcal{B}}^{L_e}(0, 0, 0) \varphi + (t-1) \mathcal{N}_{0_b}^2 \varphi^T \tilde{\mathcal{B}}^{L_e}(0, k, -k) \varphi \right], \quad (\text{SF.39})$$

with

$$\mathcal{N}_{0_e} := [1 + (t-1)\mu^{2t}], \quad \mathcal{N}_{0_b} := (1 - \mu^{2t}), \quad \varphi = \begin{pmatrix} 1 \\ i \end{pmatrix}. \quad (\text{SF.40})$$

Using (SF.8), the TopSFF with global swap operator as a spatially extended topological defect can be evaluated as

$$\bar{\mathcal{K}}_{\text{top}} = 2t [1 + (t-1)\mu^{2t}]^2 \mathcal{K}_{0_e} + 2t(t-1) (1 - \mu^{2t})^2 \mathcal{K}_{0_b}, \quad (\text{SF.41})$$

where  $\mathcal{K}_{0_e}$  and  $\mathcal{K}_{0_b}$  are given in (SF.30) and (SF.32) respectively. The implications of the presence of  $\mathcal{PT}$  symmetry and the existence of exceptional points are discussed below. As a consistency check, for  $t = 1$  and  $\alpha = 1$ , (SF.41)

reduces to

$$\begin{aligned}\bar{\mathcal{K}}_{\text{top}} &= 2(\mu^4 - 1) \frac{\lambda_{0_e,+}^{L_e} - \lambda_{0_e,-}^{L_e}}{\lambda_{0_e,+} - \lambda_{0_e,-}} = -\frac{4\sqrt{1-\mu^4}}{\sqrt{\mu^4+7}} \left(\sqrt{2(1-\mu^4)}\right)^{L_e} \sin(L_e\theta), \\ \lambda_{0_e,\pm} &= \frac{1-\mu^4}{2} \pm \frac{1}{2}\sqrt{(\mu^4-1)(\mu^4+7)} =: re^{\pm i\theta}.\end{aligned}\tag{SF.42}$$

where  $r = \sqrt{2(1-\mu^4)}$  and  $\cos\theta = \sqrt{(1-\mu^4)/8}$  or  $\sin\theta = \sqrt{(\mu^4+7)/8}$ . Eq. (SF.42) coincides with (i) the large- $q$  expansion of the exact finite- $q$  result of the TopSFF in Eq. (SI.7) at  $t = 1$ , and (ii) the exact large- $q$  calculation of the TopSFF for the RPM at  $t = 1$  in the absence of discrete time translational symmetry in Eq. (SJ.33).

#### 4. TopSFF with engineered parity inversion axes

Different momentum sectors of TopSFF, in particular the  $(\pi, \pi, 0)$  sector containing the  $\mathcal{PT}$  symmetry breaking transition, can be accessed by engineering the coupling gates along the parity inversion axes. We focus on two choices: no coupling and period-2 driving along these axes. Comparing the corresponding TopSFF allows us to isolate the  $(k_b, k_c, k_d) = (\pi, \pi, 0)$  contribution.

##### a. No coupling

Here we compute the TopSFF in Eq. (SF.37) exactly for RPM with discrete time translational symmetry, but without coupling along the parity inversion axes. The generalized Boltzmann factor  $\tilde{\mathcal{B}}$  remains the same, while the boundary states in Eq. (SE.14) in momentum space are given by

$$\tilde{\phi}(a; k_b, k_c, k_d) = i^{\delta_{a,1}} \sqrt{2t^3} \delta_{n_b,0} \delta_{n_c,0} \delta_{n_d,0},\tag{SF.43}$$

Since the boundary states lie entirely in the momentum sector  $(k_b, k_c, k_d) = (0, 0, 0)$ , the TopSFF without coupling along parity inversion axes can be evaluated as

$$\bar{\mathcal{K}}_{\text{top}} = 8t^3 \mathcal{K}_{0_e},\tag{SF.44}$$

where  $\mathcal{K}_{0_e}$  is given in (SF.30). This case is useful for removing contributions in TopSFF associated with the zero momentum sector.

##### b. Period-2 driving

Here we compute the TopSFF in Eq. (SF.37) exactly for RPM with discrete time translational symmetry, but with period-2 driving along the parity inversion axes. The generalized Boltzmann factor  $\tilde{\mathcal{B}}$  remains the same, while the boundary states in Eq. (SE.14) in momentum space are given by

$$\tilde{\phi}(a; k_b, k_c, k_d) = i^{\delta_{a,1}} \left[ \mu^{2t} \sqrt{2t^3} \delta_{n_b,0} \delta_{n_c,0} \delta_{n_d,0} + (1 - \mu^{2t}) \sqrt{\frac{t}{2}} \delta_{n_b \pmod{t}, 0} \delta_{n_c + n_d + n_b/2 \pmod{t}, 0} \right],\tag{SF.45}$$

which has support in the  $\mathcal{PT}$  symmetric sectors  $(k_b, k_c, k_d) \in \{(0, k, -k), (\pi, k, \pi - k)\}$ . Defining

$$\mathcal{N}_0 := \sqrt{\frac{t}{2}} \left[ 1 + (2t - 1)\mu^{2t} \right], \quad \mathcal{N}_* := \sqrt{\frac{t}{2}} (1 - \mu^{2t}),\tag{SF.46}$$

the TopSFF with period-2 driving along parity inversion axes can be evaluated as

$$\bar{\mathcal{K}}_{\text{top}} = \mathcal{N}_0^2 \mathcal{K}_{0_e} + (t - 1) \mathcal{N}_*^2 \mathcal{K}_{0_b} + \mathcal{N}_*^2 \left[ 2\mathcal{K}_{\pi_e} + (t - 2)\mathcal{K}_{\pi_b} \right].\tag{SF.47}$$

where  $\mathcal{K}_{0_e}$ ,  $\mathcal{K}_{0_b}$ ,  $\mathcal{K}_{\pi_e}$  and  $\mathcal{K}_{\pi_b}$  are respectively given in (SF.30), (SF.32), (SF.34) and (SF.36).

c. Isolating  $(k_b, k_c, k_d) = (\pi, \pi, 0)$  sector by engineering parity inversion axes

We extract the TopSFF directly in the  $(\pi, \pi, 0)$  sector by computing TopSFF in finite- $q$  via dual spatial propagation of the quantum circuit, as discussed in Secs. I 1 and L. However, in principle, TopSFF of  $(k_b, k_c, k_d) = (\pi, \pi, 0)$  and its  $\mathcal{PT}$  symmetry breaking transition can be extracted by engineering the parity inversion axes. More specifically, comparing the no-coupling boundary condition with period-2 driving allows one to separate the dominant contributions between the  $k_b = 0$  sector and the  $k_b = \pi$  sector. As shown in Fig. S14, among the momentum sectors accessed by period-2 driving, namely  $(0, 0, 0)$ ,  $(0, k, -k)$ ,  $(\pi, \pi, 0)$ , and  $(\pi, k, \pi - k)$ , only the  $(0, 0, 0)$  and  $(\pi, \pi, 0)$  sectors contain eigenvalues with modulus larger than unity. The contributions from the remaining sectors therefore decay exponentially with system size  $L$ . Consequently, at large  $L$ , the contribution from the  $(\pi, \pi, 0)$  sector can in principle be isolated from the period-2 TopSFF by subtracting the corresponding zero-momentum contribution,

$$\mathcal{K}_{\pi_e} = \overline{\mathcal{K}}_{p=2} - \beta \overline{\mathcal{K}}_{\text{no-coupling}}, \quad (\text{SF.48})$$

where  $\overline{\mathcal{K}}_{p=2}$  denotes TopSFF with period-2 driving along the parity-inversion axes,  $\overline{\mathcal{K}}_{\text{no-coupling}}$  denotes TopSFF without coupling along these axes, and  $\beta$  is chosen to fit the zero momentum sector contribution. This subtraction isolates the  $(\pi, \pi, 0)$  contribution up to terms that are exponentially small in  $L$ . In practice, however, we extract the TopSFF directly in the  $(\pi, \pi, 0)$  sector by computing TopSFF in finite- $q$  via dual spatial propagation of the quantum circuit, as discussed in Secs. I 1 and L.

### Appendix G: Emergent $\mathcal{PT}$ symmetric dimers

In this appendix, we first review the two-mode  $\mathcal{PT}$  dimer, and then show how the TopSFF generalized Boltzmann factor reduces to a canonical  $\mathcal{PT}$  symmetric dimer. This gives an interpretation of the  $\mathcal{PT}$  unbroken regime,  $\mathcal{PT}$  broken regime, and the exceptional point in terms of Gaussian/non-Gaussian tDW detuning and conversion.

#### 1. Review of $\mathcal{PT}$ symmetric dimers

Consider a single complex amplitude  $\psi(t)$  evolving under a generator  $H$  as

$$i \frac{d}{dt} \psi = H \psi. \quad (\text{SG.1})$$

If  $H = i\gamma$  with  $\gamma \in \mathbb{R}$ , then

$$\frac{d}{dt} \psi = \gamma \psi \quad \Rightarrow \quad \psi(t) = e^{\gamma t} \psi(0). \quad (\text{SG.2})$$

Thus  $\gamma > 0$  gives exponential growth of amplitude, which is often referred to as “gain”. If instead  $H = -i\gamma$ , then

$$\frac{d}{dt} \psi = -\gamma \psi \quad \Rightarrow \quad \psi(t) = e^{-\gamma t} \psi(0), \quad (\text{SG.3})$$

which leads to exponential decay of amplitude, which is referred to as “loss”.

Consider the canonical  $\mathcal{PT}$  dimer

$$H = \begin{pmatrix} +i\gamma & J \\ J & -i\gamma \end{pmatrix}, \quad (\text{SG.4})$$

where  $J, \gamma \in \mathbb{R}$ . The diagonal entries  $\pm i\gamma$  represent balanced gain/loss, while  $J$  coherently couples the two modes. In particular, we have  $\text{tr} H = i\gamma - i\gamma = 0$ , so the gain and loss are exactly balanced at the level of the trace. The eigenvalues of the  $\mathcal{PT}$  dimer are

$$E_{\pm} = \pm \sqrt{J^2 - \gamma^2}, \quad (\text{SG.5})$$

and a right eigenvector  $\psi = (u, v)^T$  of the eigenvalue  $E$  satisfies

$$(i\gamma - E)u + Jv = 0 \quad \Rightarrow \quad \frac{v}{u} = \frac{E - i\gamma}{J}. \quad (\text{SG.6})$$

The Hamiltonian (SG.4) satisfies the  $\mathcal{PT}$  symmetry

$$(\mathcal{PT})H(\mathcal{PT})^{-1} = H, \quad \mathcal{P} = \sigma_x, \quad (\text{SG.7})$$

and with  $\mathcal{T}$  being complex conjugation. However, individual eigenvectors need not be invariant under  $\mathcal{PT}$ . If  $H|\psi\rangle = E|\psi\rangle$ , then

$$H(\mathcal{PT}|\psi\rangle) = E^*(\mathcal{PT}|\psi\rangle), \quad (\text{SG.8})$$

so  $\mathcal{PT}$  maps an eigenvector at  $E$  to an eigenvector at  $E^*$ .

The phases of the model are given as follow.

- **Unbroken  $\mathcal{PT}$  phase ( $|\gamma| < |J|$ ): real spectrum and balanced modes.** In this strong coupling regime with  $E_{\pm} \in \mathbb{R}$ , the time evolution is governed by pure phases,  $e^{-iE_{\pm}t}$ , and there is no exponential growth/decay in time: the eigenmodes are dynamically balanced. The right eigenvectors can be chosen as  $\mathcal{PT}$  eigenstates

$$\mathcal{PT}|\psi_{\pm}\rangle = e^{i\theta_{\pm}}|\psi_{\pm}\rangle. \quad (\text{SG.9})$$

Using  $E^2 = J^2 - \gamma^2$  in (SG.6) gives

$$\left| \frac{v}{u} \right| = \frac{|E - i\gamma|}{|J|} = \frac{\sqrt{E^2 + \gamma^2}}{|J|} = \frac{\sqrt{J^2}}{|J|} = 1. \quad (\text{SG.10})$$

Thus each eigenvector has equal weight on the gain and loss sites (up to a relative phase): the eigenvectors samples both sites so that net gain/loss cancels.

- **Broken  $\mathcal{PT}$  phase ( $|\gamma| > |J|$ ): complex-conjugate spectrum and polarized modes.** Write

$$E_{\pm} = \pm i\kappa, \quad \kappa := \sqrt{\gamma^2 - J^2} > 0. \quad (\text{SG.11})$$

Then time evolution contains exponentials,  $e^{-iE_{\pm}t} = e^{\pm\kappa t}$ , so one eigenmode amplifies while the other eigenmode decays.  $\mathcal{PT}$  cannot leave an eigenvector invariant, since it maps  $E_{\pm} \mapsto E_{\pm}^* = E_{\mp}$ . In other words,

$$\mathcal{PT}|\psi_{+}\rangle \propto |\psi_{-}\rangle, \quad \mathcal{PT}|\psi_{-}\rangle \propto |\psi_{+}\rangle. \quad (\text{SG.12})$$

The ratio of the components of eigenvector becomes

$$\frac{v}{u} = \frac{i\kappa - i\gamma}{J} = i \frac{\kappa - \gamma}{J}, \quad (\text{SG.13})$$

so generically  $|v/u| \neq 1$ , i.e., the right eigenvectors become polarized toward one site/mode. This eigenvector polarization is the signature accompanying  $\mathcal{PT}$  symmetry breaking.

- **Exceptional point ( $|\gamma| = |J|$ ): coalescence of eigenvalues and eigenvectors.** At threshold,  $E_{+} = E_{-} = 0$  and the two eigenvalues merge. Generically the corresponding eigenvectors coalesce, so  $H$  becomes non-diagonalizable and is represented by a Jordan block. This coalescence of eigenvalues and eigenvectors defines the exceptional point.

## 2. TopSFF and $\mathcal{PT}$ dimers

According to Proposition E.3, in the momentum space, the generalized Boltzmann factor  $\tilde{\mathcal{B}}(k_b, k_c, k_d)$  has  $\mathcal{PT}$  symmetry with complex conjugation  $\mathcal{T}$  and  $\mathcal{P} := \sigma_z$ , if  $k_b + k_c + k_d \equiv 0 \pmod{\pi}$ . At such symmetric points, the generalized Boltzmann factor  $\tilde{\mathcal{B}}(k_b, k_c, k_d)$  is a 2-by-2 matrix in  $a$ -space with the form

$$\tilde{\mathcal{B}} = \begin{pmatrix} \tilde{\mathcal{B}}_{00} & \tilde{\mathcal{B}}_{01} \\ \tilde{\mathcal{B}}_{10} & \tilde{\mathcal{B}}_{11} \end{pmatrix} = \begin{pmatrix} A & iB \\ iB & C \end{pmatrix} = d_0 \mathbb{1} + d_z \sigma_z + iB \sigma_x, \quad d_0 := \frac{A+C}{2}, \quad d_z := \frac{A-C}{2}. \quad (\text{SG.14})$$

where  $A, B, C \in \mathbb{R}$ , and we have left labels of momentum sector implicit. In terms of the temporal domain wall basis,

$$\{|G\rangle := |a=0; k_b, k_c, k_d\rangle \quad (\text{Gaussian tDW}), \quad |nG\rangle := |a=1; k_b, k_c, k_d\rangle \quad (\text{non-Gaussian tDW})\}, \quad (\text{SG.15})$$

the entry of the Boltzmann factor has the following interpretation:

- $\tilde{\mathcal{B}}_{00} \equiv \text{A}$ : Amplitude for the Gaussian tDW to remain as Gaussian tDW,
- $\tilde{\mathcal{B}}_{11} \equiv \text{C}$ : Amplitude for the non-Gaussian tDW to remain as non-Gaussian tDW,
- $\tilde{\mathcal{B}}_{01} \equiv i\text{B}$ : Amplitude for the DW type conversion with a  $\pi/2$  phase.

Now introduce a unitary transformation

$$U := \frac{1}{\sqrt{2}} \begin{pmatrix} 1 & 1 \\ 1 & -1 \end{pmatrix}, \quad U\sigma_z U^\dagger = \sigma_x, \quad U\sigma_x U^\dagger = \sigma_z. \quad (\text{SG.16})$$

Then the rotated TopSFF Boltzmann factor is the canonical  $\mathcal{PT}$  dimer up to a trace shift,

$$U\tilde{\mathcal{B}}U^\dagger = d_0 \mathbb{1} + d_z \sigma_x + i\text{B} \sigma_z = d_0 \mathbb{1} + \begin{pmatrix} i\text{B} & \frac{\text{A}-\text{C}}{2} \\ \frac{\text{A}-\text{C}}{2} & -i\text{B} \end{pmatrix} \equiv d_0 \mathbb{1} + \begin{pmatrix} +i\gamma & J \\ J & -i\gamma \end{pmatrix}, \quad (\text{SG.17})$$

where the coupling strength and gain/loss rates are determined respectively by

$$J := d_z = \frac{\text{A} - \text{C}}{2} = \frac{\tilde{\mathcal{B}}_{00} - \tilde{\mathcal{B}}_{11}}{2}, \quad \gamma := \text{B} = -i\tilde{\mathcal{B}}_{01}. \quad (\text{SG.18})$$

Note that after the mapping,  $U\tilde{\mathcal{B}}U^\dagger$  is invariant under the  $\mathcal{PT}$  symmetry with complex conjugation  $\mathcal{T}$  and the standard parity symmetry operator  $U\mathcal{P}U^\dagger = \sigma_x$ . The basis is now

$$\left\{ |+\rangle := \frac{1}{\sqrt{2}} (|G\rangle + |nG\rangle), \quad |-\rangle := \frac{1}{\sqrt{2}} (|G\rangle - |nG\rangle) \right\}, \quad (\text{SG.19})$$

The eigenvalues of  $\tilde{\mathcal{B}}$  are  $\lambda_\pm = \frac{\text{A}+\text{C}}{2} \pm \sqrt{\Delta}$  with the transition-controlling discriminant

$$\Delta := J^2 - \gamma^2 = \left( \frac{\text{A} - \text{C}}{2} \right)^2 - \text{B}^2 = \left( \frac{\tilde{\mathcal{B}}_{00} - \tilde{\mathcal{B}}_{11}}{2} \right)^2 - \left( -i\tilde{\mathcal{B}}_{01} \right)^2, \quad (\text{SG.20})$$

i.e., the  $\mathcal{PT}$  symmetry-breaking transition is controlled by whether the Gaussian/non-Gaussian tDW conversion amplitude exceeds the detuning between the Gaussian and non-Gaussian tDW propagation amplitudes.

TopSFF can be obtained by evaluating  $\varphi^T \tilde{\mathcal{B}}^{L_e} \varphi$  with the vector  $\varphi = (\varphi_1, \varphi_2)^T$ . As discussed in F 1, using the Cayley-Hamilton theorem on  $\tilde{\mathcal{B}}$ , we can write

$$\varphi^T \tilde{\mathcal{B}}^{L_e} \varphi = A(L_e) \varphi^T \tilde{\mathcal{B}} \varphi + B(L_e) \varphi^T \varphi, \quad (\text{SG.21})$$

where

$$A(L_e) := \frac{\lambda_+^{L_e} - \lambda_-^{L_e}}{\lambda_+ - \lambda_-}, \quad B(L_e) := \frac{\lambda_+ \lambda_-^{L_e} - \lambda_- \lambda_+^{L_e}}{\lambda_+ - \lambda_-}. \quad (\text{SG.22})$$

and, in terms of components of  $\varphi$ ,

$$\varphi^T \tilde{\mathcal{B}} \varphi = \text{A} \varphi_1^2 + \text{C} \varphi_2^2 + 2i\text{B} \varphi_1 \varphi_2, \quad \varphi^T \varphi = \varphi_1^2 + \varphi_2^2. \quad (\text{SG.23})$$

For a given momentum sector  $(k_b, k_c, k_d)$  where  $\mathcal{PT}$  symmetry is present, the  $\mathcal{PT}$  symmetry breaking transition has the following interpretation:

- **Unbroken  $\mathcal{PT}$  phase** ( $\Delta > 0$  and  $|\tilde{\mathcal{B}}_{01}| < \left| \frac{\tilde{\mathcal{B}}_{00} - \tilde{\mathcal{B}}_{11}}{2} \right|$ ): **Polarization of Gaussian/non-Gaussian tDWs.**

In the rotated basis the right eigenvectors can be chosen as  $\mathcal{PT}$  eigenstates, i.e. they are balanced across the effective gain/loss modes. In the unrotated tDW basis, the eigenvectors are dominated by  $|G\rangle$  or  $|nG\rangle$ , so the propagation eigenmodes do not exhibit substantial coherent conversion between Gaussian and non-Gaussian tDWs.

The eigenvalues  $\lambda_\pm \in \mathbb{R}$  are distinct. Take the convention where  $|\lambda_+| > |\lambda_-|$ . From (SG.22),

$$A(L_e) = c \lambda_+^{L_e - 1}, \quad c := \frac{1 - (\lambda_-/\lambda_+)^{L_e}}{1 - (\lambda_-/\lambda_+)} \approx \frac{1}{1 - (\lambda_-/\lambda_+)}, \quad (\text{SG.24})$$

and similarly  $B(L_e) = \mathcal{O}(\lambda_+^{L_e - 1})$ . Hence  $\varphi^T \tilde{\mathcal{B}}^{L_e} \varphi$  grows or decays exponentially without oscillations with the dominant real eigenvalue.

- **Broken  $\mathcal{PT}$  phase ( $\Delta < 0$  and  $|\tilde{\mathcal{B}}_{01}| > |\frac{\tilde{\mathcal{B}}_{00}-\tilde{\mathcal{B}}_{11}}{2}|$ ): Hybridization of Gaussian/non-Gaussian tDWs.**

In the rotated basis the eigenvalues form a complex-conjugate pair and the eigenvectors are not  $\mathcal{PT}$  eigenstates ( $\mathcal{PT}$  exchanges them). In the unrotated tDW basis, this polarization manifests as hybridization between  $|G\rangle$  and  $|nG\rangle$ : each propagation eigenmode involves nontrivial coherent hybridization of the Gaussian and non-Gaussian tDW sectors, with one mode effectively amplified and the other mode attenuated under repeated multiplication by  $\tilde{\mathcal{B}}$ .

The eigenvalues  $\lambda_{\pm}$  form a complex-conjugate pair. Write

$$\lambda_{\pm} = d_0 \pm i\sqrt{|\Delta|} = r e^{\pm i\theta}, \quad r := |\lambda_{\pm}| = \sqrt{d_0^2 + |\Delta|}, \quad \theta := \arctan\left(\frac{\sqrt{|\Delta|}}{d_0}\right). \quad (\text{SG.25})$$

In particular,

$$A(L_e) = \frac{\lambda_+^{L_e} - \lambda_-^{L_e}}{\lambda_+ - \lambda_-} = r^{L_e-1} \frac{\sin(L_e\theta)}{\sin\theta}, \quad (\text{SG.26})$$

and  $B(L_e) = \mathcal{O}(r^{L_e-1})$ . Therefore,  $\varphi^T \tilde{\mathcal{B}}^{L_e} \varphi$  has an envelope  $r^{L_e-1}$  with oscillations set by  $\sin(L_e\theta)/\sin\theta$ .

- **Exceptional point ( $\Delta = 0$  and  $|\tilde{\mathcal{B}}_{01}| = |\frac{\tilde{\mathcal{B}}_{00}-\tilde{\mathcal{B}}_{11}}{2}|$ ): onset of hybridization and mode coalescence.**

At  $\Delta = 0$  the two eigenvalues coalesce, and generically the two eigenvectors merge into a single eigenvector in the Jordan form. This is the  $\mathcal{PT}$  threshold where the tDW sector hybridization switches on non-analytically.

The eigenvalue  $\lambda_+ = \lambda_- = d_0$  and  $\tilde{\mathcal{B}}$  is generically non-diagonalizable. Taking the coalescing limit in (SG.22) yields

$$A(L_e) = L_e d_0^{L_e-1}, \quad B(L_e) = (1 - L_e) d_0^{L_e}. \quad (\text{SG.27})$$

Thus  $\varphi^T \tilde{\mathcal{B}}^{L_e} \varphi$  acquires the characteristic Jordan non-diagonality, i.e., an extra factor of  $L_e$  relative to the generic cases. See F 1 a for the extraction of the linear scaling in  $L_e$  from TopSFF.

## Appendix H: TopSFF and exceptional points (EP)

In this appendix, we analyse exceptional points (EP) of the generalized Boltzmann factor in the  $\mathcal{PT}$  symmetric momentum sectors. Section H 1 solves the exceptional-point condition in the four selected momentum sectors  $(0, k, -k)$ ,  $(0, 0, 0)$ ,  $(\pi, \pi, 0)$ , and  $(\pi, k, \pi - k)$ . Section H 2 presents the resulting EP data. Section H 3 presents the signatures of eigenvalue and eigenvector coalescence, including the Jordan-block contribution exposed by boundary-resolved TopSFFs.

### 1. EP in selected momentum sectors

We study exceptional points (EPs) of the generalized Boltzmann factor in the  $\mathcal{PT}$ -symmetric sectors. In these sectors, the Boltzmann factor takes the form

$$\tilde{\mathcal{B}} = \begin{pmatrix} A & iB \\ iB & C \end{pmatrix}, \quad (\text{SH.1})$$

with eigenvalues

$$\lambda_{\pm} = \frac{A+C}{2} \pm \sqrt{\Delta}, \quad \Delta := \left(\frac{A-C}{2}\right)^2 - B^2. \quad (\text{SH.2})$$

Exceptional points occur when the discriminant vanishes,  $\Delta = 0$ , equivalently

$$A - C = \pm 2B. \quad (\text{SH.3})$$

For each  $\mathcal{PT}$ -symmetric sector, we define the branch polynomials

$$P^{\pm}(\mu) := A - C \mp 2B, \quad (\text{SH.4})$$

so that the EP condition is  $P^{\pm}(\mu) = 0$ . Below we identify the corresponding values of  $\mu$  for which  $\Delta = 0$ . See Sec. G 2 for further discussion of the associated  $\mathcal{PT}$  symmetry breaking transition.

a. EP for  $(k_b, k_c, k_d) = (0, k, -k)$

For the sector  $(k_b, k_c, k_d) = (0, k, -k)$  with  $k \neq 0$ , the matrix elements are given in Eq. (SF.31).  
 (+) **branch:**  $A - C = +2B$ . On this branch, the geometric sums cancel, and

$$P_{0_b}^+(\mu) = \mu^{t-1}(\mu^2 - 1)(2t\mu^4 - \mu^2 + 1). \quad (\text{SH.5})$$

The factor  $\mu^2 - 1$  gives the boundary solution  $\mu = 1$ , while for  $t \geq 2$  the factor  $\mu^{t-1}$  gives the boundary solution  $\mu = 0$ . The remaining quadratic has discriminant  $1 - 8t < 0$  for all  $t \geq 1$ , so it has no real root. Hence there is no EP with  $\mu \in (0, 1)$  on the (+) branch.

(-) **branch:**  $A - C = -2B$ . On this branch,

$$P_{0_b}^-(\mu) = 8 \sum_{m=0}^{t-1} \mu^{4m} - 16 \sum_{m=t}^{2t-1} \mu^{2m} - \mu^{4t-4} + 2\mu^{4t-2} + (6t-1)\mu^{4t} + 2t\mu^{4t+2}. \quad (\text{SH.6})$$

One checks that

$$P_{0_b}^-(1) = 0, \quad P_{0_b}^-(0) = 8 \quad (t \geq 2), \quad \frac{d}{d\mu} P_{0_b}^-(1) = 4t > 0. \quad (\text{SH.7})$$

For  $t \geq 2$ ,  $P_{0_b}^-(\mu)$  is negative just to the left of  $\mu = 1$  and positive at  $\mu = 0$ . Therefore, by continuity there is at least one non-trivial root in  $(0, 1)$ . Thus the (-) branch admits an interior EP. At large  $t$ , the interior root approaches  $\mu = 1$  as

$$\mu_{\text{EP}}(t) = 1 - \frac{1}{t^2} + O(t^{-3}), \quad t \gg 1. \quad (\text{SH.8})$$

In Fig. S13, we plot  $P_{0_b}^-$  whose roots determine  $\mu_{\text{EP}}(t)$ .

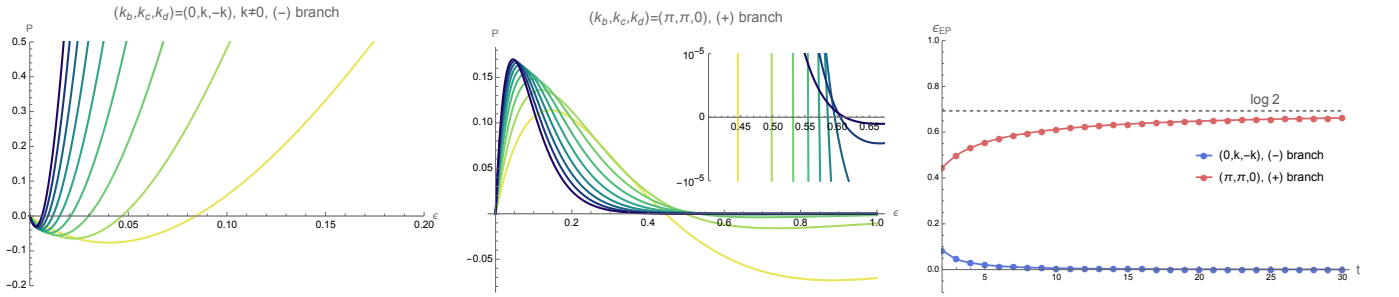


FIG. S13. **Exceptional points in the  $(0, k, -k)$  and  $(\pi, \pi, 0)$  sectors at large  $q$ .** Left and middle panels show  $P_{0_b}^-(\epsilon)$  and  $P_{0_b}^+(\epsilon)$ , respectively, as functions of  $\epsilon \equiv -2 \ln \mu$ , with  $t = 2, \dots, 10$  shown from yellow to blue. For each  $t \geq 2$ , a non-trivial root with  $\mu \in (0, 1)$  signals an exceptional point. The inset in the middle panel enlarges the root region for the  $(\pi, \pi, 0)$  sector. Right panel: exceptional-point locations versus  $t$  for the  $(\pi, \pi, 0)$  sector and the  $(0, k, -k)$  sector. As  $t$  increases, the exceptional point in the  $(\pi, \pi, 0)$  sector approaches  $\epsilon_{\text{EP}} = \log 2$ , see (SH.14).

b. EP for  $(k_b, k_c, k_d) = (0, 0, 0)$

For the sector  $(k_b, k_c, k_d) = (0, 0, 0)$ , the matrix elements are given in Eq. (SF.30).

(+) **branch:**  $A_0 - C_0 = +2B_0$ . On this branch, the geometric sums cancel, and

$$P_{0_e}^+(\mu) = \mu^{t-1}(\mu^2 - 1) \left[ 2t(t-1)\mu^4 + (2t-1)\mu^2 + 1 \right]. \quad (\text{SH.9})$$

The factor  $\mu^2 - 1$  gives the boundary solution  $\mu = 1$ , while for  $t \geq 2$  the factor  $\mu^{t-1}$  gives the boundary solution  $\mu = 0$ . The quadratic in  $\mu^2$  has discriminant  $(2t-1)^2 - 8t(t-1) = 1 + 4t(1-t) \leq 1$ , which is negative for all  $t \geq 2$ , so there is no real root. Hence there is no EP with  $\mu \in (0, 1)$  on the (+) branch.

(−) **branch:**  $A_0 - C_0 = -2B_0$ . The EP condition is  $P_{0_e}^-(\mu) = 0$ , with

$$P_{0_e}^-(\mu) = 8 \sum_{m=0}^{t-1} \mu^{2m} + 16(t-1) \sum_{m=t}^{2t-1} \mu^m + (8t(t-1)^2 - 2t^2 + 4t - 1)\mu^{2t} - \mu^{2t-2} - 2(t-1)\mu^{2t-1} + 2t(t-1)\mu^{2t+3}. \quad (\text{SH.10})$$

This can be rearranged as

$$P_{0_e}^-(\mu) = 8 \sum_{m=0}^{t-2} \mu^{2m} + 7\mu^{2t-2} + 16(t-1) \sum_{m=t}^{2t-2} \mu^m + 14(t-1)\mu^{2t-1} + (8t(t-1)^2 - 2t^2 + 4t - 1)\mu^{2t} + 2t(t-1)\mu^{2t+3}. \quad (\text{SH.11})$$

All coefficients are non-negative, and in fact strictly positive for  $t \geq 2$ . Therefore  $P_{0_e}^-(\mu) > 0$  for  $\mu \in (0, 1)$ , and the (−) branch has no interior solution.

c. EP for  $(k_b, k_c, k_d) = (\pi, \pi, 0)$

For the sector  $(k_b, k_c, k_d) = (\pi, \pi, 0)$ , the matrix elements are given in Eq. (SF.33).

(+) **branch:**  $A - C = +2B$ . The (+) branch simplifies to

$$P_{\pi_e}^+(\mu) = \mu^{4t-4}(1 - \mu^2)(2t\mu^4 - (t-1)\mu^2 - 1). \quad (\text{SH.12})$$

Besides the boundary solutions  $\mu = 0$  (for  $t \geq 2$ ) and  $\mu = 1$ , the only interior EP comes from the quadratic equation

$$2t\mu^4 - (t-1)\mu^2 - 1 = 0. \quad (\text{SH.13})$$

Solving for  $\mu^2$  gives

$$\mu_{\text{EP}}(t) = \sqrt{\frac{(t-1) + \sqrt{(t-1)^2 + 8t}}{4t}} \xrightarrow{t \gg 1} \frac{1}{\sqrt{2}}. \quad (\text{SH.14})$$

In terms of  $\epsilon$  with  $\mu = e^{-\epsilon/2}$ , we have

$$\epsilon_{\text{EP}}(t) = \log \left[ \frac{\sqrt{(t-1)^2 + 8t} - (t-1)}{2} \right] \xrightarrow{t \gg 1} \log 2. \quad (\text{SH.15})$$

See Fig. S13 for the locations of the EP for  $t = 30$ . We are particularly interested in the case of  $t = 2$  at large  $q$ , where  $\mu_{\text{EP}}(t = 2) = 0.8002$  and  $\epsilon_{\text{EP}}(t = 2) = -2 \log \mu_{\text{EP}}(t = 2) = 0.4457$ , since we can compare these prediction with our exact computation at finite  $q$ .

(−) **branch:**  $A - C = -2B$ . Using Eqs. (SF.33) and (SF.29), the branch polynomial

$$P_{\pi_e}^-(\mu) = 8 \sum_{m=0}^{t-1} \mu^{4m} + 8(t-2) \sum_{m=t}^{2t-3} \mu^{2m} + (8t-17)\mu^{4t-4} + (7t-14)\mu^{4t-2} - (8t^2 - 11t + 1)\mu^{4t} - 2t\mu^{4t+2}. \quad (\text{SH.16})$$

It can be shown that  $P_{\pi_e}^-(\mu)$  is positive for  $\mu \in (0, 1)$ , and hence this branch gives no additional root in  $\mu \in (0, 1)$ .

d. EP for  $(k_b, k_c, k_d) = (\pi, k, \pi - k)$

For the sector  $(k_b, k_c, k_d) = (\pi, k, \pi - k)$  with  $k \neq 0, \pi$ , the matrix elements are given in Eq. (SF.35).

(+) **branch:**  $A - C = +2B$ . Using Eq. (SF.35), one finds

$$P_{\pi_b}^+(\mu) = -\mu^{4t-4}(1 - \mu^2)^2. \quad (\text{SH.17})$$

Hence the (+) branch has only the boundary solution  $\mu = 1$ , and no EP in the interior  $\mu \in (0, 1)$ .

(−) **branch:**  $A - C = -2B$ . On this branch, using the definitions of  $A_{t-1}$  and  $C_t$  in (SF.29), we obtain

$$P_{\pi_b}^-(\mu) = 7\mu^{4t-4}(1-\mu^2)^2 + 8\sum_{r=2}^{t-1}\mu^{4t-4r}(1-\mu^{2r})^2 + 8(1-\mu^{2t})^2, \quad (\text{SH.18})$$

which has positive terms, leading to  $P_{\pi_b}^-(\mu) > 0$  for  $\mu \in (0, 1)$ . Therefore, the (−) branch has no interior solution. Hence the  $(\pi, k, \pi - k)$  sector has no exceptional point for  $\mu \in (0, 1)$ .

## 2. EP data

Here we provide plots of the complex eigenvalues of the generalized Boltzmann factor against the interaction strength in Fig. S14 and Fig. S15, demonstrating  $\mathcal{PT}$  symmetry breaking transition in certain momentum sectors. In Fig. S14, we plot the complex eigenvalues of the generalized Boltzmann factor of  $(k_b, k_c, k_d) \in \{(0, 0, 0), (0, 2\pi m/t, -2\pi m/t), (\pi, \pi, 0), (\pi, 2\pi m/t, \pi - 2\pi m/t)\}$  with  $m = 1$ . Among these,  $(\pi, \pi, 0)$  sector exhibits a particularly prominent  $\mathcal{PT}$  transitions, for which  $|\lambda_{\pm}|$  exceeds 1 over a finite range of  $\mu$ . Importantly, the EP of  $(\pi, \pi, 0)$  persists at finite  $\mu$ , see (SH.14). In Fig. S15, we plot complex eigenvalues of Boltzmann factor in all momentum sectors  $(k_b, k_c, k_d) = (2\pi n_b/2t, 2\pi n_c/t, 2\pi n_d/t)$  with  $n_b = [1, 2t]$  and  $n_c, n_d \in [1, t]$ .  $\Re\lambda_{\pm}$ . For  $t = 2$ ,  $\mathcal{PT}$  symmetry breaking transitions occur in  $(k_b, k_c, k_d) \in \{(0, \pi, \pi), (\pi/2, 0, 0), (\pi/2, 0, \pi), (\pi/2, \pi, 0), (\pi, 0, \pi), (\pi, \pi, 0), (3\pi/2, 0, 0), (3\pi/2, 0, \pi), (3\pi/2, \pi, 0)\}$ . Again, the transitions in the  $(\pi, 0, \pi)$  and  $(\pi, \pi, 0)$  sectors (related by the exchange symmetry between coordinates  $c$  and  $d$ ) are the most prominent, since  $|\lambda_{\pm}|$  can exceed 1, which is also generally the case for  $t > 2$ .

## 3. Eigenvalue and eigenvector coalescence at EP

In this section, we discuss the signatures of exceptional points (EPs) of the  $\mathcal{PT}$ -symmetric generalized Boltzmann factor, including eigenvalue coalescence and eigenvector coalescence, as diagnosed by eigenvector self-orthogonality and the divergence of the Petermann factor. We focus on the sector  $(k_b, k_c, k_d) = (\pi, \pi, 0)$ , although the discussion applies more generally to any  $\mathcal{PT}$ -symmetric momentum sector. In the momentum sector  $(k_b, k_c, k_d) = (\pi, \pi, 0)$ , the generalized Boltzmann factor is  $\mathcal{PT}$  symmetric and takes the form

$$\tilde{\mathcal{B}}_{\pi_e} = \begin{pmatrix} A_{\pi_e} & i B_{\pi_e} \\ i B_{\pi_e} & C_{\pi_e} \end{pmatrix}, \quad (\text{SH.19})$$

where the matrix entries are defined in Eq. (SF.33), and we use the shorthand  $\pi_e \equiv (k_b, k_c, k_d) = (\pi, \pi, 0)$  for this momentum sector. At an exceptional point, the two eigenvalues and their corresponding eigenvectors coalesce. This is a second order exceptional point (EP2), since the algebraic multiplicity is 2, while the geometric multiplicity is 1. In what follows, we examine both eigenvalue coalescence and eigenvector coalescence in the vicinity of the EP.

- **Square root scaling of eigenvalue coalescence.** The eigenvalues are

$$\lambda_{\pm} = \frac{\text{Tr} \tilde{\mathcal{B}}_{\pi_e} \pm \sqrt{\Delta_{\pi_e}}}{2}, \quad \Delta_{\pi_e} := \text{Tr} \tilde{\mathcal{B}}_{\pi_e}^2 - 4 \det \tilde{\mathcal{B}}_{\pi_e} = (A_{\pi_e} - C_{\pi_e})^2 - 4B_{\pi_e}^2. \quad (\text{SH.20})$$

At the exceptional point, the discriminant vanishes so that the two eigenvalues coalesce,

$$\Delta_{\pi_e}(\mu_{\text{EP}}) = 0 \implies \lambda_+(\mu_{\text{EP}}) = \lambda_-(\mu_{\text{EP}}) = \frac{1}{2} \text{Tr} \tilde{\mathcal{B}}_{\pi_e}(\mu_{\text{EP}}). \quad (\text{SH.21})$$

Expanding near the exceptional point, we have generically

$$\lambda_{\pm}(\mu) = \lambda_{\text{EP}} \pm \frac{1}{2} \sqrt{\Delta'_{\pi_e}(\mu_{\text{EP}}) \sqrt{\mu - \mu_{\text{EP}}}} + O(\mu - \mu_{\text{EP}}), \quad \Delta'_{\pi_e}(\mu_{\text{EP}}) := \frac{d\Delta_{\pi_e}}{d\mu} \neq 0, \quad (\text{SH.22})$$

Thus, the eigenvalue splitting, i.e., the difference between the two eigenvalues, exhibits the characteristic square-root scaling near the EP,

$$\lambda_+ - \lambda_- \propto \sqrt{\Delta(\mu)} \propto \sqrt{|\mu - \mu_{\text{EP}}|} \propto \sqrt{|\epsilon - \epsilon_{\text{EP}}|}. \quad (\text{SH.23})$$

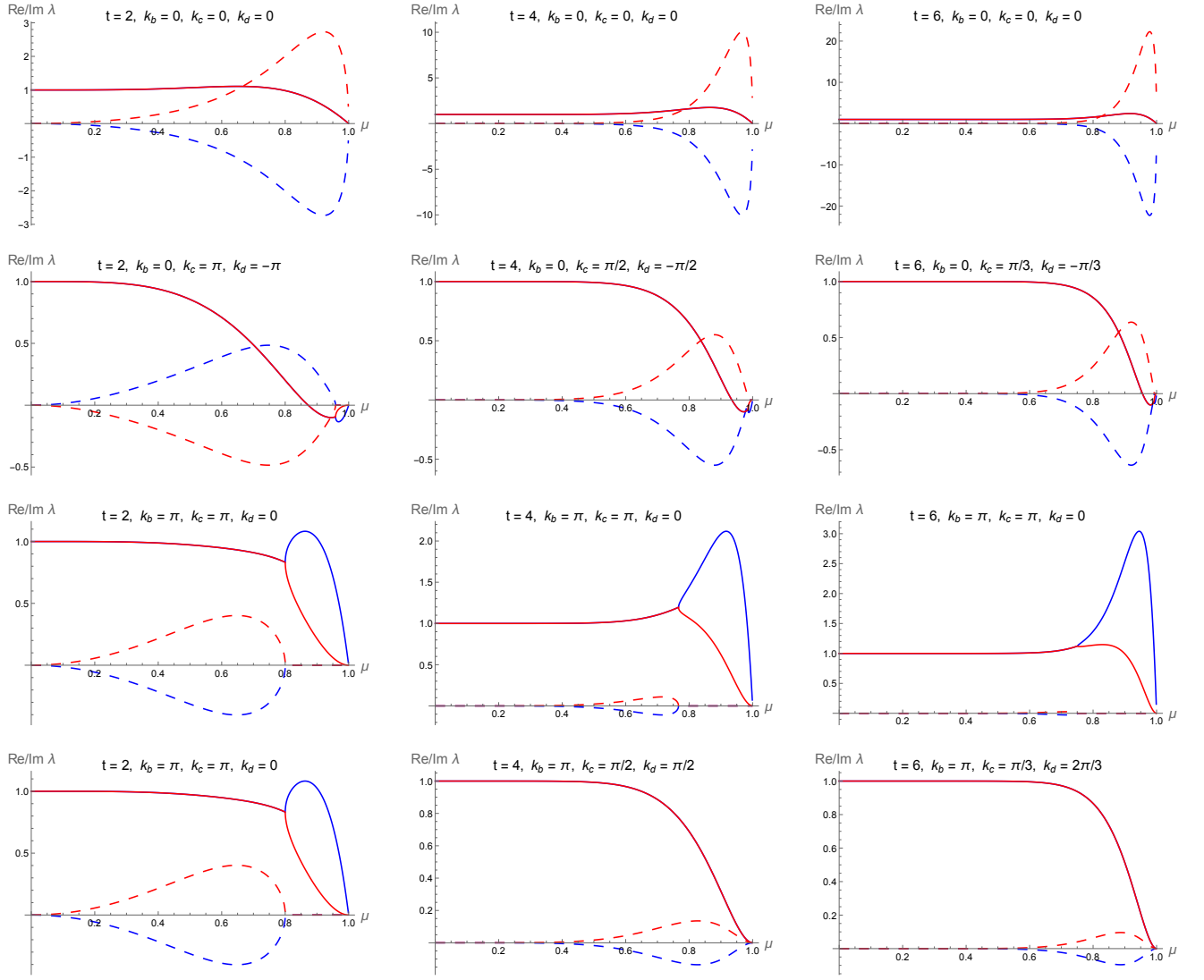


FIG. S14. **Eigenvalues of Boltzmann factor in 4 momentum sectors for  $t = 2, 4, 6$  at large  $q$ .** Complex eigenvalues of the generalized Boltzmann factor of  $(k_b, k_c, k_d) \in \{(0, 0, 0), (0, 2\pi m/t, -2\pi m/t), (\pi, \pi, 0), (\pi, 2\pi m/t, \pi - 2\pi m/t)\}$  with  $m = 1$ .  $\Re\lambda_{\pm}$  are plotted in red and blue solid lines.  $\Im\lambda_{\pm}$  are plotted in red and blue dashed lines. Exceptional points are shown in the sectors  $(\pi, \pi, 0)$  and  $(0, 2\pi m/t, -2\pi m/t)$ . Among these,  $(\pi, \pi, 0)$  sector exhibits a particularly prominent  $\mathcal{PT}$  transitions, for which  $|\lambda_{\pm}|$  exceeds 1 over a finite range of  $\mu$ . Note that the EP of  $(\pi, \pi, 0)$  persists at finite  $\mu$  (equivalently  $\epsilon = -2 \ln \mu$ ), see (SH.14).

Note that this square-root eigenvalue splitting occurs on both sides of the EP. In the unbroken  $\mathcal{PT}$  phase, the two eigenvalues split along the real axis, whereas in the broken  $\mathcal{PT}$  phase they split along the imaginary axis. See Fig. S14 and Fig. S17 for square root eigenvalue at the EP at large  $q$  for various  $t$ .

- **Square root scaling of eigenvector coalescence.** A convenient choice of right and left eigenvectors, satisfying  $\tilde{\mathcal{B}}(\pi, \pi, 0) r_{\pm} = \lambda_{\pm} r_{\pm}$  and  $\tilde{\mathcal{B}}_{\pi, \pi, 0}^{\dagger} \ell_{\pm} = \lambda_{\pm}^* \ell_{\pm}$ , is

$$r_{\pm} := \begin{pmatrix} i\mathcal{B} \\ \lambda_{\pm} - A \end{pmatrix}, \quad \ell_{\pm} := \begin{pmatrix} -i\mathcal{B} \\ \lambda_{\pm}^* - A \end{pmatrix}. \quad (\text{SH.24})$$

- **Eigenvector self-orthogonality.** Define the biorthogonal overlap

$$\mathcal{O}_{\pm} := |\ell_{\pm}^{\dagger} r_{\pm}|. \quad (\text{SH.25})$$

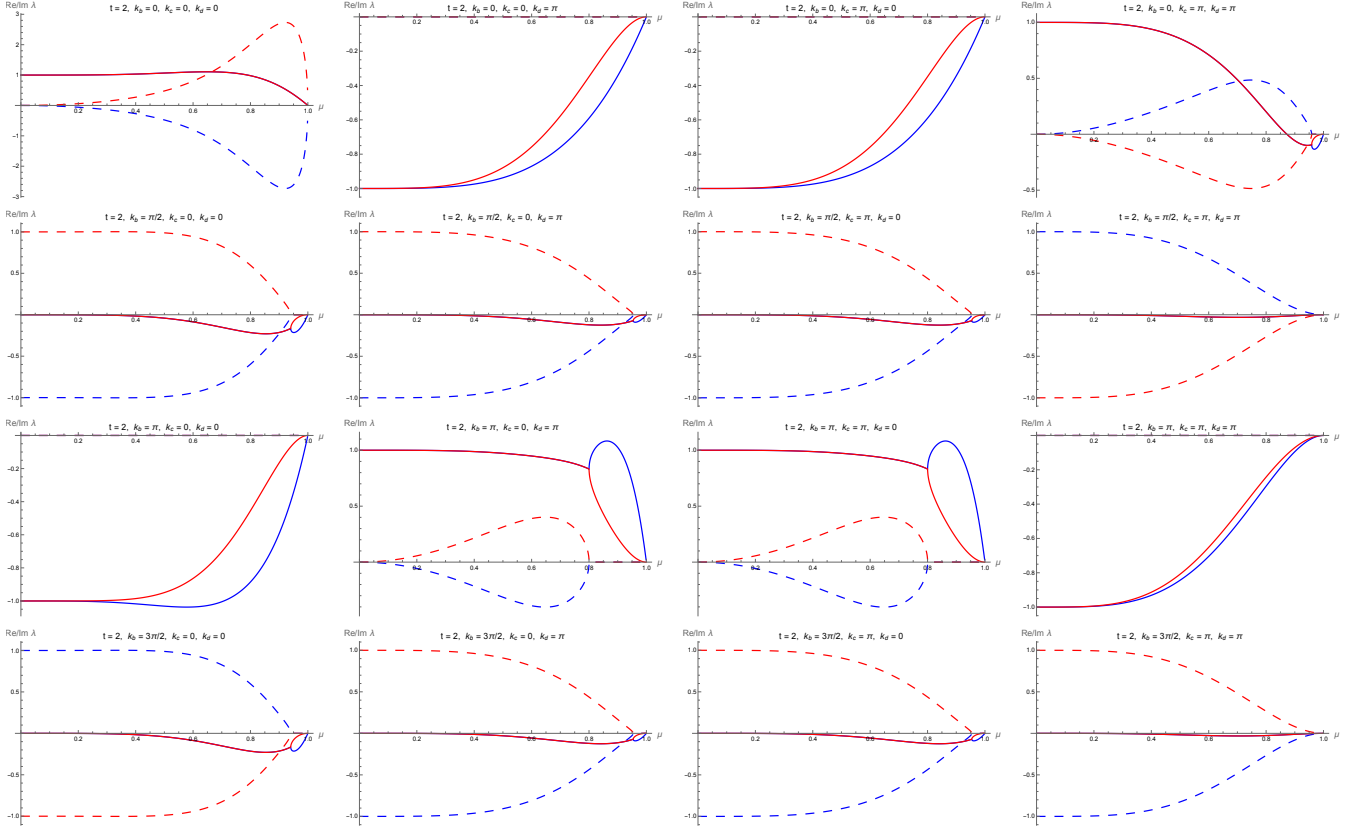


FIG. S15. **Eigenvalues of Boltzmann factor in all momentum sectors for  $t = 2$  at large  $q$ .** Complex eigenvalues of Boltzmann factor of  $(k_b, k_c, k_d) = (2\pi n_b/2t, 2\pi n_c/2t, 2\pi n_d/2t)$  for  $n_b = [1, 2t]$  and  $n_c, n_d \in [1, t]$ .  $\Re\lambda_{\pm}$  are plotted in red and blue solid lines. Note that the spectra are invariant under both the exchange of the two momentum labels  $(k_b, k_c, k_d) \sim (k_b, k_d, k_c)$  (equivalence between second and third columns) and the simultaneous momentum inversion  $(k_b, k_c, k_d) \sim (-k_b, -k_c, -k_d)$  (equivalence between second and fourth rows).  $\Im\lambda_{\pm}$  are plotted in red and blue dashed lines. For  $t = 2$ , real-to-complex spectral bifurcations occur in  $(k_b, k_c, k_d) \in \{(0, \pi, \pi), (\pi/2, 0, 0), (\pi/2, 0, \pi), (\pi/2, \pi, 0), (\pi, 0, \pi), (\pi, \pi, 0), (3\pi/2, 0, 0), (3\pi/2, 0, \pi), (3\pi/2, \pi, 0)\}$ . Note that only sectors satisfying  $k_x + k_y + k_z \equiv 0 \pmod{\pi}$  have  $\mathcal{PT}$  symmetry. Among these, the bifurcation in the  $(\pi, 0, \pi)$  and  $(\pi, \pi, 0)$  sectors are the most prominent, since  $|\lambda_{\pm}|$  can exceed 1, which is also generally the case for  $t > 2$ , see Fig. S14.

Away from the exceptional point, the left and right eigenvectors may be chosen biorthogonal and normalized so that  $\ell_n^\dagger r_m = \delta_{nm}$ . For the explicit choice in Eq. (SH.24), one finds  $\ell_{\pm}^\dagger r_{\pm} = (\lambda_{\pm} - A)^2 - B^2$ . Using  $\lambda_{\pm} - A = \frac{C - A \pm \sqrt{\Delta}}{2}$ , and  $\Delta = (A - C)^2 - 4B^2$ , we obtain

$$\ell_{\pm}^\dagger r_{\pm} = \frac{1}{2} \left[ \Delta \mp (A - C) \sqrt{\Delta} \right]. \quad (\text{SH.26})$$

At an EP2,  $\Delta = 0$ , we have

$$\mathcal{O}_{\pm}(\mu_{\text{EP}}) = 0 \quad \text{at EP}, \quad (\text{SH.27})$$

i.e., the coalesced eigenvector is self-orthogonal at the EP. Expanding around the EP, we write  $\Delta(\mu) = \Delta'(\mu_{\text{EP}})(\mu - \mu_{\text{EP}}) + O((\mu - \mu_{\text{EP}})^2)$  with  $\Delta'(\mu_{\text{EP}}) \neq 0$ . Therefore, around the EP, we have

$$\ell_{\pm}^\dagger r_{\pm} = \mp \frac{A - C}{2} \sqrt{\Delta} \left[ 1 + O(\sqrt{\Delta}) \right]. \quad (\text{SH.28})$$

Provided  $A - C \neq 0$  at  $\mu = \mu_{\text{EP}}$ , which is generically the case, we obtain

$$\mathcal{O}_{\pm}(\mu) = \left| \ell_{\pm}^\dagger r_{\pm} \right| \propto \left| \sqrt{\Delta(\mu)} \right| \propto \sqrt{|\mu - \mu_{\text{EP}}|} \propto \sqrt{|\epsilon - \epsilon_{\text{EP}}|}. \quad (\text{SH.29})$$

i.e., the biorthogonal overlap vanishes with a square root exponent at a generic EP2. See Fig. S18 for the vanishing biorthogonal overlap at the EP in the  $(\pi, \pi, 0)$  sector at large- $q$ .

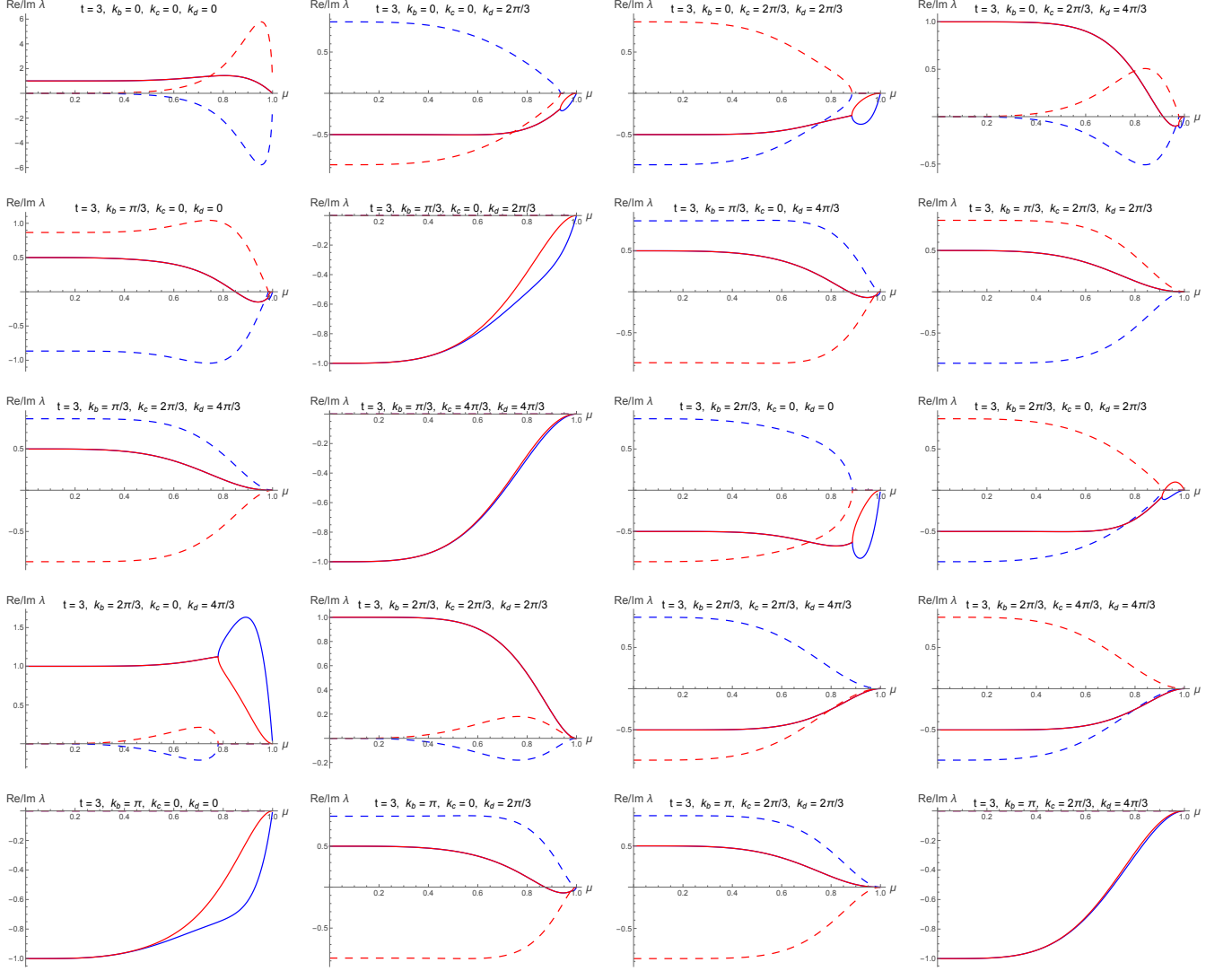


FIG. S16. **Eigenvalues of Boltzmann factor in all momentum sectors for  $t = 3$  at large  $q$ .** Complex eigenvalues of Boltzmann factor of  $(k_b, k_c, k_d) = (2\pi n_b/2t, 2\pi n_c/t, 2\pi n_d/t)$  for  $n_b = [1, 2t]$  and  $n_c, n_d \in [n_c, t]$ .  $\Re\lambda_{\pm}$  are plotted in red and blue solid lines.  $\Im\lambda_{\pm}$  are plotted in red and blue dashed lines. Note that the spectra are invariant under both the exchange of the two momentum labels  $(k_b, k_c, k_d) \sim (k_b, k_d, k_c)$ , and the simultaneous momentum inversion  $(k_b, k_c, k_d) \sim (-k_b, -k_c, -k_d)$ . For  $t = 3$ , there are many  $\mathcal{PT}$  symmetry breaking transitions, notably in the  $(2\pi/3, 0, 4\pi/3)$ ,  $(2\pi/3, 4\pi/3, 0)$ ,  $(4\pi/3, 0, 2\pi/3)$ , and  $(4\pi/3, 2\pi/3, 0)$ , with  $|\lambda_{\pm}|$  exceeding 1.

– **Divergence of the Petermann factor.** A standard measure of eigenvector coalescence in non-Hermitian systems is the Petermann factor

$$\mathcal{P}_{\pm}(\mu) := \frac{\|\ell_{\pm}\|^2 \|r_{\pm}\|^2}{|\ell_{\pm}^{\dagger} r_{\pm}|^2}, \quad (\text{SH.30})$$

where  $r_{\pm}$  and  $\ell_{\pm}$  are respectively the right and left eigenvectors, and  $\|\cdot\|$  denotes the Euclidean norm. This quantity is invariant under independent rescalings of  $r_{\pm}$  and  $\ell_{\pm}$ . At a generic second-order exceptional point, we have  $\Delta(\mu_{\text{EP}}) = 0$  and  $A - C \neq 0$ , and the norms  $\|r_{\pm}\|$  and  $\|\ell_{\pm}\|$  remain finite and non-zero as  $\mu \rightarrow \mu_{\text{EP}}$ . Using (SH.29), we obtain

$$\mathcal{P}_{\pm}(\mu) \propto \frac{1}{|\ell_{\pm}^{\dagger} r_{\pm}|^2} \propto \frac{1}{|\Delta(\mu)|} \propto \frac{1}{|\mu - \mu_{\text{EP}}|} \propto \frac{1}{|\epsilon - \epsilon_{\text{EP}}|}, \quad (\text{SH.31})$$

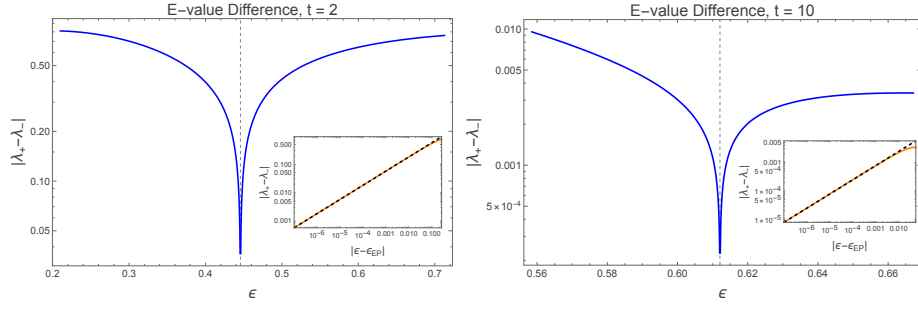


FIG. S17. **Square-root eigenvalue splitting at the EP at large  $q$ .** For the exact large- $q$  Boltzmann factor of TopSFF in the  $(\pi, \pi, 0)$  sector, we plot the eigenvalue splitting  $|\lambda_+ - \lambda_-|$  as a function of the interaction parameter  $\epsilon$  for  $t = 2$  (left) and  $t = 10$  (right). The vertical dashed line marks the exceptional point  $\epsilon_{\text{EP}}(t) = -2 \log \mu_{\text{EP}}(t)$ , with  $\mu_{\text{EP}}(t)$  given in Eq. (SH.14). At this point the two eigenvalues coalesce, so that  $|\lambda_+ - \lambda_-|$  vanishes. The insets show the same data as a function of  $|\epsilon - \epsilon_{\text{EP}}|$  on log-log axes. The dashed black guide highlights the characteristic EP scaling  $|\lambda_+ - \lambda_-| \propto |\epsilon - \epsilon_{\text{EP}}|^{1/2}$  as given in (SH.23).

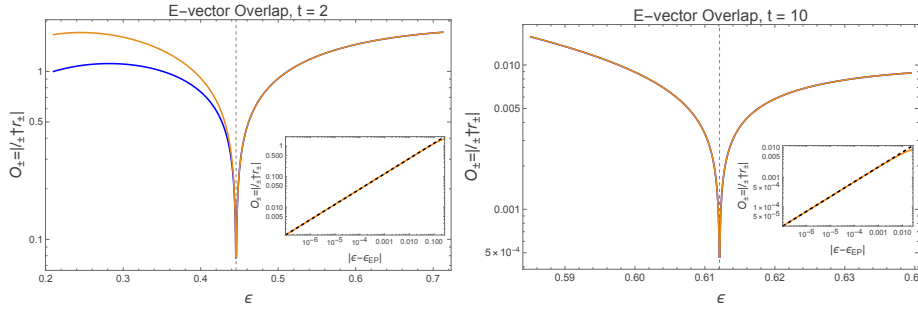


FIG. S18. **Eigenvector self-orthogonality at the EP at large  $q$ .** We plot the left-right eigenvector overlap  $O_{\pm} = |\ell_{\pm}^T r_{\pm}|$  for the two eigenmodes of the exact large- $q$  Boltzmann factor of TopSFF in the  $(\pi, \pi, 0)$  sector, for  $t = 2$  (left) and  $t = 10$  (right). The vertical dashed line marks  $\epsilon_{\text{EP}}(t) = -2 \log \mu_{\text{EP}}(t)$ . The overlap collapses to zero at the exceptional point, showing that the coalescing eigenmode becomes self-orthogonal in the biorthogonal sense. The insets plot the approach to the exceptional point on log-log axes and show the expected scaling  $O_{\pm} \propto |\epsilon - \epsilon_{\text{EP}}|^{1/2}$  as given in (SH.29).

i.e. the Petermann factor diverges with exponent  $-1$  at a generic EP2. See Fig. S19 for the divergent Petermann factor at the EP in the  $(\pi, \pi, 0)$  sector at large  $q$ .

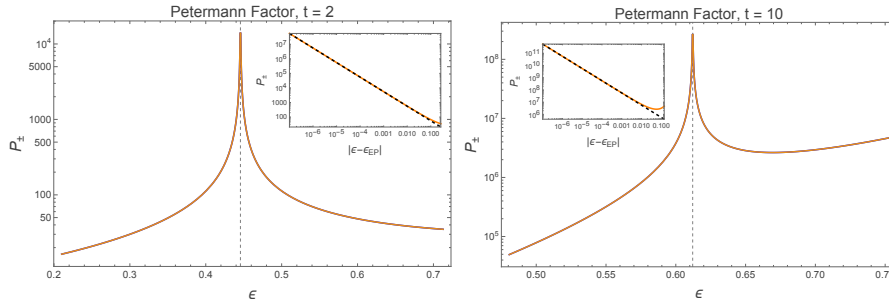


FIG. S19. **Divergent Petermann factor at the EP at large  $q$ .** We plot the Petermann factor  $P_{\pm}$  of the two eigenmodes of the exact large- $q$  Boltzmann factor of TopSFF in the  $(\pi, \pi, 0)$  sector, for  $t = 2$  (left) and  $t = 10$  (right). The vertical dashed line marks  $\epsilon_{\text{EP}}(t) = -2 \log \mu_{\text{EP}}(t)$ . As the exceptional point is approached, the biorthogonal overlap vanishes and the Petermann factor diverges. The insets show the same data against  $|\epsilon - \epsilon_{\text{EP}}|$  on log-log axes, with the dashed black guide indicating the EP divergence as described by  $P_{\pm} \propto |\epsilon - \epsilon_{\text{EP}}|^{-1}$  in (SH.31).

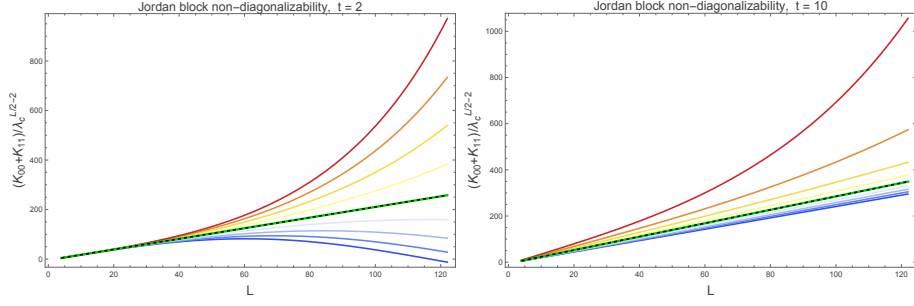


FIG. S20. **Jordan block non-diagonality of TopSFF at the EP at large  $q$ .** We plot the boundary-resolved TopSFF  $(K_{00} + K_{11})/\lambda_c^{L/2-2}$  in the  $(k_b, k_c, k_d) = (\pi, \pi, 0)$  sector as a function of the physical system size  $L$  for  $t = 2$  (left) and  $t = 10$  (right), where  $\lambda_c(\mu) := \text{Tr} \tilde{\mathcal{B}}/2 = (\lambda_+ + \lambda_-)/2$  reduces to the coalesced eigenvalue  $\lambda_{\text{EP}}$  at  $\epsilon = \epsilon_{\text{EP}}$ . The curves correspond to different values of  $\epsilon \in [\epsilon_{\text{EP}} - \delta\epsilon, \epsilon_{\text{EP}} + \delta\epsilon]$ , with  $\delta\epsilon = 10^{-3}$  for  $t = 2$  and  $\delta\epsilon = 0.1$  for  $t = 10$ . The TopSFF at EP (green line) agree with a guideline linear in  $L_e$  and  $L$  (dashed black line), as predicted in Eq. (SF.27). At the EP, the two eigenvalues of the generalized Boltzmann factor coalesce and the matrix becomes non-diagonalizable, producing the Jordan-block scaling  $K_{00} - K_{11} \propto L_{\text{eff}} \lambda^{L_{\text{eff}}-1}$ , resulting in a linear growth with  $L$  after dividing the TopSFF by the exponential envelope. Away from  $\mu_{\text{EP}}$ , the eigenvalues split, the matrix is diagonalizable, and the curves depart from the linear EP form.

### Appendix I: Exact TopSFF with spatially extended defects at finite $q$

In this appendix, we present an exact finite- $q$  evaluation of the TopSFF with a spatially extended swap defect. We first formulate the computation for finite  $q$  and small  $t$  using an ensemble-averaged transfer matrix, and then give a analytic evaluation at  $t = 1$  and finite  $q$ .

#### 1. Exact finite- $q$ symbolic evaluation of TopSFF

We now describe the exact finite- $q$  symbolic computation of the TopSFF,  $K_{\text{top}}(t, L) = \text{Tr}[\hat{\mathcal{D}}(\hat{U} \otimes \hat{U}^*)] = \text{Tr}[\hat{S}\hat{U}] \text{Tr}[\hat{U}^\dagger]$ , with  $[\hat{\mathcal{D}}, (\hat{U} \otimes \hat{U}^*)] = 0$ , where the spatially extended topological defect is  $\hat{\mathcal{D}} = \hat{S} \otimes \mathbb{1}$ . Here  $\hat{S}$  is the global swap operator, which reverses the ordering of the  $L$  qudits according to  $\hat{S} |a_1, a_2, \dots, a_{L-1}, a_L\rangle = |a_L, a_{L-1}, \dots, a_2, a_1\rangle$ , with  $a_i = 1, \dots, q$ . We analyse  $K_{\text{top}}$  in a generic many-body quantum chaotic system satisfying  $[\hat{\mathcal{D}}, \hat{U} \otimes \hat{U}^*] = 0$ , i.e. the system possesses parity inversion symmetry. Such a system is minimally realised by the Random Phase Model (RPM) with parity inversion symmetry and discrete time translation symmetry, defined in App. A 2 a, i.e.,  $\hat{U} = \hat{U}_{\text{f-P-RPM}}$ . The local Hilbert-space dimension is denoted by  $q$ . Instead of generating an ensemble of quantum circuits and computing the averaged TopSFF, this approach computes the generalized Boltzmann factor after the ensemble average over the quantum circuits. In particular, this computation keeps *all* permutations in Eq. (SE.2) at finite  $q$ , as opposed to retaining only the large- $q$  Mickey Mouse diagrams. For a single folded site, the two permutations appearing in the Weingarten contraction are labelled by the pair  $(\sigma, \tau) \in S_{2t} \times S_{2t}$ . The Kronecker deltas generated by Eq. (SE.2) identify the local time indices into closed loops. We denote the resulting set of loops by  $\mathcal{L}(\sigma, \tau)$ , and its cardinality by  $\ell(\sigma, \tau) := |\mathcal{L}(\sigma, \tau)|$ . At finite  $q$ , each loop carries an explicit colour index  $a \in \{1, \dots, q\}$ . The basis state for a single folded site is labelled by  $|\rho\rangle \equiv |\sigma, \tau; \mathbf{a}\rangle$ , with  $(\sigma, \tau) \in S_{2t} \times S_{2t}$ , and  $\mathbf{a} = (a_1, \dots, a_{\ell(\sigma, \tau)}) \in \{1, \dots, q\}^{\mathcal{L}(\sigma, \tau)}$ .

In order to perform the average over the 2-site coupling gate, consider the colour index  $\Theta_\rho(x)$  associated to each endpoint, see dotted lines along  $b$ -,  $c$ - and  $d$ -loops in Fig. S5(e), for a given configuration  $\rho$ . The endpoint label  $x$  runs over  $1, \dots, 4t$ . The first  $2t$  labels are the endpoints associated to  $\text{Tr}[\hat{S}\hat{U}]$ , and the labels  $2t+1, \dots, 4t$  are the endpoints associated to  $\text{Tr}[\hat{U}^\dagger]$ . For a given pair  $(\sigma, \tau)$ , the loop partition  $\mathcal{L}(\sigma, \tau)$  is obtained by following the contractions around the folded site. Let  $R_U$  be the cyclic rotation acting on the  $2t$  endpoints associated to  $\text{Tr}[\hat{S}\hat{U}]$ , and let  $R_{U^\dagger}$  be the cyclic rotation acting separately on the two  $t$ -blocks associated to  $\text{Tr}[\hat{U}^\dagger]$ . Explicitly, for  $m \in \{1, \dots, 2t\}$ ,

$$R_U(m) = \begin{cases} m+1, & 1 \leq m < 2t, \\ 1, & m = 2t, \end{cases}$$

while

$$R_{U^\dagger}(m) = \begin{cases} m+1, & 1 \leq m < t, \\ 1, & m = t, \\ m+1, & t+1 \leq m < 2t, \\ t+1, & m = 2t. \end{cases}$$

Starting from an endpoint  $y \in \{1, \dots, 2t\}$  associated to  $\text{Tr}[\hat{S}\hat{U}]$ , one first reaches the endpoint  $2t + \tau(y)$  associated to  $\text{Tr}[\hat{U}^\dagger]$ , and then returns to an endpoint associated to  $\text{Tr}[\hat{S}\hat{U}]$ . The resulting map on the  $\text{Tr}[\hat{S}\hat{U}]$  endpoints is

$$\Phi_{\sigma,\tau}(y) := R_U^{-1} \sigma^{-1} R_{U^\dagger} \tau(y).$$

The loops are the orbits of  $\Phi_{\sigma,\tau}$ , together with their associated endpoints on  $\text{Tr}[\hat{U}^\dagger]$ . Explicitly, we write

$$L_\alpha = \mathcal{O}_\alpha \cup \{2t + \tau(y) : y \in \mathcal{O}_\alpha\}, \quad \mathcal{O}_\alpha \in \text{Cyc}(\Phi_{\sigma,\tau}),$$

and the set of all loops are given by  $\mathcal{L}(\sigma,\tau) = \{L_1, \dots, L_{\ell(\sigma,\tau)}\}$ . The total number of coloured basis states is

$$N(t, q) = \sum_{\sigma, \tau \in S_{2t}} q^{\ell(\sigma, \tau)} = (2t)! \sum_{\pi \in S_{2t}} q^{C(\pi)} = (2t)! \prod_{r=0}^{2t-1} (q+r),$$

where  $C(\pi)$  denotes the number of cycles of  $\pi$ . For example, one finds, for  $t = 2$ ,  $\{N(2, q)\}_{q=2}^5 = \{2880, 8640, 20160, 40320\}$ , and for  $t = 3$ ,  $\{N(3, q)\}_{q=2}^3 = \{3628800, 14515200\}$ .

The two-site coupling comes from averaging the random diagonal phases in the coupling gates. Define the colour function as  $\Theta_\rho(x) = a_\alpha$  if and only if  $x \in L_\alpha$ . Let  $\rho_1 = (\sigma_1, \tau_1; \mathbf{a}_1)$  and  $\rho_2 = (\sigma_2, \tau_2; \mathbf{a}_2)$  be two adjacent one-site basis states. We write  $\Theta_{\rho_1}(x), \Theta_{\rho_2}(x) \in \{1, \dots, q\}$  for the colours carried by endpoint  $x$  in the loop configurations  $\rho_1$  and  $\rho_2$ , respectively. The endpoints are split into those associated to  $\text{Tr}[\hat{S}\hat{U}]$ ,  $x = 1, \dots, 2t$ , and those associated to  $\text{Tr}[\hat{U}^\dagger]$ ,  $x = 2t + 1, \dots, 4t$ . The phase average depends only on the imbalance of colour pairs between the endpoints associated to  $\text{Tr}[\hat{S}\hat{U}]$  and the endpoints associated to  $\text{Tr}[\hat{U}^\dagger]$ . Then the diagonal phase average gives the factor

$$D_{\rho_1 \rho_2}(\mu) = \mu^{Q(\rho_1, \rho_2)}, \quad Q(\rho_1, \rho_2) := \sum_{r,s=1}^q \left[ \sum_{x=1}^{2t} \delta_{\Theta_{\rho_1}(x), r} \delta_{\Theta_{\rho_2}(x), s} - \sum_{x=2t+1}^{4t} \delta_{\Theta_{\rho_1}(x), r} \delta_{\Theta_{\rho_2}(x), s} \right]^2. \quad (\text{SI.1})$$

From this expression, we see that the interaction does not depend on the absolute values of the loop colours, but only on which loop colours coincide with which other loop colours. We will use this fact to compress the size of  $\mathcal{B}(\rho_1, \rho_2)$  below. Combining the one-site Weingarten function  $\text{Wg}(\sigma^{-1}\tau, q)$  with the two-site phase average gives the exact finite- $q$  generalized Boltzmann factor as an  $N(t, q)$ -dimensional transfer matrix

$$\mathcal{B}(\rho_1, \rho_2) = \sqrt{\text{Wg}(\sigma_1^{-1}\tau_1, q)} D_{\rho_1 \rho_2}(\mu) \sqrt{\text{Wg}(\sigma_2^{-1}\tau_2, q)}. \quad (\text{SI.2})$$

Note that, at finite  $q$ , the generalized Boltzmann factor  $\mathcal{B}$  acts on the full permutation-and-colour basis, and therefore has a much larger matrix dimension than the large- $q$  generalized Boltzmann factor, which is restricted to the leading Mickey Mouse diagrams. The generalized Boltzmann factor can have signs and phases, and as a result, the emergent physics is non-Hermitian. Although each Weingarten weight is increasingly suppressed in the large- $q$  expansion as  $t$  increases, the matrix dimension of the generalized Boltzmann factor  $\mathcal{B}(\rho_1, \rho_2)$  grows rapidly with  $t$ . After summing over the finite- $q$  basis states in the transfer-matrix contraction, the unnormalized TopSFF scales as  $\overline{K_{\text{top}}} = O(q^{-L_e})$ .

The TopSFF in a momentum sector is obtained by contracting powers of the position-space transfer matrix  $\mathcal{B}$  between momentum-resolved boundary states via  $\overline{K_{\text{top}}} = \phi_k^T \mathcal{B}^{L_e} \phi_k$ . We consider a single momentum sector  $k = (k_b, k_c, k_d)$ , where  $k_b = 2\pi n_b / (2t)$ ,  $k_c = 2\pi n_c / t$ , and  $k_d = 2\pi n_d / t$ , with  $n_b = 0, 1, \dots, 2t-1$  and  $n_c, n_d = 0, 1, \dots, t-1$ . Let  $(\sigma_{abcd}, \tau_{abcd})$ , defined in Eq. (SE.7), denote the Mickey Mouse diagrams labelled by  $a = 0, 1$ ,  $b = 1, \dots, 2t$ , and  $c, d = 1, \dots, t$ . We define the phase function

$$\Psi_k(\sigma, \tau) = \begin{cases} \exp[i(bk_b + ck_c + dk_d)], & \text{if } (\sigma, \tau) = (\sigma_{abcd}, \tau_{abcd}), \\ 0, & \text{otherwise.} \end{cases} \quad (\text{SI.3})$$

The corresponding boundary state has components  $\langle \sigma, \tau; \mathbf{a} | \phi_k \rangle = \sqrt{\text{Wg}(\sigma^{-1}\tau, q)} \Psi_k(\sigma, \tau)$ . This boundary state is independent of the explicit loop-colour assignment  $\mathbf{a}$ . The colour degrees of freedom enter only through the bulk transfer matrix  $\mathcal{B}$ , while  $\phi_k$  selects the desired coherent superposition of Mickey Mouse permutation-pair sectors.

Lastly, the colour structure in Eq. (SI.1) allows an exact compression. Since the bulk interaction and the momentum boundary states are invariant under a global relabelling of the  $q$  colours, one may replace explicit colour assignments by their equality patterns. Let  $m = \ell(\sigma, \tau)$ , and write  $\mathcal{L}(\sigma, \tau) = \{L_1, \dots, L_m\}$ . Instead of assigning an explicit colour  $a_\alpha \in \{1, \dots, q\}$  to each loop  $L_\alpha$ , we assign an equality pattern, namely a partition  $\lambda = \{P_1, \dots, P_r\}$  of the loop labels  $\{1, \dots, m\}$ , with  $1 \leq r \leq \min(m, q)$ . Two loops have the same colour if and only if their labels belong to the same block of  $\lambda$ , i.e.  $a_\alpha = a_\beta$  if  $\alpha, \beta \in P_j$  for some  $j$ . For example, for  $m = 3$ , the partition  $\lambda = \{\{1, 2\}, \{3\}\}$  represents all explicit colour assignments with  $a_1 = a_2 \neq a_3$ , such as  $(a_1, a_2, a_3) = (1, 1, 2)$ ,  $(3, 3, 1)$ , or  $(q, q, 1)$ . The compressed one-site basis state is labelled by  $|\rho\rangle_{\text{orb}} = |\sigma, \tau; \lambda\rangle_{\text{orb}}$ . For a partition  $\lambda = \{P_1, \dots, P_r\}$ , define the block-colour function  $\widehat{\Theta}_{\sigma, \tau; \lambda}(x) = j$  if  $x \in L_\alpha$  with  $\alpha \in P_j$ . Choosing a physical colours amounts to choosing  $r$  distinct colours using the map  $\iota : \{1, \dots, r\} \rightarrow \{1, \dots, q\}$  with distinct values  $\iota(j) = c_j$ , and set  $\Theta_{\sigma, \tau; \lambda, \iota}(x) = \iota(\widehat{\Theta}_{\sigma, \tau; \lambda}(x))$ . For a fixed equality pattern with  $r$  colour blocks, the number of explicit colour assignments represented by this orbit is  $w(\lambda) = (q)_r = q(q-1) \cdots (q-r+1)$ . The number of possible equality patterns for  $m$  loops is the restricted Bell number  $B_m^{(q)} = \sum_{r=1}^{\min(m, q)} S(m, r)$ , where  $S(m, r)$  is the Stirling number of the second kind. Hence an  $m$ -loop sector contributes  $B_m^{(q)}$  orbit states rather than  $q^m$  explicit-colour states. The corresponding basis size can be evaluated as

$$N_{\text{orb}}(t, q) = \sum_{\sigma, \tau \in \mathcal{S}_{2t}} B_{\ell(\sigma, \tau)}^{(q)} = (2t)! \sum_{m=1}^{2t} c(2t, m) \sum_{r=1}^{\min(m, q)} S(m, r),$$

where  $c(n, m)$  is the unsigned Stirling number of the first kind. For fixed  $t$ , the orbit-compressed basis size  $N_{\text{orb}}(t, q)$  stops growing once  $q \geq 2t$  and becomes independent of  $q$ , since an  $m$ -loop sector can use at most  $m \leq 2t$  distinct colours. This allows us to compute TopSFF for arbitrary large  $q$  for the case of  $t = 2$ . For example, one finds for  $t = 2$ ,  $\{N_{\text{orb}}(2, q)\}_{q=2}^5 = \{1440, 1728, 1752, 1752\}$ , and for  $t = 3$ ,  $\{N_{\text{orb}}(3, q)\}_{q=2}^5 = \{1814400, 2678400, 2894400, 2916000\}$ . In a normalized orbit basis,  $|\sigma, \tau; \lambda\rangle_{\text{orb}} = w(\lambda)^{-1/2} \sum_{\mathbf{a} \in \text{Orb}(\lambda)} |\sigma, \tau; \mathbf{a}\rangle$ , the matrix element of the compressed transfer matrix is

$$\mathcal{B}_{\text{orb}}(\rho_1, \rho_2) = \frac{1}{\sqrt{w(\lambda_1)w(\lambda_2)}} \sqrt{\text{Wg}(\sigma_1^{-1}\tau_1, q)} \sqrt{\text{Wg}(\sigma_2^{-1}\tau_2, q)} \sum_{\iota_1} \sum_{\iota_2} \mu^{Q(\sigma_1, \tau_1; \lambda_1, \iota_1; \sigma_2, \tau_2; \lambda_2, \iota_2)}, \quad (\text{SI.4})$$

where  $\rho_j = (\sigma_j, \tau_j; \lambda_j)$ , and the sums are over all choices of distinct physical colours for the blocks of  $\lambda_j$ , equivalently over maps  $\iota_j : \{1, \dots, r_j\} \rightarrow \{1, \dots, q\}$  with distinct values. The exponent  $Q$  is the same phase exponent as in Eq. (SI.1), but with  $\Theta_{\rho_j}(x)$  replaced by  $\Theta_{\sigma_j, \tau_j; \lambda_j, \iota_j}(x)$ . In the same normalized orbit basis, the momentum-resolved boundary state becomes

$$\langle \sigma, \tau; \lambda | \phi_k \rangle_{\text{orb}} = \sqrt{w(\lambda)} \sqrt{\text{Wg}(\sigma^{-1}\tau, q)} \Psi_k(\sigma, \tau), \quad (\text{SI.5})$$

such that  $\overline{K_{\text{top}}} = \phi_{\text{orb}, k}^T \mathcal{B}_{\text{orb}}^{L_e} \phi_{\text{orb}, k}$ .

## 2. Exact finite- $q$ analytical evaluation of TopSFF at $t = 1$

For  $t = 1$  at finite- $q$ , we evaluate exactly the TopSFF,  $K_{\text{top}}(t, L) = \text{Tr}[\widehat{\mathcal{D}}(\widehat{U} \otimes \widehat{U}^*)] = \text{Tr}[\widehat{S}\widehat{U}] \text{Tr}[\widehat{U}^\dagger]$ , for the Random Phase Model (RPM) with parity inversion symmetry, defined in App. A 2 a. At  $t = 1$ , imposing time translation symmetry makes no difference, since there is only a single time step. The computation follows the colour-orbit construction above. For  $t = 1$ , the explicit colour basis has size  $N(1, q) = 2q(q+1)$ , while the compressed basis has size  $N_{\text{orb}}(1, q) = 6$  for  $q \geq 2$ . The boundary state further restricts the problem to a three-dimensional invariant subspace. Diagonalizing the corresponding finite- $q$  generalized Boltzmann factor gives

$$\overline{K_{\text{top}}}(t = 1, L_e, \mu, q) = \frac{2(1 - \mu^4 + \rho)}{(q+1)(\mu^4 + 7 - \rho)} \lambda_+^{L_e} + \frac{2(1 - \mu^4)}{(q+1)\rho} \lambda_-^{L_e}, \quad (\text{SI.6})$$

where  $\lambda_\pm(\mu, q) = (1 - \mu^4 \pm \rho)/[2(q+1)]$ ,  $\rho(\mu) = \sqrt{(\mu^4 - 1)(\mu^4 + 7)}$ ,  $\mu = e^{-\epsilon/2} \in [0, 1]$ , and  $L_e = L/2 - 1$  for even  $L$  (the case for odd  $L$  can be analysed easily). For  $0 \leq \mu < 1$ ,  $\rho = i\sqrt{(1 - \mu^4)(\mu^4 + 7)}$ , so  $\lambda_\pm$  form a complex-conjugate pair,

and the  $t = 1$  finite- $q$  Boltzmann factor is in the broken  $\mathcal{PT}$  symmetric regime. Writing  $\lambda_{\pm} = \sqrt{2(1 - \mu^4)} e^{\pm i\theta} / (q+1)$ , with  $\cos \theta = \sqrt{(1 - \mu^4)/8}$  and  $\sin \theta = \sqrt{(\mu^4 + 7)/8}$ , the result becomes

$$\overline{K}_{\text{top}}(t = 1, L_e, \mu, q) = -\frac{4\sqrt{1 - \mu^4}}{\sqrt{\mu^4 + 7}} \left( \sqrt{2(1 - \mu^4)} \right)^{L_e} \sin(L_e \theta) \left( \frac{1}{q+1} \right)^{L_e+1}, \quad (\text{SI.7})$$

which makes the oscillatory dependence on  $L_e$  explicit. Note that  $\overline{K}_{\text{top}}(t = 1, L_e, \mu, q) = O(q^{-L_e-1}) = O(q^{-L/2})$ . The finite- $q$  answer has the same  $\mu$ - and  $L_e$ -dependence as the large- $q$  result. The only difference is the replacement  $q^{-(L_e+1)}$  to  $(q+1)^{-(L_e+1)}$ . Therefore, at  $t = 1$ , finite  $q$  therefore preserves the  $\mathcal{PT}$  symmetric structure and the oscillatory behaviour in  $L$ , but renormalizes the overall large- $q$  factor from  $q^{-L_e-1}$  to  $(q+1)^{-L_e-1}$ . The finite- $q$  TopSFF at  $t = 1$  is plotted as a function of the system size  $L$  in Fig. S21.

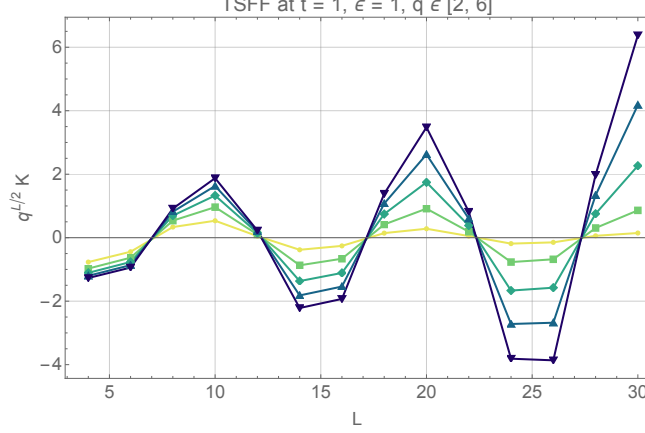


FIG. S21. **Exact TopSFF at  $t = 1$  at finite  $q$ .** TopSFF (SI.7) of the parity symmetric RPM at  $\epsilon = 1$  (with or without discrete time translational symmetry) against system size  $L$  at  $t = 1$  from  $q = 2$  (yellow) to  $q = 6$  (blue).

## Appendix J: TopSFF with spatially extended topological defects without time translational symmetry

In this appendix, we exactly compute the TopSFF with a spatially extended defect for the RPM in the absence of discrete time translation symmetry. We show that the TopSFF still gives rise to an emergent non-Hermitian  $\mathcal{PT}$ -symmetric single-particle problem for a temporal domain wall. However, any  $\mathcal{PT}$  symmetry breaking transitions are pushed towards the boundaries of parameter space, corresponding to zero or infinite interaction strength, as  $t$  increases in the pre-Heisenberg regime. This contrasts with the time-translation symmetric case, where a  $\mathcal{PT}$  transition can occur at finite interaction strength for arbitrary  $t$ .

### 1. Boltzmann factor $\mathcal{B}$ in position space

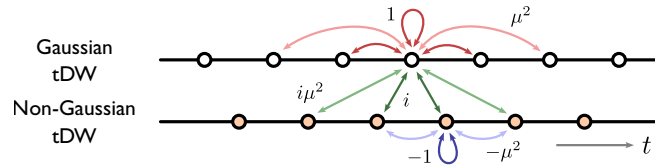


FIG. S22. **Emergent non-Hermitian single-particle model**, as defined in (SJ.6). The single particle residing in the top (bottom) chain corresponds to the Gaussian (non-Gaussian) temporal domain wall. The intra-chain and inter-chain hopping terms are Hermitian and non-Hermitian respectively. We illustrate hopping amplitudes up to  $O(\mu^2)$ .

Here we exactly compute TopSFF for a spatially extended defect for the RPM in the absence of discrete time translational symmetry. As in the case with time translational symmetry, we compute the TopSFF  $K_{\text{top}}(t, L) =$

$\text{Tr}[\hat{\mathcal{D}}(\hat{U} \otimes \hat{U}^*)] = \text{Tr}[\hat{S}\hat{U}] \text{Tr}[\hat{U}^\dagger]$ , where  $\hat{\mathcal{D}} = \hat{S} \otimes \mathbb{1}$  with global swap operator  $\hat{S}$ .  $\hat{U}$  is defined in (SA.4), which commutes with  $\hat{D}$ , but does not have discrete time translational symmetry, i.e., the RPM is temporally random and globally parity-inversion symmetric. Upon ensemble averaging over (SA.4), the TopSFF  $\bar{\mathcal{K}}_{\text{top}}$  can be expressed in terms of a transfer matrix, which describes a single-particle non-Hermitian hopping problem:

$$\begin{aligned} \bar{\mathcal{K}}_{\text{top}} &=: q^{-L_e-1} \bar{\mathcal{K}}_{\text{top}} + O(q^{-L_e-2}), \\ \bar{\mathcal{K}}_{\text{top}} &= \phi^T \mathcal{B}^{L_e} \phi := \sum_{\sigma_1, \sigma_2} \phi(\sigma_1) [\mathcal{B}^{L_e}]_{\sigma_1 \sigma_2} \phi(\sigma_2), \end{aligned} \quad (\text{SJ.1})$$

where  $\mathcal{B}$  and  $\phi$  are respectively the generalized Boltzmann factor encoding the many-body interactions and the boundary state in the folded representation. The effective length is  $L_e = L/2 - 1$  for even  $L$ . For odd  $L$ , TopSFF can be evaluated analogously. The local TopSFF configurations are labelled by  $\sigma = (a, b)$  in the folded representation. Here  $a \in \{0, 1\}$  labels the type of temporal domain wall (tDW): Gaussian tDW with  $a = 0$  consists only of Gaussian contractions, while non-Gaussian tDW with  $a = 1$  involves both Gaussian and non-Gaussian contractions. Further,  $b \in \{1, 2, \dots, 2t\}$  labels the position along the local length- $2t$  loop in  $\text{tr}[\hat{D}\hat{U}]$  in the folded representation. There are in total  $4t$  local TopSFF configurations. Writing  $\sigma_i = (a_i, b_i)$  and  $\Delta b := (b_2 - b_1) \pmod{2t}$ , the generalized Boltzmann factor can be written as

$$\mathcal{B}(\sigma_1, \sigma_2) = [\mathcal{B}_{a_1 a_2}(\Delta b)]_{a_1, a_2=0,1} = \begin{bmatrix} \mathcal{B}_{00} & \mathcal{B}_{01} \\ \mathcal{B}_{10} & \mathcal{B}_{11} \end{bmatrix}, \quad (\text{SJ.2})$$

where the matrix elements are

$$\begin{aligned} \mathcal{B}_{00}(\Delta b) &= \delta_{\Delta b, 0}^{(2t)} + \mu^{4t-4} \delta_{\Delta b, t}^{(2t)} + \sum_{\ell=1}^{t-1} \mu^{4\ell-4} \left( \delta_{\Delta b, \ell}^{(2t)} + \delta_{\Delta b, -\ell}^{(2t)} \right), \\ \mathcal{B}_{11}(\Delta b) &= -\delta_{\Delta b, 0}^{(2t)} - \mu^{4t} \delta_{\Delta b, t}^{(2t)} - \sum_{\ell=1}^{t-1} \mu^{4\ell} \left( \delta_{\Delta b, \ell}^{(2t)} + \delta_{\Delta b, -\ell}^{(2t)} \right), \\ \mathcal{B}_{01}(\Delta b) &= i \sum_{\ell=1}^t \mu^{4\ell-4} \left( \delta_{\Delta b, -\ell}^{(2t)} + \delta_{\Delta b, \ell-1}^{(2t)} \right), \\ \mathcal{B}_{10}(\Delta b) &= i \sum_{\ell=1}^t \mu^{4\ell-4} \left( \delta_{\Delta b, \ell}^{(2t)} + \delta_{\Delta b, 1-\ell}^{(2t)} \right). \end{aligned} \quad (\text{SJ.3})$$

where  $\delta_{x,y}^{(2t)} = 1$  if  $x \equiv y \pmod{2t}$  and 0 otherwise.

It is natural to represent  $\mathcal{B}$  as a single-particle hopping problem of the temporal domain wall in second-quantized form by introducing creation and annihilation operators  $\hat{c}_{A,j}^{(\dagger)}$  and  $\hat{c}_{B,j}^{(\dagger)}$ ,

$$|a=0, b\rangle := \hat{c}_{A,b}^\dagger |0\rangle, \quad |a=1, b\rangle := \hat{c}_{B, b-\frac{1}{2}}^\dagger |0\rangle, \quad (\text{SJ.4})$$

with periodic boundary condition  $b \equiv b + 2t$ . Here  $|0\rangle$  denotes the vacuum state annihilated by all annihilation operators, and  $A$  and  $B$  label the two sublattices. In this basis,

$$H = \sum_{\sigma_1, \sigma_2} \mathcal{B}(\sigma_1, \sigma_2) |\sigma_1\rangle \langle \sigma_2|, \quad \mathcal{B}(\sigma_1, \sigma_2) := \langle \sigma_1 | H | \sigma_2 \rangle. \quad (\text{SJ.5})$$

Note that such a Hamiltonian representation can also be made for Eq. (SE.15) in the presence of discrete time translational symmetry. In terms of creation and annihilation operators, in the absence of time translational symmetry, the Hamiltonian can then be written as

$$\begin{aligned} H &= H_A + H_B + H_{AB}, \\ H_A &= \sum_{j=1}^{2t} \left[ \hat{c}_{A,j}^\dagger \hat{c}_{A,j} + \mu^{4t-4} \hat{c}_{A,j}^\dagger \hat{c}_{A,j+t} + \sum_{\ell=1}^{t-1} \mu^{4\ell-4} \left( \hat{c}_{A,j}^\dagger \hat{c}_{A,j+\ell} + \hat{c}_{A,j}^\dagger \hat{c}_{A,j-\ell} \right) \right], \\ H_B &= - \sum_{j=1/2}^{2t-1/2} \left[ \hat{c}_{B,j}^\dagger \hat{c}_{B,j} + \mu^{4t} \hat{c}_{B,j}^\dagger \hat{c}_{B,j+t} + \sum_{\ell=1}^{t-1} \mu^{4\ell} \left( \hat{c}_{B,j}^\dagger \hat{c}_{B,j+\ell} + \hat{c}_{B,j}^\dagger \hat{c}_{B,j-\ell} \right) \right], \\ H_{AB} &= i \sum_{j=1}^{2t} \sum_{\ell=1}^t \mu^{4\ell-4} \left( \hat{c}_{A,j}^\dagger \hat{c}_{B, j-\ell-\frac{1}{2}} + \hat{c}_{A,j}^\dagger \hat{c}_{B, j+\ell-\frac{3}{2}} + \hat{c}_{B, j-\ell-\frac{1}{2}}^\dagger \hat{c}_{A,j} + \hat{c}_{B, j+\ell-\frac{3}{2}}^\dagger \hat{c}_{A,j} \right). \end{aligned} \quad (\text{SJ.6})$$

Here  $\hat{c}_{A,j}^{(\dagger)}$  with  $j = 1, 2, \dots, 2t$  and  $\hat{c}_{B,j}^{(\dagger)}$  with  $j = 1/2, 3/2, \dots, 2t - 1/2$  act on the two legs of the ladder, with periodic identification  $\hat{c}_{X,2tm+j}^{(\dagger)} = \hat{c}_{X,j}^{(\dagger)}$  for  $X = A, B$ .

## 2. Boltzmann factor $\tilde{\mathcal{B}}$ in momentum space

Utilizing the translational invariance of  $\mathcal{B}$ , we can express the TopSFF in terms of the generalized Boltzmann factor in momentum space as

$$\bar{\mathcal{K}}_{\text{top}} = \phi^T \mathcal{B}^{L_e} \phi = \sum_k \tilde{\phi}(-k)^T \tilde{\mathcal{B}}(k)^{L_e} \tilde{\phi}(k), \quad (\text{SJ.7})$$

where the discrete Fourier transforms of  $\phi$  and  $\mathcal{B}$  are defined as

$$\begin{aligned} \tilde{\phi}(a; k) &:= \frac{1}{\sqrt{2t}} \sum_{b=0}^{2t-1} e^{ikb} \phi(a, b), \\ \tilde{\mathcal{B}}_{a_1 a_2}(k) &:= \sum_{\Delta b=0}^{2t-1} \mathcal{B}_{a_1 a_2}(\Delta b) e^{-ik\Delta b}. \end{aligned} \quad (\text{SJ.8})$$

where  $k = 2\pi n/(2t)$  with  $n = 0, 1, \dots, 2t-1$ . A compatible momentum-space convention for the annihilation operators is

$$\hat{c}_{A,b} = \frac{1}{\sqrt{2t}} \sum_k e^{-ikb} \hat{c}_{A,k}, \quad \hat{c}_{A,k} = \frac{1}{\sqrt{2t}} \sum_{b=1}^{2t} e^{ikb} \hat{c}_{A,b}, \quad (\text{SJ.9})$$

and

$$\hat{c}_{B,b-\frac{1}{2}} = \frac{1}{\sqrt{2t}} \sum_k e^{-ikb} \hat{c}_{B,k}, \quad \hat{c}_{B,k} = \frac{1}{\sqrt{2t}} \sum_{b=1}^{2t} e^{ikb} \hat{c}_{B,b-\frac{1}{2}}. \quad (\text{SJ.10})$$

where  $k = \pi n/t$ ,  $n = 0, 1, \dots, 2t-1$ . With these conventions, the hopping Hamiltonian becomes

$$H = \sum_k \begin{pmatrix} \hat{c}_{A,k}^\dagger & \hat{c}_{B,k}^\dagger \end{pmatrix} \tilde{\mathcal{B}}(k) \begin{pmatrix} \hat{c}_{A,k} \\ \hat{c}_{B,k} \end{pmatrix}, \quad \tilde{\mathcal{B}}(k) = \begin{pmatrix} \tilde{\mathcal{B}}_{00}(k) & \tilde{\mathcal{B}}_{01}(k) \\ \tilde{\mathcal{B}}_{10}(k) & \tilde{\mathcal{B}}_{11}(k) \end{pmatrix}. \quad (\text{SJ.11})$$

Evaluating the Fourier sums gives

$$\tilde{\mathcal{B}}_{00}(k) = 1 + \mu^{4t-4} e^{-itk} + 2 \sum_{\ell=1}^{t-1} \mu^{4\ell-4} \cos(\ell k) =: \mathbf{A}(k), \quad (\text{SJ.12})$$

$$\tilde{\mathcal{B}}_{11}(k) = -\left[ 1 + \mu^{4t} e^{-itk} + 2 \sum_{\ell=1}^{t-1} \mu^{4\ell} \cos(\ell k) \right] =: \mathbf{C}(k), \quad (\text{SJ.13})$$

$$\tilde{\mathcal{B}}_{01}(k) = i \sum_{\ell=1}^t \mu^{4\ell-4} \left( e^{i\ell k} + e^{-i(\ell-1)k} \right) = i e^{ik/2} \mathbf{B}(k), \quad (\text{SJ.14})$$

$$\tilde{\mathcal{B}}_{10}(k) = i \sum_{\ell=1}^t \mu^{4\ell-4} \left( e^{-i\ell k} + e^{i(\ell-1)k} \right) = i e^{-ik/2} \mathbf{B}(k), \quad (\text{SJ.15})$$

where

$$\tilde{\mathcal{B}}(k) = \begin{pmatrix} \mathbf{A}(k) & i e^{ik/2} \mathbf{B}(k) \\ i e^{-ik/2} \mathbf{B}(k) & \mathbf{C}(k) \end{pmatrix}, \quad (\text{SJ.16})$$

and after evaluating the geometric sums,

$$A(k) = \frac{(1 - \mu^4)(1 - \mu^4 + 2 \cos k) - (1 - \mu^8)\mu^{4t-4}e^{-itk}}{1 - 2\mu^4 \cos k + \mu^8}, \quad (\text{SJ.17})$$

$$C(k) = -\frac{(1 - \mu^8)(1 - \mu^{4t}e^{-itk})}{1 - 2\mu^4 \cos k + \mu^8}, \quad (\text{SJ.18})$$

$$B(k) = \frac{2(1 - \mu^4)(1 - \mu^{4t}e^{-itk}) \cos(k/2)}{1 - 2\mu^4 \cos k + \mu^8}. \quad (\text{SJ.19})$$

In this basis, the off-diagonal entries differ by the phase factors  $e^{\pm ik/2}$ . We can remove the off-diagonal phases by a momentum-dependent unitary transformation,

$$\hat{\mathbf{c}}_k := \begin{pmatrix} \hat{c}_{A,k} \\ \hat{c}_{B,k} \end{pmatrix}, \quad \hat{\mathbf{d}}_k := \begin{pmatrix} \hat{d}_{A,k} \\ \hat{d}_{B,k} \end{pmatrix}, \quad \hat{\mathbf{d}}_k = U(k) \hat{\mathbf{c}}_k, \quad U(k) := \begin{pmatrix} 1 & 0 \\ 0 & e^{ik/2} \end{pmatrix}. \quad (\text{SJ.20})$$

In terms of  $\hat{d}$ , the  $B$ -sublattice Fourier transform becomes

$$\hat{c}_{B,b-\frac{1}{2}} = \frac{1}{\sqrt{2t}} \sum_k e^{-ik(b+\frac{1}{2})} \hat{d}_{B,k} = \frac{1}{\sqrt{2t}} \sum_k e^{-ikj} \hat{d}_{B,k}, \quad j := b + \frac{1}{2}. \quad (\text{SJ.21})$$

In terms of the  $\hat{d}$ ,

$$H = \sum_k \begin{pmatrix} \hat{d}_{A,k}^\dagger & \hat{d}_{B,k}^\dagger \end{pmatrix} \tilde{\mathcal{B}}_{\mathcal{PT}}(k) \begin{pmatrix} \hat{d}_{A,k} \\ \hat{d}_{B,k} \end{pmatrix}, \quad \tilde{\mathcal{B}}_{\mathcal{PT}}(k) = U(k) \tilde{\mathcal{B}}(k) U(k)^\dagger = \begin{pmatrix} A(k) & iB(k) \\ iB(k) & C(k) \end{pmatrix}. \quad (\text{SJ.22})$$

Since  $k = \pi n/t$  implies  $e^{-itk} = (-1)^n$ , the coefficients  $A(k)$ ,  $B(k)$ , and  $C(k)$  are real. Therefore  $\tilde{\mathcal{B}}_{\mathcal{PT}}(k)$  is in the  $\mathcal{PT}$  symmetric dimer form; see Sec. G 2.

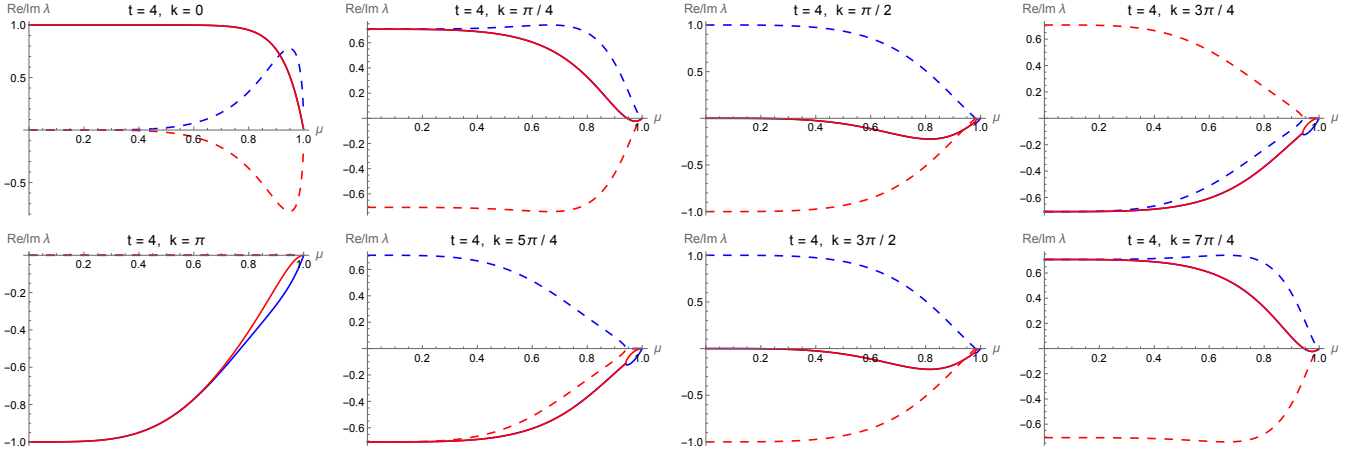


FIG. S23. **Eigenvalues of Boltzmann factor for  $t = 4$  in the absence of time translational symmetry.** Complex eigenvalues of the generalized Boltzmann factor of  $k \in \{0, 1, 2, \dots, 2t - 1\}$ .  $\Re\lambda_{\pm}$  are plotted in red and blue solid lines.  $\Im\lambda_{\pm}$  are plotted in red and blue dashed lines. All sectors are  $\mathcal{PT}$  symmetric. Exceptional points are shown in the sectors  $k = \pi/2, 3\pi/4, 5\pi/4, 3\pi/2$ . Unlike the case with time translational symmetry,  $|\lambda_{\pm}|$  do not exceed 1, see S14.

### 3. Properties of $\tilde{\mathcal{B}}(k)$ and $\mathcal{PT}$ symmetry

Here we describe the properties of the momentum space generalized Boltzmann factor in Eq. (SJ.16) and Eq. (SJ.22):

- **Reality of  $\det \tilde{\mathcal{B}}(k)$  and  $\text{tr} \tilde{\mathcal{B}}(k)$ , and spectral pairing.** Since the allowed momenta are  $k = \pi n/t$  with  $n = 0, 1, \dots, 2t - 1$ , we have  $e^{-itk} = (-1)^n \in \mathbb{R}$ . It follows directly from Eqs. (SJ.16)–(SJ.22) that

$$A(k), B(k), C(k) \in \mathbb{R}, \quad A(-k) = A(k), \quad B(-k) = B(k), \quad C(-k) = C(k). \quad (\text{SJ.23})$$

As a consequence,

$$\text{tr } \tilde{\mathcal{B}}(k) = \mathbf{A}(k) + \mathbf{C}(k) \in \mathbb{R}, \quad \det \tilde{\mathcal{B}}(k) = \mathbf{A}(k)\mathbf{C}(k) + \mathbf{B}(k)^2 \in \mathbb{R}. \quad (\text{SJ.24})$$

Hence the characteristic polynomial has real coefficients, and the eigenvalues are

$$\lambda_{\pm}(k) = \frac{\text{tr } \tilde{\mathcal{B}}(k) \pm \sqrt{\Delta(k)}}{2}, \quad \Delta(k) := [\mathbf{A}(k) - \mathbf{C}(k)]^2 - 4\mathbf{B}(k)^2 \in \mathbb{R}. \quad (\text{SJ.25})$$

- **$\mathcal{PT}$  symmetry and antiunitary symmetry with respect to  $\sigma_z$ .** Take  $\mathcal{P} := \sigma_z$  and  $\mathcal{T}$  to be complex conjugation, then the generalized Boltzmann factor is  $\mathcal{PT}$  symmetric in the sense that

$$\sigma_z \tilde{\mathcal{B}}_{\mathcal{PT}}(k)^* \sigma_z = \tilde{\mathcal{B}}_{\mathcal{PT}}(k), \quad \sigma_z \tilde{\mathcal{B}}(k)^* \sigma_z = \tilde{\mathcal{B}}(-k), \quad (\text{SJ.26})$$

i.e., every momentum sector is  $\mathcal{PT}$  symmetric. As described in more details in Sec. G, the standard  $\mathcal{PT}$  symmetry breaking transition applies here and is controlled by  $\Delta(k)$  as

- if  $\Delta(k) > 0$ , the two eigenvalues are real and distinct.
- if  $\Delta(k) = 0$ , the eigenvalues and eigenvectors coalesce, giving the candidate locus for an exceptional point.
- if  $\Delta(k) < 0$ , the eigenvalues form a complex-conjugate pair.

- **Complex symmetricity.** Let the superscript  $T$  denotes transposition, then the generalized Boltzmann factor satisfies

$$\tilde{\mathcal{B}}_{\mathcal{PT}}(k)^T = \tilde{\mathcal{B}}_{\mathcal{PT}}(k), \quad \tilde{\mathcal{B}}(k)^T = \tilde{\mathcal{B}}(-k). \quad (\text{SJ.27})$$

- **Pseudo-Hermiticity with respect to  $\sigma_z$ .** Combining the  $\mathcal{PT}$  symmetry (or antiunitary symmetry) and complex symmetricity above, the generalized Boltzmann factor has pseudo-Hermiticity condition,

$$\sigma_z \tilde{\mathcal{B}}_{\mathcal{PT}}(k)^\dagger \sigma_z = \tilde{\mathcal{B}}_{\mathcal{PT}}(k), \quad \sigma_z \tilde{\mathcal{B}}(k)^\dagger \sigma_z = \tilde{\mathcal{B}}(k). \quad (\text{SJ.28})$$

Pseudo-Hermiticity is not an independent property once complex symmetricity and  $\mathcal{PT}$  symmetry are established.

#### 4. Boundary states

The TopSFF with a spatially extended topological defect is given in Eq. (SJ.1). Here we describe the boundary states in the folded representation, both in position space and in momentum space. Away from the parity-inversion axes, the bulk of the quantum many-body system is parity-inversion symmetric, since it commutes with the global swap-defect operator. Along the parity-inversion axes, the parity-inversion-symmetric coupling gates of the RPM are chosen according to Eqs. (SA.8) and (SA.9) in Sec. A 2, subject to the constraint  $\text{SWAP } w(t, r) \text{ SWAP} = w(t, r)$ , where SWAP denotes the swap operator acting on the same Hilbert space as  $w(t, r)$ . Coupling gates at different times are drawn independently, so discrete time translational symmetry is absent, i.e.,  $w(t, r) \neq w(t', r)$  for  $t \neq t'$ . After performing the ensemble average over the random phase gates, the boundary state  $\phi$  and its Fourier transform, defined in Eq. (SJ.8), are given by

$$\phi(a, b) = i^{\delta_{a,1}}, \quad \tilde{\phi}(a; k) = i^{\delta_{a,1}} \sqrt{2t} \delta_{n,0}, \quad (\text{SJ.29})$$

where  $k = 2\pi n/(2t)$  with  $n = 0, 1, \dots, 2t - 1$ . Note that the imaginary factors arising from the Weingarten calculus have been absorbed into the boundary state. The boundary state in Eq. (SJ.29) lies entirely in the momentum sector  $k = 0$ . Hence

$$\bar{\mathcal{K}}_{\text{top}} = \tilde{\phi}(0)^T \tilde{\mathcal{B}}(0)^{L_e} \tilde{\phi}(0). \quad (\text{SJ.30})$$

In fact, in the absence of time translational symmetry, turning off the coupling gates along the parity-inversion axes of the RPM gives rise to the same boundary state as in Eq. (SJ.29). The presence of these coupling gates can only be detected by probing higher moments of the TopSFF and likewise of the SFF [31], or in the presence of time translational symmetry, see Sec. E.

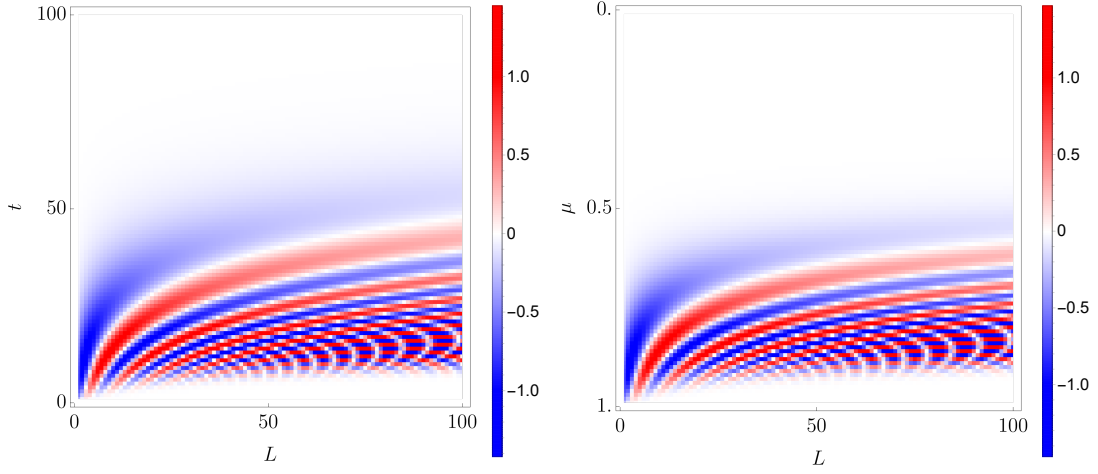


FIG. S24. **TopSFF without time translational symmetry at large  $q$ .**  $\overline{\mathcal{K}}_{\text{top}}$  in the  $t$ - $L$  plane at  $\mu = 0.85$  (left) and in the  $\mu$ - $L$  plane at  $t = 15$  (right).

### 5. Exact expression of TopSFF without time translational symmetry

Since the boundary state has support only at  $k = 0$ , using the Cayley-Hamilton form in Eq. (SF.8), we obtain the TopSFF as

$$\overline{\mathcal{K}}_{\text{top}} = \tilde{\phi}(0)^T \tilde{\mathcal{B}}(0)^{L_e} \tilde{\phi}(0) = 2t \varphi^T \tilde{\mathcal{B}}(0)^{L_e} \varphi = 2t g(0) u_{L_e}(0), \quad (\text{SJ.31})$$

where  $\varphi = (1, i)^T$ , and  $u_{L_e}(k)$  and  $g(k)$  are defined in Eq. (SF.8). For  $k = 0$ , one finds

$$\begin{aligned} g(0) &= \text{A}(0) - \text{C}(0) - 2\text{B}(0) = -\mu^{4t-4}(1 - \mu^4), \\ \text{tr } \tilde{\mathcal{B}}(0) &= 2 - (1 + \mu^4)\mu^{4t-4}, \\ \det \tilde{\mathcal{B}}(0) &= (1 - \mu^{4t})(1 + \mu^{4t-4}), \\ \Delta(0) &:= \text{tr } \tilde{\mathcal{B}}(0)^2 - 4 \det \tilde{\mathcal{B}}(0) = \mu^{4t-8} \left[ \mu^{4t}(1 + 6\mu^4 + \mu^8) - 8\mu^4 \right] \leq 0, \\ \lambda_{\pm}(0) &= \frac{\text{tr } \tilde{\mathcal{B}}(0) \pm \sqrt{\Delta(0)}}{2} = 1 - \frac{(1 + \mu^4)\mu^{4t-4}}{2} \pm \frac{1}{2} \sqrt{\Delta(0)} \end{aligned} \quad (\text{SJ.32})$$

Observe that for  $k = 0$  sector,  $\Delta(0) < 0$  for  $\mu \in (0, 1)$ , i.e., there is not an exceptional point for  $\mu \in (0, 1)$ , and the generalized Boltzmann factor is in the  $\mathcal{PT}$  broken phase with  $\lambda_{\pm}$  forming complex conjugate pairs. Therefore, the TopSFF with spatially extended topological defects in the absence of time translational symmetry can be evaluated as

$$\begin{aligned} \overline{\mathcal{K}}_{\text{top}} &= -2t\mu^{4t-4}(1 - \mu^4) \frac{\lambda_+^{L_e} - \lambda_-^{L_e}}{\sqrt{\Delta}} = -\frac{4t\mu^{4t-4}(1 - \mu^4)}{\sqrt{-\Delta}} |\lambda|^{L_e} \sin(L_e \arg \lambda), \\ \lambda &\equiv \lambda_+ = \lambda_-^* = 1 - \frac{1}{2}(1 + \mu^4)\mu^{4t-4} + \frac{1}{2}\sqrt{\Delta}, \\ \Delta &= \mu^{4t-8} \left[ \mu^{4t}(1 + 6\mu^4 + \mu^8) - 8\mu^4 \right] \leq 0. \end{aligned} \quad (\text{SJ.33})$$

where  $L_e = L/2 - 1$  for even  $L$ , and  $L_e = (L - 1)/2 - 1$  for odd  $L$ .  $\mu = e^{-\epsilon/2}$  with  $\epsilon \in [0, \infty)$  is the RPM parameter that sets the coupling strength, with larger  $\epsilon$  corresponds to stronger coupling. Typical behaviour of TopSFF are plotted Fig. S24.

## 6. Consistency check with finite- $q$ result at $t = 1$

As a consistency check, at  $t = 1$ ,  $\overline{\mathcal{K}_{\text{top}}}$  with spatially extended topological defects reduces to

$$\overline{\mathcal{K}_{\text{top}}} = -\frac{4\sqrt{1-\mu^4}}{\sqrt{\mu^4+7}} \left( \sqrt{2(1-\mu^4)} \right)^{L_e} \sin(L_e \theta), \quad (\text{SJ.34})$$

where the angle  $\theta$  is defined such that  $\cos \theta = \sqrt{(1-\mu^4)/8}$  or  $\sin \theta = \sqrt{(\mu^4+7)/8}$ . Eq. (SJ.34) coincides with (i) the large- $q$  expansion of the exact finite- $q$  result of the TopSFF in Eq. (SI.6) at  $t = 1$ , and with (ii) the exact large- $q$  calculation of the TopSFF in Eq. (SF.42) for the Floquet parity symmetric RPM at  $t = 1$ .

## Appendix K: Temporally extended topological defects

In this appendix, we analyse TopSFF with temporally extended topological defects inserted in the spatial evolution. We consider two representative defects: a global swap defect in time reversal symmetric dynamics, and a time translation defect in Floquet dynamics. In both cases, we derive exact large- $q$  expressions and the associated Thouless scaling forms for the topological free energy cost.

### 1. Temporally extended global swap defects

Here we consider the TopSFF of a temporally extended global swap defect  $\hat{\mathcal{D}} = \hat{S} \otimes \hat{\mathbb{1}}$  acting on  $U_s \otimes U_s$  in the spatial direction. The one-dimensional generic quantum many-body chaotic circuit  $\hat{U}_s(t, L) := \prod_{i=1}^L \hat{V}(t, L)$  is realized generated by the space-time dual transfer matrices  $\hat{V}(t, L)$  [Fig. 3(a) purple] of RPM defined in (SA.20), satisfying the  $[\hat{V}(t, L), \hat{S}] = 0$ , and therefore has time reversal symmetry (TRS). We will also use the RHM with TRS, defined in Eq. (SA.27), to verify the universal scaling form derived below from the RPM.

Using the methods described in App. E and Ref. [44], the TopSFF with temporally extended defects in the TRS RPM can be evaluated exactly in the large- $q$  limit as  $\overline{K_{\text{top}}} = \text{Tr}[\mathcal{B}^L \sigma_x]$ , where  $\alpha(t) = t - 1 - \delta_{0,t \bmod 2}$  and  $[\mathcal{B}]_{mn} = 1 + (1 - \delta_{mn})(e^{-\epsilon\alpha(t)} - 1)$  is the transfer matrix, or equivalently the Boltzmann factor, of an effective Ising model.  $\sigma_x$  is the Pauli- $x$  matrix, which emerges because the global swap operator exchange the role of the ladder mode and the twisted mode described in [44]. Thus, upon ensemble averaging, the temporally extended global swap topological defect becomes a spin-flip defect in the effective Ising description. Diagonalizing  $\mathcal{B}$  gives an exact expression for TopSFF with temporally extended defects in the large- $q$  limit as

$$\overline{K_{\text{top}}} = [1 + e^{-\epsilon\alpha(t)}]^L - [1 - e^{-\epsilon\alpha(t)}]^L. \quad (\text{SK.1})$$

In the Thouless double scaling limit [26], where  $\ell \equiv L/L_{\text{Th}}$  is held fixed with  $L_{\text{Th}} = e^{\epsilon\alpha(t)}$ , the TopSFF obeys

$$\kappa_{\text{top}} := \lim_{\substack{L, t \rightarrow \infty \\ \ell = L/L_{\text{Th}}}} \overline{K_{\text{top}}} = 2 \sinh \ell. \quad (\text{SK.2})$$

In the absence of topological defects, the large- $q$  SFF of the TRS RPM is  $\lim_{q \rightarrow \infty} \overline{K} = [1 + e^{-\epsilon\alpha(t)}]^L + [1 - e^{-\epsilon\alpha(t)}]^L$ , see App. C and [44]. In the same Thouless scaling limit, the corresponding SFF scaling form is  $\kappa := \lim_{t, L \rightarrow \infty} \overline{K} = 2 \cosh \ell$ . Interpreting the TopSFF and SFF as partition functions, with  $t$  playing the role of an inverse temperature, we define the topological free energy difference as

$$\Delta F_{\text{top}} := -\frac{1}{t} \ln \frac{\overline{K_{\text{top}}}}{\overline{K}} = -\frac{1}{t} \ln \left[ \tanh \left( L \operatorname{atanh} e^{-\epsilon\alpha(t)} \right) \right], \quad (\text{SK.3})$$

where the second equality is evaluated at the large- $q$  limit.

$\Delta F_{\text{top}}$  has the bounds  $0 \leq \Delta F_{\text{top}} \leq \epsilon$  where  $\epsilon$  is the spatial domain wall (sDW) effective tension and also controls the coupling strength of the quantum many-body system.  $\Delta F_{\text{top}}$  is monotonically increasing in  $t$  and decreasing in  $L$ , i.e.,  $\partial_t \Delta F_{\text{top}} \geq 0$ , and  $\partial_L \Delta F_{\text{top}} \leq 0$ . At late time and fixed system size, we have  $\Delta F_{\text{top}} = \epsilon - \frac{\ln L}{t}$ . On the other hand, in the thermodynamic limit with large system size  $L$  at fixed time  $t$ , we have  $\Delta F_{\text{top}} = \frac{2}{t} e^{-2L \operatorname{atanh} e^{-\epsilon\alpha(t)}}$ , and the spatial correlation length can be extracted as  $\xi = \frac{1}{2 \operatorname{atanh} e^{-\epsilon\alpha(t)}} \rightarrow \frac{1}{2e^{-\epsilon\alpha(t)}} \propto L_{\text{Th}}$ . Together, we have

$\lim_{L \rightarrow \infty} \lim_{t \rightarrow \infty} \Delta F_{\text{top}} = \epsilon$  and  $\lim_{t \rightarrow \infty} \lim_{L \rightarrow \infty} \Delta F_{\text{top}} = 0$ , i.e., the late-time and thermodynamic limits do not commute.

We begin with the first Thouless scaling limit, where  $t, L \rightarrow \infty$  with the Thouless ratio  $\ell \equiv L/L_{\text{Th}} = Le^{-\epsilon\alpha(t)}$  held fixed. In this limit, we have the free energy scaling form

$$\mathcal{F}_{\text{top},1} \equiv \lim_{\substack{L, t \rightarrow \infty \\ \ell \equiv L/L_{\text{Th}}}} t\Delta F_{\text{top}} = -\ln \tanh \ell. \quad (\text{SK.4})$$

In Fig. S25 left panel, we provide a finite- $t$  check of the corresponding Thouless scaling limit, where the finite- $t$  curves at fixed  $\mu = 0.67$  collapse onto this universal scaling function as  $t$  is increased. The inset shows the unscaled  $\Delta F_{\text{top}}$  as a function of  $L$ . This demonstrates that the temporally extended global swap defect measures the free-energy cost of a spatial domain wall, which becomes universal in the Thouless scaling limit.

We take the second Thouless scaling limit to be where  $t$  and  $L$  are sent to infinity, while  $\tau \equiv t/t_{\text{Th}} = \epsilon t/\ln L$  is fixed, we can write  $\Delta F_{\text{top}} = -\frac{1}{t} \ln L^{1-\tau}$  and

$$\mathcal{F}_{\text{top},2} \equiv \lim_{\substack{L, t \rightarrow \infty \\ \tau \equiv t/t_{\text{Th}}}} \Delta F_{\text{top}} = \begin{cases} 0 & \tau \leq 1, \\ \epsilon \left(1 - \frac{1}{\tau}\right) & \tau > 1, \end{cases} \quad (\text{SK.5})$$

i.e., in the Thouless scaling limit, the universal scaling form has a sharp crossover at  $\tau = 1$ , i.e. at  $t = t_{\text{Th}}$ . In Fig. S25 right panel, we test this second Thouless scaling limit at fixed  $\mu = 0.67$ , using finite- $L$  data while varying  $t$ . As  $L$  is increased, the curves collapse onto the universal scaling form  $\mathcal{F}_{\text{top},2}$ , with a rounded finite-size crossover sharpening near  $\tau = 1$ . The inset shows the corresponding unscaled  $\Delta F_{\text{top}}$  as a function of  $t$ , illustrating the crossover from the thermodynamic-limit regime, where  $\Delta F_{\text{top}} \simeq 0$ , to the late-time regime, where the topological free energy cost becomes finite.

As apparent in Fig. S25, the convergence to the second Thouless scaling form is slower than that of the first because the two limits have parametrically different finite-size corrections. In the first Thouless limit, fixing  $\ell = Le^{-\epsilon t}$  gives  $L \operatorname{atanh} e^{-\epsilon t} = L(e^{-\epsilon t} + e^{-3\epsilon t}/3 + \dots)$ , so the free energy difference differ from its scaling form only by power-law corrections,

$$t\Delta F_{\text{top}} = \mathcal{F}_{\text{top},1}(\ell) + O(L^{-2}). \quad (\text{SK.6})$$

at large finite system size  $L$ .

In contrast, in the second Thouless scaling limit, fixing  $\tau = t/t_{\text{Th}} = \epsilon t/\ln L$  gives  $e^{-\epsilon t} = L^{-\tau}$ , and hence  $Le^{-\epsilon t} = L^{1-\tau}$ . The sharp crossover at  $\tau = 1$  is therefore rounded over the regime  $|\tau - 1|\ln L = O(1)$ . Correspondingly, the approach to the limiting scaling form is only logarithmic,

$$\Delta F_{\text{top}} = \mathcal{F}_{\text{top},2}(\tau) + O\left(\frac{1}{\ln L}\right), \quad (\text{SK.7})$$

at fixed  $\tau = t/t_{\text{Th}} = \epsilon t/\ln L$ . Equivalently, the finite-size rounding of the crossover has width  $\delta\tau \sim 1/\ln L$ . Thus the second scaling form suffers from logarithmically slow convergence with  $L$ .

#### a. TRS and time translation symmetry

The TopSFF with temporally extended global swap defects for TRS RPM with additional discrete time translational symmetry can be exactly evaluated in the large- $q$  limit as

$$\overline{K}_{\text{top}} = \begin{cases} \left[ \begin{array}{l} [1 + te^{-\epsilon(t-1)} + (t-1)e^{-\epsilon t}]^L \\ - [1 - te^{-\epsilon(t-1)} + (t-1)e^{-\epsilon t}]^L \end{array} \right], & t \text{ odd} \\ \left[ \begin{array}{l} [1 + \frac{1}{2}te^{-\epsilon(t-2)} + (\frac{3t}{2} - 1)e^{-\epsilon t}]^L \\ - [1 + \frac{1}{2}te^{-\epsilon(t-2)} - (\frac{t}{2} + 1)e^{-\epsilon t}]^L \end{array} \right], & t \text{ even.} \end{cases} \quad (\text{SK.8})$$

From this expression, one can straightforwardly generalize the above procedure to derive similar universal scaling form for  $\overline{K}_{\text{top}}$  as in the previous section and [44].

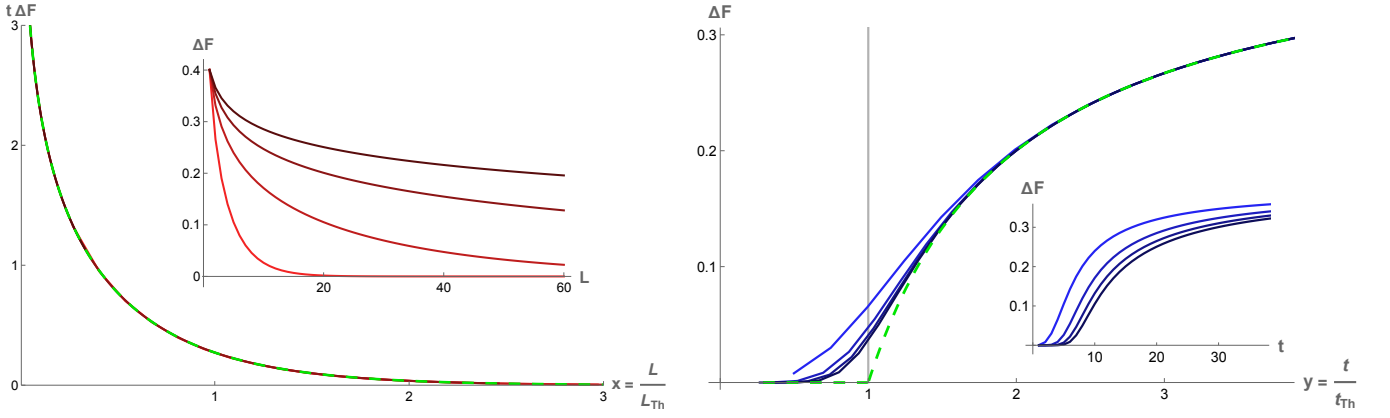


FIG. S25. **Scaling collapse of free energy differences for temporally extended global swap defects.** Left:  $\mathcal{F}_{\text{top},1}$  plotted as a function of  $\ell \equiv L/L_{\text{Th}}$  at fixed  $\mu = 0.67$ , using finite- $t$  data with  $t \in \{5, 10, 15, 20\}$  and varying  $L$ . Darker red curves denote larger  $t$ . The inset shows the corresponding unscaled free-energy difference  $\Delta F_{\text{top}}$  as a function of  $L$ . Right:  $\mathcal{F}_{\text{top},2}$  plotted as a function of  $y = t/t_{\text{Th}}$  at fixed  $\mu = 0.67$ , using finite- $L$  data with  $L \in \{5, 10, 15, 20\}$  and varying  $t$ . Darker blue curves denote larger  $L$ . The inset shows  $\Delta F_{\text{top}}$  as a function of  $t$ .

## 2. Temporally extended time translation defects.

Now we consider the TopSFF of a temporally extended time translation defect  $\hat{D} = \hat{T} \otimes \hat{1}$  acting on  $U_s \otimes U_s$  in the spatial direction. Here  $T$  is the time translational operator defined by  $T|a_1, a_2, \dots, a_t\rangle = |a_t, a_1, \dots, a_{t-1}\rangle$ , which cyclically shifts the time indices. The one-dimensional generic quantum many-body chaotic circuit  $\hat{U}_s(t, L) := \prod_{i=1}^L \hat{V}(t, L)$  is realized generated by the space-time dual transfer matrices  $\hat{V}(t, L)$  [Fig. 3(a) purple] of RPM defined in (SA.30), satisfying the  $[\hat{V}(t, L), \hat{T}] = 0$ , and therefore has discrete time translational symmetry. We will also use the RHM with TRS, defined in Eq. (SA.34), to verify the universal scaling form derived below from the RPM.

The TopSFF with the discrete time translational operator as topological defects for the Floquet RPM can be evaluated exactly in the large- $q$  limit as

$$\overline{K}_{\text{top}} = [1 + (t-1)e^{-\epsilon t}]^L - (1 - e^{-\epsilon t})^L, \quad (\text{SK.9})$$

Taking the Thouless scaling limit [26] where  $\ell \equiv L/L_{\text{Th}}$  is fixed with  $L_{\text{Th}} = e^{\epsilon t}/t$ , the TopSFF scaling form gives

$$\kappa_{\text{top}} := \lim_{\substack{L, t \rightarrow \infty \\ \ell \equiv L/L_{\text{Th}}}} [\overline{K}_{\text{top}} + 1] = e^{\ell}. \quad (\text{SK.10})$$

In the absence of topological defect, the SFF can be evaluated in the large- $q$  limit as  $\overline{K} = [1 + (t-1)e^{-\epsilon t}]^L + (t-1)(1 - e^{-\epsilon t})^L$  [13]. In the Thouless scaling limit, the corresponding SFF scaling form is  $\kappa := \lim_{t, L \rightarrow \infty} \overline{K} - t + 1 = e^{\ell} - \ell$ .

Interpreting the TopSFF and SFF as partition functions, with  $t$  playing the role of an inverse temperature, we define the topological free energy difference as

$$\Delta F_{\text{top}} := -\frac{1}{t} \ln \frac{\overline{K}_{\text{top}}}{\overline{K}} = -\frac{1}{t} \ln \frac{1 - \omega^L}{1 + (t-1)\omega^L}, \quad (\text{SK.11})$$

where  $\omega = (1 - e^{-\epsilon t})/[1 + (t-1)e^{-\epsilon t}]$ , and the second equality is evaluated at the large- $q$  limit.

Similar to the global TRS case,  $\Delta F_{\text{top}}$  has the bounds  $0 \leq \Delta F_{\text{top}} \leq \epsilon$  where  $\epsilon$  is the spatial domain wall (sDW) effective tension and also controls the coupling strength of the quantum many-body system.  $\Delta F_{\text{top}}$  is monotonically increasing in  $t$  and decreasing in  $L$ , i.e.,  $\partial_t \Delta F_{\text{top}} \geq 0$ , and  $\partial_L \Delta F_{\text{top}} \leq 0$ . The upper bound is obtained by expanding at small  $e^{-\epsilon t}$ . At late time and at fixed system size  $L$ , we have  $\Delta F_{\text{top}} = \epsilon - \frac{\ln L}{t}$ . On the other hand, in the thermodynamic limit with large system size  $L$  at fixed time  $t$ , we have  $\Delta F_{\text{top}} = e^{-L/\xi}$ , where the spatial correlation length is  $\xi = \left[ \ln \frac{1+(t-1)e^{-\epsilon t}}{1-e^{-\epsilon t}} \right]^{-1} \rightarrow 1/te^{-\epsilon t} \propto L_{\text{Th}}$ . Together, we have  $\lim_{L \rightarrow \infty} \lim_{t \rightarrow \infty} \Delta F_{\text{top}} = \epsilon$  and  $\lim_{t \rightarrow \infty} \lim_{L \rightarrow \infty} \Delta F_{\text{top}} = 0$ , i.e., the late-time and thermodynamic limits do not commute.

We now take the corresponding first Thouless scaling limit for the time translation topological defect. In the scaling limit  $L, t \rightarrow \infty$  with  $\ell := L/L_{\text{Th}} = Lte^{-\epsilon t}$  fixed, we have  $e^{-\epsilon t} \rightarrow 0$ . Thus  $\ln \omega = \ln(1 - e^{-\epsilon t}) - \ln[1 + (t-1)e^{-\epsilon t}] =$

$-te^{-\epsilon t} + O(t^2 e^{-2\epsilon t})$ , so  $L \ln \omega = -\ell + O(\ell^2/L)$ , and hence  $\omega^L \rightarrow e^{-\ell}$ . The free energy therefore becomes  $t\Delta F_{\text{top}} = -\ln \left[ \frac{1-e^{-\ell}}{1+(t-1)e^{-\ell}} \right] = \ln t - \ln(e^\ell - 1) + o(1)$ . The free energy therefore becomes, keeping the leading finite- $t$  dependence,

$$t\Delta F_{\text{top}} - \ln t = -\ln \left[ \frac{t(1-e^{-\ell})}{1+(t-1)e^{-\ell}} \right]. \quad (\text{SK.12})$$

Therefore, in the large- $q$  limit, the universal scaling form of TopSFF with a temporally extended time translation defect in the Thouless scaling limit is

$$\mathcal{F}_{\text{top},1}^{\text{floq}} \equiv \lim_{\substack{L,t \rightarrow \infty \\ \ell \equiv Lte^{-\epsilon t}}} [t\Delta F_{\text{top}} - \ln t] = -\ln(e^\ell - 1). \quad (\text{SK.13})$$

This convergence uses  $1 + (t-1)e^{-\ell} \simeq te^{-\ell}$ , and therefore requires  $(t-1)e^{-\ell} \gg 1$  or  $\ell \ll \ln t$ . Thus, at finite  $t$ , the asymptotic scaling form is valid only before the crossover at  $\ell \sim \ln t$ .

We consider next the second Thouless scaling limit in which  $\tau := t/t_{\text{Th}} = \epsilon t / \ln L$  is kept fixed as  $L, t \rightarrow \infty$ . Since  $e^{-\epsilon t} = L^{-\tau}$ , we have  $\ln \omega = \ln(1 - e^{-\epsilon t}) - \ln[1 + (t-1)e^{-\epsilon t}] \simeq -te^{-\epsilon t}$ , and therefore  $\omega^L \simeq \exp[-tL^{1-\tau}]$ . For  $\tau \leq 1$ , we have  $\omega^L \rightarrow 0$  and hence  $\Delta F_{\text{top}} \rightarrow 0$ . For  $\tau > 1$ , we have  $1 - \omega^L \simeq tL^{1-\tau}$ , while  $1 + (t-1)\omega^L \simeq t$ . Therefore,

$$\Delta F_{\text{top}} \simeq -\frac{1}{t} \ln L^{1-\tau} = \frac{(\tau-1) \ln L}{t} = \epsilon \left(1 - \frac{1}{\tau}\right). \quad (\text{SK.14})$$

Hence, in the large- $q$  limit, the second Thouless scaling form of TopSFF with temporally extended time translation defect is

$$\mathcal{F}_{\text{top},2} \equiv \lim_{\substack{L,t \rightarrow \infty \\ \tau \equiv t/t_{\text{Th}}}} \Delta F_{\text{top}} = \begin{cases} 0, & \tau \leq 1, \\ \epsilon \left(1 - \frac{1}{\tau}\right), & \tau > 1, \end{cases} \quad (\text{SK.15})$$

which has the same functional form as in Eq. (SK.5).

## Appendix L: Finite- $q$ numerical simulations

### 1. Spatially extended topological defects

We numerically simulate the finite- $q$  TopSFF with a spatially extended topological defect,  $K_{\text{top}}(t, L) = \text{Tr}[\hat{\mathcal{D}}(\hat{U} \otimes \hat{U}^*)] = \text{Tr}[\hat{S}\hat{U}] \text{Tr}[\hat{U}^\dagger]$ , where  $\hat{\mathcal{D}} = \hat{S} \otimes \mathbb{1}$  with global swap operator  $\hat{S}$ . We take  $\hat{U}$  to be the parity inversion symmetric Random Phase Model (RPM) with discrete time translation symmetry, defined in App. A 2 a. The local Hilbert-space dimension is denoted by  $q$ .

We compute the TopSFF using two complementary finite- $q$  methods. Firstly, we estimate the TopSFF by sampling over random circuit realizations. Secondly, by constructing a transfer matrix after the ensemble average of the RPM tensor network, we exactly compute TopSFF for small  $t$  and arbitrary  $L$ , as described in App. I 1. The two methods agree, as demonstrated in Fig. S26. We primarily use the second method, despite its restriction to  $t = 2$ , because it is fluctuation free and exact up to machine precision. This enables access to large  $L$ , allowing us to verify at finite  $q$  the  $\mathcal{PT}$  symmetry breaking signatures predicted in the large- $q$  limit.

Figure S27 shows the time dependence of the TopSFF for the parity symmetric RPM. For  $q = 3, 4$ , at late times, the data approach the plateau predicted  $\bar{K}_{\text{top}} \propto q^{L/2}$  by Eq. (SB.4), consistent with the many-body quantum system being described by a zero-dimensional RMT after the Heisenberg time  $t_{\text{Hei}} \propto q^L$ . However, for  $q = 3, 4$ , unlike the conventional SFF, the TopSFF does not show a clear ramp plateau behaviour in the pre-Heisenberg regime. The TopSFF behaviour in the pre-Heisenberg regime is investigated in the main text and below. For  $q = 2$ , the many-body dynamics is non-chaotic, and the TopSFF approaches the plateau on a timescale shorter than the Heisenberg time.

In Fig. S28, we compute the space dependence of momentum-unresolved TopSFF for period-one driving along the parity-inversion axes and the momentum-resolved TopSFF in the  $k = (0, 0, 0)$  sector, for  $q = 2, 3$ . For period-one driving, the dominant contribution comes from the  $k = (0, 0, 0)$  sector, consistent with the large- $q$  analysis. However, the quantitative test described below [Fig. S31] shows that neither  $q = 2$  nor  $q = 3$  is described by the large- $q$  chaotic TopSFF theory. This description applies only for  $q \geq 4$ , and we therefore focus on this regime below. While the

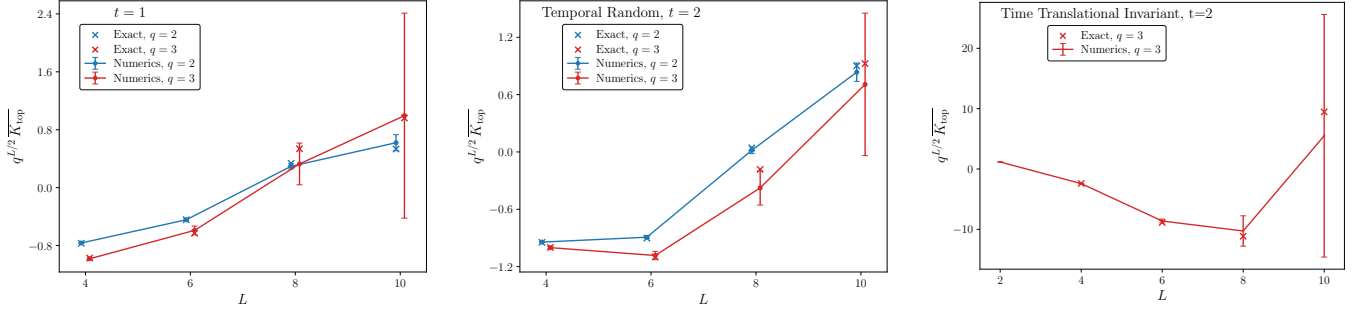


FIG. S26. **Two independent methods of obtaining finite- $q$  small- $t$  TopSFF**  $\overline{K}_{\text{top}}$  for parity symmetric RPM SA.4 at variance  $\epsilon = 1$  via sampling over  $5 \times 10^6$  circuit realizations (dots) and exact symbolic computation (crosses) as described in I1. In both panels, blue data denotes  $q = 2$  and red data denotes  $q = 3$ . The exact finite- $q$  results are overlaid for comparison, showing good agreement with the numerical results.

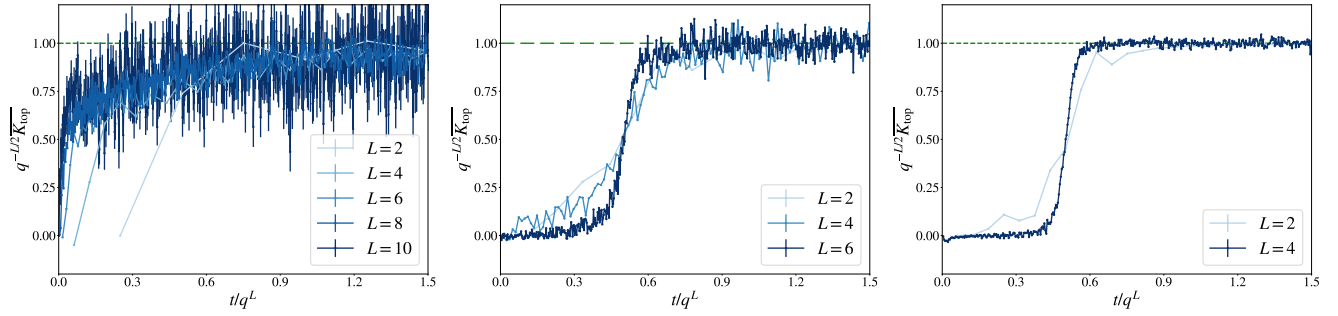


FIG. S27. **TopSFF  $\overline{K}_{\text{top}}$  against time** for the parity symmetric RPM (SA.5) at variance  $\epsilon = 1$ , obtained by sampling for  $q = 2$  (left),  $q = 3$  (middle), and  $q = 4$  (right). We plot the rescaled quantity  $q^{-L/2} \overline{K}_{\text{top}}$  against  $t/q^L$  for several system sizes. For  $q = 3, 4$ , the data show good agreement with the predicted long-time plateau and Heisenberg time scaling from Eq. (SB.4), namely  $\overline{K}_{\text{top}} \propto q^{L/2}$  for  $t \gtrsim t_{\text{Hei}}$ , with  $t_{\text{Hei}} \propto q^L$ . However, the pre-Heisenberg regime for  $q = 3, 4$  is not well described by the conventional SFF ramp-plateau behaviour. This regime is investigated in the main text and below. For  $q = 2$ , the many-body dynamics is non-chaotic, and the TopSFF approaches the plateau on a timescale shorter than the Heisenberg time.

absence of chaos in the  $q = 2$  RPM was previously noted in Ref. [13], the corresponding  $q = 3$  behaviour had not been established.

Fig. S29 provides a sector-by-sector check of the finite- $q$  TopSFF at  $t = 2$  and  $q = 4$ . We sweep all momentum sectors  $k = (k_b, k_c, k_d)$ , and find that the exact finite- $q$  data obey the symmetry constraints predicted by the large- $q$  generalized Boltzmann factor, including invariance under  $k_c \leftrightarrow k_d$  and momentum inversion  $k \leftrightarrow -k$ . The qualitative sector dependence in finite- $q$  in Fig. S29 is also consistent with the large- $q$  prediction in Fig. S15: symmetry-related sectors coincide, while sectors governed by real negative or complex-conjugate leading eigenvalues show the corresponding

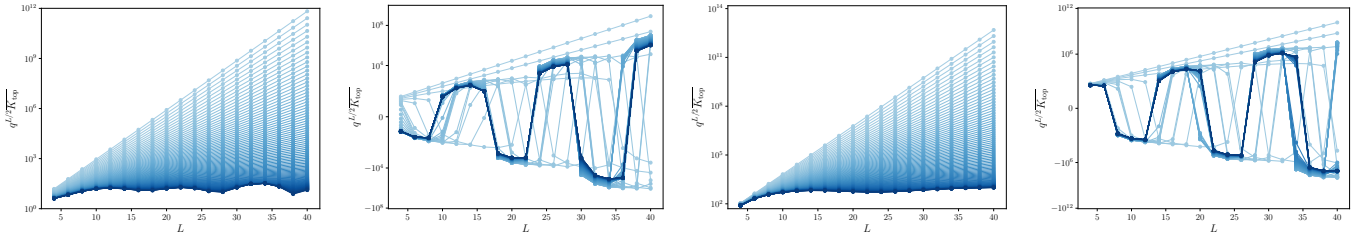


FIG. S28. **Exact TopSFF at  $t = 2$  for small  $q$ .** From left to right: momentum-unresolved TopSFF with period-1 driving along parity inversion axes for  $q = 2$  and  $q = 3$ , and momentum-resolved TopSFF in the  $k = (0, 0, 0)$  sector for  $q = 2$  and  $q = 3$ . We plot  $q^{L/2} \overline{K}_{\text{top}}$  for 100 values of  $\epsilon$  ranging from 0.01 (lighter curves) to 2 (darker curves). Note that a test described below [Fig. S31] shows that the large- $q$  chaotic description of the TopSFF applies only for  $q \geq 4$ .

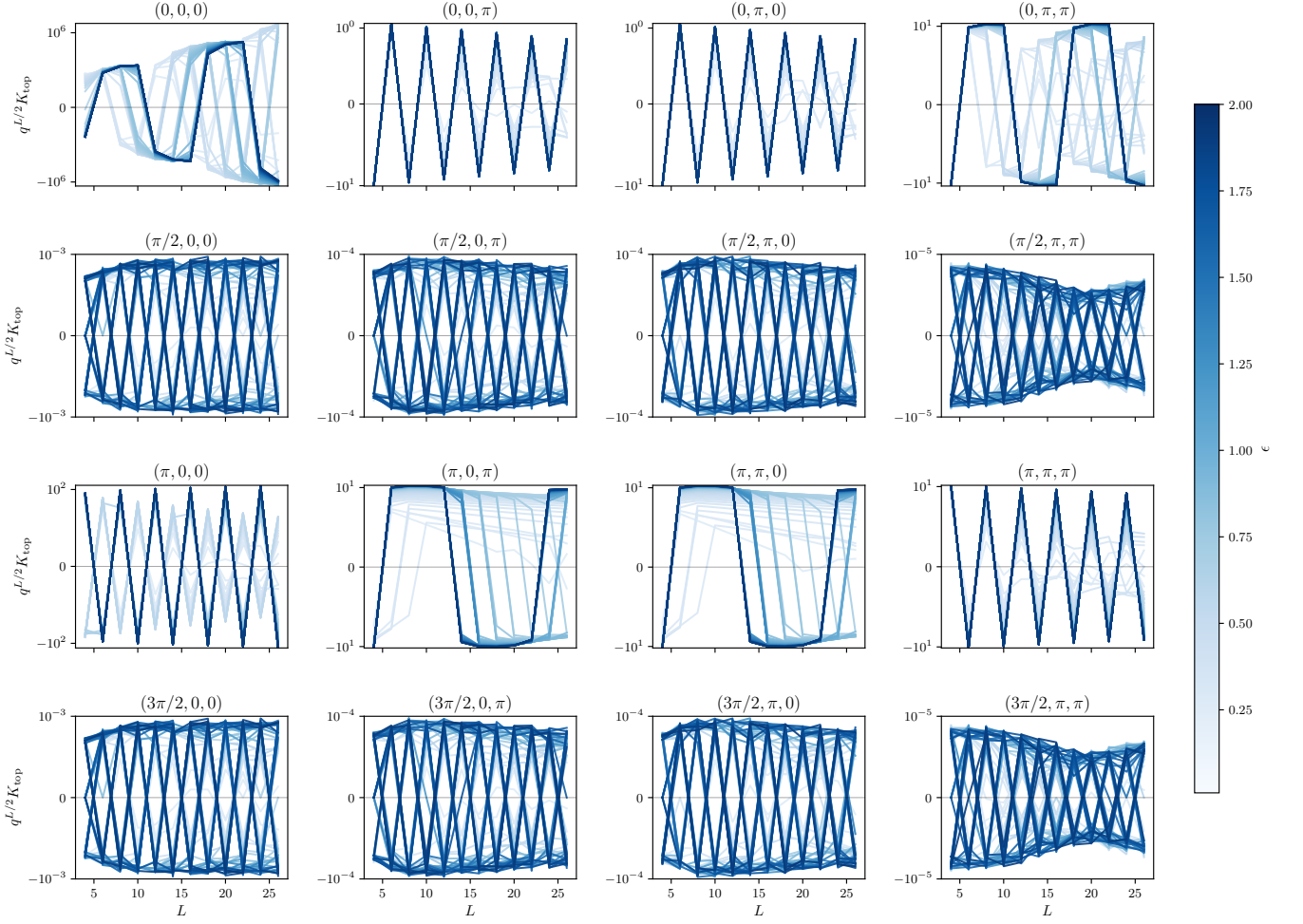


FIG. S29. **Exact TopSFF at  $t = 2$  and  $q = 4$  for all momentum sectors.** Consistent with the large- $q$  analysis in Fig. S15, the data exhibit the expected symmetries under the exchange  $k_c \leftrightarrow k_d$  and under momentum inversion  $k \leftrightarrow -k$ : in the figure, column 2 is identical to column 3, and row 2 is identical to row 4. In particular, as predicted in Fig. S15, the sectors  $(\pi, 0, 0)$  and  $(\pi, \pi, \pi)$  are governed by a negative real eigenvalue, leading to sign-flipping behaviour as a function of  $L$ . The sector  $(0, 0, 0)$  displays oscillatory behaviour, consistent with the dominant eigenvalues forming a complex conjugate pair. The sectors exhibiting a  $\mathcal{PT}$  transition, such as  $(\pi, \pi, 0)$ , are analysed in the main text.

monotonic/sign-changing or oscillatory dependence on  $L$ . In the following, we focus on the  $k = (\pi, \pi, 0)$  sector. As discussed in the main text, this sector is singled out by the large- $q$  analysis because its leading eigenvalues can have moduli exceeding unity for sufficiently large  $q$ , giving exponential growth with system size, while also exhibiting a  $\mathcal{PT}$  transition at finite interaction strength. It therefore provides the cleanest setting in which to diagnose the emergent  $\mathcal{PT}$  transition of TopSFF.

In Fig. S30, we examine the finite- $q$  dynamics in the momentum sector  $k = (\pi, \pi, 0)$ , showing the exact TopSFF at  $t = 2$  for  $q = 4, 5, 6, 20, 30$  while sweeping  $\epsilon$ . For  $\epsilon < \epsilon_{\text{EP}}$ , the data are non-oscillatory at sufficiently large  $L$ , with either exponential decay or, for sufficiently large  $q$ , exponential growth, consistent with the large- $q$  prediction. This is consistent with the  $\mathcal{PT}$  unbroken phase. For  $\epsilon > \epsilon_{\text{EP}}$ , the TopSFF exhibits oscillations in  $L$  with an exponential envelope, consistent with the  $\mathcal{PT}$  broken phase. Near  $\epsilon = \epsilon_{\text{EP}}$ , as discussed in the main text, the unresolved TopSFF does not directly expose the Jordan-block contribution, because the corresponding prefactor vanishes for the physical boundary vector. Below, we make this qualitative finite- $q$  signature quantitative by extracting  $\epsilon_{\text{EP}}$ , together with effective traces, determinants and eigenvalues, using the Cayley-Hamilton relation. We then resolve the TopSFF into Gaussian and non-Gaussian boundary sectors to diagnose the polynomial-in- $L$  scaling induced by Jordan non-diagonality.

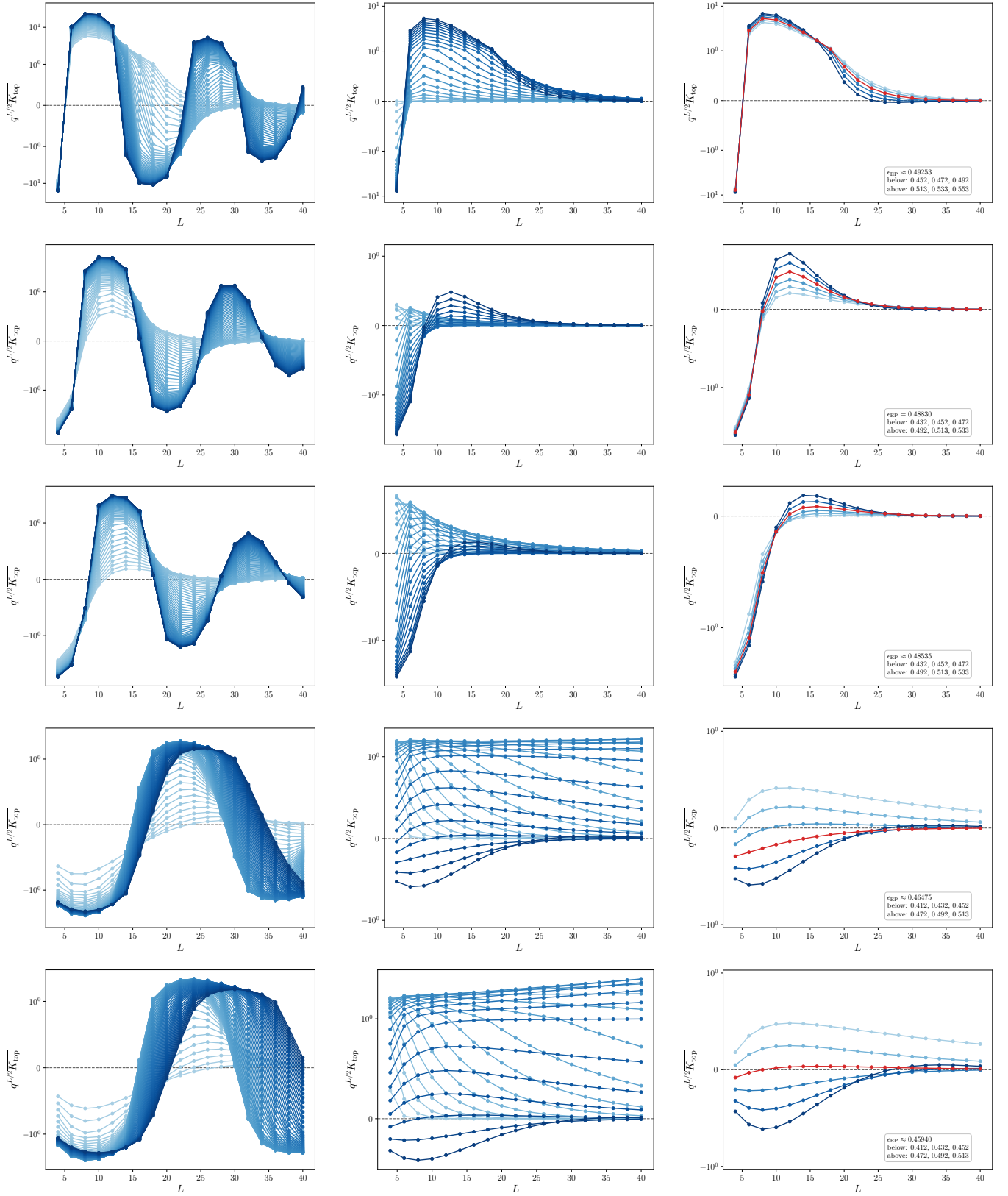


FIG. S30. **Exact TopSFF at  $t = 2$  in the momentum sector  $(k_b, k_c, k_d) = (\pi, \pi, 0)$  for  $q = 4, 5, 6, 20, 30$ .** We plot  $q^{L/2} \overline{K}_{top}$  as a function of  $L$  for 100 values of  $\epsilon$  in the range  $0.01 \leq \epsilon \leq 2$ . The rows correspond, from top to bottom, to  $q = 4$ ,  $q = 5$ ,  $q = 6$ ,  $q = 20$  and  $q = 30$ . The columns show, from left to right: curves classified as oscillatory, curves classified as non-oscillatory, and the six values of  $\epsilon$  closest to the estimated transition point  $\epsilon_{EP}$ . For  $q = 4$ ,  $q = 5$ ,  $q = 6$ ,  $q = 20$  and  $q = 30$ , the estimated transition points are  $\epsilon_{EP} \approx 0.4925$ ,  $0.488$ ,  $0.48535$ ,  $0.46475$  and  $0.45627$  respectively. Within each panel, lighter to darker curves indicate increasing  $\epsilon$ . Note that an exponential increase in  $L$  can be observed in  $q \geq 20$  (e.g. the light blue curves in the middle panel of row 4), consistent with the large- $q$  prediction.

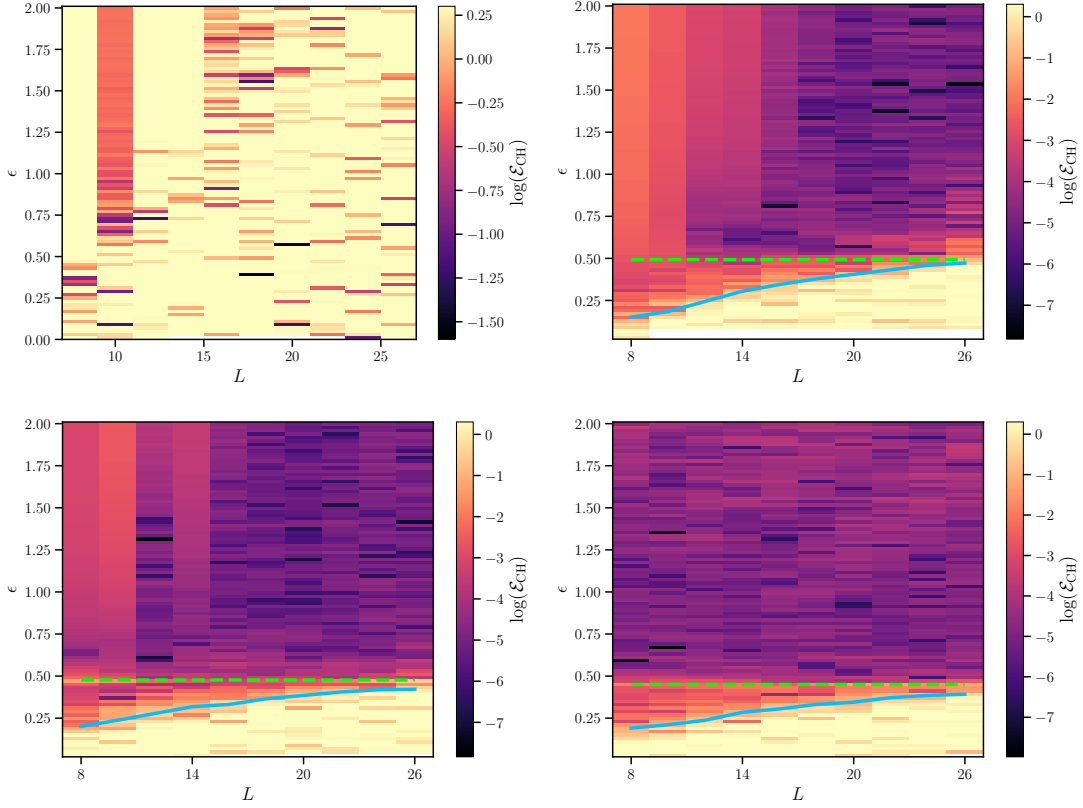


FIG. S31. **Validity of the TopSFF chaotic description in the  $(\epsilon, L)$  plane.** We quantify the chaotic description by probing the accuracy of the Cayley-Hamilton description using  $\mathcal{E}_{\text{CH}}$ , defined in Eq. (SL4), for  $q = 3$  (top left),  $q = 4$  (top right),  $q = 10$  (bottom left) and  $q = 100$  (bottom right). The dashed green lines indicate the  $\mathcal{PT}$  transition, while the blue lines indicate the boundary between chaotic and non-chaotic regimes.

### a. Cayley-Hamilton extraction and stability

In the large- $q$  expansion, the TopSFF in each momentum sector is governed by a  $2 \times 2$  transfer matrix. As discussed in App. F 1, the Cayley-Hamilton (CH) relation then allows one to extract the trace and determinant of the transfer matrix, and hence its eigenvalues and signatures of the  $\mathcal{PT}$  transition. At finite  $q$ , the TopSFF can be evaluated as  $\overline{\mathcal{K}}_{\text{top}}(\ell) = \phi^T \tilde{\mathcal{B}}^\ell \phi$ , with the finite- $q$  transfer matrix defined in App. I 1, and with  $\ell \equiv L_e$ . At finite  $q$ , we conjecture, and verify numerically, that the momentum sectors remain decoupled and that each sector is governed by an effective two-dimensional Cayley-Hamilton relation,  $\tilde{\mathcal{B}}^2 = \hat{\mathbf{t}} \tilde{\mathcal{B}} - \hat{\mathbf{d}} \mathbb{1}$ , where  $\hat{\mathbf{t}} := \text{tr} \tilde{\mathcal{B}}$  and  $\hat{\mathbf{d}} := \det \tilde{\mathcal{B}}$ . Multiplying this identity by  $\phi^T \tilde{\mathcal{B}}^\ell$  from the left and by  $\phi$  from the right gives the recurrence relation

$$\overline{\mathcal{K}}_{\text{top}}(\ell + 2) = \hat{\mathbf{t}} \overline{\mathcal{K}}_{\text{top}}(\ell + 1) - \hat{\mathbf{d}} \overline{\mathcal{K}}_{\text{top}}(\ell). \quad (\text{SL.1})$$

Thus, from four consecutive TopSFF values, one can locally estimate the effective trace and determinant as

$$\hat{\mathbf{t}}_\ell := \frac{\overline{\mathcal{K}}_{\text{top}}(\ell + 1)\overline{\mathcal{K}}_{\text{top}}(\ell + 2) - \overline{\mathcal{K}}_{\text{top}}(\ell)\overline{\mathcal{K}}_{\text{top}}(\ell + 3)}{\overline{\mathcal{K}}_{\text{top}}(\ell + 1)^2 - \overline{\mathcal{K}}_{\text{top}}(\ell)\overline{\mathcal{K}}_{\text{top}}(\ell + 2)}, \quad \hat{\mathbf{d}}_\ell := \frac{\overline{\mathcal{K}}_{\text{top}}(\ell + 2)^2 - \overline{\mathcal{K}}_{\text{top}}(\ell + 1)\overline{\mathcal{K}}_{\text{top}}(\ell + 3)}{\overline{\mathcal{K}}_{\text{top}}(\ell + 1)^2 - \overline{\mathcal{K}}_{\text{top}}(\ell)\overline{\mathcal{K}}_{\text{top}}(\ell + 2)}, \quad (\text{SL.2})$$

and we define the effective discriminant as

$$\hat{\Delta}_\ell(\epsilon) := \hat{\mathbf{t}}_\ell(\epsilon)^2 - 4\hat{\mathbf{d}}_\ell(\epsilon). \quad (\text{SL.3})$$

At finite  $q$ , the CH relation is overdetermined when applied over a range of  $\ell$ . The extracted quantities  $\hat{\mathbf{t}}_\ell$  and  $\hat{\mathbf{d}}_\ell$  therefore acquire a  $\ell$ -dependence, and can be interpreted as effective trace and determinant only in regimes where this dependence is weak. This is illustrated in Fig. S32, where we compare the exact TopSFF data with the locally extracted CH discriminant  $\hat{\Delta}_\ell$  in the  $k = (\pi, \pi, 0)$  sector. The left panels show  $\overline{\mathcal{K}}_{\text{top}}$  as a function of  $L$ , while the right

panels show the corresponding  $\widehat{\Delta}_\ell$  obtained from the local CH extraction. Curves are coloured by  $\epsilon$ . For  $q = 3$ , the extracted discriminant is strongly unstable, showing that the effective CH description does not apply. By contrast, for  $q \geq 4$ ,  $\widehat{\Delta}_{L_e}$  is stable over an extended range of  $(\epsilon, L)$ , and its sign separates the oscillatory and non-oscillatory regimes of the TopSFF. The remaining breakdown occurs mainly at small  $\epsilon$  and large  $L$ , where the chaotic CH description fails, and at very large  $L$ , where numerical instabilities set in.

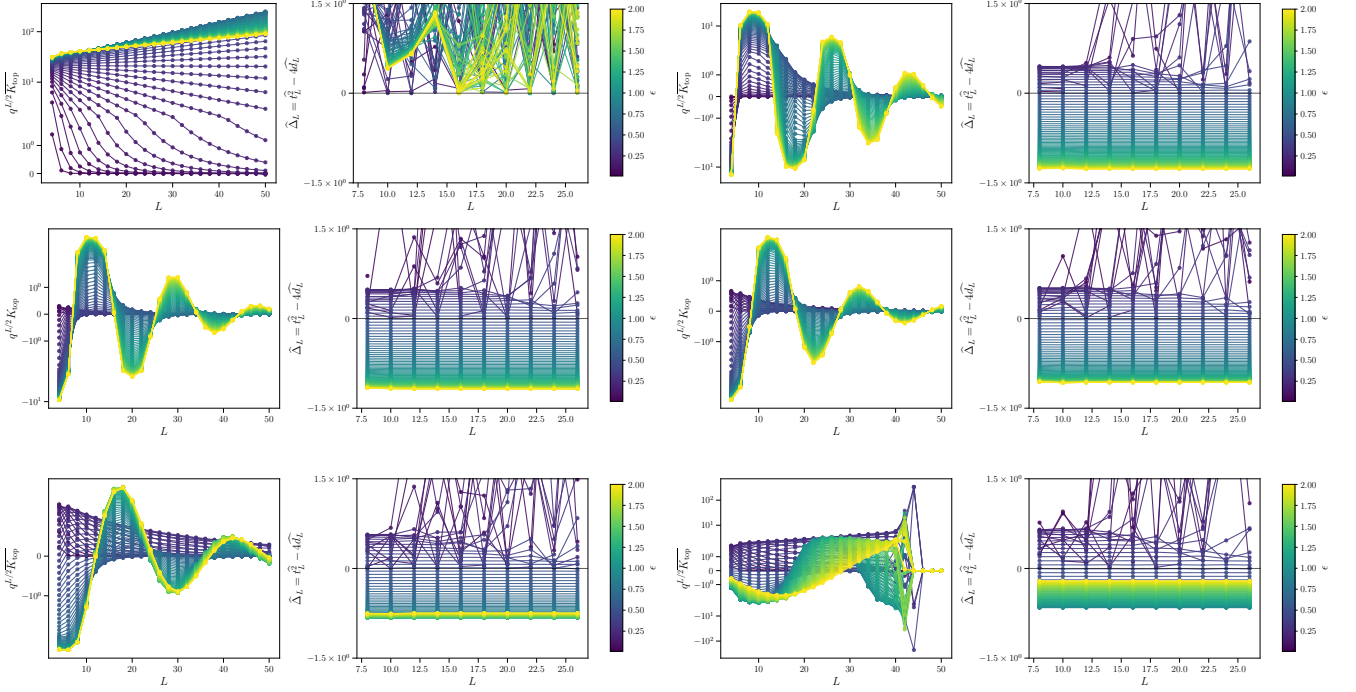


FIG. S32. **Comparison of the TopSFF data and the extracted Cayley-Hamilton discriminant.** For the  $k = (\pi, \pi, 0)$  sector, we compare TopSFF as functions of system size  $L$  with the corresponding locally extracted discriminant  $\widehat{\Delta}_L = \widehat{t}_L^2 - 4\widehat{d}_L$ . The left column shows the TopSFF data, while the right column shows  $\widehat{\Delta}_L$  extracted locally from the local Cayley-Hamilton recurrence. From top to bottom the rows correspond to  $q = 3, 4, 10, 100$  respectively. Curves are coloured by  $\epsilon$ . The comparison highlights two effects: (i) for small  $\epsilon$ , the chaotic description, as quantified by the Cayley-Hamilton extraction, fails at sufficiently large  $L$ , and (ii) at large enough  $L$ , numerical instability also sets in.

To diagnose the stability of the extracted effective trace  $\widehat{t}_\ell$  and determinant  $\widehat{d}_\ell$ , we compute the relative variation

$$\mathcal{E}_{\text{CH}}(\ell, \epsilon) := \max \left[ \frac{|\widehat{t}_{\ell+\delta\ell}(\epsilon) - \widehat{t}_\ell(\epsilon)|}{\frac{1}{2} (|\widehat{t}_{\ell+\delta\ell}(\epsilon)| + |\widehat{t}_\ell(\epsilon)|) + \eta}, \frac{|\widehat{d}_{\ell+\delta\ell}(\epsilon) - \widehat{d}_\ell(\epsilon)|}{\frac{1}{2} (|\widehat{d}_{\ell+\delta\ell}(\epsilon)| + |\widehat{d}_\ell(\epsilon)|) + \eta} \right], \quad (\text{SL.4})$$

where  $\eta = 10^{-12}$  is a small regularizer that prevents singular denominators. Small values of  $\mathcal{E}_{\text{CH}}$  indicate that the locally extracted  $\widehat{t}_\ell$  and  $\widehat{d}_\ell$  are stable upon varying  $\ell$ , and hence that the effective two-dimensional Cayley-Hamilton description is self-consistent. In this stable regime, the sign change of  $\widehat{\Delta}_\ell$  provides a reliable finite- $q$  diagnostic of the  $\mathcal{PT}$  transition.

Figure S31 shows  $\log \mathcal{E}_{\text{CH}}$  in the  $(\epsilon, L)$  plane for  $q = 3, 4, 10, 100$ . The  $q = 3$  data do not exhibit an extended stable region, consistent with the absence of the large- $q$  chaotic TopSFF description. By contrast, for  $q \geq 4$ , a broad region with small  $\mathcal{E}_{\text{CH}}$  appears at sufficiently large  $\epsilon$ , showing that the effective CH description is valid over an extended part of the  $(\epsilon, L)$  plane. The dashed green line marks the extracted  $\mathcal{PT}$  transition, while the blue curve indicates the boundary below which the CH description becomes unstable.

We define a truncation length  $L_{\text{trunc}}$ , above which the CH extraction is unstable. For each fixed  $(q, \epsilon)$ , we scan the local estimates in increasing  $L$  and retain the initial stable region satisfying

$$\mathcal{E}_{\text{CH}}(\ell) \leq \mathcal{E}_{\text{CH}}^{\text{cut}}, \quad \mathcal{E}_{\text{CH}}^{\text{cut}} = 1. \quad (\text{SL.5})$$

We define  $L_{\text{trunc}}$  as the largest retained value of  $\ell$  before this stability criterion fails. Thus  $L_{\text{trunc}}$  gives the maximum effective length up to which the locally extracted Cayley-Hamilton coefficients can be treated as stable for a given

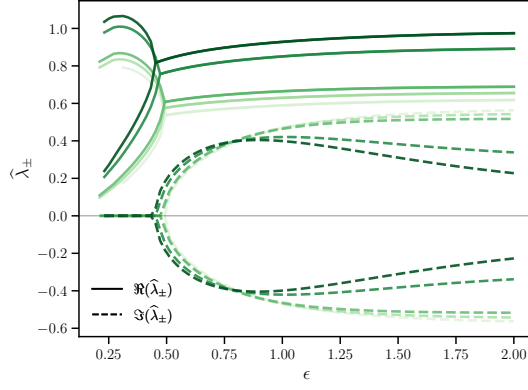


FIG. S33. **Effective eigenvalues from the Cayley-Hamilton extraction for increasing  $q$ .** The real and imaginary parts of the effective eigenvalues  $\hat{\lambda}_{\pm}$  are obtained from the extracted Cayley-Hamilton coefficients and plotted as functions of  $\epsilon$  for  $q = 4, 5, 6, 20$  and  $100$ , from light to dark shades. Solid and dashed curves denote  $\Re(\hat{\lambda}_{\pm})$  and  $\Im(\hat{\lambda}_{\pm})$ , respectively. For each  $q$ , the real branches coalesce near the exceptional point, after which the eigenvalues acquire non-zero imaginary parts. As  $q$  increases, the EP persists, and the moduli of the eigenvalues increase, approaching the spectrum predicted by the large- $q$  analysis.

$(q, \epsilon)$ . In the stable regime, we obtain the final effective coefficients by averaging the local estimates  $\{\hat{\mathbf{t}}_{\ell}\}$  and  $\{\hat{\mathbf{d}}_{\ell}\}$  over the retained window,

$$\hat{\mathbf{t}} = \frac{1}{|\mathcal{W}|} \sum_{\ell \in \mathcal{W}} \hat{\mathbf{t}}_{\ell}, \quad \hat{\mathbf{d}} = \frac{1}{|\mathcal{W}|} \sum_{\ell \in \mathcal{W}} \hat{\mathbf{d}}_{\ell}, \quad \hat{\Delta} := \hat{\mathbf{t}}^2 - 4\hat{\mathbf{d}},$$

where  $\mathcal{W}$  denotes the retained CH stable range,  $L \leq L_{\text{trunc}}$ . These averaged coefficients are then used to form the effective discriminant and eigenvalues used below.

#### b. Cayley-Hamilton extraction and $\mathcal{PT}$ transitions

The corresponding effective discriminant and eigenvalues are

$$\hat{\Delta} = \hat{\mathbf{t}}^2 - 4\hat{\mathbf{d}}, \quad \hat{\lambda}_{\pm} = \frac{\hat{\mathbf{t}} \pm \sqrt{\hat{\Delta}}}{2}. \quad (\text{SL.6})$$

Since  $\hat{\mathbf{t}}$  and  $\hat{\mathbf{d}}$  are real, the sign of  $\hat{\Delta}$  diagnoses the  $\mathcal{PT}$  transition:  $\hat{\Delta} > 0$  gives two real effective eigenvalues, while  $\hat{\Delta} < 0$  gives a complex-conjugate pair,  $\hat{\lambda}_{-} = \hat{\lambda}_{+}^*$ . Thus the zero of  $\hat{\Delta}$  locates the finite- $q$  exceptional point. In Fig. S33, we plot the effective eigenvalues in the  $k = (\pi, \pi, 0)$  sector for increasing  $q$ . Across the transition, the two real branches coalesce and split into a complex-conjugate pair, providing a direct finite- $q$  signature of  $\mathcal{PT}$  symmetry breaking. The extracted spectra show qualitative agreement with the large- $q$  eigenvalues in the same momentum sector, see figures in main text and Fig. S15, and approach them as  $q$  is increased. In particular, the eigenvalue moduli in the  $\mathcal{PT}$  unbroken phase increase with  $q$  and eventually exceed unity, so that the TopSFF changes from exponential decay to exponential growth with system size. For larger  $t$ , the large- $q$  analytics predicts exponential growth of the TopSFF in the  $\mathcal{PT}$  unbroken phase throughout the pre-Heisenberg regime.

Although the TopSFF extraction gives access to effective eigenvalues rather than eigenvectors, the effective discriminant still provides a useful proxy for eigenvector coalescence. We define the discriminant based proxy Petermann factor  $P_{\pm}^{\text{proxy}}$  and proxy eigenvector overlap  $O_{\pm}^{\text{proxy}}$  as

$$P^{\text{proxy}}(\epsilon) = \frac{1}{|\hat{\Delta}(\epsilon)| + \eta}, \quad O^{\text{proxy}}(\epsilon) = \left| \sqrt{\hat{\Delta}(\epsilon)} \right|, \quad (\text{SL.7})$$

where  $\eta = 10^{-12}$  is a small regularizer that removes the numerical singularity at  $\hat{\Delta} = 0$ . The first quantity mimics the divergence of the Petermann factor at an exceptional point, while the second tracks the square-root eigenvalue

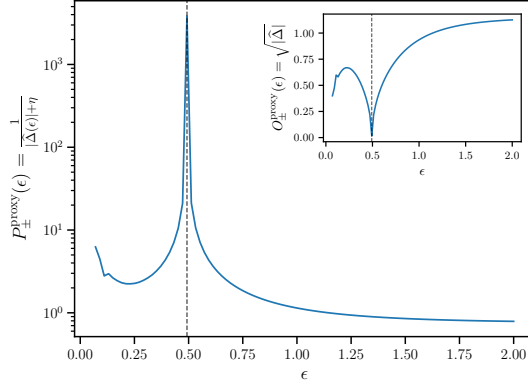


FIG. S34. **Finite- $q$  Petermann factor proxy for the exceptional point.** For  $q = 4$ , we plot the Petermann factor proxy  $P_{\pm}^{\text{proxy}}(\epsilon) := 1/(\sqrt{|\widehat{\Delta}(\epsilon)|} + \eta)$ , where  $\widehat{\Delta}$  is the discriminant of the two leading modes and  $\eta = 10^{-12}$  is a small regulator. The vertical dashed line marks  $\epsilon_{\text{EP}} \simeq 0.490495$ . The peak in  $P_{\pm}^{\text{proxy}}$ , together with the collapse of  $\sqrt{|\widehat{\Delta}|}$  in the inset, provide proxy signatures of eigenvector coalescence at the EP.

splitting and vanishes as the two effective eigenvalues coalesce. As shown in Fig. S34, these finite- $q$  proxies display the same qualitative behaviour as the large- $q$  Petermann factor and eigenvector overlap diagnostics in Figs. S19 and S18.

At finite  $q$ , at the extracted exceptional point, the boundary-resolved TopSFF combination  $\frac{\overline{\mathcal{K}}_{\text{top}}^{00} + \overline{\mathcal{K}}_{\text{top}}^{11}}{[\widehat{t}/2]^{L e^{-1}}}$  exhibits linear scaling in  $L$ , consistent with the Jordan-block contribution expected at an EP. Away from the transition, the curves bend away from this linear form, as expected when the effective spectrum consists either of two distinct real eigenvalues or of a complex-conjugate pair. Thus the boundary-resolved TopSFF exposes the Jordan contribution that is hidden in the unresolved TopSFF by the vanishing physical-boundary prefactor. In the main text, we demonstrated this boundary-resolved scaling for  $q = 4$  in the  $k = (\pi, \pi, 0)$  sector. In Fig. S35, left panel, we show the corresponding finite- $q$  data for  $q = 6$ , again observing the linear-in- $L$  scaling after the exponential envelope is divided out. The same behaviour is observed more generally for  $q \geq 4$ , whenever the Cayley-Hamilton extraction is stable. The right panel of Fig. S35 checks that the EP extracted from the boundary-resolved amplitudes coincides with that obtained from the full TopSFF. We compare the transition points extracted independently from  $\overline{\mathcal{K}}_{\text{top}}^{00}$  and  $\overline{\mathcal{K}}_{\text{top}}^{11}$  with  $\epsilon_{\text{EP}}^{\text{R}}$  obtained from the unresolved TopSFF. The small differences indicate that the boundary-resolved amplitudes locate the same finite- $q$  exceptional point, up to numerical extraction errors.

## 2. Temporally extended topological defects

We consider the TopSFF of a temporally extended global swap defect  $\widehat{\mathcal{D}} = \widehat{\mathcal{S}} \otimes \widehat{\mathbb{1}}$  acting on  $U_s \otimes U_s$  in the spatial direction. The generic quantum many-body chaotic systems  $\widehat{U}_s(t, L) := \prod_{i=1}^L \widehat{V}(t, L)$  is generated by the space-time dual transfer matrices  $\widehat{V}(t, L)$  [Fig. 3(a) purple] of RPM defined in (SA.20) and HRM defined in (SA.27), satisfying the  $[\widehat{V}(t, L), \widehat{\mathcal{S}}] = 0$ , and therefore has time reversal symmetry (TRS).

We follow the scheme of Ref. [26] to compute the SFF and TopSFF in the Thouless double-scaling limit

$$\kappa(\ell) = \lim_{\substack{L, t \rightarrow \infty \\ \ell \equiv L/L_{\text{Th}}(t)}} K(t, L), \quad (\text{SL.8})$$

and analogously for the TopSFF, where  $L_{\text{Th}}(t)$  is the Thouless length. We collapse the numerical data by estimating  $L_{\text{Th}}(t)$  independently for each time  $t$ . To do this, we choose a reference point  $\ell_0$  and set  $y_0 = \kappa(\ell_0)$ . For each fixed  $t$ , we interpolate the numerical curve  $K(t, L)$  and find the first intersection with the horizontal line  $y = y_0$ , which defines an intermediate scale  $L^*(t)$  through  $K(t, L^*(t)) = y_0$ . Since  $L^*(t)/L_{\text{Th}}(t) = \ell_0$  in the scaling regime, this yields the estimator  $L_{\text{Th}}(t) = L^*(t)/\ell_0$ . Finally, plotting  $K(t, L)$  against the rescaled variable  $L/L_{\text{Th}}(t)$  produces the desired collapse.

In addition to the above procedure, we make two practical adjustments to improve the robustness of the collapse. First, there is residual freedom in the choice of the reference point  $\ell_0$ . We therefore scan over a range of  $\ell_0$  values and quantify the quality of the resulting collapse by a sum of squared errors, defined as the squared distance between the

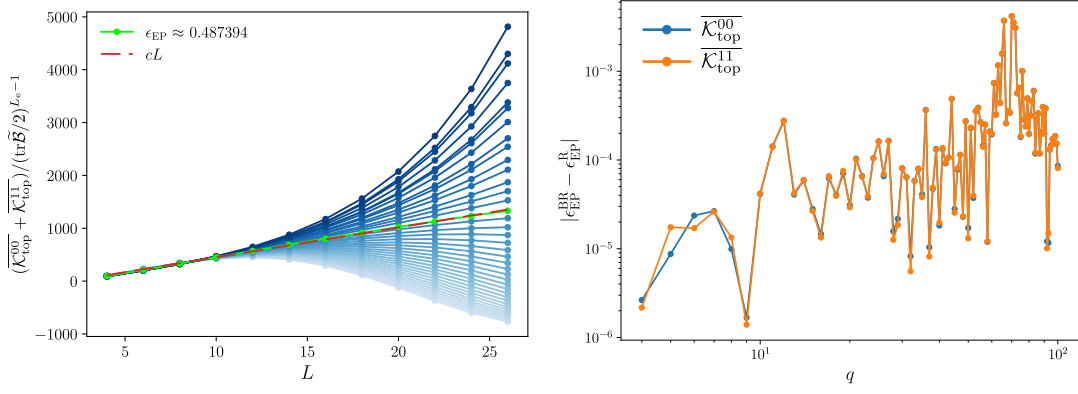


FIG. S35. **Finite- $q$  evidence for EP non-diagonalizability.** Left and middle: the boundary-resolved combination  $(\overline{\mathcal{K}}_{\text{top}}^{00} + \overline{\mathcal{K}}_{\text{top}}^{11}) / (\text{tr} \tilde{\mathcal{B}}/2)^{L_e - 1}$  is plotted as a function of the physical system size  $L$  in the  $k = (\pi, \pi, 0)$  sector for  $q = 6$  (see also the case of  $q = 4$  in the main text), respectively. Here  $L_e = L/2 - 1$ , and  $\hat{\mathbf{t}}/2$  becomes the degenerate effective eigenvalue at the exceptional point. The highlighted curve at  $\epsilon = \epsilon_{\text{EP}}$  follows the dashed linear guide, showing that, after the exponential envelope is divided out, the remaining growth is linear in  $L_e \propto L$ . This provides a finite- $q$  signature of the non-diagonalizable Jordan block. The extracted transition points are  $\epsilon_{\text{EP}}^{\text{BR}} \simeq 0.490495$  for  $q = 4$  and  $\epsilon_{\text{EP}}^{\text{BR}} \simeq 0.487394$  for  $q = 6$ . Right: comparison between the exceptional point  $\epsilon_{\text{EP}}^{\text{BR}}$  extracted from the boundary-resolved TopSFF  $\overline{\mathcal{K}}_{\text{top}}^{00}$  and  $\overline{\mathcal{K}}_{\text{top}}^{11}$ , and  $\epsilon_{\text{EP}}^{\text{R}}$  extracted from the regular TopSFF. The small difference  $|\epsilon_{\text{EP}}^{\text{BR}} - \epsilon_{\text{EP}}^{\text{R}}|$  shows that the boundary-resolved amplitudes locate the same EP as the regular TopSFF, up to finite- $q$  and numerical extraction errors.

collapsed data points and the scaling function  $\kappa(\ell)$ . The optimal  $\ell_0$  is chosen by minimising this sum over the scan range.

Second, to improve the robustness of the interpolation and intersection-finding step in the presence of noisy data, we optionally apply Gaussian filtering. Writing the measured data as  $y_i = s_i + \eta_i$ , with underlying signal  $s_i$  and noise  $\eta_i$ , we define the filtered data by the discrete convolution

$$y_i^{(\text{flt})} = \sum_k g_k y_{i-k}, \quad g_k = \frac{\exp[-k^2/(2\sigma_g^2)]}{\sum_m \exp[-m^2/(2\sigma_g^2)]}, \quad \sum_k g_k = 1, \quad (\text{SL.9})$$

where  $\sigma_g$  controls the smoothing width. Assuming uncorrelated noise with variance  $\sigma_\eta^2$ , the filtered noise variance is  $\text{Var}(\eta_i^{(\text{flt})}) = \sum_k g_k^2 \text{Var}(\eta_{i-k}) = \sigma_\eta^2 \sum_k g_k^2 \leq \sigma_\eta^2$ . Thus the filter suppresses fluctuations by forming a weighted average over neighbouring points, leading to a more stable estimate of  $L^*(t)$  and  $L_{\text{Th}}(t)$ . We use this step only mildly, since excessive smoothing can wash out genuine fine structure in the data.

In Fig. S36, we apply this procedure to the TRS RPM and TRS RHM with a temporally extended global swap defect. The left and middle panels show the resulting collapse of the SFF and TopSFF, respectively, after rescaling the system size by the extracted Thouless length  $L_{\text{Th}}(t)$ . The data for different  $t$  and for both models collapse onto the large- $q$  scaling functions,  $\kappa(\ell) = 2 \cosh \ell$  for the SFF and  $\kappa_{\text{top}}(\ell) = 2 \sinh \ell$  for the TopSFF. These results demonstrate the universality of the scaling forms of SFF and TopSFF with temporally extended global swap defect. The right panel shows the extracted  $L_{\text{Th}}(t)$  for the two models, obtained independently from the SFF and TopSFF collapses. The SFF and TopSFF estimates agree within the numerical uncertainty, confirming that the two observables identify the same Thouless length.

In Fig. S37, we apply the same collapse procedure to the Floquet RPM and Floquet RHM with a temporally extended time translation defect. After rescaling the system size by the extracted Thouless length  $L_{\text{Th}}(t)$ , the SFF and TopSFF data for different  $t$  and for both models collapse onto the large- $q$  scaling functions  $\kappa(\ell) = e^\ell - \ell - 1$  and  $\kappa_{\text{top}}(\ell) = e^\ell - 1$ , respectively. Again, this demonstrates the universality of the time translation defect scaling forms beyond the large- $q$  limit. In the right panel, the independently extracted  $L_{\text{Th}}(t)$  values from the SFF and TopSFF collapses agree within numerical uncertainty, confirming that both observables identify the same Thouless length.

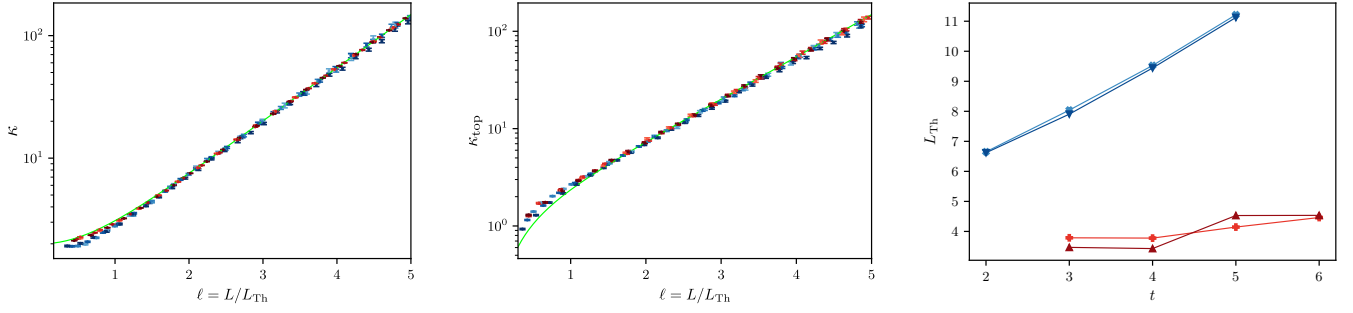


FIG. S36. **Scaling collapse of TopSFF with temporally extended global swap defect.** Left: scaling collapse of the SFF for TRS RPM defined in (SA.20) and TRS RHM defined in (SA.27). Middle: corresponding scaling collapse of the TopSFF. RPM (RHM) data are shown for timesteps  $t \in [2, 6]$  ( $t \in [2, 5]$ ), with darker shades of red (blue) indicating larger  $t$ . Results are averaged over 7500 realizations for RPM and 5100 realizations for RHM. In the left and middle panels, the data collapse onto the large- $q$  exact scaling forms,  $\kappa = 2 \cosh(\ell)$  for the SFF and  $\kappa_{\text{top}} = 2 \sinh(\ell)$  for the TopSFF (green lines). The RPM (RHM) data correspond to  $\epsilon = 1.56$  ( $\epsilon = 2.94$ ). Right: effective Thouless length  $L_{\text{th}}(t)$  for RPM (red) and RHM (blue). For each model, the SFF and TopSFF are shown in lighter and darker shades, respectively.

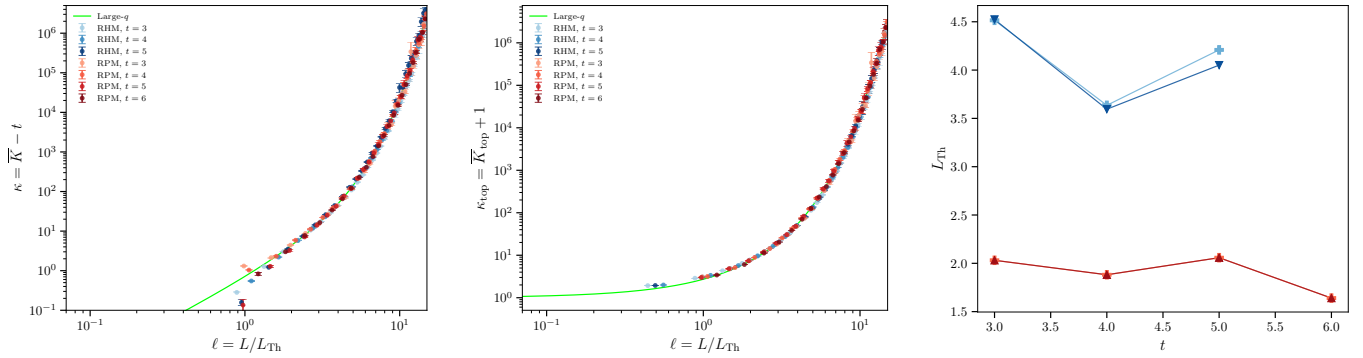


FIG. S37. **Scaling collapse of TopSFF with temporally extended translation defect.** Left: scaling collapse of the SFF for Floquet RPM defined in (SA.29) and Floquet RHM defined in (SA.33). Middle: corresponding scaling collapse of the TopSFF with a temporally extended time translation defect. RPM and RHM data are shown in red and blue, respectively, with darker shades indicating larger  $t$ . The data is averaged over 10000 circuit realisations. The RPM data is evaluated at  $\epsilon = 2$ , while the RHM data are evaluated at  $\epsilon = 1.85$ . In the left panel the SFF collapses onto  $\kappa = e^\ell - \ell - 1$ , while middle panel, the TopSFF collapses onto the large- $q$  scaling form  $\kappa_{\text{top}} = e^\ell - 1$ , shown as green reference curves. Right: effective Thouless length  $L_{\text{th}}(t)$  extracted from the SFF and TopSFF collapses for the RPM and RHM. For each model, the SFF and TopSFF are shown in lighter and darker shades, respectively.